

1

2

3

4

5

Simultaneous Measurement of Oscillation Parameters in Beam and Atmospheric Neutrino Data from Tokai-to-Kamioka and Super-Kamiokande Experiments

6

Daniel Robert Clement Barrow

7

8

Magdalen College,
Oxford University

9

Version 1.2

10

A Dissertation Submitted to Oxford University
11 for the Degree of Doctor of Philosophy

13 **Simultaneous Measurement of**

14 **Oscillation Parameters in Beam and**

15 **Atmospheric Neutrino Data from**

16 **Tokai-to-Kamioka and**

17 **Super-Kamiokande Experiments**

18 *Abstract*

19 Lorem ipsum dolor sit amet, consectetur adipiscing elit, sed do eiusmod tempor incididunt ut labore et dolore magna aliqua. Nulla aliquet porttitor lacus luctus accumsan tortor posuere. Pulvinar neque laoreet suspendisse interdum. Sem viverra aliquet eget sit. Nunc sed velit dignissim sodales ut eu sem integer vitae. At erat pellentesque adipiscing commodo elit at imperdiet dui accumsan. Fames ac turpis egestas integer eget aliquet nibh. Scelerisque eu ultrices vitae auctor eu augue. Purus non enim praesent elementum facilisis leo vel. Sollicitudin nibh sit amet commodo. Vitae auctor eu augue ut. Vel quam elementum pulvinar etiam. A condimentum vitae sapien pellentesque habitant morbi tristique senectus. Viverra accumsan in nisl nisi scelerisque eu ultrices. Sed viverra ipsum nunc aliquet bibendum enim.

32 Declaration

33 This dissertation is the result of my own work, except where ex-
34 plicit reference is made to the work of others, and has not been sub-
35 mitted for another qualification to this or any other university. This
36 dissertation does not exceed the word limit for the respective Degree
37 Committee.

38 Daniel Robert Clement Barrow

39 ©The copyright of this thesis rests with the author and is made available under a Creative
40 Commons Attribution Non-Commercial No Derivatives licence. Researchers are free to copy,
41 distribute or transmit the thesis on the condition that they attribute it, that they do not use
42 it for commercial purposes and that they do not alter, transform or build upon it. For any
43 reuse or redistribution, researchers must make clear to others the licence terms of this work.

44

Acknowledgements

45 at pretium nibh ipsum. Eget nunc scelerisque viverra mauris in aliquam. Arcu vitae
46 elementum curabitur vitae nunc sed velit dignissim. Sed arcu non odio euismod lacinia
47 at quis risus sed. Vitae tempus quam pellentesque nec nam aliquam sem et tortor.
48 Viverra aliquet eget sit amet tellus cras adipiscing. Purus sit amet luctus venenatis
49 lectus magna. In aliquam sem fringilla ut morbi tincidunt augue. Fermentum dui
50 faucibus in ornare. Aliquam malesuada bibendum arcu vitae elementum curabitur
51 vitae nunc sed.

52 Ultricies leo integer malesuada nunc vel risus commodo. Tellus cras adipiscing
53 enim eu turpis egestas pretium. Dictumst quisque sagittis purus sit amet volutpat
54 consequat mauris nunc. Vitae congue mauris rhoncus aenean vel elit scelerisque
55 mauris pellentesque. Vel facilisis volutpat est velit egestas dui id ornare. Suscipit
56 adipiscing bibendum est ultricies. At in tellus integer feugiat scelerisque varius
57 morbi enim. Cras semper auctor neque vitae tempus. Commodo sed egestas egestas
58 fringilla phasellus faucibus. Cras pulvinar mattis nunc sed blandit. Pretium viverra
59 suspendisse potenti nullam ac tortor vitae. Purus sit amet volutpat consequat. Orci
60 sagittis eu volutpat odio facilisis mauris. Sit amet massa vitae tortor condimentum
61 lacinia quis. Commodo sed egestas egestas fringilla phasellus. Sed libero enim sed
62 faucibus turpis. Vitae tempus quam pellentesque nec.

63 Blandit massa enim nec dui. Viverra tellus in hac habitasse platea dictumst vestibulu-
64 lum. Bibendum enim facilisis gravida neque convallis. Sagittis nisl rhoncus mattis
65 rhoncus urna neque. Nisl rhoncus mattis rhoncus urna neque. Ac tortor vitae purus
66 faucibus ornare. Aenean sed adipiscing diam donec adipiscing tristique risus. Sapien
67 nec sagittis aliquam malesuada bibendum. Et leo duis ut diam quam nulla. Tellus
68 rutrum tellus pellentesque eu tincidunt tortor aliquam nulla facilisi.

69 **Contents**

70	1. Introduction	1
71	2. Neutrino Oscillation Physics	2
72	2.1. Discovery of Neutrinos	2
73	2.2. Theory of Neutrino Oscillation	4
74	2.2.1. Three Flavour Oscillations	4
75	2.2.2. The MSW Effect	8
76	2.3. Neutrino Oscillation Measurements	9
77	2.3.1. Solar Neutrinos	11
78	2.3.2. Atmospheric Neutrinos	13
79	2.3.3. Accelerator Neutrinos	16
80	2.3.4. Reactor Neutrinos	18
81	2.4. Summary	20
82	3. T2K and SK Experiment Overview	23
83	3.1. The Super-Kamiokande Experiment	23
84	3.1.1. The SK Detector	24
85	3.1.2. Calibration	28
86	3.1.3. Data Acquisition and Triggering	31
87	3.1.4. Cherenkov Radiation	33
88	3.2. The Tokai to Kamioka Experiment	35
89	3.2.1. The Neutrino Beam	37
90	3.2.2. The Near Detector at 280m	40
91	3.2.2.1. Fine Grained Detectors	43
92	3.2.2.2. Time Projection Chambers	44

93	3.2.2.3. π^0 Detector	46
94	3.2.2.4. Electromagnetic Calorimeter	46
95	3.2.2.5. Side Muon Range Detector	48
96	3.2.3. The Interactive Neutrino GRID	48
97	4. Bayesian Statistics and Markov Chain Monte Carlo Techniques	50
98	4.1. Bayesian Statistics	51
99	4.2. Monte Carlo Simulation	52
100	4.2.1. Markov Chain Monte Carlo	53
101	4.2.2. Metropolis-Hastings Algorithm	56
102	4.2.3. MCMC Optimisation	58
103	4.3. Understanding the MCMC Results	61
104	4.3.1. Marginalisation	62
105	4.3.2. Parameter Estimation and Credible Intervals	63
106	4.3.3. Bayesian Model Comparisons	65
107	4.3.4. Comparison of MCMC Output to Expectation	66
108	5. Simulation, Reconstruction, and Event Reduction	68
109	5.1. Simulation	68
110	5.2. Event Reconstruction at SK	73
111	5.2.1. Validation of Reconstruction in SK-V	81
112	5.3. Event Reduction at SK	85
113	6. Sample Selections and Systematics	91
114	6.1. Atmospheric Samples	93
115	6.2. Near Detector Beam Samples	99
116	6.3. Far Detector Beam Samples	101
117	6.4. Systematic Uncertainties	107
118	6.4.1. Beam Flux	107

119	6.4.2. Atmospheric Flux	109
120	6.4.3. Neutrino Interaction	110
121	6.4.4. Near Detector	116
122	6.4.5. Far Detector	118
123	6.4.5.1. Beam Samples	118
124	6.4.5.2. Atmospheric Samples	121
125	6.4.5.3. Correlated Detector Model	122
126	7. Oscillation Probability Calculation	130
127	7.1. Overview	131
128	7.2. Treatment of Fast Oscillations	139
129	7.3. Calculation Engine	146
130	7.4. Matter Density Profile	151
131	7.5. Production Height Averaging	156
132	8. Oscillation Analysis	160
133	8.1. Likelihood Calculation	160
134	8.1.1. Likelihood Scans	163
135	8.2. Monte Carlo Prediction	166
136	A. Atmospheric Sample Spectra	170
137	A.1. Binning	170
138	A.2. Fully Contained Sub-GeV Samples	170
139	A.3. Fully Contained Multi-GeV Samples	174
140	A.4. Fully Contained Multi-Ring Samples	175
141	A.5. Partially Contained Samples	176
142	A.6. Upward-Going Muon Samples	177
143	Bibliography	178

¹⁴⁴	List of Figures	191
¹⁴⁵	List of Tables	203

¹⁴⁷ **Chapter 1**

¹⁴⁸ **Introduction**

¹⁴⁹ **Chapter 2**

¹⁵⁰ **Neutrino Oscillation Physics**

¹⁵¹ When first proposed, neutrinos were expected to be massless fermions that only in-
¹⁵² teract through weak and gravitational forces. This meant they were very difficult to
¹⁵³ detect as they can pass through significant amounts of matter without interacting. De-
¹⁵⁴ spite this, experimental neutrino physics has developed with many different detection
¹⁵⁵ techniques and neutrino sources being used today. In direct tension with standard
¹⁵⁶ model physics, neutrinos have been determined to oscillate between different lepton
¹⁵⁷ flavours, requiring them to have mass.

¹⁵⁸ The observation techniques which lead to the discovery of the neutrino are doc-
¹⁵⁹ umented in section 2.1. The theory underpinning neutrino oscillation is described
¹⁶⁰ in section 2.2 and includes the approximations which can be made to simplify the
¹⁶¹ understanding of neutrino oscillation in the two-flavour approximation. Past, current,
¹⁶² and future neutrino experiments are detailed in section 2.3, including the reactor,
¹⁶³ atmospheric, and long-baseline accelerator neutrino sources that have been used to
¹⁶⁴ successfully constrain oscillation parameters. Finally, the current state of oscillation
¹⁶⁵ parameter measurements are summarised in section 2.4.

¹⁶⁶ **2.1. Discovery of Neutrinos**

¹⁶⁷ At the start of the 20th century, the electrons emitted from the β -decay of the nucleus
¹⁶⁸ were found to have a continuous energy spectrum [1,2]. This observation seemingly
¹⁶⁹ broke the energy conservation invoked within that period's nuclear models. Postulated

170 in 1930 by Pauli as the solution to this problem, the neutrino (originally termed
171 “neutron”) was theorized to be an electrically neutral spin-1/2 fermion with a mass of
172 the same order of magnitude as the electron [3]. This neutrino was to be emitted with
173 the electron in β -decay to alleviate the apparent breaking of energy conservation. As a
174 predecessor of today’s weak interaction model, Fermi’s theory of β -decay developed
175 the understanding by coupling the four constituent particles; electron, proton, neutron,
176 and neutrino, into a consistent model [4].

177 Whilst Pauli was not convinced of the ability to detect neutrinos, the first observa-
178 tions of the particle were made in the mid-1950s when neutrinos from a reactor were
179 observed via the inverse β -decay (IBD) process, $\bar{\nu}_e + p \rightarrow n + e^+$ [5, 6]. The detector
180 consisted of two parts: a neutrino interaction medium and a liquid scintillator. The
181 interaction medium was built from two water tanks. These were loaded with cadmium
182 chloride to allow increased efficiency of neutron capture. The positron emitted from
183 IBD annihilates, $e^+ + e^- \rightarrow 2\gamma$, generating a prompt signal and the neutron is captured
184 on the cadmium via $n + {}^{108}Cd \rightarrow {}^{109*}Cd \rightarrow {}^{109}Cd + \gamma$, producing a delayed signal. An
185 increase in the coincidence rate was observed when the reactor was operating which
186 was interpreted as interactions from neutrinos generated in the reactor.

187 After the discovery of the ν_e , the natural question of how many flavours of neutrino
188 exist was asked. In 1962, a measurement of the ν_μ was conducted at the Brookhaven
189 National Laboratory [7]. A proton beam was directed at a beryllium target, generating
190 a π -dominated beam which then decayed via $\pi^\pm \rightarrow \mu^\pm + (\nu_\mu, \bar{\nu}_\mu)$, and the subsequent
191 interactions of the ν_μ were observed. As the subsequent interaction of the neutrino
192 generates muons rather than electrons, it was determined the ν_μ was fundamentally
193 different from ν_e . The final observation to be made was that of the ν_τ from the DONUT
194 experiment [8]. Three neutrinos seem the obvious solution as it mirrors the known
195 number of charged lepton (as they form weak isospin doublets) but there could be

196 evidence of more. Several neutrino experiments have found anomalous results [9, 10]
197 which could be attributed to sterile neutrinos. However, cosmological observations
198 indicate the number of neutrino species $N_{eff} = 2.99 \pm 0.17$ [11], as measured from
199 the cosmic microwave background power spectrum, and LEP measured the number
200 of active neutrino flavours to be $N_\nu 2.9840 \pm 0.0082$ [12] from measurements of the
201 Z -decay width.

202 2.2. Theory of Neutrino Oscillation

203 As direct evidence of beyond Standard Model physics, a neutrino generated with
204 lepton flavour α can change into a different lepton flavour β after propagating some
205 distance. This phenomenon is called neutrino oscillation and requires that neutrinos
206 must have a non-zero mass (as seen in subsection 2.2.1). This observation is direct
207 evidence of beyond standard model physics. This behaviour has been characterised
208 by the Pontecorvo-Maki-Nakagawa-Sakata (PMNS) [13–15] mixing matrix which
209 describes how the flavour and mass of neutrinos are associated. This is analogous to
210 the Cabibbo-Kobayashi-Maskawa (CKM) [16] matrix measured in quark physics.

211 2.2.1. Three Flavour Oscillations

212 The PMNS parameterisation defines three flavour eigenstates, ν_e , ν_μ and ν_τ (indexed
213 ν_α), which are eigenstates of the weak interaction and three mass eigenstates, ν_1 , ν_2 and
214 ν_3 (indexed ν_i). Each mass eigenstate is the superposition of all three flavour states,

$$|\nu_i\rangle = \sum_\alpha U_{\alpha i} |\nu_\alpha\rangle. \quad (2.1)$$

215 Where U is the PMNS matrix which is unitary and connects the mass and flavour

216 eigenstates.

217 The weak interaction couples to flavour eigenstates so neutrinos interact with
218 leptons of the same flavour. The propagation of a neutrino flavour eigenstate, in a
219 vacuum, can be re-written as a plane-wave solution to the time-dependent Schrödinger
220 equation,

$$|\nu_\alpha(t)\rangle = \sum_i U_{\alpha i}^* |\nu_i\rangle e^{-i\phi_i}. \quad (2.2)$$

221 The probability of observing a neutrino of flavour eigenstate β from one which
222 originated as flavour α can be calculated as,

$$P(\nu_\alpha \rightarrow \nu_\beta) = |\langle \nu_\beta | \nu_\alpha(t) \rangle|^2 = \sum_{i,j} U_{\alpha i}^* U_{\beta i} U_{\alpha j} U_{\beta j}^* e^{-i(\phi_j - \phi_i)} \quad (2.3)$$

223 The ϕ_i term can be expressed in terms of the energy, E_i , and magnitude of the
224 three momenta, p_i , of the neutrino, $\phi_i = E_i t - p_i x$ (t and x being time and position
225 coordinates). Therefore,

$$\phi_j - \phi_i = E_j t - E_i t - p_j x + p_i x. \quad (2.4)$$

226 For a relativistic particle, $E_i \gg m_i$,

$$p_i = \sqrt{E_i^2 - m_i^2} \approx E_i - \frac{m_i^2}{2E_i}. \quad (2.5)$$

²²⁷ Making the approximations that neutrinos are relativistic, the mass eigenstates
²²⁸ were created with the same energy and that $x = L$, where L is the distance traveled by
²²⁹ the neutrino, Equation 2.4 then becomes

$$\phi_j - \phi_i = \frac{\Delta m_{ij}^2 L}{2E}, \quad (2.6)$$

²³⁰ where $\Delta m_{ij}^2 = m_j^2 - m_i^2$. This, combined with further use of unitarity relations
²³¹ results in Equation 2.3 becoming

$$P(\nu_\alpha \rightarrow \nu_\beta) = \delta_{\alpha\beta} - 4 \sum_{i>j} \Re \left(U_{\alpha i}^* U_{\beta i} U_{\alpha j} U_{\beta j}^* \right) \sin^2 \left(\frac{\Delta m_{ij}^2 L}{4E} \right) + (-) 2 \sum_{i>j} \Im \left(U_{\alpha i}^* U_{\beta i} U_{\alpha j} U_{\beta j}^* \right) \sin \left(\frac{\Delta m_{ij}^2 L}{2E} \right). \quad (2.7)$$

²³² Where $\delta_{\alpha\beta}$ is the Kronecker delta function and the negative sign on the last term is
²³³ included for the oscillation probability of antineutrinos.

²³⁴ Typically, the PMNS matrix is parameterised into three mixing angles, a charge
²³⁵ parity (CP) violating phase δ_{CP} , and two Majorana phases $\alpha_{1,2}$,

$$U = \underbrace{\begin{pmatrix} 1 & 0 & 0 \\ 0 & c_{23} & s_{23} \\ 0 & -s_{23} & c_{23} \end{pmatrix}}_{\text{Atmospheric, Accelerator}} \underbrace{\begin{pmatrix} c_{13} & 0 & s_{13}e^{-i\delta_{CP}} \\ 0 & 1 & 0 \\ -s_{13}e^{-i\delta_{CP}} & 0 & c_{13} \end{pmatrix}}_{\text{Reactor, Accelerator}} \underbrace{\begin{pmatrix} c_{12} & s_{12} & 0 \\ -s_{12} & c_{12} & 0 \\ 0 & 0 & 1 \end{pmatrix}}_{\text{Reactor, Solar}} \underbrace{\begin{pmatrix} e^{i\alpha_1/2} & 0 & 0 \\ 0 & e^{i\alpha_2/2} & 0 \\ 0 & 0 & 1 \end{pmatrix}}_{\text{Majorana}}. \quad (2.8)$$

²³⁶ Where $s_{ij} = \sin(\theta_{ij})$ and $c_{ij} = \cos(\theta_{ij})$. The oscillation parameters are often
²³⁷ grouped; (1,2) as “solar”, (2,3) as “atmospheric” and (1,3) as “reactor”. Many
²³⁸ neutrino experiments aim to measure the PMNS parameters from a wide array of
²³⁹ origins, as is the purpose of this thesis.

²⁴⁰ The Majorana phase, $\alpha_{1,2}$, included within the fourth matrix in Equation 2.8 is only
²⁴¹ included for completeness. For an oscillation analysis experiment, any terms contain-
²⁴² ing this phase disappear due to taking the expectation value of the PMNS matrix.
²⁴³ Measurements of these phases are typically performed by experiments searching for
²⁴⁴ neutrino-less double β -decay [17].

²⁴⁵ A two flavour approximation can be obtained when one assumes the third mass
²⁴⁶ eigenstate is degenerate with another. As discussed in section 2.3, it is found that
²⁴⁷ $\Delta m_{21}^2 \ll |\Delta m_{31}^2|$. This results in the two flavour approximation being reasonable for
²⁴⁸ understanding the features of the oscillation. In this two flavour case, the mixing
²⁴⁹ matrix becomes,

$$U_{2 \text{ Flav.}} = \begin{pmatrix} \cos(\theta) & \sin(\theta) \\ -\sin(\theta) & \cos(\theta) \end{pmatrix}. \quad (2.9)$$

250 This culminates in the oscillation probability,

$$\begin{aligned} P(\nu_\alpha \rightarrow \nu_\alpha) &= 1 - \sin^2(2\theta) \sin^2\left(\frac{\Delta m^2 L}{4E}\right), \\ P(\nu_\alpha \rightarrow \nu_\beta) &= \sin^2(2\theta) \sin^2\left(\frac{\Delta m^2 L}{4E}\right). \end{aligned} \quad (2.10)$$

251 Where $\alpha \neq \beta$. For a fixed neutrino energy, the oscillation probability is a sinusoidal
252 function depending upon the distance over which the neutrino propagates. The
253 frequency and amplitude of oscillation are dependent upon $\Delta m^2/4E$ and $\sin^2 2\theta$,
254 respectively. The oscillation probabilities presented thus far assume $c = 1$, where
255 c is the speed of light in vacuum. In more familiar units, the maximum oscillation
256 probability for a fixed value of θ is given at $L[\text{km}]/E[\text{GeV}] \sim 1.27/\Delta m^2$. It is this
257 calculation that determines the best L/E value for a given experiment to be designed
258 around for measurements of a specific value of Δm^2 .

259 2.2.2. The MSW Effect

260 The theory of neutrino oscillation in a vacuum has been described in subsection 2.2.1.
261 However, the beam neutrinos and atmospheric neutrinos originating from below the
262 horizon propagate through matter in the Earth. The coherent scattering of neutrinos
263 from a material target modifies the Hamiltonian of the system. This results in a change
264 in the oscillation probability. Notably, charged current scattering ($\nu_e + e^- \rightarrow \nu_e + e^-$,
265 propagated by a W boson) only affects electron neutrinos whereas the neutral current
266 scattering ($\nu_l + l^- \rightarrow \nu_l + l^-$, propagated by a Z^0 boson) interacts through all neutrino
267 flavours equally. In the two-flavour approximation, the effective mixing parameter
268 becomes

$$\sin^2(2\theta) \rightarrow \sin^2(2\theta_m) = \frac{\sin^2(2\theta)}{(A/\Delta m^2 - \cos(2\theta))^2 + \sin^2(2\theta)}, \quad (2.11)$$

269 where $A = 2\sqrt{2}G_F N_e E$, N_e is the electron density of the medium and G_F is Fermi's
270 constant. It is clear to see that there exists a value of $A = \Delta m^2 \cos(2\theta)$ for $\Delta m^2 > 0$
271 which results in a divergent mixing parameter. This resonance is termed the Mikheyev-
272 Smirnov-Wolfenstein (MSW) effect (or more colloquially, the matter resonance) which
273 regenerates the electron neutrino component of the neutrino flux [18–20]. The density
274 at which the resonance occurs is given by

$$N_e = \frac{\Delta m^2 \cos(2\theta)}{2\sqrt{2}G_F E}. \quad (2.12)$$

275 At densities lower than this critical value, the oscillation probability will be much
276 closer to that of vacuum oscillation. For antineutrinos, $N_e \rightarrow -N_e$ [21]. The resonance
277 occurring from the MSW effect depends on the sign of Δm^2 . Therefore, any neutrino
278 oscillation experiment which observes neutrinos and antineutrinos which have propa-
279 gated through matter can have some sensitivity to the ordering of the neutrino mass
280 eigenstates.

281 2.3. Neutrino Oscillation Measurements

282 As evidence of beyond standard model physics, the 2015 Nobel Prize in Physics was
283 awarded to the Super-Kamiokande (SK) [22] and Sudbury Neutrino Observatory
284 (SNO) [23] collaborations for the first definitive observation of solar and atmospheric

²⁸⁵ neutrino oscillation [24]. Since then, the field has seen a wide array of oscillation
²⁸⁶ measurements from a variety of neutrino sources. As seen in subsection 2.2.1, the
²⁸⁷ neutrino oscillation probability is dependent on the ratio of the propagation baseline, L ,
²⁸⁸ to the neutrino energy, E . It is this ratio that determines the type of neutrino oscillation
²⁸⁹ a particular experiment is sensitive to.

²⁹⁰ As illustrated in Figure 2.1, there are many neutrino sources that span a wide
²⁹¹ range of energies. The least energetic neutrinos are from diffuse supernovae and
²⁹² terrestrial neutrinos at $O(1)$ MeV whereas the most energetic neutrinos originate from
²⁹³ atmospheric and galactic neutrinos of $> O(1)$ TeV.

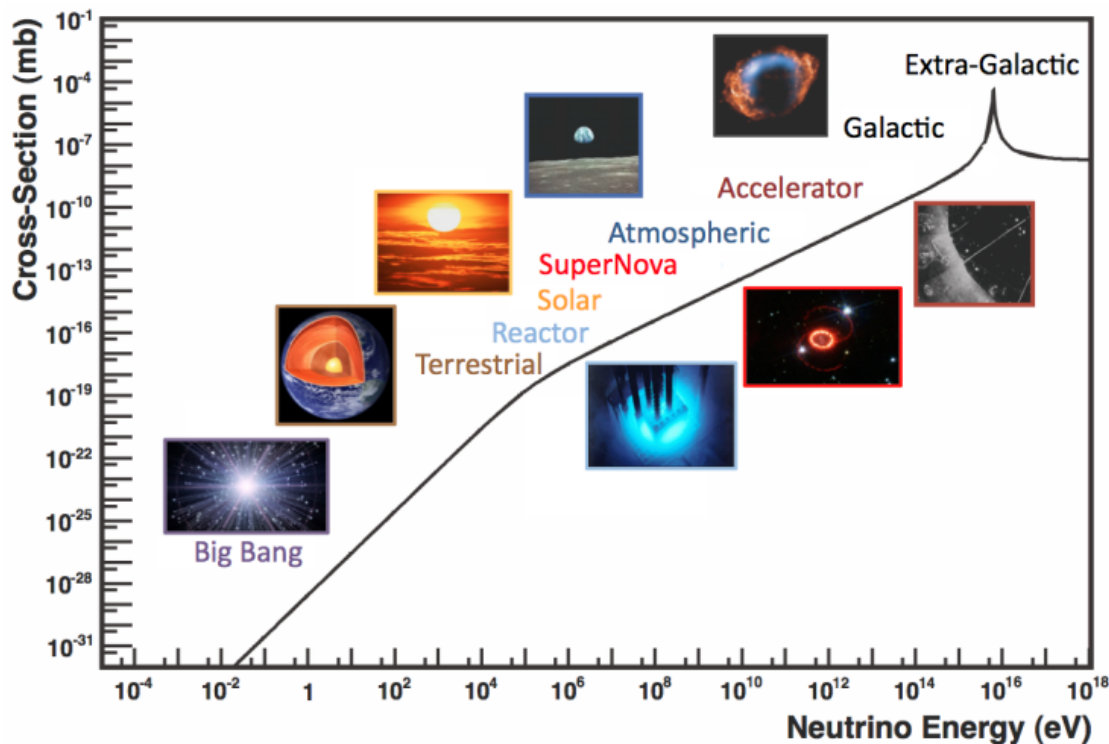


Figure 2.1.: The cross-section of neutrinos from various natural and man-made sources as a function of neutrino energy. Taken from [25]

²⁹⁴ 2.3.1. Solar Neutrinos

²⁹⁵ Solar neutrinos are emitted from fusion reaction chains at the center of the Sun. The
²⁹⁶ solar neutrino flux, given as a function of neutrino energy for different fusion and
²⁹⁷ decay chains, is illustrated in Figure 2.2. Whilst proton-proton fusion generates the
²⁹⁸ largest flux of neutrinos, the neutrinos are of low energy and are difficult to reconstruct
²⁹⁹ due to the IBD interaction threshold of 1.8MeV. Consequently, most experiments focus
³⁰⁰ on the neutrinos from the decay of 8B (via $^8B \rightarrow ^8Be^* + e^+ + \nu_e$), which are higher
³⁰¹ energy.

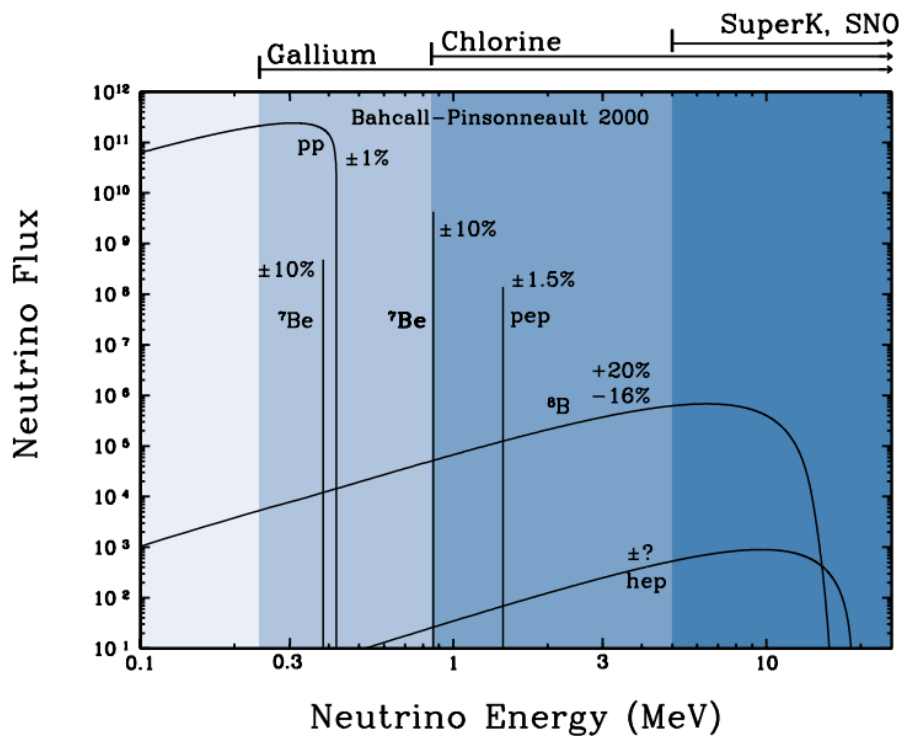
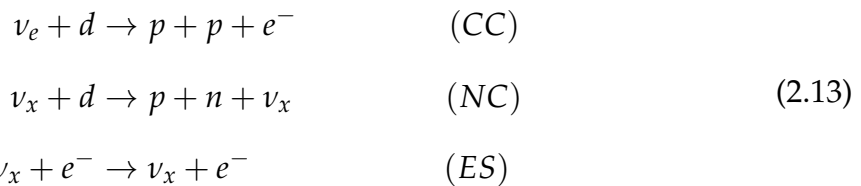


Figure 2.2.: The solar neutrino flux as a function of neutrino energy for various fusion reactions and decay chains as predicted by the Standard Solar Model. Taken from [26].

³⁰² The first measurements of solar neutrinos observed a significant reduction in the
³⁰³ event rate compared to predictions from the Standard Solar Model [27, 28]. The
³⁰⁴ proposed solution to this “solar neutrino problem” was $\nu_e \leftrightarrow \nu_\mu$ oscillations in a

³⁰⁵ precursory version of the PMNS model [29]. The Kamiokande [30], Gallex [31] and
³⁰⁶ Sage [32] experiments confirmed the ~ 0.5 factor deficit of solar neutrinos.

³⁰⁷ The conclusive solution to this problem was determined by the SNO collaboration
³⁰⁸ [33]. Using a deuterium water target to observe 8B neutrinos, the event rate of charged
³⁰⁹ current (CC), neutral current (NC), and elastic scattering (ES) interactions (Given in
³¹⁰ Equation 2.13) was simultaneously measured. CC events can only occur for electron
³¹¹ neutrinos, whereas the NC channel is agnostic to neutrino flavour, and the ES reaction
³¹² has a slight excess sensitivity to electron neutrino interactions. This meant that there
³¹³ were direct measurements of the ν_e and ν_x neutrino flux. It was concluded that the
³¹⁴ CC and ES interaction rates were consistent with the deficit previously observed.
³¹⁵ Most importantly, the NC reaction rate was only consistent with the others under the
³¹⁶ hypothesis of flavour transformation.



³¹⁷ Many experiments have since measured the neutrino flux of different interaction
³¹⁸ chains within the sun [34–36]. The most recent measurement was that of CNO neutrinos
³¹⁹ which were recently observed with 5σ significance by the Borexino collaboration.
³²⁰ Future neutrino experiments aim to further these spectroscopic measurements of
³²¹ different fusion chains within the Sun [37–39]. Solar neutrinos act as an irreducible
³²² background for dark matter experiments like DARWIN but oscillation parameter
³²³ measurements can be made [40].

³²⁴ 2.3.2. Atmospheric Neutrinos

- ³²⁵ The interactions of primary cosmic ray protons in Earth's upper atmosphere generate
³²⁶ showers of energetic hadrons. These are mostly pions and kaons which when they
³²⁷ decay produce a natural source of neutrinos spanning energies of MeV to TeV [41].
³²⁸ The main decay is via

$$\begin{aligned} \pi^\pm &\rightarrow \mu^\pm + (\nu_\mu, \bar{\nu}_\mu) \\ \mu^\pm &\rightarrow e^\pm + (\nu_e, \bar{\nu}_e) + (\nu_\mu, \bar{\nu}_\mu) \end{aligned} \tag{2.14}$$

³²⁹ such that for a single pion decay, three neutrinos are typically produced. The
³³⁰ atmospheric neutrino flux energy spectra as predicted by the Bartol [42], Honda
³³¹ [43–45], and FLUKA [46] models are illustrated in Figure 2.3. The flux distribution
³³² peaks at an energy of $O(10)\text{GeV}$. The uncertainties associated with these models
³³³ are dominated by the hadronic production of kaon and pions as well as the primary
³³⁴ cosmic flux.

³³⁵ Unlike long-baseline experiments which have a fixed baseline, the distance at-
³³⁶ mospheric neutrinos propagate is dependent upon the zenith angle at which they
³³⁷ interact. This is illustrated in Figure 2.4. Neutrinos that are generated directly above
³³⁸ the detector ($\cos(\theta) = 1.0$) have a baseline equivalent to the height of the atmosphere
³³⁹ whereas neutrinos that interact directly below the detector ($\cos(\theta) = -1.0$) have to
³⁴⁰ travel a length equal to the diameter of the Earth. This means atmospheric neutrinos
³⁴¹ have a baseline that varies from $O(20)\text{km}$ to $O(6 \times 10^3)\text{km}$. Any neutrino generated
³⁴² at or below the horizon will be subject to matter effects as they propagate through the
³⁴³ Earth.

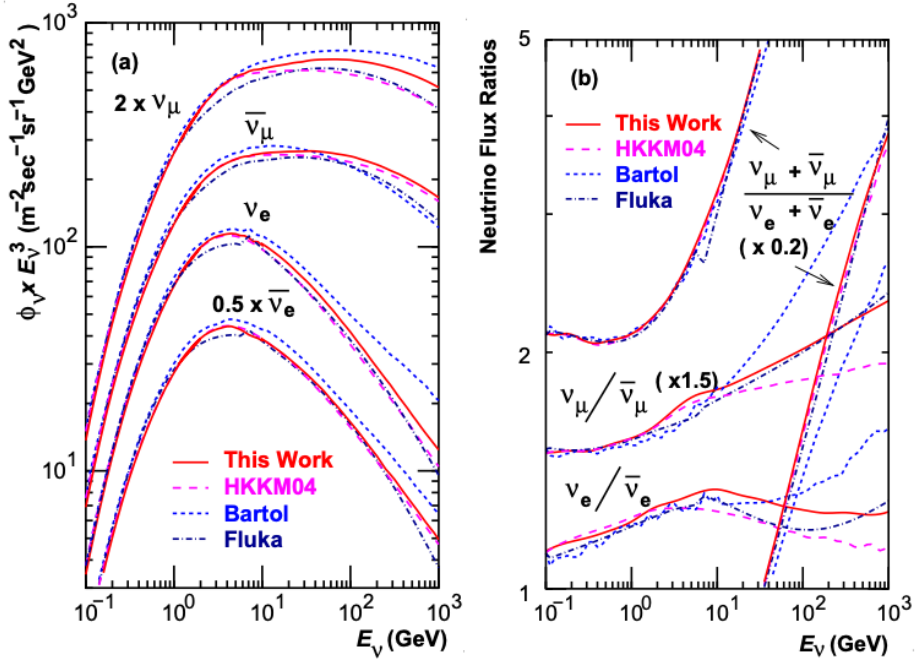


Figure 2.3.: Left panel: The atmospheric neutrino flux for different neutrino flavours as a function of neutrino energy as predicted by the 2007 Honda model (“This work”) [43], the 2004 Honda model (“HKKM04”) [44], the Bartol model [42] and the FLUKA model [46]. Right panel: The ratio of the muon to electron neutrino flux as predicted by all the quoted models. Both figures taken from [43].

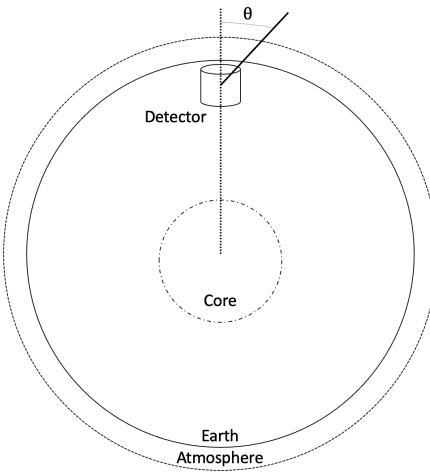


Figure 2.4.: A diagram illustrating the definition of zenith angle as used in the Super Kamiokande experiment [47].

Figure 2.5 highlights the neutrino flux as a function of the zenith angle for different

slices of neutrino energy. For medium to high-energy neutrinos (and to a lesser degree

for low-energy neutrinos), the flux is approximately symmetric around $\cos(\theta) = 0$.

³⁴⁴ Figure 2.5 highlights the neutrino flux as a function of the zenith angle for different
³⁴⁵ slices of neutrino energy. For medium to high-energy neutrinos (and to a lesser degree
³⁴⁶ for low-energy neutrinos), the flux is approximately symmetric around $\cos(\theta) = 0$.

³⁴⁷ To the accuracy of this approximation, the systematic uncertainties associated with
³⁴⁸ atmospheric flux for comparing upward-going and down-going neutrino cancels. This
³⁴⁹ allows the down-going events, which are mostly insensitive to oscillation probabilities,
³⁵⁰ to act as an unoscillated prediction (similar to a near detector in an accelerator neutrino
³⁵¹ experiment).

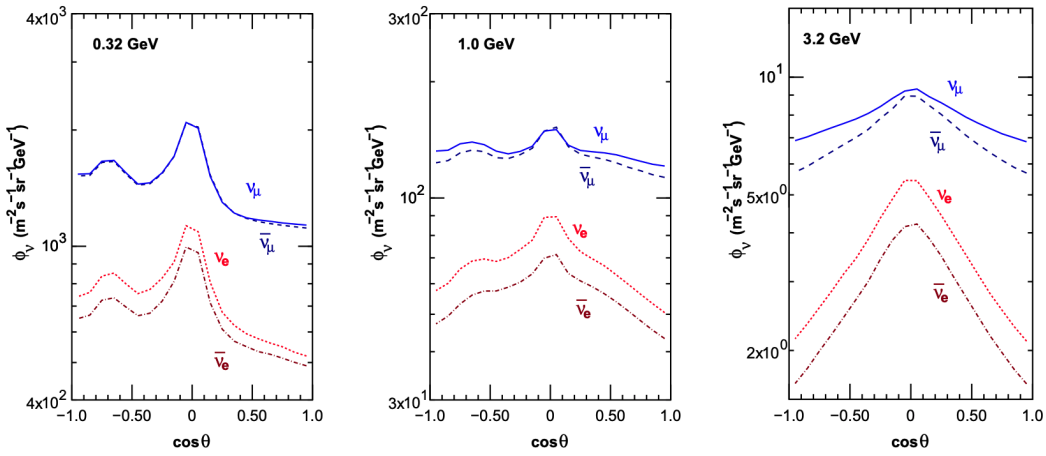


Figure 2.5.: Prediction of ν_e , $\bar{\nu}_e$, ν_μ , $\bar{\nu}_\mu$ fluxes as a function of zenith angle as calculated by the HKKM model [45]. The left, middle and right panels represent three values of neutrino energy, 0.32GeV, 1.0GeV and 3.2GeV respectively. Predictions for other models including Bartol [42], Honda [43] and FLUKA [46] are given in [47].

³⁵² Precursory hints of atmospheric neutrinos were observed in the mid-1960s search-
³⁵³ ing for $\nu_\mu + X \xrightarrow{(-)} X^* + \mu^\pm$ [48], although it was called an anomaly at the time of
³⁵⁴ measurement. This was succeeded with the IMB-3 [49] and Kamiokande [50] experi-
³⁵⁵ ments which measured the ratio of muon neutrinos compared to electron neutrinos
³⁵⁶ $R(\nu_\mu/\nu_e)$. Both experiments were found to have a consistent deficit of muon neutrinos,
³⁵⁷ with $R(\nu_\mu/\nu_e) = 0.67 \pm 0.17$ and $R(\nu_\mu/\nu_e) = 0.60^{+0.07}_{-0.06} \pm 0.05$. Super-Kamiokande
³⁵⁸ (SK) [47] extended this analysis by fitting oscillation parameters in $P(\nu_\mu \rightarrow \nu_\tau)$ which
³⁵⁹ found best fit parameters $\sin^2(2\theta) > 0.92$ and $1.5 \times 10^{-3} < \Delta m^2 < 3.4 \times 10^{-3} \text{ eV}^2$.

³⁶⁰ Since then, atmospheric neutrino experiments have been making precision mea-
³⁶¹ surements of the $\sin^2(\theta_{23})$ and Δm^2_{32} oscillation parameters. Atmospheric neutrino
³⁶² oscillation is dominated by $P(\nu_\mu \rightarrow \nu_\tau)$, where SK observed a 4.6σ discovery of ν_τ

³⁶³ appearance [51]. Figure 2.6 illustrates the current estimates on the atmospheric mixing
³⁶⁴ parameters from a wide range of atmospheric and accelerator neutrino observatories.

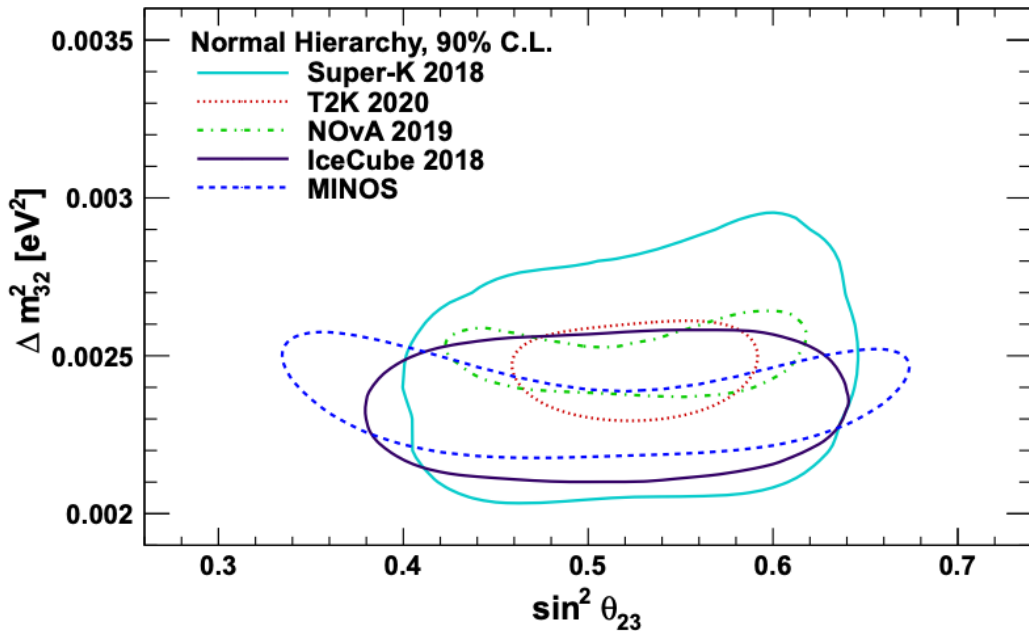


Figure 2.6.: Constraints on the atmospheric oscillation parameters, $\sin^2(\theta_{23})$ and Δm_{23}^2 , from atmospheric and long baseline experiments: SK [52], T2K [53], NOvA [54], IceCube [55] and MINOS [56]. Figure taken from [57].

³⁶⁵ 2.3.3. Accelerator Neutrinos

³⁶⁶ The concept of using a man-made “neutrino beam” was first realised in 1962 [58].
³⁶⁷ Since then, many experiments have followed which all use the same fundamental
³⁶⁸ concepts. Typically, a proton beam is aimed at a target producing charged mesons that
³⁶⁹ decay to neutrinos. The mesons can be sign-selected by the use of magnetic focusing
³⁷⁰ horns to generate a neutrino or antineutrino beam. Pions are the primary meson that
³⁷¹ decay and depending on the orientation of the magnetic field, a muon (anti-)neutrino
³⁷² beam is generated via $\pi^+ \rightarrow \mu^+ + \nu_\mu$ or $\pi^- \rightarrow \mu^- + \bar{\nu}_\mu$. The decay of muons and
³⁷³ kaons does result in an irreducible intrinsic electron neutrino background. In T2K,
³⁷⁴ this background contamination is $O(< 1\%)$ [59]. There is also an approximately $\sim 5\%$

³⁷⁵ “wrong-sign” neutrino background of $\bar{\nu}_\mu$ generated via the same decays. As the beam is
³⁷⁶ generated by proton interactions (rather than anti-proton interactions), the wrong-sign
³⁷⁷ component in the antineutrino beam is larger when operating in neutrino mode.

³⁷⁸ Tuning the proton energy in the beam and using beam focusing techniques allows
³⁷⁹ the neutrino energy to be set to a value that maximises the disappearance oscillation
³⁸⁰ probability in the L/E term in Equation 2.10. This means that accelerator experiments
³⁸¹ are typically more sensitive to the mixing parameters as compared to a natural neutrino
³⁸² source. However, the disadvantage compared to atmospheric neutrino experiments is
³⁸³ that the baseline has to be shorter due to the lower flux. Consequently, there is typically
³⁸⁴ less sensitivity to matter effects and the ordering of the neutrino mass eigenstates.

³⁸⁵ A neutrino experiment measures

$$R(\vec{x}) = \Phi(E_\nu) \times \sigma(E_\nu) \times \epsilon(\vec{x}) \times P(\nu_\alpha \rightarrow \nu_\beta), \quad (2.15)$$

³⁸⁶ where $R(\vec{x})$ is the event rate of neutrinos at position \vec{x} , $\Phi(E_\nu)$ is the flux of neutrinos
³⁸⁷ with energy E_ν , $\sigma(E_\nu)$ is the cross-section of the neutrino interaction and $\epsilon(\vec{x})$ is the
³⁸⁸ efficiency and resolution of the detector. In order to leverage the most out of an
³⁸⁹ accelerator neutrino experiment, the flux and cross-section systematics need to be
³⁹⁰ constrained. This is typically done via the use of a “near detector”, situated at a baseline
³⁹¹ of $O(1)$ km. This detector observes the unoscillated neutrino flux and constrains the
³⁹² parameters used within the flux and cross-section model.

³⁹³ The first accelerator experiments to precisely measure oscillation parameters were
³⁹⁴ MINOS [60] and K2K [61]. These experiments confirmed the ν_μ disappearance seen in
³⁹⁵ atmospheric neutrino experiments by finding consistent parameter values for $\sin^2(\theta_{23})$
³⁹⁶ and Δm_{23}^2 . The current generation of accelerator neutrino experiments, T2K and NO ν A

³⁹⁷ extended this field by observing $\bar{\nu}_\mu \rightarrow \bar{\nu}_e$ and lead the sensitivity to atmospheric mix-
³⁹⁸ ing parameters as seen in Figure 2.6 [62]. The two experiments differ in their peak
³⁹⁹ neutrino energy, baseline, and detection technique. The NO ν A experiment is situated
⁴⁰⁰ at a baseline of 810km from the NuMI beamline which delivers 2GeV neutrinos. The
⁴⁰¹ T2K neutrino beam is peaked around 0.6GeV and propagates 295km. The NO ν A
⁴⁰² experiment also uses functionally identical detectors (near and far) which allow the
⁴⁰³ approximate cancellation of detector systematics whereas T2K uses a plastic scintil-
⁴⁰⁴ lator technique at the near detector and a water Cherenkov far detector. The future
⁴⁰⁵ generation experiments DUNE [63] and Hyper-Kamiokande [64] will succeed these
⁴⁰⁶ experiments as the high-precision era of neutrino oscillation parameter measurements
⁴⁰⁷ develops.

⁴⁰⁸ Several anomalous results have been observed in the LSND [9] and MiniBooNE [10]
⁴⁰⁹ detectors which were designed with purposefully short baselines. Parts of the neu-
⁴¹⁰ trino community attributed these results to oscillations induced by a fourth “sterile”
⁴¹¹ neutrino [65] but several searches in other experiments, MicroBooNE [66] and KAR-
⁴¹² MEN [67], found no hints of additional neutrino species. The solution to the anomalous
⁴¹³ results is still being determined.

⁴¹⁴ 2.3.4. Reactor Neutrinos

⁴¹⁵ As illustrated in the first discovery of neutrinos (section 2.1), nuclear reactors are a very
⁴¹⁶ useful man-made source of electron antineutrinos. For reactors that use low-enriched
⁴¹⁷ uranium ^{235}U as fuel, the antineutrino flux is dominated by the β -decay fission of ^{235}U ,
⁴¹⁸ ^{238}U , ^{239}Pu and ^{241}Pu [68] as illustrated in Figure 2.7.

⁴¹⁹ Due to their low energy, reactor electron antineutrinos predominantly interact
⁴²⁰ via the inverse β -decay (IBD) interaction. The typical signature contains two signals

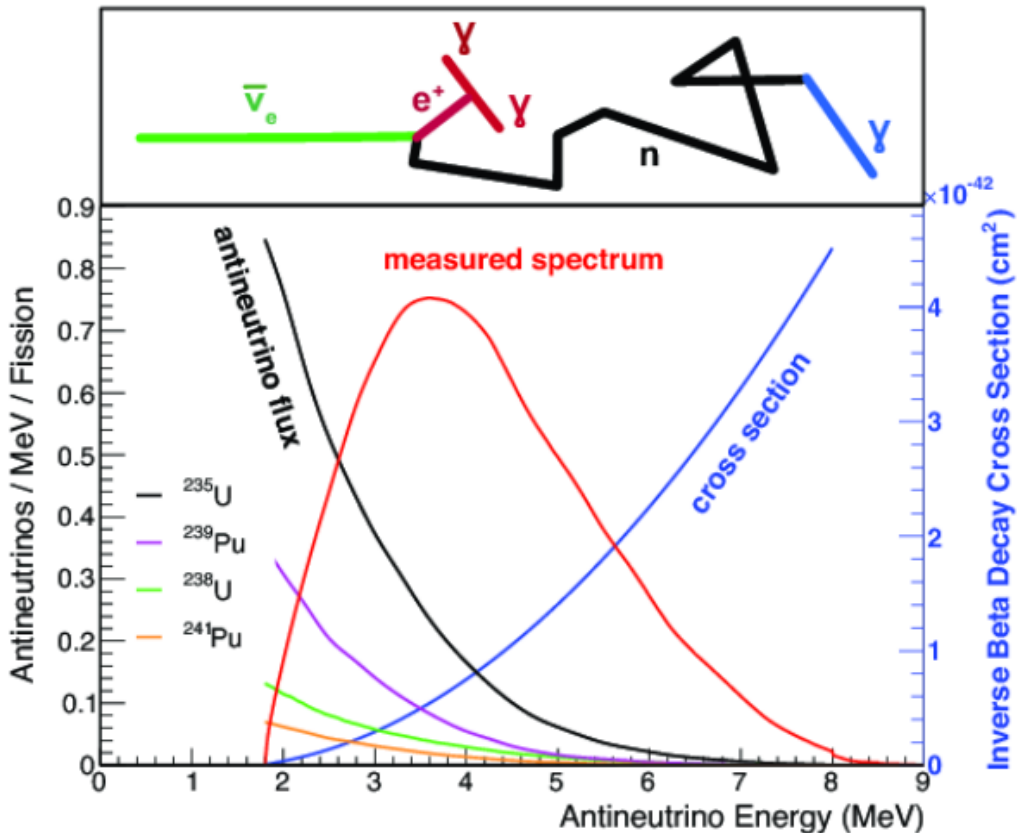


Figure 2.7.: Reactor electron antineutrino fluxes for ^{235}U (Black), ^{238}U (Green), ^{239}Pu (Purple), and ^{241}Pu (Orange) isotopes. The inverse β -decay cross-section (Blue) and corresponding measurable neutrino spectrum (Red) are also given. Top panel: Schematic of Inverse β -decay interaction including the eventual capture of the emitted neutron. This capture emits a γ -ray which provides a second signal of the event. Taken from [69].

delayed by $O(200)\mu\text{s}$; firstly the prompt photons from positron annihilation, and secondly the photons emitted ($E_{tot}^\gamma = 2.2\text{MeV}$) from de-excitation after neutron capture on hydrogen. Searching for both signals improves the detector's ability to distinguish between background and signal events [70]. Recently, SK included gadolinium dopants into the ultra-pure water to increase the energy released from the photon cascade to $\sim 8\text{MeV}$ and reduce the time of the delayed signal to $\sim 28\mu\text{s}$.

There are many short baseline experiments ($L \sim O(1)\text{km}$) that have measured the $\sin^2(\theta_{13})$ and Δm_{23}^2 oscillation parameters. Daya Bay [71], RENO [72] and Double Chooz [73] have all provided precise measurements, with the first discovery of a

430 non-zero θ_{13} made by Daya Bay and RENO (and complemented by T2K [73]). The
431 constraints on $\sin^2(\theta_{13})$ by the reactor experiments lead the field and are often used as
432 external inputs to accelerator neutrino experiments to improve their sensitivity to δ_{CP}
433 and mass hierarchy determination. JUNO-TAO [74], a small collaboration within the
434 larger JUNO experiment, is a next-generation reactor experiment that aims to precisely
435 measure the isotopic antineutrino yields from the different fission chains. Alongside
436 this, it aims to explain the ‘5MeV excess’ [75–77] by conducting a search for sterile
437 neutrinos with a mass scale of around 1eV.

438 Kamland [78] is the only experiment to have observed reactor neutrinos using a
439 long baseline (flux weighted averaged baseline of $L \sim 180\text{km}$) which allows it to have
440 sensitivity to Δm_{12}^2 . Combined with the SK solar neutrino experiment, the combined
441 analysis puts the most stringent constraint on Δm_{12}^2 [79].

442 2.4. Summary

443 Since observing the first evidence of neutrino oscillations in the late 1990’s, numerous
444 measurements of the mixing parameters have been made. Many experiments use
445 neutrinos as a tool for discovery of new physics (diffuse supernova background,
446 neutrinoless double beta decay and others) so the PMNS parameters are summarised
447 in the Particle Data Group (PDG) review tables. The analysis presented in this thesis
448 focuses on the 2020 T2K oscillation analysis presented in [80] where the 2018 PDG
449 constraints [81] were used. These constraints are outlined in Table 2.1.

450 The $\sin^2(\theta_{13})$ measurement stems from the electron antineutrino disappearance,
451 $P(\bar{\nu}_e \rightarrow \bar{\nu}_e)$, and is take as the average best-fit from the combination of Daya Bay,
452 Reno and Double Chooz. It is often used as a prior uncertainty within other neu-
453 trino oscillation experiments, typically termed the reactor constraint. The $\sin^2(\theta_{12})$

Parameter	2018 Constraint
$\sin^2(\theta_{12})$	0.307 ± 0.013
Δm_{21}^2	$(7.53 \pm 0.18) \times 10^{-5} \text{ eV}^2$
$\sin^2(\theta_{13})$	$(2.12 \pm 0.08) \times 10^{-2}$
$\sin^2(\theta_{23})$ (I.H., Q1)	$0.421^{+0.033}_{-0.025}$
$\sin^2(\theta_{23})$ (I.H., Q2)	$0.592^{+0.023}_{-0.030}$
$\sin^2(\theta_{23})$ (N.H., Q1)	$0.417^{+0.025}_{-0.028}$
$\sin^2(\theta_{23})$ (N.H., Q2)	$0.597^{+0.024}_{-0.030}$
Δm_{32}^2 (I.H.)	$(-2.56 \pm 0.04) \times 10^{-3} \text{ eV}^2$
Δm_{32}^2 (N.H.)	$(2.51 \pm 0.05) \times 10^{-3} \text{ eV}^2$

Table 2.1.: The 2018 Particle Data Group constraints of the oscillation parameters taken from [81]. The value of Δm_{23}^2 is given for both normal hierarchy (N.H.) and inverted hierarchy (I.H.) and $\sin^2(\theta_{23})$ is broken down by whether its value is below (Q1) or above (Q2) 0.5.

parameter is predominantly measured through electron neutrino disappearance, $P(\nu_e \rightarrow \nu_{\mu,\tau})$, in solar neutrino experiments. The long-baseline reactor neutrino experiment Kamland also has sensitivity to this parameter and is used in a joint fit to solar data from SNO and SK, using the reactor constraint. Measurements of $\sin^2(\theta_{23})$ are made by long-baseline and atmospheric neutrino experiments. The PDG value is a joint fit of T2K, NOvA, MINOS and IceCube DeepCore experiments. The latest T2K-only measurement, provided at Neutrino2020 and is the basis of this thesis, is given as $\sin^2(\theta_{23}) = 0.546^{+0.024}_{-0.046}$ [80]. The PDG constraint on Δm_{12}^2 is provided by the KamLAND experiment using solar and geoneutrino data. This measurement utilised a $\sin^2(\theta_{13})$ constraint from accelerator (T2K, MINOS) and reactor neutrino (Daya Bay, RENO, Double Chooz) experiments. Accelerator measurements make some of the most stringent constraints on Δm_{23}^2 although atmospheric experiments have more sensitivity to the mass hierarchy determination. The PDG performs a joint fit of accelerator and atmospheric data, in both normal and inverted hierarchy separately. The latest T2K-only result is $\Delta m_{32}^2 = 2.49^{+0.058}_{-0.082} \times 10^{-3} \text{ eV}^2$ favouring normal hierarchy [80]. The value of δ_{CP} is largely undetermined. CP-conserving values of 0 and π were

⁴⁷⁰ rejected with $\sim 2\sigma$ intervals, as published in Nature, although more recent analysis
⁴⁷¹ have reduced the rejection intervals to 90%. Since the 2018 PDG publication, there has
⁴⁷² been a new measurement of $\sin^2(\theta_{13}) = (2.20 \pm 0.07) \times 10^{-2}$ [82], alongside updated
⁴⁷³ Δm_{23}^2 and $\sin^2(\theta_{23})$ measurements.

⁴⁷⁴ Throughout this thesis, several sample spectra predictions and contours are pre-
⁴⁷⁵ sented which require oscillation parameters to be assumed. Table 2.2 defines two sets
⁴⁷⁶ of oscillation parameters, with “Asimov A” set being close to the preferred values
⁴⁷⁷ from a previous T2K-only fit [83] and “Asimov B” being CP-conserving and further
⁴⁷⁸ from maximal θ_{23} mixing.

Parameter	Asimov A	Asimov B
Δm_{12}^2	$7.53 \times 10^{-5} \text{ eV}^2$	
Δm_{32}^2	$2.509 \times 10^{-3} \text{ eV}^2$	
$\sin^2(\theta_{12})$	0.304	
$\sin^2(\theta_{13})$	0.0219	
$\sin^2(\theta_{23})$	0.528	0.45
δ_{CP}	-1.601	0.0

Table 2.2.: Reference values of the neutrino oscillation parameters for two different oscillation parameter sets.

⁴⁷⁹ **Chapter 3**

⁴⁸⁰ **T2K and SK Experiment Overview**

⁴⁸¹ As the successor of the Kamiokande experiment, the Super-Kamiokande (SK) collabora-
⁴⁸² ration has been leading atmospheric neutrino oscillation analyses for over two decades.
⁴⁸³ The detector has provided some of the strongest constraints on proton decay and the
⁴⁸⁴ first precise measurements of the Δm_{23}^2 and $\sin^2(\theta_{23})$ neutrino oscillation parameters.
⁴⁸⁵ The ability of the detector to low-energy neutrino events has been significantly im-
⁴⁸⁶ proved with the recent gadolinium doping of the ultra-pure water target. The history,
⁴⁸⁷ detection technique, and operation of the SK detector is described in section 3.1.

⁴⁸⁸ The Tokai-to-Kamioka (T2K) experiment was one of the first long-baseline ex-
⁴⁸⁹ periments to use both neutrino and antineutrino beams to precisely measure the
⁴⁹⁰ charge parity violation within the neutrino sector. With the SK detector observing
⁴⁹¹ the oscillated neutrino flux, the T2K experiment observed the first hints of a non-zero
⁴⁹² $\sin^2(\theta_{13})$ measurement and continues to lead the field with the constraints it provides
⁴⁹³ on $\sin^2(\theta_{13})$, $\sin^2(\theta_{23})$, Δm_{23}^2 and δ_{CP} . The techniques which T2K uses in gener-
⁴⁹⁴ ating its neutrino beam as well as the near-detector used to constrain the flux and
⁴⁹⁵ cross-section parameters used in this analysis are documented in section 3.2.

⁴⁹⁶ **3.1. The Super-Kamiokande Experiment**

⁴⁹⁷ The SK experiment began taking data in 1996 [84] and has had many modifications
⁴⁹⁸ throughout its lifespan. There have been seven defined periods of data taking as
⁴⁹⁹ noted in Table 3.1. Data taking began in SK-I which ran for five years. Between the

500 SK-I and SK-II periods, a significant proportion of the PMTs were damaged during
 501 maintenance. Those that survived were equally distributed throughout the detector
 502 in the SK-II era, which resulted in a reduced photo-coverage. From SK-III onwards,
 503 repairs to the detector meant the full suite of PMTs was operational. Before the
 504 start of SK-IV, the data acquisition and electronic systems were upgraded. Between
 505 SK-IV and SK-V, a significant effort was placed into tank open maintenance and
 506 repair/replacement of defective PMTs, a task for which the author of this thesis was
 507 required. Consequently, the detector conditions were significantly different between
 508 the two operational periods. SK-VI saw the start of the 0.01% gadolinium doped water.
 509 SK-VII, which started during the writing of this thesis, has increased the gadolinium
 510 concentration to 0.03% for continued operation [85].

Period	Start Date	End Date	Live-time (days)
I	April 1996	July 2001	1489.19
II	October 2002	October 2005	798.59
III	July 2006	September 2008	518.08
IV	September 2008	May 2018	3244.4
V	January 2019	July 2020	461.02
VI	July 2020	May 2022	583.3
VII	May 2022	Ongoing	N/A

Table 3.1.: The various SK periods and respective live-time. The SK-VI live-time is calculated until 1st April 2022. SK-VII started during the writing of this thesis.

511 3.1.1. The SK Detector

512 The basic structure of the Super-Kamiokande (SK) detector is a cylindrical tank with a
 513 diameter 39.3m and height 41.1m filled with ultrapure water [86]. A diagram of the
 514 significant components of the SK detector is given in Figure 3.1. The SK detector is
 515 situated in the Kamioka mine in Gifu, Japan. The mine is underground with roughly
 516 1km rock overburden (2.7km water equivalent overburden) [87]. At this depth, the

⁵¹⁷ rate of cosmic ray muons is significantly decreased to a value of $\sim 2\text{Hz}$. The top of
⁵¹⁸ the tank is covered with stainless steel which is designed as a working platform for
⁵¹⁹ maintenance, calibration, and location for high voltage and data acquisition electronics.

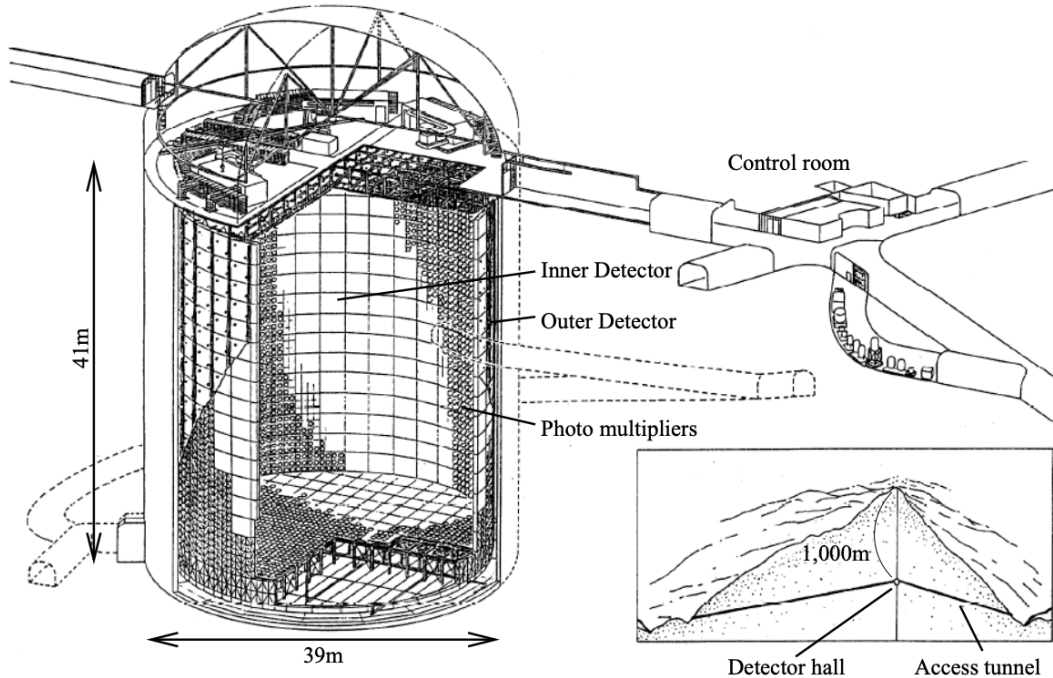


Figure 3.1.: A schematic diagram of the Super-Kamiokande Detector. Taken from [88].

⁵²⁰ A smaller cylindrical structure (36.2m diameter, 33.8m height) is situated inside the
⁵²¹ tank, with an approximate 2m gap between this structure and the outer tank wall. The
⁵²² purpose of this structure is to support the photomultiplier tubes (PMTs). The volume
⁵²³ inside and outside the support structure is referred to as the inner detector (ID) and
⁵²⁴ outer detector (OD), respectively. In the SK-IV era, the ID and OD are instrumented
⁵²⁵ by 11,129 50cm and 1,885 20cm PMTs respectively [86]. The ID contains a 32kton
⁵²⁶ mass of water. Many analyses performed at SK use a “fiducial volume” defined by the
⁵²⁷ volume of water inside the ID excluding some distance to the ID wall. This reduces the
⁵²⁸ volume of the detector which is sensitive to neutrino events but reduces radioactive
⁵²⁹ backgrounds and allows for better reconstruction performance. The nominal fiducial

volume is defined as the area contained inside 2m from the ID wall for a total of 22.5kton water [89].

The two regions of the detector (ID and OD) are optically separated with opaque black plastic. The purpose of this is to determine whether a track entered or exited the ID. This allows cosmic ray muons and partially contained events to be tagged and separated from neutrino events entirely contained within the ID. This black plastic is also used to cover the area between the ID PMTs to reduce photon reflection from the ID walls. Opposite to this, the OD is lined with a reflective material to allow photons to reflect around inside the OD until collected by one of the PMTs. Furthermore, each OD PMT is backed with $50 \times 50\text{cm}$ plates of wavelength shifting acrylic which increases the efficiency of light collection [87].

In the SK-IV data-taking period, the photocathode coverage of the detector, or the fraction of the ID wall instrumented with PMTs, is $\sim 40\%$ [87]. The PMTs have a quantum efficiency (the ratio of detected electrons to incident photons) of $\sim 21\%$ for photons with wavelengths of $360\text{nm} < \lambda < 390\text{nm}$. The proportion of photoelectrons that produce a signal in the dynode of a PMT, termed the collection efficiency, is $> 70\%$ [87]. The PMTs used within SK are most sensitive to photons with wavelength $300\text{nm} \leq \lambda \leq 600\text{nm}$ [87]. One disadvantage of using PMTs as the detection media is that the Earth's geomagnetic field can modify its response. Therefore, a set of compensation coils is built around the inner surface of the detector to mitigate this effect [90].

As mentioned, the SK detector is filled with ultrapure water, which in a perfect world would contain no impurities. However, bacteria and organic compounds can significantly degrade the water quality. This decreases the attenuation length, which reduces the total number of photons that hit a PMT. To combat this, a sophisticated water treatment system has been developed [87, 91]. UV lights, mechanical filters,

and membrane degasifiers are used to reduce the bacteria, suspended particulates, and radioactive materials from the water. The flow of water within the tank is also critical as it can remove stagnant bacterial growth or build-up of dust on the surfaces within the tank. Gravity drifts impurities in the water towards the bottom of the tank which, if left uncontrolled, can create asymmetric water conditions between the top and bottom of the tank. Typically, the water entering the tank is cooled below the ambient temperature of the tank to control convection and inhibit bacteria growth. Furthermore, the rate of dark noise hits within PMTs is sensitive to the PMT temperature [92] so controlling the temperature gradients within the tank is beneficial for stable measurements.

SK-VI is the first phase of the SK experiment to use gadolinium dopants within the ultrapure water [85]. As such, the SK water system had to be replaced to avoid removing the gadolinium concentrate from the ultrapure water [93]. For an inverse β -decay (IBD) interaction in a water target, the emitted neutron is thermally captured on hydrogen. This process releases 2.2MeV γ rays which are difficult to detect as the resulting Compton scattered electrons are very close to the Cherenkov threshold, limiting the number of photons produced. Thermal capture of neutrons on gadolinium generates γ rays with higher energy (8MeV [70]) meaning they are more easily detected. SK-VI has 0.01% Gd loading (0.02% gadolinium sulphate by mass) which causes \approx 50% of neutrons emitted by IBD to be captured on gadolinium [94, 95]. Whilst predominantly useful for low energy analyses, Gd loading allows better $\nu/\bar{\nu}$ separation for atmospheric neutrino event selections [96]. Efforts are currently in place to increase the gadolinium concentrate to 0.03% for \approx 75% neutron capture efficiency on gadolinium [97]. The final stage of loading targets 0.1% concentrate.

580 3.1.2. Calibration

581 The calibration of the SK detector is documented in [86] and summarised below. The
582 analysis presented within this thesis is dependent upon ‘high energy events’ (Charged
583 particles with $O(> 100)\text{MeV}$ momenta). These are events that are expected to generate
584 a larger number of photons such that each PMT will be hit with multiple photons.
585 The reconstruction of these events depends upon the charge deposited within each
586 PMT and the timing response of each individual PMT. Therefore, the most relevant
587 calibration techniques to this thesis are outlined.

588 Before installation, 420 PMTs were calibrated to have identical charge responses
589 and then distributed throughout the tank in a cross-shape pattern (As illustrated by
590 Figure 3.2). These are used as a standardised measure for the rest of the PMTs installed
591 at similar geometric positions within SK to be calibrated against. To perform this
592 calibration, a xenon lamp is located at the center of the SK tank which flashes uniform
593 light at 1Hz. This allows for geometrical effects, water quality variation, and timing
594 effects to be measured in-situ throughout normal data-taking periods.

595 When specifically performing calibration of the detector (in out-of-data taking
596 mode), the water in the tank was circulated to avoid top/bottom asymmetric water
597 quality. Any non-uniformity within the tank significantly affects the PMT hit proba-
598 bility through scattering or absorption. This becomes a dominant effect for the very
599 low-intensity light sources discussed later which are designed such that only one
600 photon is incident upon a given PMT.

601 The “gain” of a PMT is defined as the ratio of the total charge of the signal produced
602 compared to the charge of photoelectrons emitted by the photocathodes within the
603 PMT. To calibrate the signal of each PMT, the “relative” and “absolute” gain values are

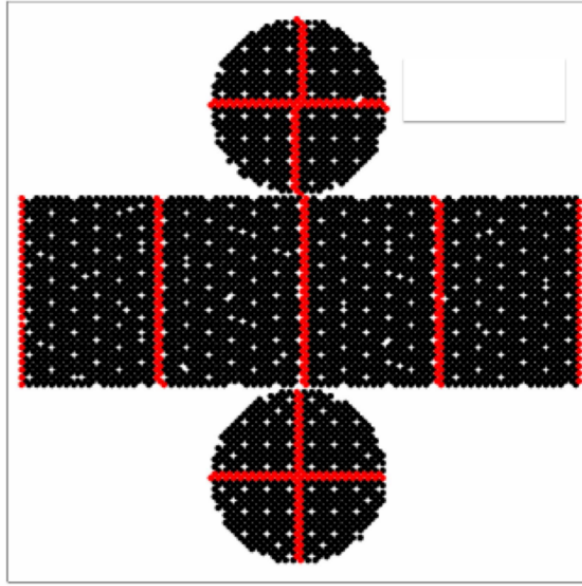


Figure 3.2.: The location of “standard PMTs” (red) inside the SK detector. Taken from [86].

604 measured. The relative gain is the variation of gain among each of the PMTs whereas
 605 the absolute gain is the average gain of all PMTs.

606 The relative gain is calibrated as follows. A laser is used to generate two measure-
 607 ments: a high-intensity flash that illuminates every PMT with a sufficient number of
 608 photons, and a low-intensity flash in which only a small number of PMTs collect light.
 609 The first measurement creates an average charge, $Q_{obs}(i)$ on PMT i , whereas the second
 610 measurement ensures that each hit PMT only generates a single photoelectron. For the
 611 low-intensity measurement, the number of times each PMT records a charge larger
 612 than 1/4 photoelectrons, $N_{obs}(i)$, is counted. The values measured can be expressed as

$$\begin{aligned} Q_{obs}(i) &\propto I_H \times f(i) \times \epsilon(i) \times G(i), \\ N_{obs}(i) &\propto I_L \times f(i) \times \epsilon(i), \end{aligned} \tag{3.1}$$

613 Where I_H and I_L is the intensity of the high and low flashes, $f(i)$ is the acceptance
 614 efficiency of the i^{th} PMT, $\epsilon(i)$ is the product of the quantum and collection efficiency

615 of the i^{th} PMT and $G(i)$ is the gain of the i^{th} PMT. The relative gain for each PMT can
616 determined by taking the ratio of these quantities.

617 The absolute gain calibration is performed by observing fixed energy γ -rays of
618 $E_{\gamma} \sim 9\text{MeV}$ emitted isotropically from neutron capture on a NiCf source situated at
619 the center of the detector. This generates a photon yield of about 0.004 photoelec-
620 trons/PMT/event, meaning that $> 99\%$ of PMT signals are generated from single
621 photoelectrons. A charge distribution is generated by performing this calibration over
622 all PMTs, and the average value of this distribution is taken to be the absolute gain
623 value.

624 As mentioned in subsection 3.1.1, the average quantum and collection efficiency
625 for the SK detector is $\sim 21\%$ and $> 70\%$ respectively. However, these values do differ
626 between each PMT and need to be calibrated accordingly. Consequently, the NiCf
627 source is also used to calibrate the “quantum \times collection” efficiency (denoted “QE”)
628 value of each PMT. The NiCf low-intensity source is used as the PMT hit probability
629 is proportional to the QE ($N_{\text{obs}}(i) \propto \epsilon(i)$ in Equation 3.1). A Monte Carlo prediction
630 which includes photon absorption, scattering, and reflection is made to estimate the
631 number of photons incident on each PMT and the ratio of the number of predicted
632 to observed hits is calculated. The difference is attributed to the QE efficiency of that
633 PMT. This technique is extended to calculate the relative QE efficiency by normalizing
634 the average of all PMTs which removes the dependence on the light intensity.

635 Due to differing cable lengths and readout electronics, the timing response between
636 a photon hitting the PMT and the signal being captured by the data acquisition can be
637 different between each PMT. Due to threshold triggers (Described in subsection 3.1.3),
638 the time at which a pulse reaches a threshold is dependent upon the size of the pulse.
639 This is known as the ‘time-walk’ effect and also needs to be accounted for in each PMT.
640 To calibrate the timing response, a pulse of light with width 0.2ns is emitted into the

641 detector through a diffuser. Two-dimensional distributions of time and pulse height
642 (or charge) are made for each PMT and are used to calibrate the timing response. This
643 is performed in-situ during data taking with the light source pulsing at 0.03Hz.

644 The top/bottom water quality asymmetry is measured using the NiCf calibration
645 data and cross-referencing these results to the “standard PMTs”. The water attenuation
646 length is continuously measured by the rate of vertically-downgoing cosmic-ray
647 muons which enter via the top of the tank.

648 Dark noise is the phenomenon where a PMT registers a pulse that is consistent
649 with a single photoelectron emitted from photon detection despite the PMT being in
650 complete darkness. This is predominately caused by two processes. Firstly there is
651 intrinsic dark noise which is where photoelectrons gain enough thermal energy to be
652 emitted from the photocathode, and secondly, the radioactive decay of contaminants
653 inside the structure of the PMT. Typical dark noise rate for PMTs used within SK are
654 $O(3)$ kHz [87]. This is lower than the expected number of photons generated for a ‘high
655 energy event’ (As described in subsection 3.1.4) but instability in this value can cause
656 biases in reconstruction. Dark noise is related to the gain of a PMT and is calibrated
657 using hits inside a time window recorded before an event trigger [98].

658 3.1.3. Data Acquisition and Triggering

659 The analysis presented in this thesis only uses the SK-IV period of the SK experiment
660 so this subsection focuses on the relevant points of the data acquisition and triggering
661 systems to that SK period. The earlier data acquisition and triggering systems are
662 documented in [99, 100].

663 Before the SK-IV period started, the existing front-end electronics were replaced
664 with “QTC-Based Electrons with Ethernet, QBEE” systems [101]. When the QBEE

observes a signal above a 1/4 photoelectron threshold, the charge-to-time (QTC) converter generates a rectangular pulse. The start of the rectangular pulse indicates the time at which the analog photoelectron signal was received and the width of the pulse indicates the total charge integrated throughout the signal. This is then digitized by time-to-digital converters and sent to the “front-end” PCs. The digitized signal from every QBEE is then chronologically ordered and sent to the “merger” PCs. It is the merger PCs that apply the software trigger. Any triggered events are passed to the “organizer” PC. This sorts the data stream of multiple merger PCs into chronologically ordered events which are then saved to disk. The schematic of data flow from PMTs to disk is illustrated in Figure 3.3.

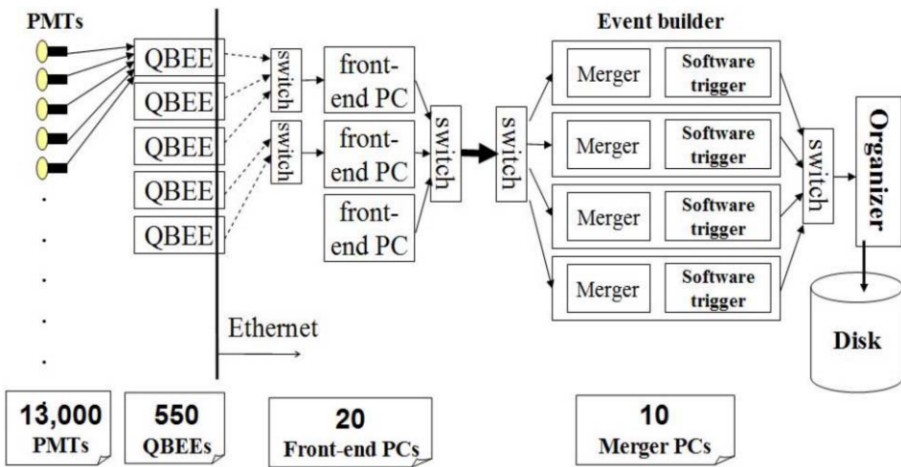


Figure 3.3.: Schematic view of the data flow through the data acquisition and online system. Taken from [102].

The software trigger (described in [103]) operates by determining the number of PMT hits within a 200ns sliding window, N_{200} . This window coincides with the maximum time that a Cherenkov photon would take to traverse the length of the SK tank [100]. For lower energy events that generate fewer photons, this technique is useful for eliminating background processes like dark noise and radioactive decay which would be expected to separate in time. When the value of N_{200} exceeds some threshold, a software trigger is issued. There are several trigger thresholds used within

the SK-IV period which are detailed in Table 3.2. If one of these thresholds is met, the PMT hits within an extended time window are also read out and saved to disk. In the special case of an event that exceeds the SHE trigger but does not exceed the OD trigger, the AFT trigger looks for delayed coincidences of 2.2MeV gamma rays emitted from neutron capture in a $535\mu\text{s}$ window after the SHE trigger. A similar but more complex “Wideband Intelligent Trigger (WIT)” has been deployed and is described in [104].

Trigger	Acronym	Condition	Extended time window (μs)
Super Low Energy	SLE	>34/31 hits	1.3
Low Energy	LE	>47 hits	40
High Energy	HE	>50 hits	40
Super High Energy	SHE	>70/58 hits	40
Outer Detector	OD	>22 hits in OD	N/A

Table 3.2.: The trigger thresholds and extended time windows saved around an event which were utilised throughout the SK-IV period. The exact thresholds can change and the values listed here represent the thresholds at the start and end of the SK-IV period.

3.1.4. Cherenkov Radiation

Cherenkov light is emitted from any highly energetic charged particle traveling with relativistic velocity, β , greater than the local speed of light in a medium [105]. Cherenkov light is formed at the surface of a cone with characteristic pitch angle,

$$\cos(\theta) = \frac{1}{\beta n}. \quad (3.2)$$

693 where n is the refractive index of the medium. Consequently, the Cherenkov
 694 momentum threshold, P_{thres} , is dependent upon the mass, m , of the charged particle
 695 moving through the medium,

$$P_{thres} = \frac{m}{\sqrt{n^2 - 1}} \quad (3.3)$$

696 For water, where $n = 1.33$, the Cherenkov threshold momentum and energy for
 697 various particles are given in Table 3.3. In contrast, γ -rays are detected indirectly via
 698 the combination of photons generated by Compton scattering and pair production.
 699 The threshold for detection in the SK detector is typically higher than the threshold
 700 for photon production. This is due to the fact that the attenuation of photons in the
 701 water means that typically $\sim 75\%$ of Cherenkov photons reach the ID PMTs. Then the
 702 collection and quantum efficiencies described in subsection 3.1.1 result in the number
 703 of detected photons being lower than the number of photons which reach the PMTs.

Particle	Threshold Momentum (MeV)	Threshold Energy (MeV)
Electron	0.5828	0.7751
Muon	120.5	160.3
Pion	159.2	211.7
Proton	1070.0	1423.1

Table 3.3.: The threshold momentum and energy for a particle to generate Cherenkov light in ultrapure water, as calculated in Equation 3.2 in ultrapure water which has refractive index $n = 1.33$.

704 The Frank-Tamm equation [106] describes the relationship between the number of
 705 Cherenkov photons generated per unit length, dN/dx , the wavelength of the photons
 706 generated, λ , and the relativistic velocity of the charged particle,

$$\frac{d^2N}{dxd\lambda} = 2\pi\alpha \left(1 - \frac{1}{n^2\beta^2}\right) \frac{1}{\lambda^2}. \quad (3.4)$$

where α is the fine structure constant. For a 100MeV momentum electron, approximately 330 photons will be produced per centimeter in the $300\text{nm} \leq \lambda \leq 700\text{nm}$ region which the ID PMTs are most sensitive to [87].

3.2. The Tokai to Kamioka Experiment

The Tokai to Kamioka (T2K) experiment is a long-baseline neutrino oscillation experiment located in Japan. Proposed in the early 2000s [107, 108] to replace K2K [109], T2K was designed to observe electron neutrino appearance whilst precisely measuring the oscillation parameters associated with muon neutrino disappearance [110]. The experiment consists of a neutrino beam generated at the Japan Proton Accelerator Research Complex (J-PARC), a suite of near detectors situated 280m from the beam target, and the Super Kamiokande far detector positioned at a 295km baseline. The cross-section view of the T2K experiment is drawn in Figure 3.4.

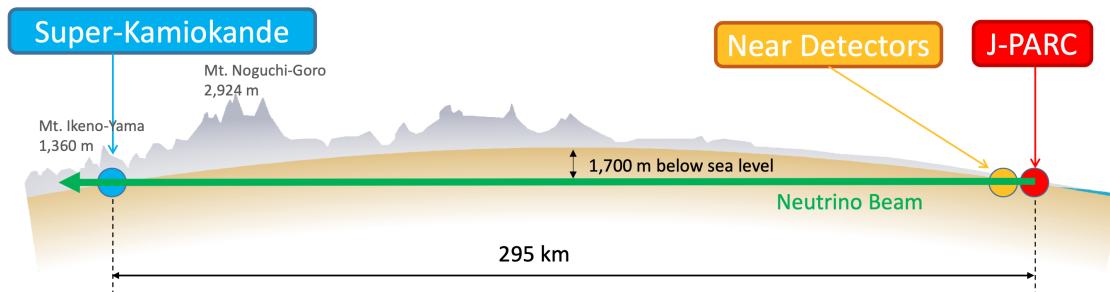


Figure 3.4.: The cross-section view of the Tokai to Kamioka experiment illustrating the beam generation facility at J-PARC, the near detector situated at a baseline of 280m and the Super Kamiokande far detector situated 295km from the beam target.

The T2K collaboration makes world-leading measurements of the $\sin^2(\theta_{23})$, Δm_{23}^2 , and δ_{CP} oscillation parameters. Improvements in the precision and accuracy of parameter estimates are still being made by including new data samples and developing the models which describe the neutrino interactions and detector responses [111]. Electron neutrino appearance was first observed at T2K in 2014 [112] with 7.3σ significance.

The near detectors provide constraints on the beam flux and cross-section model parameters used within the oscillation analysis by observing the unoscillated neutrino beam. There are a host of detectors situated in the near detector hall (As illustrated in Figure 3.5): ND280 (subsection 3.2.2), INGRID (subsection 3.2.3), NINJA [113], WAGASCI [114], and Baby-MIND [115]. The latter three are not currently used within the oscillation analysis presented within this thesis.

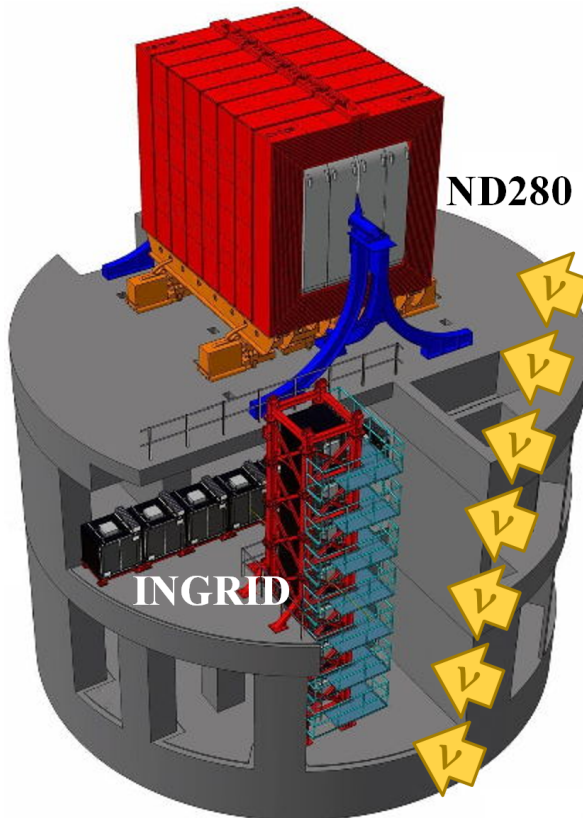


Figure 3.5.: The near detector suite for the T2K experiment showing the ND280 and INGRID detectors. The distance between the detectors and the beam target is 280m.

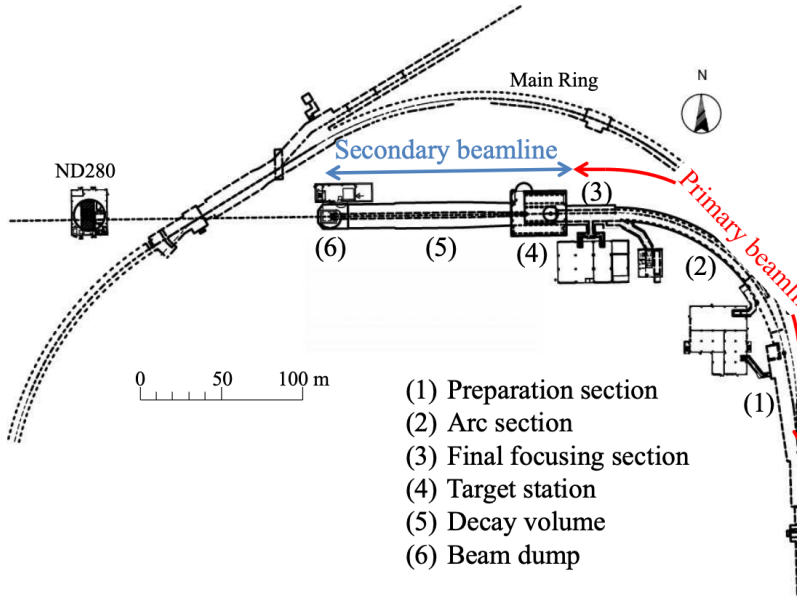
Whilst this thesis presents the ND280 in terms of its purpose for the oscillation analysis, the detector can also make many cross-section measurements at neutrino energies of $O(1)$ GeV for the different targets within the detector [116, 117]. These measurements are of equal importance as they can lead the way in determining the model parameters used in the interaction models for the future high-precision era of neutrino physics.

DB: Discuss BANFF, PTheta, MaCh3 and covariance

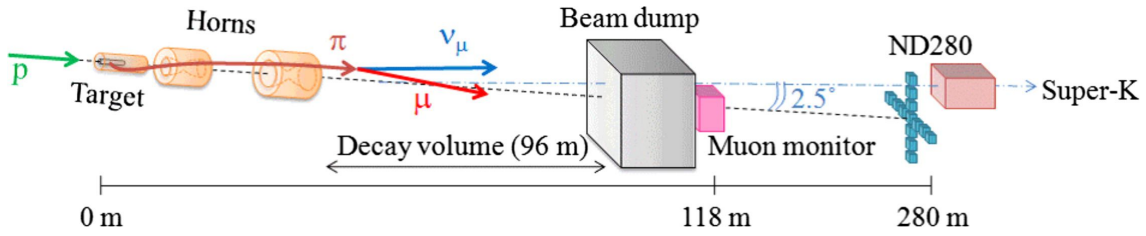
3.2.1. The Neutrino Beam

The neutrino beam used within the T2K experiment is described in [59, 118] and summarised below. The accelerating facility at J-PARC is composed of two sections; the primary and secondary beamlines. Figure 3.6 illustrates a schematic of the beamline, focusing mostly on the components of the secondary beamline. The primary beamline has three accelerators that progressively accelerate protons; a linear accelerator, a rapid-cycling synchrotron, and the main-ring (MR) synchrotron. Once fully accelerated by the MR, the protons have a kinetic energy of 30GeV. Eight bunches of these protons, separated by 500ns, are extracted per “spill” from the MR and directed towards a graphite target (a rod of length 91.4cm and diameter 2.6cm). Spills are extracted at 0.5Hz with $\sim 3 \times 10^{14}$ protons contained per spill.

The secondary beamline consists of three main components: the target station, the decay volume, and the beam dump. The target station is comprised of the target, beam monitors, and three magnetic focusing horns. The proton beam interacts with the graphite target to form a secondary beam of mostly pions and kaons. The secondary beam travels through a 96m long decay volume, generating neutrinos through the following decays [59],



(a) Primary and secondary beamline



(b) Secondary beamline

Figure 3.6.: Top panel: Bird's eye view of the most relevant part of primary and secondary beamline used within the T2K experiment. The primary beamline is the main-ring proton synchrotron, kicker magnet, and graphite target. The secondary beamline consists of the three focusing horns, decay volume, and beam dump. Figure taken from [118]. Bottom panel: The side-view of the secondary beamline including the focusing horns, beam dump and neutrino detectors. Figure taken from [119].

$$\pi^+ \rightarrow \mu^+ + \nu_\mu$$

$$\pi^- \rightarrow \mu^- + \bar{\nu}_\mu$$

$$K^+ \rightarrow \mu^+ + \nu_\mu$$

$$K^- \rightarrow \mu^- + \bar{\nu}_\mu$$

$$\rightarrow \pi^0 + e^+ + \nu_e$$

$$\rightarrow \pi^0 + e^- + \bar{\nu}_e$$

$$\rightarrow \pi^0 + \mu^+ + \nu_\mu$$

$$\rightarrow \pi^0 + \mu^- + \bar{\nu}_\mu$$

$$K_L^0 \rightarrow \pi^- + e^+ + \nu_e$$

$$K_L^0 \rightarrow \pi^+ + e^- + \bar{\nu}_e$$

$$\rightarrow \pi^- + \mu^+ + \nu_\mu$$

$$\rightarrow \pi^+ + \mu^- + \bar{\nu}_\mu$$

$$\mu^+ \rightarrow e^+ + \bar{\nu}_\mu + \nu_e$$

$$\mu^- \rightarrow e^- + \nu_\mu + \bar{\nu}_e$$

The electrically charged component of the secondary beam is focused towards the far detector by the three magnetic horns. These horns direct charged particles of a particular polarity towards SK whilst defocusing the oppositely charged particles. This allows a mostly neutrino or mostly antineutrino beam to be used within the experiment, denoted as “forward horn current (FHC)” or “reverse horn current (RHC)” respectively.

Figure 3.7 illustrates the different contributions to the FHC and RHC neutrino flux.

The low energy flux is dominated by the decay of pions whereas kaon decay becomes the dominant source of neutrinos for $E_\nu > 3\text{GeV}$. The “wrong-sign” component, which is the $\bar{\nu}_\mu$ background in a ν_μ beam, and the intrinsic irreducible ν_e background, are predominantly due to muon decay for $E_\nu < 2\text{GeV}$. As the antineutrino production cross-section is smaller than the neutrino cross-section, the wrong-sign component is more dominant in the RHC beam as compared to that in the FHC beam.

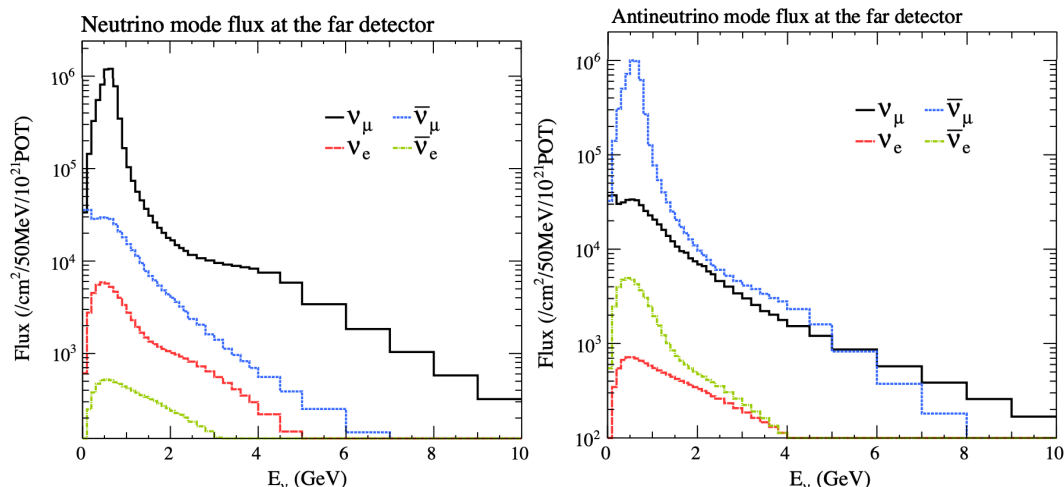


Figure 3.7.: The Monte Carlo prediction of the energy spectrum for each flavour of neutrino (ν_e , $\bar{\nu}_e$, ν_μ and $\bar{\nu}_\mu$) in the neutrino dominated beam FHC mode (Left) and antineutrino dominated beam RHC mode (Right) expected at SK. Taken from [120].

The beam dump, situated at the end of the decay volume, stops all charged particles other than highly energetic muons ($p_\mu > 5\text{GeV}$). The MuMon detector monitors the

⁷⁷⁰ penetrating muons to determine the beam direction and intensity which is used to
⁷⁷¹ constrain some of the beam flux systematics within the analysis [119, 121].

⁷⁷² The T2K experiment uses an off-axis beam to narrow the neutrino energy distribution.
⁷⁷³ This was the first implementation of this technique in a long-baseline neutrino
⁷⁷⁴ oscillation experiment after its original proposal [122]. Pion decay, $\pi \rightarrow \mu + \nu_\mu$, is a
⁷⁷⁵ two-body decay. Consequently, the neutrino energy, E_ν , can be determined based on
⁷⁷⁶ the pion energy, E_π , and the angle at which the neutrino is emitted, θ ,

$$E_\nu = \frac{m_\pi^2 - m_\mu^2}{2(E_\pi - p_\pi \cos(\theta))}, \quad (3.5)$$

⁷⁷⁷ where m_π and m_μ are the mass of the pion and muon respectively. For a fixed
⁷⁷⁸ energy pion, the neutrino energy distribution is dependent upon the angle at which the
⁷⁷⁹ neutrinos are observed from the initial pion beam direction. For the 295km baseline at
⁷⁸⁰ T2K, $E_\nu = 0.6\text{GeV}$ maximises the electron neutrino appearance probability, $P(\nu_\mu \rightarrow \nu_e)$,
⁷⁸¹ whilst minimising the muon disappearance probability, $P(\nu_\mu \rightarrow \nu_\mu)$. Figure 3.8
⁷⁸² illustrates the neutrino energy distribution for a range of off-axis angles, as well as the
⁷⁸³ oscillation probabilities most relevant to T2K.

⁷⁸⁴ 3.2.2. The Near Detector at 280m

⁷⁸⁵ Whilst all the near detectors are situated in the same “pit” located at 280m from the
⁷⁸⁶ beamline, the “ND280” detector is the off-axis detector which is situated at the same
⁷⁸⁷ off-axis angle as the Super-Kamiokande far detector. It has two primary functions;
⁷⁸⁸ firstly it measures the neutrino flux and secondly it counts the event rates of different
⁷⁸⁹ types of neutrino interactions. Both of these constrain the flux and cross-section

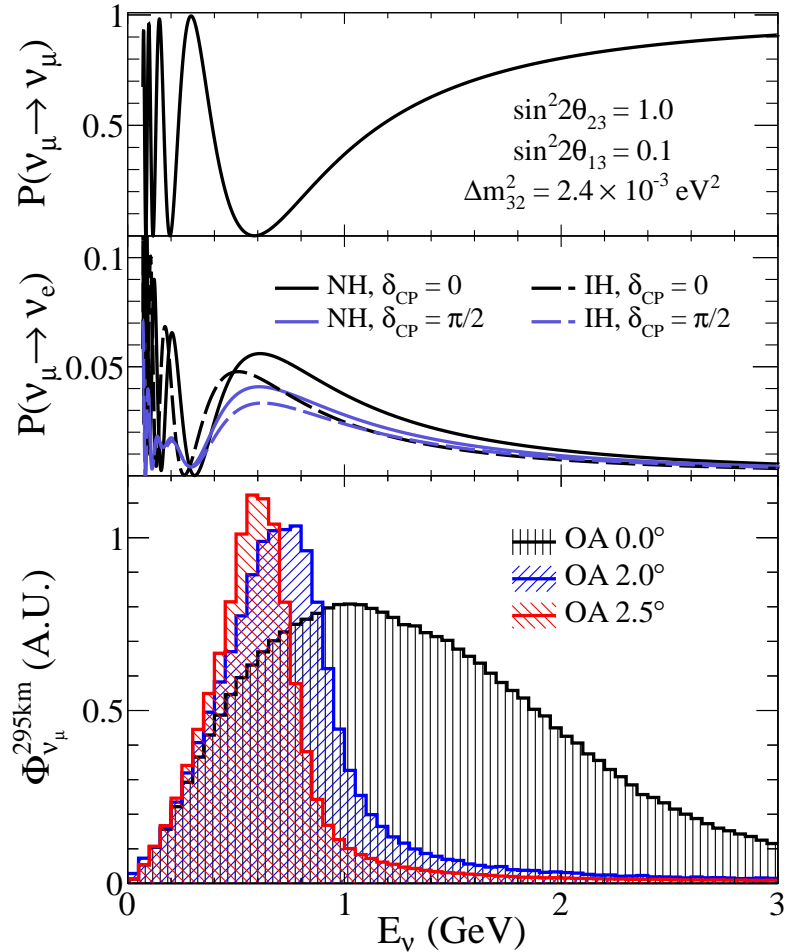


Figure 3.8.: Top panel: T2K muon neutrino disappearance probability as a function of neutrino energy. Middle panel: T2K electron neutrino appearance probability as a function of neutrino energy. Bottom panel: The neutrino flux distribution for three different off-axis angles (Arbitrary units) as a function of neutrino energy.

790 systematics invoked within the model for a more accurate prediction of the expected
791 event rate at the far detector.

792 As illustrated in Figure 3.9, the ND280 detector consists of several sub-detectors.
793 The most important part of the detector for this analysis is the tracker region. This is
794 comprised of two time projection chambers (TPCs) sandwiched between three fine
795 grain detectors (FGDs). The FGDs contain both hydrocarbon plastics and water tar-
796 gets for neutrino interactions and provide track reconstruction near the interaction
797 vertex. The emitted charged particles can then propagate into the TPCs which pro-
798 vide particle identification and momentum reconstruction. The FGDs and TPCs are

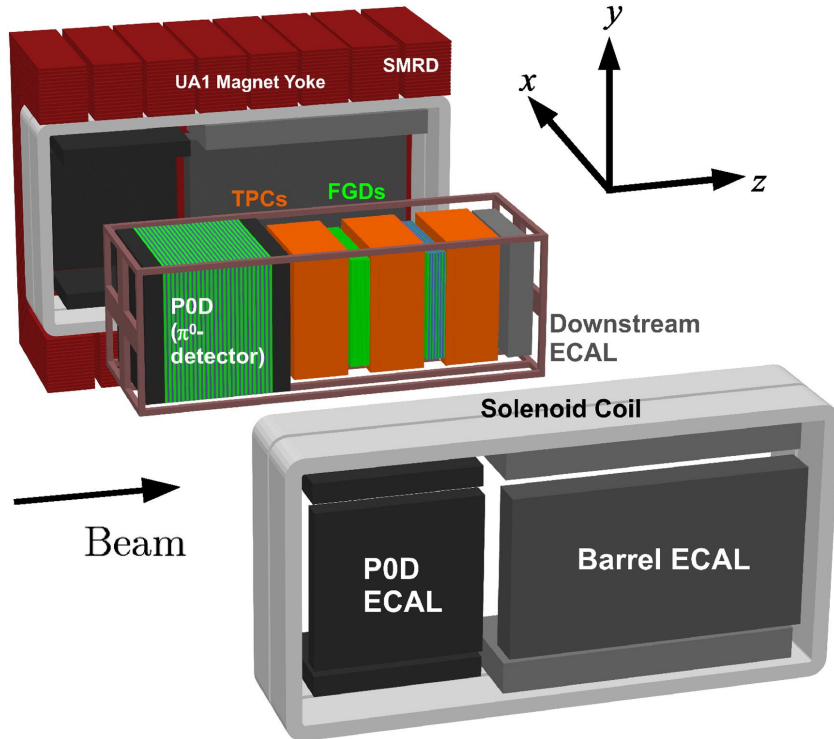


Figure 3.9.: The components of the ND280 detector. The neutrino beam travels from left to right. Taken from [118].

799 further described in subsubsection 3.2.2.1 and subsubsection 3.2.2.2 respectively. The
 800 electromagnetic calorimeter (ECAL) encapsulates the tracker region alongside the π^0
 801 detector (P0D). The ECAL measures the deposited energy from photons emitted from
 802 interactions within the FGD. The P0D constrains the cross-section of neutral current
 803 interactions which generate neutral pions, which is one of the largest backgrounds in
 804 the electron neutrino appearance oscillation channel. The P0D and ECAL detectors
 805 are detailed in subsubsection 3.2.2.3 and subsubsection 3.2.2.4 respectively. The entire
 806 detector is located within a large yoke magnet which produces a 0.2T magnetic field.
 807 This design of the magnet also includes a scintillating detector called the side muon
 808 range detector (SMRD) which is used to track high-angle muons as well as acting as a
 809 cosmic veto. The SMRD is described in subsubsection 3.2.2.5.

810 **3.2.2.1. Fine Grained Detectors**

811 The T2K tracker region is comprised of two fine grained detectors (FGD) and three
812 Time Projection Chambers (TPC). A detailed description of the FGD design, construc-
813 tion, and assembly is found in [123] and summarised below. The FGDs are the primary
814 target for neutrino interactions with a mass of 1.1 tonnes per FGD. Alongside this,
815 the FGDs are designed to be able to track short-range particles which do not exit the
816 FGD. Typically, short-range particles are low momentum and are observed as tracks
817 that deposit a large amount of energy per unit length. This means the FGD needs
818 good granularity to resolve these particles. The FGDs have the best timing resolution
819 ($\sim 3\text{ns}$) of any of the sub-detectors of the ND280 detector. As such, the FGDs are
820 used for time of flight measurements to distinguish forward going positively charged
821 particles from backward going negatively charged particles. Finally, any tracks which
822 pass through multiple sub-detectors are required to be track matched to the FGD.

823 Both FGDs are made from square scintillator planes of side length 186cm and
824 width 2.02cm. Each plane consists of two layers of 192 scintillator bars in an X or Y
825 orientation. A wavelength shifting fiber is threaded through the center of each bar and
826 is read out by a multi-pixel photon counter (MPPC). FGD1 is the most upstream of
827 the two FGDs and contains 15 planes of carbon plastic scintillator which is a common
828 target in external neutrino scattering data. As the far detector is a pure water target, 7
829 of the 15 scintillator planes in FGD2 have been replaced with a hybrid water-scintillator
830 target. Due to the complexity of the nucleus, nuclear effects can not be extrapolated
831 between different nuclei. Therefore having the ability to take data on one target which
832 is the same as external data and another target which is the same as the far detector
833 target is beneficial for reliable model parameter estimates.

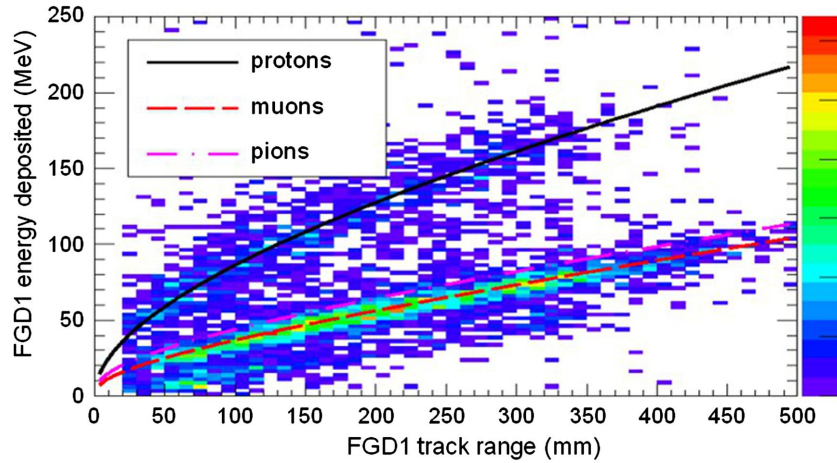


Figure 3.10.: Comparison of data to Monte Carlo prediction of integrated deposited energy as a function of track length for particles that stopped in FGD1. Taken from [123].

The integrated deposited energy is used for particle identification. The FGD can distinguish protons from other charged particles by comparing the integrated deposited energy from data to Monte Carlo prediction as seen in Figure 3.10.

3.2.2.2. Time Projection Chambers

The majority of particle identification and momentum measurements within ND280 are provided by three Time Projection Chambers (TPCs) [124]. The TPCs are located on either side of the FGDs. They are located inside of the magnetic field meaning the momentum of a charged particle can be determined from the bending of the track.

Each TPC module consists of two gas-tight boxes, as shown in Figure 3.11, which are made of non-magnetic material. The outer box is filled with CO₂ which acts as an electrical insulator between the inner box and the ground. The inner box forms the field cage which produces a uniform electric drift field of $\sim 275\text{V}/\text{cm}$ and is filled with an argon gas mixture. Charged particles moving through this gas mixture ionize the gas and the ionised charge is drifted towards micromegas detectors which measure the ionization charge. The time and position information in the readout allows a three-dimensional image of the neutrino interaction.

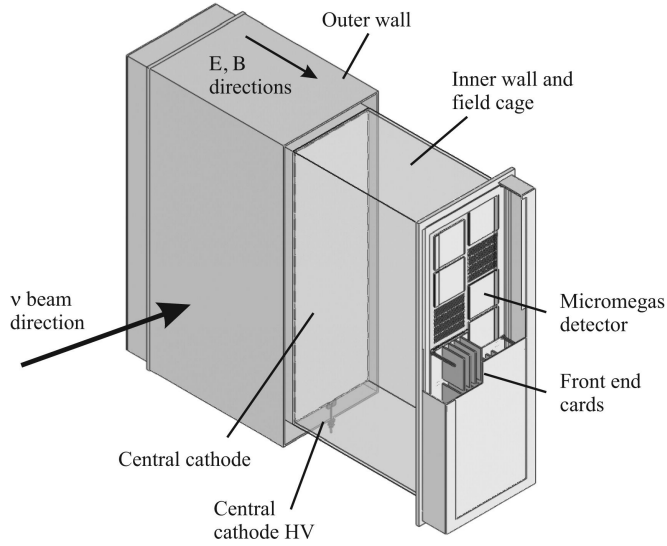


Figure 3.11.: Schematic design of a Time Projection Chamber detector. Taken from [124].

The particle identification of tracks that pass through the TPCs is performed using

dE/dx measurements. Figure 3.12 illustrates the data to Monte Carlo distributions of the energy lost by a charged particle passing through the TPC as a function of the reconstructed particle momentum. The resolution is $7.8 \pm 0.2\%$ meaning that electrons and muons can be distinguished. This allows reliable measurements of the intrinsic ν_e component of the beam.

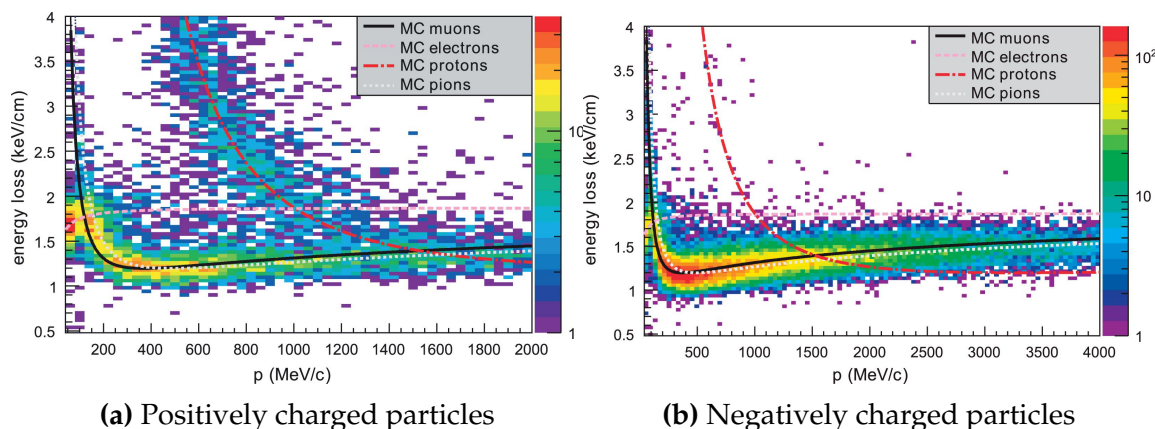


Figure 3.12.: The distribution of energy loss as a function of reconstructed momentum for charged particles passing through the TPC, comparing data to Monte Carlo prediction. Taken from [124].

⁸⁵⁶ 3.2.2.3. π^0 Detector

⁸⁵⁷ If one of the γ -rays from a $\pi^0 \rightarrow 2\gamma$ decay is missed at the far detector, the recon-
⁸⁵⁸ struction will determine that event to be a charge current ν_e -like event. This is one of
⁸⁵⁹ the main backgrounds hindering the electron neutrino appearance searches. The π^0
⁸⁶⁰ detector (P0D) measures the cross-section of the neutral current induced neutral pion
⁸⁶¹ production on a water target to constrain this background.

⁸⁶² The P0D is a cube of approximately 2.5m length consisting of layers of scintillating
⁸⁶³ bars, brass and lead sheets, and water bags as illustrated in Figure 3.13. Two electro-
⁸⁶⁴ magnetic calorimeters are positioned at the most upstream and most downstream
⁸⁶⁵ position in the sub-detector and the water target is situated in between them. The
⁸⁶⁶ scintillator layers are built from two triangular bars orientated in opposite directions
⁸⁶⁷ to form a rectangular layer. Each triangular scintillator bar is threaded with optical
⁸⁶⁸ fiber which is read out by MPPCs. The high-Z brass and lead regions produce electron
⁸⁶⁹ showers from the photons emitted in π^0 decay.

⁸⁷⁰ The sub-detector can generate measurements of NC1 π^0 cross-sections on a water
⁸⁷¹ target by measuring the event rate both with and without the water target, with the
⁸⁷² cross-section on a water target being determined as the difference. The total active
⁸⁷³ mass is 16.1 tonnes when filled with water and 13.3 tonnes when empty.

⁸⁷⁴ 3.2.2.4. Electromagnetic Calorimeter

⁸⁷⁵ The electromagnetic calorimeter [126] (ECal) encapsulates the P0D and tracking sub-
⁸⁷⁶ detectors. Its primary purpose is to aid π^0 reconstruction from any interaction in
⁸⁷⁷ the tracker. To do this, it measures the energy and direction of photon showers from
⁸⁷⁸ $\pi^0 \rightarrow 2\gamma$ decay. It can also distinguish pion and muon tracks depending on the shape
⁸⁷⁹ of the photon shower deposited.

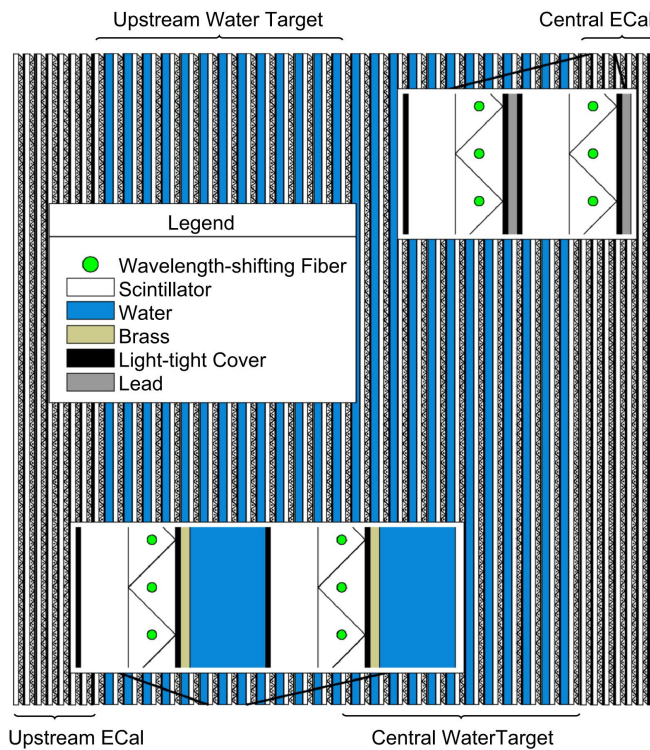


Figure 3.13.: A schematic of the P0D side-view. Taken from [125].

The ECal is comprised of three sections; the P0D ECal which surrounds the P0D, the barrel ECal which encompasses the tracking region, and the downstream ECal which is situated downstream of the tracker region. The barrel and downstream ECals are tracking calorimeters that focus on electromagnetic showers from high-angle particles emitted from the tracking sub-detectors. Particularly in the TPC, high-angle tracks (those which travel perpendicularly to the beam-axis) can travel along a single scintillator bar resulting in very few hits. The width of the barrel and downstream ECal corresponds to ~ 11 electron radiation lengths to ensure a significant amount of the π^0 energy is contained. As the P0D has its own calorimetry which reconstructs showers, the P0D ECal determines the energy which escapes the P0D.

Each ECal is constructed of multiple layers of scintillating bars sandwiched between lead sheets. The scintillating bars are threaded with optical fiber and read out by MPPCs. Each sequential layer of the scintillator is orientated perpendicular to the previous which allows a three dimensional event reconstruction. The target mass

894 of the P0D ECal, barrel ECal, and downstream ECal are 1.50, 4.80 and 6.62 tonnes
895 respectively.

896 **3.2.2.5. Side Muon Range Detector**

897 As illustrated in Figure 3.9, the ECal, FGDs, P0D, and TPCs are enclosed within the
898 UA1 magnet. Originally designed for the NOMAD [127] experiment and reconditioned
899 for use in the T2K experiment [128], the UA1 magnet provides a uniform horizontal
900 magnetic field of 0.2T with an uncertainty of 2×10^{-4} T.

901 Built into the UA1 magnet, the side muon range detector (SMRD) [129] monitors
902 high-energy muons which leave the tracking region and permeate through the ECal.
903 It additionally acts as a cosmic muon veto and trigger.

904 **3.2.3. The Interactive Neutrino GRID**

905 The Interactive Neutrino GRID (INGRID) detector is situated within the same “pit” as
906 the other near detectors. It is aligned with the beam in the “on-axis” position and mea-
907 sures the beam direction, spread, and intensity. The detector was originally designed
908 with 16 identical modules [118] (two modules have since been decommissioned) and a
909 “proton” module. The design of the detector is cross-shaped with length and height
910 10m × 10m as illustrated in Figure 3.14.

911 Each module is composed of iron sheets interlaced with eleven tracking scintillator
912 planes for a total target mass of 7.1 tonnes per module. The scintillator design is an X-Y
913 pattern of 24 bars in both orientations, where each bar contains wave-length shifting
914 fibers which are connected to multi-pixel photon counters (MPPCs). Each module is
915 encapsulated inside veto planes to aid the rejection of charged particles entering the
916 module.

917 The proton module is different from the other modules in that it consists of entirely
 918 scintillator planes with no iron target. The scintillator bars are also smaller than those
 919 used in the other modules to increase the granularity of the detector and improve
 920 tracking capabilities. The module sits in the center of the beamline and is designed to
 921 give precise measurements of quasi-elastic charged current interactions to evaluate
 922 the performance of the Monte Carlo simulation of the beamline.

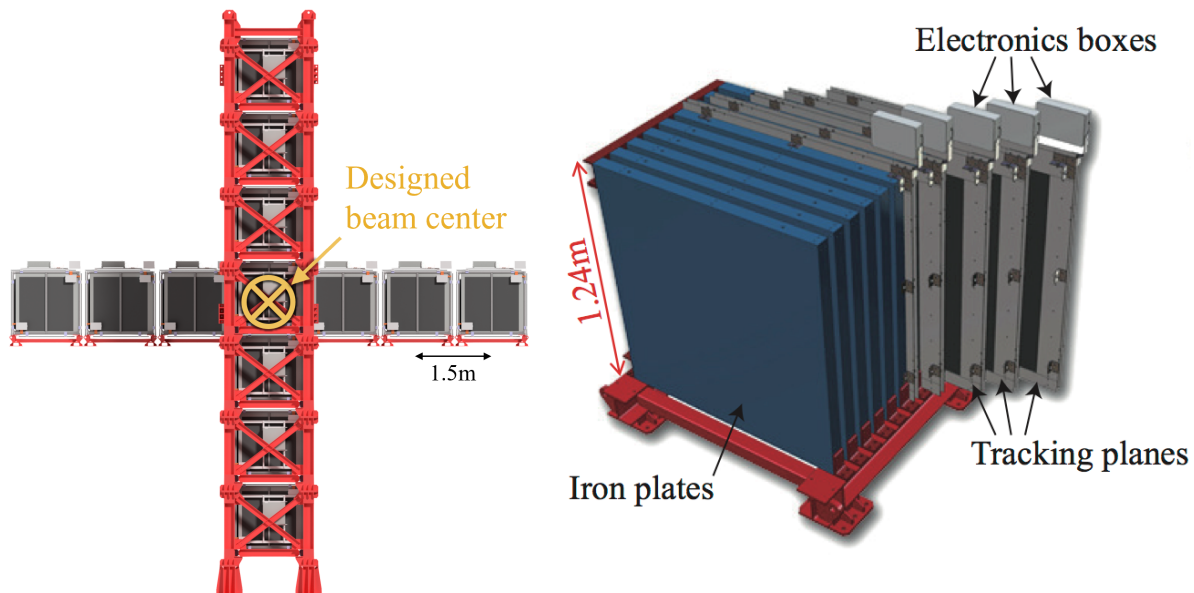


Figure 3.14.: Left panel: The Interactive Neutrino GRID on-axis Detector. 14 modules are arranged in a cross-shape configuration, with the center modules being directly aligned with the on-axis beam. Right panel: The layout of a single module of the INGRID detector. Both figures are recreated from [118].

923 The INGRID detector can measure the beam direction to an uncertainty of 0.4mrad
 924 and the beam center within a resolution of 10cm [118]. The beam direction in both the
 925 vertical and horizontal directions is discussed in [130] and it is found to be in good
 926 agreement with the MUMON monitor described in subsection 3.2.1.

₉₂₇ **Chapter 4**

₉₂₈ **Bayesian Statistics and Markov Chain
Monte Carlo Techniques**

₉₃₀ This thesis presents a Bayesian oscillation analysis. To extract the oscillation parameters,
₉₃₁ a Markov Chain Monte Carlo (MCMC) method is used. This chapter explains
₉₃₂ the theory of how parameter estimates can be determined using this technique and
₉₃₃ condenses the material found in the literature [131–134].

₉₃₄ The oscillation parameter determination presented within this thesis is built upon
₉₃₅ a simultaneous fit to neutrino beam data in the near detector, beam data at SK and
₉₃₆ atmospheric data at SK. In total, there are four oscillation parameters of interest
₉₃₇ ($\sin^2(\theta_{23})$, $\sin^2(\theta_{13})$, Δm_{23}^2 , and δ_{CP}), two oscillation parameters to which this study
₉₃₈ will not be sensitive ($\sin^2(\theta_{12})$, Δm_{12}^2) and many nuisance parameters that control the
₉₃₉ systematic uncertainty models invoked within this study.

₉₄₀ The MCMC technique generates a multi-dimensional probability distribution across
₉₄₁ all of the model parameters used in the fit. To determine the parameter estimate of a
₉₄₂ single parameter, this multi-dimensional object is integrated over all other parameters.
₉₄₃ This process is called Marginalisation and is further described in subsection 4.3.1.
₉₄₄ Monte Carlo techniques approximate the probability distribution of each parameter
₉₄₅ within the limit of generating infinite samples. As ever, generating a large number of
₉₄₆ samples is time and resource-dependent. Therefore, an MCMC technique is utilised
₉₄₇ within this analysis to reduce the required number of steps to sufficiently sample the
₉₄₈ parameter space. This technique is described in further detail in subsection 4.2.1.

⁹⁴⁹ 4.1. Bayesian Statistics

⁹⁵⁰ Bayesian inference treats observable data, D , and model parameters, $\vec{\theta}$, on equal
⁹⁵¹ footing such that a probability model of both data and parameters is required. This is
⁹⁵² the joint probability distribution $P(D, \vec{\theta})$ and can be described by the prior distribution
⁹⁵³ for model parameters $P(\vec{\theta})$ and the likelihood of the data given the model parameters
⁹⁵⁴ $P(D|\vec{\theta})$,

$$P(D, \vec{\theta}) = P(D|\vec{\theta})P(\vec{\theta}). \quad (4.1)$$

⁹⁵⁵ The prior distribution, $P(\vec{\theta})$, describes all previous knowledge about the parameters
⁹⁵⁶ within the model. For example, if the risk of developing health problems is known
⁹⁵⁷ to increase with age, the prior distribution would describe the increase. For the
⁹⁵⁸ purpose of this analysis, the prior distribution is typically the best-fit values taken
⁹⁵⁹ from external data measurements with a Gaussian uncertainty. The prior distribution
⁹⁶⁰ can also contain correlations between model parameters. In an analysis using Monte
⁹⁶¹ Carlo techniques, the likelihood of measuring some data assuming some set of model
⁹⁶² parameters is calculated by comparing the Monte Carlo prediction generated at that
⁹⁶³ particular set of model parameters to the data.

⁹⁶⁴ It is parameter estimation that is important for this analysis and as such, we apply
⁹⁶⁵ Bayes' theorem [135] to calculate the probability for each parameter to have a certain
⁹⁶⁶ value given the observed data, $P(\vec{\theta}|D)$, which is known as the posterior distribution
⁹⁶⁷ (often termed the posterior). This can be expressed as

$$P(\vec{\theta}|D) = \frac{P(D|\vec{\theta})P(\vec{\theta})}{\int P(D|\vec{\theta})P(\vec{\theta})d\vec{\theta}}. \quad (4.2)$$

968 The denominator in Equation 4.2 is the integral of the joint probability distribution

969 over all values of all parameters used within the fit. For brevity, we say that the
 970 posterior distribution is

$$P(\vec{\theta}|D) \propto P(D|\vec{\theta})P(\vec{\theta}). \quad (4.3)$$

971 In subsection 4.3.1, we see that for the cases used within this analysis, it is reason-
 972 able to know the posterior to some normalisation constant.

973 4.2. Monte Carlo Simulation

974 Monte Carlo techniques are used to numerically solve a complex problem that does
 975 not necessarily have an analytical solution. These techniques rely on building a large
 976 ensemble of samples from an unknown distribution and then using the ensemble to
 977 approximate the properties of the distribution.

978 An example that uses Monte Carlo techniques is to calculate the area underneath
 979 a curve. For example, take the problem of calculating the area under a straight line
 980 with gradient $M = 0.4$ and intercept $C = 1.0$. Analytically, one can calculate the area
 981 under the line is equal to 30 units for $0 \leq x \leq 10$. Using Monte Carlo techniques,
 982 one can calculate the area under this line by throwing many random values for the x
 983 and y components of each sample and then calculating whether that point falls below

the line. The area can then be calculated by the ratio of points below the line to the total number of samples thrown multiplied by the total area in which samples were scattered. The study is shown in Figure 4.1 highlights this technique and finds the area under the curve to be 29.9 compared to an analytical solution of 30.0. The deviation of the numerical to analytical solution can be attributed to the number of samples used in the study. The accuracy of the approximation in which the properties of the Monte Carlo samples replicate those of the desired distribution is dependent on the number of samples used. Replicating this study with a differing number of Monte Carlo samples used in each study (As shown in Figure 4.2) highlights how the Monte Carlo techniques are only accurate within the limit of a high number of samples.

Whilst the above example has an analytical solution, these techniques are just as applicable to complex solutions. Clearly, any numerical solution is only as useful as its efficiency. As discussed, the accuracy of the Monte Carlo technique is dependent upon the number of samples generated to approximate the properties of the distribution. Furthermore, if the positions at which the samples are evaluated are not ‘cleverly’ picked, the efficiency of the Monte Carlo technique significantly drops. Given the example in Figure 4.1, if the region in which the samples are scattered significantly extends passed the region of interest, many calculations will be calculated but do not add to the ability of the Monte Carlo technique to achieve the correct result. For instance, any sample evaluated at a $y \geq 5$ could be removed without affecting the final result. This does bring in an aspect of the ‘chicken and egg’ problem in that to achieve efficient sampling, one needs to know the distribution beforehand.

4.2.1. Markov Chain Monte Carlo

This analysis utilises a multi-dimensional probability distribution, with some dimensions being significantly more constrained than others. This could be from prior

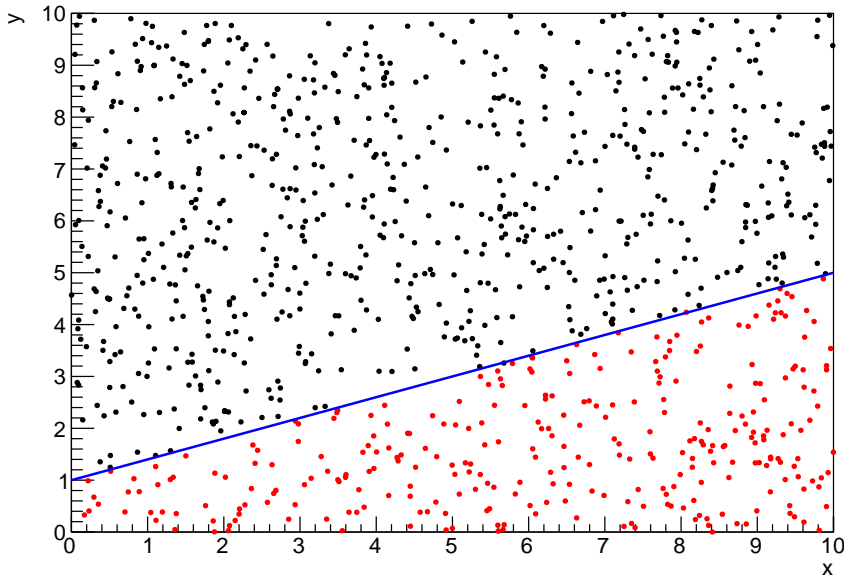


Figure 4.1.: Example of using Monte Carlo techniques to find the area under the blue line. The gradient and intercept of the line are 0.4 and 1.0 respectively. The area found to be under the curve using one thousand samples is 29.9 units.

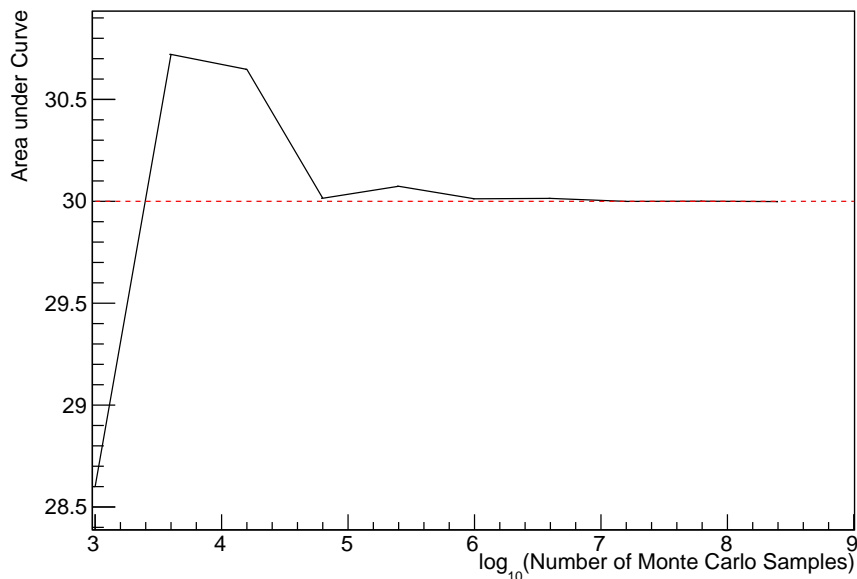


Figure 4.2.: The area under a line of gradient 0.4 and intercept 1.0 for the range $0 \leq x \leq 10$ as calculated using Monte Carlo techniques as a function of the number of samples used in each repetition. The analytical solution to the area is 30 units as given by the red line.

knowledge of parameter distributions from external data or un-physical regions in which parameters can not exist. Consequently, the Monte Carlo techniques used need to be as efficient as possible. For this analysis, the Markov Chain Monte Carlo (MCMC) technique is chosen. An MCMC technique is a Monte Carlo technique that uses a Markov chain to select which points at which to sample the parameter distribution. This technique performs a semi-random stochastic walk through the allowable parameter space. This builds a posterior distribution which has the property that the density of sampled points is proportional to the probability density of that parameter. This does mean that the samples produced by this technique are not statistically independent but they will cover the space of the distribution.

A Markov chain functions by selecting the position of step \vec{x}_{i+1} based on the position of \vec{x}_i . The space in which the Markov chain selects samples is dependent upon the total number of parameters utilised within the fit, where a discrete point in this space is described by the N-dimensional space \vec{x} . In a perfectly operating Markov chain, the position of the next step depends solely on the previous step and not on the further history of the chain (\vec{x}_0, \vec{x}_1 , etc.). However, in solving the multi-dimensionality of the fit used within this analysis, each step becomes correlated with several of the steps preceding itself. This behaviour is further explained in subsection 4.2.3. Providing the MCMC chain is well optimised, it will begin to converge towards a unique stationary distribution. The period between the chain's initial starting point and the convergence to the unique stationary distribution is colloquially known as the burn-in period. This is discussed further in subsection 4.2.3. Once the chain reaches the stationary distribution, all points sampled after that point will look like samples from that distribution.

1033 Further details of the theories underpinning MCMC techniques are discussed
1034 in [132] but can be summarised by the requirement that the chain satisfies the three
1035 ‘regularity conditions’:

- 1036 • Irreducibility: From every position in the parameter space \vec{x} , there must exist a
1037 non-zero probability for every other position in the parameter space to be reached.
- 1038 • Recurrence: Once the chain arrives at the stationary distribution, every step fol-
1039 lowing from that position must be samples from the same stationary distribution.
- 1040 • Aperiodicity: The chain must not repeat the same sequence of steps at any point
1041 throughout the sampling period.

1042 The output of the chain after burn-in (ie. the sampled points after the chain
1043 has reached the stationary distribution) can be used to approximate the posterior
1044 distribution and model parameters $\vec{\theta}$. To achieve the requirement that the unique
1045 stationary distribution found by the chain be the posterior distribution, one can use
1046 the Metropolis-Hastings algorithm. This guides the stochastic process depending on
1047 the likelihood of the current proposed step compared to that of the previous step.
1048 Implementation and other details of this technique are discussed in subsection 4.2.2.

1049 4.2.2. Metropolis-Hastings Algorithm

1050 As a requirement for MCMCs, the Markov chain implemented in this technique must
1051 have a unique stationary distribution that is equivalent to the posterior distribution.
1052 To ensure this requirement and that the regularity conditions are met, this analysis
1053 utilises the Metropolis-Hastings (MH) algorithm [136,137]. For the i^{th} step in the chain,
1054 the MH algorithm determines the position in the parameter space to which the chain
1055 moves to based on the current step, \vec{x}_i , and the proposed step, \vec{y}_{i+1} . The proposed step
1056 is randomly selected from some proposal function $f(\vec{x}_{i+1}|\vec{x}_i)$, which depends solely

on the current step (ie. not the further history of the chain). The next step in the chain \vec{x}_{i+1} can be either the current step or the proposed step determined by whether the proposed step is accepted or rejected. To decide if the proposed step is selected, the acceptance probability, $\alpha(\vec{x}_i, \vec{y}_i)$, is calculated as

$$\alpha(\vec{x}_i, \vec{y}_{i+1}) = \min \left(1, \frac{P(\vec{y}_{i+1}|D)f(\vec{x}_i|\vec{y}_{i+1})}{P(\vec{x}_i|D)f(\vec{y}_{i+1}|\vec{x}_i)} \right). \quad (4.4)$$

Where $P(\vec{y}_{i+1}|D)$ is the posterior distribution as introduced in section 4.1. To simplify this calculation, the proposal function is required to be symmetric such that $f(\vec{x}_i|\vec{y}_{i+1}) = f(\vec{y}_{i+1}|\vec{x}_i)$. In practice, a multi-variate Gaussian distribution is used to throw parameter proposals from. This reduces Equation 4.4 to

$$\alpha(\vec{x}_i, \vec{y}_{i+1}) = \min \left(1, \frac{P(\vec{y}_{i+1}|D)}{P(\vec{x}_i|D)} \right). \quad (4.5)$$

After calculating this quantity, a random number, β , is generated uniformly between 0 and 1. If $\beta \leq \alpha(\vec{x}_i, \vec{y}_{i+1})$, the proposed step is accepted. Otherwise, the chain sets the next step equal to the current step and this procedure is repeated. This can be interpreted as if the posterior probability of the proposed step is greater than that of the current step, ($P(\vec{y}_{i+1}|D) \geq P(\vec{x}_i|D)$), the proposed step will always be accepted. If the opposite is true, ($P(\vec{y}_{i+1}|D) \leq P(\vec{x}_i|D)$), the proposed step will be accepted with probability $P(\vec{x}_i|D)/P(\vec{y}_{i+1}|D)$. This ensures that the Markov chain does not get trapped in any local minima in the potentially non-Gaussian posterior distribution. The outcome of this technique is that the density of steps taken in a discrete region is directly proportional to the probability density in that region.

1075 4.2.3. MCMC Optimisation

1076 As discussed in subsection 4.2.2, the proposal function invoked within the MH algo-
1077 rithm can take any form and the chain will still converge to the stationary distribution.
1078 At each set of proposed parameter values, a prediction of the same spectra has to be
1079 generated which requires significant computational resources. Therefore, the number
1080 of steps taken before the unique stationary distribution is found should be minimised
1081 as only steps after convergence add information to the oscillation analysis. Further-
1082 more, the chain should entirely cover the allowable parameter space to ensure that all
1083 values have been considered. Tuning the distance that the proposal function jumps
1084 between steps on a parameter-by-parameter basis can both minimise the length of the
1085 burn-in period and ensure that the correlation between step \vec{x}_i and \vec{x}_j is sufficiently
1086 small.

1087 The effect of changing the width of the proposal function is highlighted in Figure 4.3.
1088 Three scenarios, each with the same underlying stationary distribution (A Gaussian of
1089 width 1.0 and mean 0.), are presented. The only difference between the three scenarios
1090 is the width of the proposal function, colloquially known as the ‘step size σ ’. Each
1091 scenario starts at an initial parameter value of 10.0 which would be considered an
1092 extreme variation. For the case where $\sigma = 0.1$, it is clear to see that the chain takes
1093 a long time to reach the expected region of the parameter. This indicates that this
1094 chain would have a large burn-in period and does not converge to the stationary
1095 distribution until step ~ 500 . Furthermore, whilst the chain does move towards the
1096 expected region, each step is significantly correlated with the previous. Considering
1097 the case where $\sigma = 5.0$, the chain approaches the expected parameter region almost
1098 instantly meaning that the burn-in period is not significant. However, there are clearly
1099 large regions of steps where the chain does not move. This is likely due to the chain
1100 proposing steps in the tails of the distribution which have a low probability of being

1101 accepted. Consequently, this chain would take a significant number of steps to fully
 1102 span the allowable parameter region. For the final scenario, where $\sigma = 0.5$, you can see
 1103 a relatively small burn-in period of approximately 100 steps. Once the chain reaches
 1104 the stationary distribution, it moves throughout the expected region of parameter
 1105 values many times, sufficiently sampling the full parameter region. This example is a
 1106 single parameter varying across a continuous distribution and does not fully reflect
 1107 the difficulties in the many-hundred multi-variate parameter distribution used within
 1108 this analysis. However, it does give a conceptual idea of the importance of selecting
 1109 the proposal function and associated step size.

1110 As discussed, step size tuning directly correlates to the average step acceptance
 1111 rate. If the step size is too small, many steps will be accepted but the chain moves
 1112 slowly. If the opposite is true, many steps will be rejected as the chain proposes steps
 1113 in the tails of the distribution. Discussion in [138] suggests that the ‘ideal’ acceptance
 1114 rate of a high dimension MCMC chain should be approximately $\sim 25\%$. An “ideal”
 1115 step size [138] of

$$\sigma = \frac{2.4}{N_p}, \quad (4.6)$$

1116 where N_p is the number of parameters included in the MCMC fit. However, the
 1117 complex correlations between systematics mean that some parameters have to be hand
 1118 tuned and many efforts have been taken to select a set of parameter-by-parameter step
 1119 sizes to approximately reach the ideal acceptance rate.

1120 Figure 4.3 highlights the likelihood as calculated by the fit in [DB: Link to AsimovA](#)
 1121 **Sensitivity Section** as a function of the number of steps in each chain. In practice,
 1122 many independent MCMC chains are run simultaneously to parallelise the task of

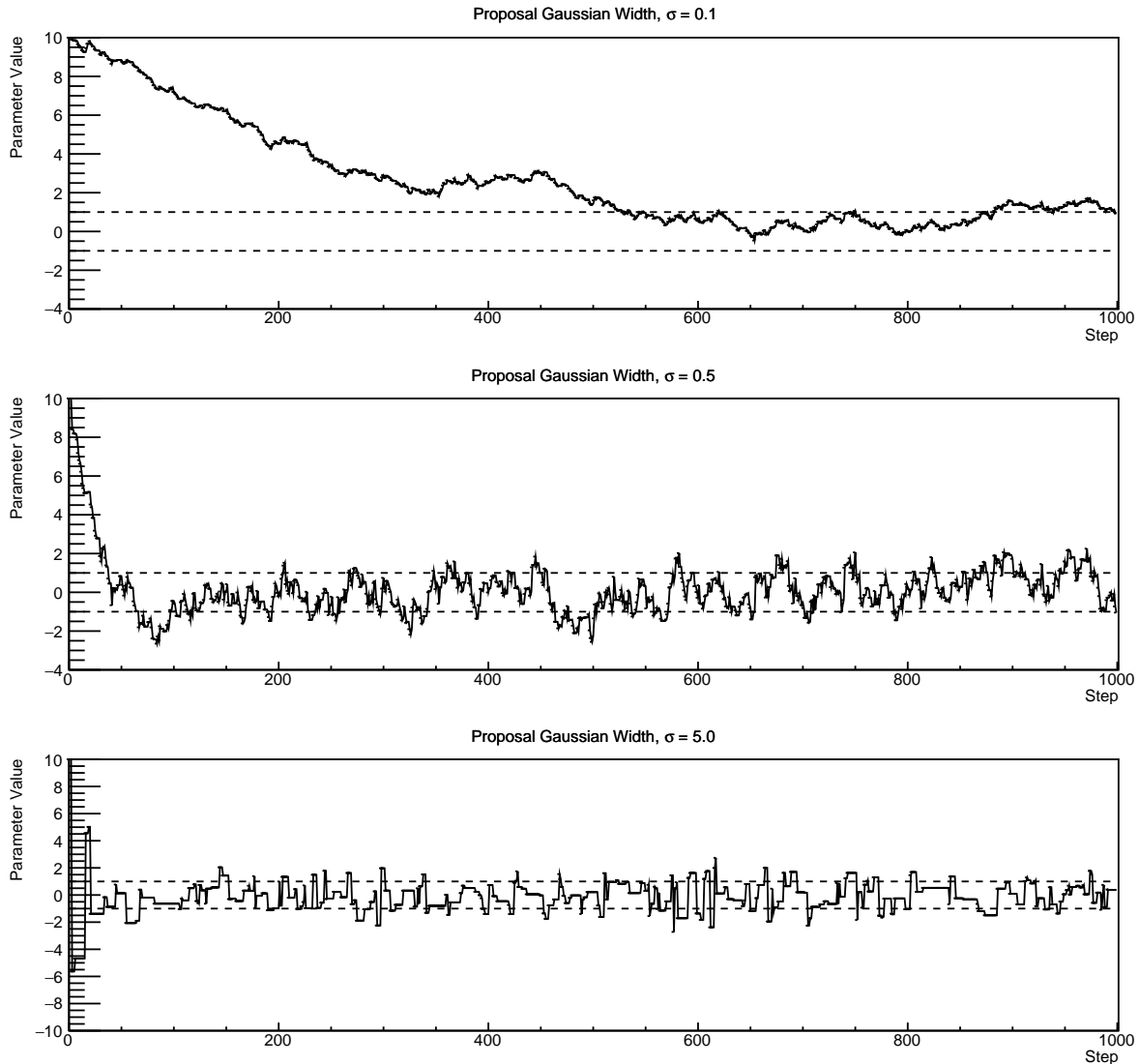


Figure 4.3.: Three MCMC chains, each with a stationary distribution equal to a Gaussian centered at 0 and width 1 (As indicated by the black dotted lines). All of the chains use a Gaussian proposal function but have different widths (or ‘step size σ ’). The top panel has $\sigma = 0.1$, middle panel has $\sigma = 0.5$ and the bottom panel has $\sigma = 5.0$.

1123 performing the fit. This figure overlays the distribution found in each chain. As seen,
 1124 the likelihood decreases from its initial value and converges towards a stationary
 1125 distribution after $\sim 1 \times 10^5$ steps.

1126 Multiple configurations of this analysis have been performed throughout this thesis
 1127 where different samples or systematics have been used. For all of these configurations,
 1128 it was found that a burnin period of 1×10^5 was sufficient in all cases.

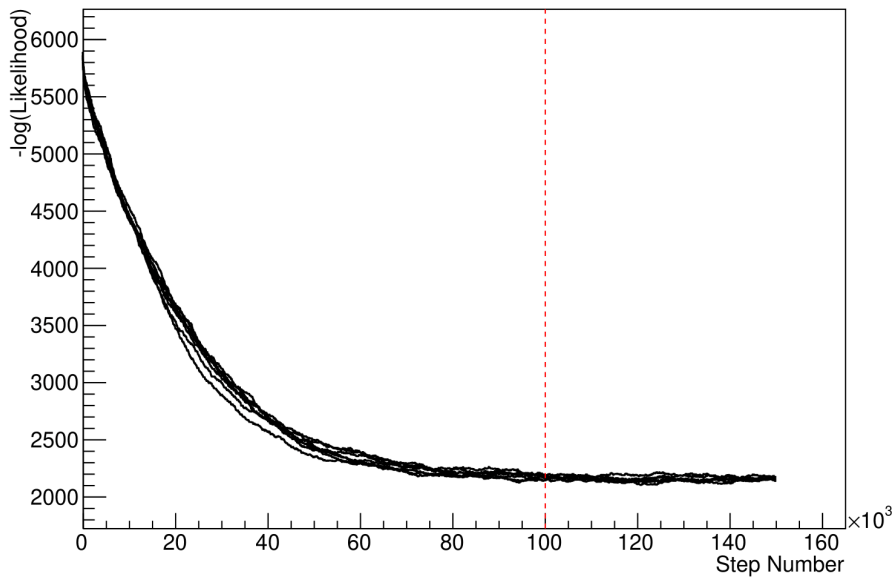


Figure 4.4.: The log-likelihood from the fit detailed in DB: Link to AsimovA Sensitivity Section as a function of the number of steps accumulated in each fit. Many independent MCMC chains were run in parallel and overlaid on this plot. The red line indicates the 1×10^5 step burn-in period after which the log-likelihood becomes stable.

¹¹²⁹ 4.3. Understanding the MCMC Results

¹¹³⁰ The previous sections have described how to generate the posterior probability distri-
¹¹³¹ bution using Bayesian MCMC techniques. However, this analysis focuses on oscillation
¹¹³² parameter determination. The posterior distribution output from the chain is a high
¹¹³³ dimension object, with as many dimensions as there are parameters included in the os-
¹¹³⁴ cillation analysis. However, this multi-dimensional object is difficult to conceptualize
¹¹³⁵ so parameter estimations are often presented in one or two-dimensional projections
¹¹³⁶ of this probability distribution. To do this, we invoke the marginalisation technique
¹¹³⁷ highlighted in subsection 4.3.1.

¹¹³⁸ 4.3.1. Marginalisation

¹¹³⁹ The output of the MCMC chain is a highly dimensional probability distribution
¹¹⁴⁰ which is very difficult to interpret. From the standpoint of an oscillation analysis
¹¹⁴¹ experiment, the one or two-dimensional ‘projections’ of the oscillation parameters of
¹¹⁴² interest are most relevant. Despite this, the best fit values and uncertainties on the
¹¹⁴³ oscillation parameters of interest should correctly encapsulate the correlations to the
¹¹⁴⁴ other systematic uncertainties (colloquially called ‘nuisance’ parameters). For this joint
¹¹⁴⁵ beam and atmospheric analysis, the oscillation parameters of interest are $\sin^2(\theta_{23})$,
¹¹⁴⁶ $\sin^2(\theta_{13})$, Δm_{23}^2 , and δ_{CP} . All other parameters (Including the oscillation parameter
¹¹⁴⁷ this fit is insensitive to) are deemed nuisance parameters. To generate these projections,
¹¹⁴⁸ we rely upon integrating the posterior distribution over all nuisance parameters. This
¹¹⁴⁹ is called marginalisation. A simple example of this technique is to imagine the scenario
¹¹⁵⁰ where two coins are flipped. To determine the probability that the first coin returned
¹¹⁵¹ a ‘head’, the exact result of the second coin flip is disregarded and simply integrated
¹¹⁵² over. For the parameters of interest, $\vec{\theta}_i$, we can calculate the marginalised posterior by
¹¹⁵³ integrating over the nuisance parameters, $\vec{\theta}_n$. In this case, Equation 4.2 becomes

$$P(\vec{\theta}_i|D) = \frac{\int P(D|\vec{\theta}_i, \vec{\theta}_n)P(\vec{\theta}_i, \vec{\theta}_n)d\vec{\theta}_n}{\int P(D|\vec{\theta})P(\vec{\theta})d\vec{\theta}} \quad (4.7)$$

¹¹⁵⁴ Where $P(\vec{\theta}_i, \vec{\theta}_n)$ encodes the prior knowledge about the uncertainty and correlations
¹¹⁵⁵ between the parameters of interest and the nuisance parameters. In practice, this
¹¹⁵⁶ is simply taking the one or two-dimensional projection of the multi-dimensional
¹¹⁵⁷ probability distribution.

Whilst in principle an easy solution to a complex problem, correlations between the interesting and nuisance parameters can bias the marginalised results. A similar effect is found when the parameters being marginalised over have non-Gaussian probability distributions. For example, Figure 4.5 highlights the marginalisation bias in the probability distribution found for a parameter when requiring a correlated parameter to have a positive parameter value. Due to the complex nature of this oscillation parameter fit presented in this thesis, there are correlations occurring between the oscillation parameters of interest and the other nuisance parameters included in the fit.

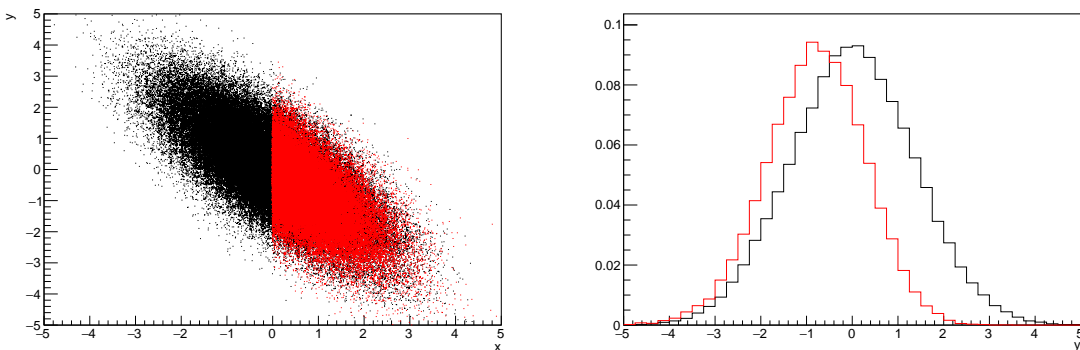


Figure 4.5.: Left: The two dimensional probability distribution for two correlated parameters x and y . The red distribution shows the two dimensional probability distribution when $0 \leq x \leq 5$. Right: The marginalised probability distribution for the y parameter found when requiring the x to be bound between $-5 \leq x \leq 5$ and $0 \leq x \leq 5$ for the black and red distribution, respectively.

4.3.2. Parameter Estimation and Credible Intervals

The purpose of this analysis is to determine the best fit values for the oscillation parameters that the beam and atmospheric samples are sensitive to: $\sin^2(\theta_{23})$, $\sin^2(\theta_{13})$, Δm_{23}^2 , and δ_{CP} . Typically, the results presented take the form of one or two-dimension marginalised probability distributions for the appearance ($\sin^2(\theta_{13})$ and δ_{CP}) and disappearance ($\sin^2(\theta_{23})$ and Δm_{23}^2) parameters. The posterior probability density

₁₁₇₃ taken from the output MCMC chain is binned in these parameters. The parameter
₁₁₇₄ best-fit point is then taken to be the value that has the highest posterior probability.
₁₁₇₅ This is performed in both one and two-dimensional projections.

₁₁₇₆ However, the single best-fit point in a given parameter is not of much use on its
₁₁₇₇ own. We would also like to determine the uncertainty, or credible interval, on that
₁₁₇₈ best-fit point. The definition of the 1σ credible interval is that we have 68% belief that
₁₁₇₉ the parameter is within those bounds. For a more generalised definition, the credible
₁₁₈₀ interval is the region, R , of the posterior distribution that contains a specific fraction of
₁₁₈₁ the total probability, such that

$$\int_R P(\theta|D)d\theta = \alpha \quad (4.8)$$

₁₁₈₂ Where θ is the parameter on which we calculate the credible interval. This technique
₁₁₈₃ then calculates the $\alpha \times 100\%$ credible interval.

₁₁₈₄ In practice, this analysis uses the highest posterior density (HPD) credible intervals
₁₁₈₅ which are calculated through the following method. First, the probability distribution
₁₁₈₆ is area-normalised such that it has an integrated area equal to 1.0. The bins of proba-
₁₁₈₇ bility are then summed from the highest to lowest until the sum exceeds the 1σ level
₁₁₈₈ (0.68 in this example). This process is repeated for a range of credible intervals, notably
₁₁₈₉ the 1σ , 2σ and 3σ along with other levels where the critical values for each level can
₁₁₉₀ be found in [139]. This process can be repeated for the two-dimensional probability
₁₁₉₁ distributions by creating two-dimensional contours of credible intervals rather than a
₁₁₉₂ one-dimensional result.

¹¹⁹³ 4.3.3. Bayesian Model Comparisons

¹¹⁹⁴ Due to the matter resonance, this analysis has some sensitivity to the mass hierarchy
¹¹⁹⁵ of neutrino states (whether Δm_{23}^2 is positive or negative) and the octant of $\sin^2(\theta_{23})$
¹¹⁹⁶ . The Bayesian approach utilised within this analysis gives an intuitive method of
¹¹⁹⁷ model comparison by determining which hypothesis is most favourable. Taking the
¹¹⁹⁸ ratio of Equation 4.3 for the two hypotheses of normal hierarchy, NH , and inverted
¹¹⁹⁹ hierarchy, IH , gives

$$\frac{P(\vec{\theta}_{NH}|D)}{P(\vec{\theta}_{IH}|D)} = \frac{P(D|\vec{\theta}_{NH})}{P(D|\vec{\theta}_{IH})} \times \frac{P(\vec{\theta}_{NH})}{P(\vec{\theta}_{IH})}. \quad (4.9)$$

¹²⁰⁰ The middle term defines the Bayes factor which is a data-driven interpretation of
¹²⁰¹ how strong the data prefers one hierarchy to the other. For this analysis, equal priors
¹²⁰² on both mass hierarchy hypotheses are chosen ($P(\vec{\theta}_{NH}) = P(\vec{\theta}_{IH}) = 0.5$). In practice,
¹²⁰³ the MCMC chain proposes a value of $|\Delta m_{23}^2|$ and then applies a 50% probability
¹²⁰⁴ that the value is sign flipped. Consequently, the Bayes factor can be calculated from
¹²⁰⁵ the ratio of the probability density in either hypothesis. This equates to counting the
¹²⁰⁶ number of steps taken in the normal and inverted hierarchies and taking the ratio. The
¹²⁰⁷ same approach can be taken to compare the upper octant (UO) compared to the lower
¹²⁰⁸ octant (LO) hypothesis of $\sin^2(\theta_{23})$.

¹²⁰⁹ Whilst the value of the Bayes factor should always be shown, the Jeffreys scale [140]
¹²¹⁰ (highlighted in Table 4.1) gives an indication of the strength of preference for one model
¹²¹¹ compared to the other. Other interpretations of the strength of preference of a model
¹²¹² exist, e.g. the Kass and Raferty Scale [141].

$\log_{10}(B_{AB})$	B_{AB}	Strength of Preference
< 0.0	< 1	No preference for hypothesis A (Supports hypothesis B)
0.0 – 0.5	1.0 – 3.16	Preference for hypothesis A is weak
0.5 – 1.0	3.16 – 10.0	Preference for hypothesis A is substantial
1.0 – 1.5	10.0 – 31.6	Preference for hypothesis A is strong
1.5 – 2.0	31.6 – 100.0	Preference for hypothesis A is very strong
> 2.0	> 100.0	Decisive preference for hypothesis A

Table 4.1.: Jeffreys scale for strength of preference for two models A and B as a function of the calculated Bayes factor ($B_{AB} = B(A/B)$) between the two models [140]. The original scale is given in terms of $\log_{10}(B(A/B))$ but converted to linear scale for easy comparison throughout this thesis.

¹²¹³ 4.3.4. Comparison of MCMC Output to Expectation

¹²¹⁴ To ensure the fit is performing well, a best-fit spectrum is produced using the pos-
¹²¹⁵ terior probability distribution and compared with the data, allowing easy by-eye
¹²¹⁶ comparisons to be made. A simple method of doing this is to perform a comparison
¹²¹⁷ in the fitting parameters (For instance, the reconstructed neutrino energy and lepton
¹²¹⁸ direction for T2K far detector beam samples) of the spectra generated by the MCMC
¹²¹⁹ chain to ‘data’. This ‘data’ could be true data or some variation of Monte Carlo predic-
¹²²⁰ tion. This allows easy comparison of the MCMC probability distribution to the data.
¹²²¹ To perform this, N steps from the post burn-in MCMC chain are randomly selected
¹²²² (Where for all plots of this style in this thesis, $N = 3000$). From these, the Monte Carlo
¹²²³ prediction at each step is generated by reweighting the model parameters to the values
¹²²⁴ specified at that step. Due to the probability density being directly correlated with
¹²²⁵ the density of steps in a certain region, parameter values close to the best fit value are
¹²²⁶ most likely to be selected.

¹²²⁷ In practice, for each bin of the fitting parameters has a probability distribution
¹²²⁸ of event rates, with one entry per sampled MCMC step. This distribution is binned
¹²²⁹ where the bin with the highest probability is selected as the mean and an error on

1230 the width of this probability distribution is calculated using the approach highlighted
1231 in subsection 4.3.2. Consequently, the best fit distribution in the fit parameter is not
1232 necessarily that which would be attained by reweighting the Monte Carlo prediction
1233 to the most probable parameter values.

1234 A similar study can be performed to illustrate the freedom of the model parameter
1235 space prior to the fit. This can be done by throwing parameter values from the prior
1236 uncertainty of each parameter. This becomes troublesome for parameters with no
1237 prior uncertainty as the range is technically infinite. Where applicable solutions to
1238 remove these have been addressed.

1239 **Chapter 5**

1240 **Simulation, Reconstruction, and Event
Reduction**

1242 As a crucial part of the oscillation analysis, an accurate prediction of the expected
1243 neutrino spectrum at the far detector is required. This includes modeling the flux
1244 generation, neutrino interactions, and detector effects. All of the simulation packages
1245 required to do this are briefly described in section 5.1. The reconstruction of neutrino
1246 events inside the far detector, including the `fitQun` algorithm, is documented in
1247 section 5.2. This also includes data quality checks of the SK-V data which the author
1248 performed for the T2K oscillation analysis presented at Neutrino 2020 [80]. Finally,
1249 section 5.3 describes the steps taken in the SK detector to trigger on events of interest
1250 whilst removing the comparatively large rate of cosmic ray muon events.

1251 **5.1. Simulation**

1252 In order to generate a Monte Carlo prediction of the expected event rate at the far
1253 detector, all the processes in the beam and atmospheric flux, neutrino interaction, and
1254 detector need to be modeled. Each of these parts is individually modeled and each of
1255 them is detailed below.

1256 The beamline simulation consists of three distinct parts: the initial hadron inter-
1257 action modeled by FLUKA [142], the target station geometry and particle tracking

performed by JNUBEAM, [143, 144] and any hadronic re-interactions simulated by GCALOR [145]. The primary hadronic interactions are $O(10)\text{GeV}$, where FLUKA matches external cross-section data better than GCALOR [146]. However, FLUKA is not very adaptable so a small simulation is built to model the interactions in the target and the output is then passed to JNUBEAM and GCALOR for propagation. The hadronic interactions are tuned to data from the NA61/SHINE [147–149] and HARP [150] experiments. The tuning is done by reweighting the FLUKA and GCALOR predictions to match the external data multiplicity and cross-section measurements, based on final state particle kinematics [146]. The culmination of this simulation package generates the predicted flux for neutrino and antineutrino beam modes which are illustrated in Figure 3.7.

The atmospheric neutrino flux is simulated by the HKKM model [43, 45]. The primary cosmic ray flux is tuned to AMS [151] and BESS [152] data assuming the US-standard atmosphere '76 [153] density profile and includes geomagnetic field effects. The primary cosmic rays interact to generate pions and muons. The interaction of these secondary particles to generate neutrinos is handled by DPMJET-III [154] for energies above 32GeV and JAM [45, 155] for energies below that value **DB: Question for Giles: Why different generators for above/below 32GeV?** These hadronic interactions are tuned to BESS and L3 data [156, 157] using the same methodology as the tuning of the beamline simulation. The energy and cosine zenith predictions of $\nu_e, \bar{\nu}_e, \nu_\mu, \bar{\nu}_\mu$ flux are given in Figure 2.3 and Figure 2.5, respectively. The flux is approximately symmetrical and peaked around the horizon ($\cos(\theta_Z) = 0.0$). This is because horizontally-going pions and kaons can travel further than their vertically-going counterparts resulting in a larger probability of decaying to neutrinos. The symmetry is broken in lower-energy neutrinos due to geomagnetic effects, which modify the track of the primary cosmic rays. Updates to the HKKM model are currently ongoing [158].

Once a flux prediction has been made for all three detectors, NEUT 5.4.0 [159, 160] models the interactions of the neutrinos in the detectors. For the purposes of this analysis, quasi-elastic (QE), meson exchange (MEC), single meson production (PROD), coherent pion production (COH), and deep inelastic scattering (DIS) interactions are simulated. These interaction categories can be further broken down by whether they were propagated via a W^\pm boson in Charged Current (CC) interactions or via a Z^0 boson in Neutral Current (NC) interactions. CC interactions have a charged lepton in the final state, which can be flavour-tagged in reconstruction to determine the flavour of the neutrino. In contrast, NC interactions have a neutrino in the final state so no flavour information can be determined from the observables left in the detector after an interaction. This is the reason why neutrinos which interact through NC modes are assumed to not oscillate within this analysis. Both CC and NC interactions are modeled for all the above interaction categories, other than MEC interactions which are only modeled for CC events.

As illustrated in Figure 5.1, CCQE interactions dominate the cross-section of neutrino interactions around $E_\nu \sim 0.5\text{GeV}$. The NEUT implementation adopts the Llewellyn Smith [161] model for neutrino-nucleus interactions, where the nuclear ground state of any bound nucleons (neutrino-oxygen interactions) is approximated by a spectral-function [162] model that simulates the effects of Fermi momentum and Pauli blocking. The cross-section of QE interactions is controlled by vector and axial-vector form factors parameterised by the BBBA05 [163] model and a dipole form factor with $M_A^{QE} = 1.21\text{GeV}$ fit to external data [164], respectively. NEUT implements the Valencia [165] model to simulate MEC events, where two nucleons and two holes in the nuclear target are produced (Often called 2p2h interactions).

For neutrinos of energy $O(1)\text{GeV}$, PROD interactions become dominant. These predominantly produce charged and neutral pions although γ , kaon, and η production

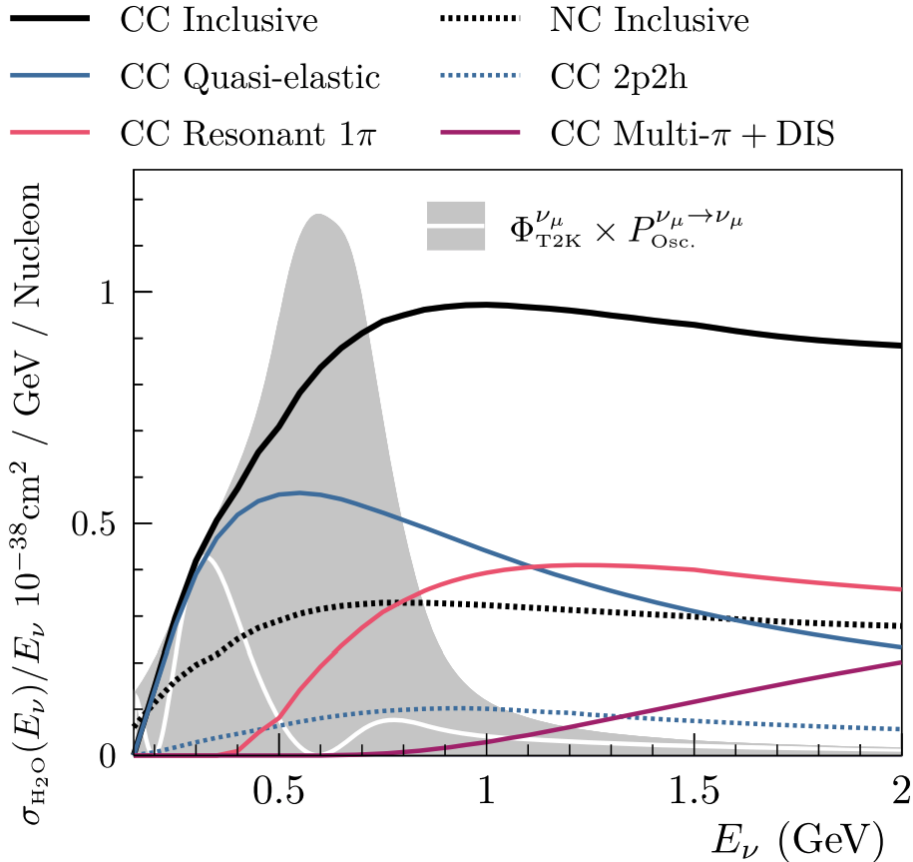


Figure 5.1.: The NEUT prediction of the ν_μ -H₂O cross-section overlaid on the T2K ν_μ flux. The charged current (black, solid) and neutral current (black, dashed) inclusive, charged current quasi-elastic (blue, solid), charged current 2p2h (blue, dashed), charged current single pion production (pink), and charged current multi- π and DIS (Purple) cross-sections are illustrated. Figure taken from [159].

is also considered. To simulate these interactions, the Berger-Sehgal [166] model is implemented within NEUT. It simulates the excitation of a nucleon from a neutrino interaction, production of an intermediate baryon, and the subsequent decay to a single meson or γ . Pions can also be produced through COH interactions, which occur when the incoming neutrino interacts with the entire oxygen nucleus leaving a single pion outside of the nucleus. NEUT utilises the Berger-Sehgal [167] model to simulate these COH interactions.

DIS and multi- π producing interactions become the most dominant for energies $> O(5)$ GeV. PYTHIA [168] is used to simulate any interaction with invariant mass

1319 $W > 2\text{GeV}/c^2$, which produces at least one meson. For any interaction which produces
1320 at least two mesons but has $W < 2\text{GeV}/c^2$, the Bronner model is used [169]. Both
1321 of these models use parton distribution functions based on the Bodek-Yang model
1322 [170–172].

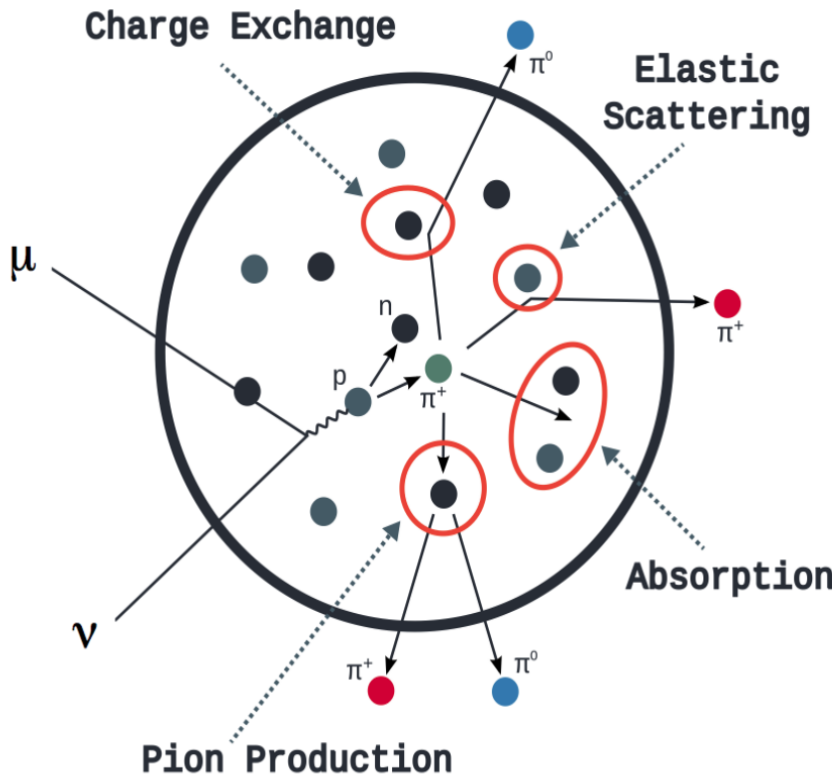


Figure 5.2.: Illustration of the various processes which a pion can undergo before exiting the nucleus. Taken from [173].

1323 Any pion which is produced within the nucleus can re-interact through final state
1324 interactions before it exits, as illustrated by the scattering, absorption, production, and
1325 exchange interactions in Figure 5.2. These re-interactions alter the observable particles
1326 within the detector. For instance, if the charged pion from a CC PROD interaction is
1327 absorbed, the observables would mimic a CC QE interaction. To simulate these effects,
1328 NEUT uses a semi-classical intranuclear cascade model [159]. This cascade functions by
1329 stepping the pion through the nucleus in fixed-length steps equivalent to $dx = R_N/100$,

1330 where R_N is the radius of the nucleus. At each step, the simulation allows the pion
1331 to interact through scattering, charged exchange, absorption, or production with an
1332 interaction-dependent probability calculated from a fit to external data [174]. This
1333 cascade continues until the pion is absorbed or exits the nucleus.

1334 Once the final state particle kinematics have been determined by NEUT, they are
1335 passed into the detector simulation. The near detectors, ND280 and INGRID, are
1336 simulated using a GEANT4 package [118,175] to simulate the detector geometry, particle
1337 tracking, and energy deposition. The response of the detectors is simulated using
1338 the elecSim package [118]. The far detector simulation is based upon the original
1339 Kamiokande experiment software which uses the GEANT3-based SKDETSIM [118,176]
1340 package. This simulates the interactions of particles in the water as well as Cherenkov
1341 light production. The water quality and PMT calibration measurements detailed in
1342 subsection 3.1.2 are also used within this simulation to make accurate predictions of
1343 the detector response.

1344 5.2. Event Reconstruction at SK

1345 Any event which generates optical photons that occurs in SK will be observed by the
1346 PMT array, where each PMT records the time and accumulated charge. This recorded
1347 information is shown in event displays similar to those illustrated in Figure 5.3. To
1348 be useful for physics analyses, this series of PMT hit information needs to be recon-
1349 structed to determine the particle's identity and kinematics (or track parameters):
1350 four-vertex, direction, and momenta. The reconstruction uses the fact that the charge
1351 and timing distribution of photons generated by a particular particle in an event is
1352 dependent upon its initial kinematics. Electron and muon rings are distinguished by
1353 their "fuzziness". Muons are heavier and less affected by scattering or showering

1354 meaning they typically produce “crisp” rings. Electrons are more likely to interact
1355 via electromagnetic showering or scattering which results in larger variations of their
1356 direction from the initial direction. Consequently, electrons typically produce “fuzzier”
1357 rings compared to muons.

1358 For the purposes of this analysis, the `fitQun` reconstruction algorithm is utilised.
1359 Its core function is to compare a prediction of the accumulated charged and timing
1360 distribution from each PMT, generated for a particular particle identity and track
1361 parameters, to that observed in the neutrino event. It determines the preferred values
1362 by minimising a likelihood function which includes information from PMTs which
1363 were hit and those that were not hit. `fitQun` performs a simultaneous fit of particle
1364 kinematics and identity, improving both the accuracy of the fit parameters and the
1365 rejection of neutral current π^0 events [177, 178]. The `fitQun` algorithm is based on
1366 the key concepts of the MiniBooNE reconstruction algorithm [179] and is described
1367 in [180] which is summarised below. The `fitQun` algorithm improves upon the APFit
1368 reconstruction algorithm which has been used for many previous SK analyses. APFit
1369 fits the vertex from timing information and then fits the momentum and direction
1370 of the particle from PMT hits within a 43 deg Cherenkov cone (which assumes an
1371 ultra-relativistic particle). It then fits the particle identity once the track parameters
1372 have been fit.

1373 The `fitQun` reconstruction algorithm proceeds by:

- 1374 • **Vertex pre-fitting:** An estimate of the vertex is made using a goodness-of-fit
1375 metric
- 1376 • **Peak finding:** The initial time of the event is determined by clustering events by
1377 time residuals

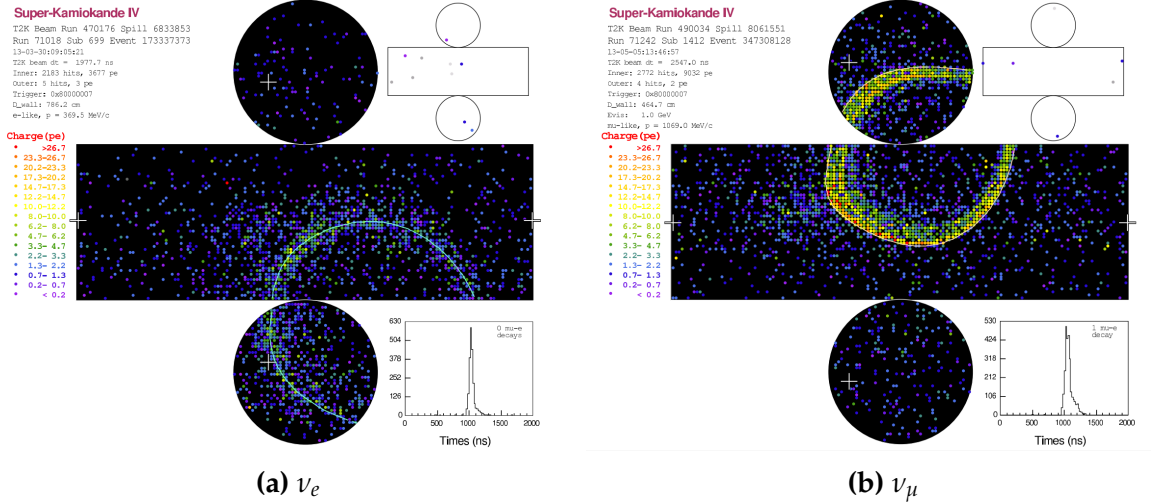


Figure 5.3.: Event displays from Super Kamiokande illustrating the “crisp” ring from a muon and the typically “fuzzy” electron ring. Each pixel represents a PMT and the color scheme denotes the accumulated charge deposited on that PMT. Figures taken from [181].

- **Single-ring fits:** Given the pre-fit vertex and estimated time of interaction, a maximum likelihood technique searches for a single particle generating light
 - **Multi-ring fits:** Seeded from the single-ring fits, hypotheses with multiple light-producing particles are considered using the same maximum likelihood technique
- An event in SK can consist of a primary and decay particles. For example, a charged current muon neutrino interaction can generate two particles that have the potential of generating Cherenkov photons: the primary muon, and the secondary decay-electron from the muon. To ensure the particles are reconstructed separately, each event is divided into time clusters which are called “subevents”. Subevents after the primary subevent are considered to be decay electrons. To find all the subevents in an event, a vertex goodness metric is calculated for some vertex position \vec{x} and time t ,

$$G(\vec{x}, t) = \sum_i^{\text{hit PMTs}} \exp \left(-\frac{1}{2} \left(\frac{T_{\text{Res}}^i(\vec{x}, t)}{\sigma} \right)^2 \right) \quad (5.1)$$

1389 where

$$T_{Res}^i(\vec{x}, t) = t^i - t - |R_{PMT}^i - \vec{x}| / c_n \quad (5.2)$$

1390 is the residual hit time. It is the difference in time between the PMT hit time, t^i ,
1391 of the i^{th} PMT and the expected time of the PMT hit if the photon was emitted at
1392 the start of the vertex. R_{PMT}^i is the position of the i^{th} PMT, c_n is the speed of light in
1393 water and $\sigma = 4\text{ns}$ which is comparable to the time resolution of the PMT. When the
1394 proposed fit values of time and vertex are close to the true values, $T_{Res}^i(\vec{x}, t)$ tends to
1395 zero resulting in subevents appearing as spikes in the goodness metric. The proposed
1396 fit vertex and time are grid-scanned, and the values which maximise the goodness
1397 metric are selected as the “pre-fit vertex”. Whilst this predicts a vertex for use in
1398 the clustering algorithm, the final vertex is fit using the higher-precision maximum
1399 likelihood method described below.

1400 Once the pre-fit vertex has been determined, the goodness metric is scanned as
1401 a function of t to determine the number of subevents. A peak-finding algorithm is
1402 then used on the goodness metric, requiring the goodness metric to exceed some
1403 threshold and drop below a reduced threshold before any subsequent additional
1404 peaks are considered. The thresholds are set such that the rate of false peak finding
1405 is minimised while still attaining good data to Monte Carlo agreement. To improve
1406 performance, the pre-fit vertex for each delayed subevent is re-calculated after PMT
1407 hits from the previous subevent are masked. This improves the decay-electron tagging
1408 performance. Once all subevents have been determined, the time window around
1409 each subevent is then defined by the earliest and latest time which satisfies $-180 <$

₁₄₁₀ $T_{Res}^i < 800\text{ns}$. The subevents and associated time windows are then used as seeds for
₁₄₁₁ further reconstruction.

₁₄₁₂ For a given subevent, the `fitQun` algorithm constructs a likelihood based on the
₁₄₁₃ accumulated charge q_i and time information t_i from the i^{th} PMT,

$$L(\Gamma, \vec{\theta}) = \prod_j^{\text{unhit}} P_j(\text{unhit}|\Gamma, \vec{\theta}) \prod_i^{\text{hit}} \{1 - P_i(\text{unhit}|\Gamma, \vec{\theta})\} f_q(q_i|\Gamma, \vec{\theta}) f_t(t_i|\Gamma, \vec{\theta}), \quad (5.3)$$

₁₄₁₄ where $\vec{\theta}$ defines the track parameters; vertex position, direction vector and mo-
₁₄₁₅ ments, and Γ represents the particle hypothesis. $P_i(\text{unhit}|\Gamma, \vec{\theta})$ is the probability of the
₁₄₁₆ i^{th} tube to not register a hit given the track parameters and particle hypothesis. The
₁₄₁₇ charge likelihood, $f_q(q_i|\Gamma, \vec{\theta})$, and time likelihood, $f_t(t_i|\Gamma, \vec{\theta})$, represents the probability
₁₄₁₈ density function of observing charge q_i and time t_i on the i^{th} PMT given the specified
₁₄₁₉ track parameters and particle hypothesis.

₁₄₂₀ The predicted charge is calculated based on contributions from both the direct
₁₄₂₁ light and the scattered light. The direct light contribution is determined based on the
₁₄₂₂ integration of the Cherenkov photon profile along the track. PMT angular acceptance,
₁₄₂₃ water quality, and calibration measurements discussed in subsection 3.1.2 are included
₁₄₂₄ to accurately predict the charge probability density at each PMT. The scattered light
₁₄₂₅ is calculated in a similar way, although it includes a scattering function that depends
₁₄₂₆ on the vertex of the particle and the position of the PMT. The charge likelihood is
₁₄₂₇ calculated by comparing the prediction to the observed charge in the PMT.

₁₄₂₈ The time likelihood is approximated to depend on the vertex \vec{x} , direction \vec{d} , and
₁₄₂₉ time t of the track as well as the particle hypothesis. The expected time for PMT hits is

¹⁴³⁰ calculated by assuming unscattered photons being emitted from the midpoint of the
¹⁴³¹ track, S_{mid} ,

$$t_{exp}^i = t + S_{mid}/c + |R_{PMT}^i - \vec{x} - S_{mid}\vec{d}|/c_n, \quad (5.4)$$

¹⁴³² where c is the speed of light in a vacuum. The time likelihood is then expressed in
¹⁴³³ terms of the residual difference between the PMT hit time and the expected hit time,
¹⁴³⁴ $t_{Res}^i = t^i - t_{exp}^i$. The particle hypothesis and momentum also affect the Cherenkov
¹⁴³⁵ photon distribution. These parameters modify the shape of the time likelihood density
¹⁴³⁶ since in reality not all photons are emitted at the midpoint of the track. As with the
¹⁴³⁷ charge likelihood, the contributions from both the direct and scattered light to the time
¹⁴³⁸ likelihood density are calculated separately, which are both calculated from particle
¹⁴³⁹ gun studies.

¹⁴⁴⁰ The track parameters and particle identity which maximise $L(\Gamma, \vec{\theta})$ are defined as
¹⁴⁴¹ the best-fit parameters. In practice MINUIT [182] is used to minimise the value of
¹⁴⁴² $-\ln L(\Gamma, \vec{\theta})$. The `fitQun` algorithm considers an electron-like, muon-like, and charged
¹⁴⁴³ pion-like hypothesis for events with a single final state particle, denoted “single-ring
¹⁴⁴⁴ events”. The particle’s identity is determined by taking the ratio of the likelihood
¹⁴⁴⁵ of each of the hypotheses. For instance, electrons and muons are distinguished by
¹⁴⁴⁶ considering the value of $\ln(L(e, \vec{\theta}_e)/L(\mu, \vec{\theta}_\mu))$ in comparison to the reconstructed
¹⁴⁴⁷ momentum of the electron hypothesis, as illustrated by Figure 5.4. The coefficients of
¹⁴⁴⁸ the discriminator between electron-like and muon-like events are determined from
¹⁴⁴⁹ Monte Carlo studies [180]. Similar distributions exist for distinguishing electron-like
¹⁴⁵⁰ events from π^0 -like events, and muon-like events from pion-like events. The cuts are
¹⁴⁵¹ defined as,

$$\text{Electron/Muon} : \ln(L_e/L_\mu) > 0.2 \times p_e^{rec} [\text{MeV}],$$

$$\text{Electron}/\pi^0 : \ln(L_e/L_{\pi^0}) < 175 - 0.875 \times m_{\gamma\gamma} [\text{MeV}], \quad (5.5)$$

$$\text{Muon/Pion} : \ln(L_\mu/L_{\pi^\pm}) < 0.15 \times p_\mu^{rec} [\text{MeV}],$$

as taken from [183], where p_e^{rec} and p_μ^{rec} are the reconstructed momentum of the single-ring electron and muon fits, respectively. $m_{\gamma\gamma}$ represents the reconstructed invariant mass of the two photons emitted from π^0 decay. Typically, the distance between a particular entry in these two-dimensional distributions and the cut-line is termed the PID parameter and is illustrated in Figure 5.5.

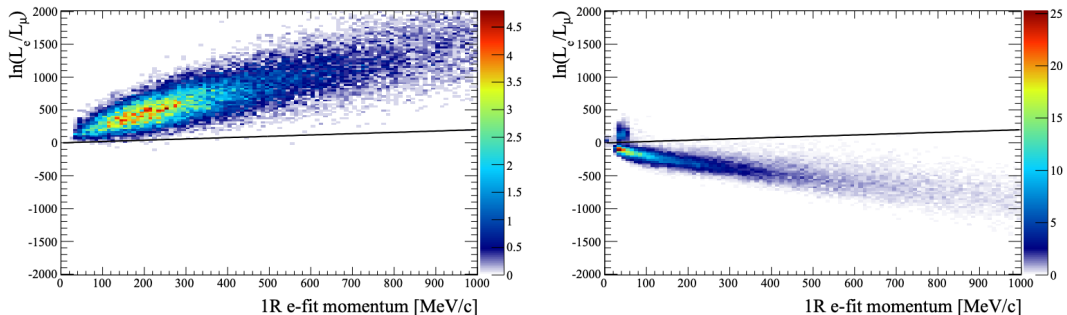


Figure 5.4.: The difference of the electron-like and muon-like log-likelihood compared to the reconstructed single-ring fit momentum for atmospheric ν_e (left) and ν_μ (right) samples. The black line represents the cut used to discriminate electron-like and muon-like events, which coefficients obtained from Monte Carlo studies. Figures taken from [180].

The `fitQun` algorithm also considers a π^0 hypothesis. To do this, it performs a fit looking for two standard electron-hypothesis tracks which point to the same four-vertex. This assumes the electron tracks are generated from photon-conversion so the electron tracks actually appear offset from the proposed π^0 vertex. For these fits, the conversion length, direction, and momentum of each photon are also considered as track parameters which are then fit in the same methodology as the standard single-ring hypotheses.

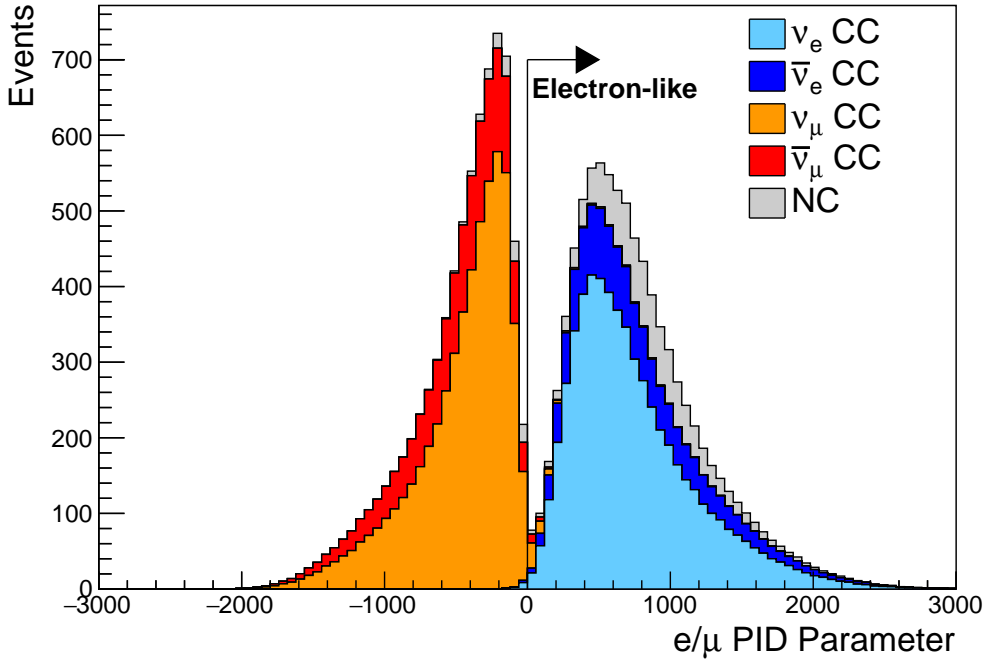


Figure 5.5.: The electron/muon PID separation parameter for all sub-GeV single-ring events in SK-IV. The charged current (CC) component is broken down in four flavours of neutrino (ν_μ , $\bar{\nu}_\mu$, ν_e and $\bar{\nu}_e$). Events with positive values of the parameter are determined to be electron-like.

Whilst lower energy events are predominantly single-ring events, higher energy neutrino events can generate final states with multiple particles which generate Cherenkov photons. These “multi-ring” hypotheses are also considered in the `fitQun` algorithm. When calculating the charge likelihood density, the predicted charge associated with each ring is calculated separately and then summed to calculate the total accumulated charge on each PMT. Similarly, the time likelihood for the multi-ring hypothesis is calculated assuming each ring is independent. Each track is time-ordered based on the time of flight from the center of the track to the PMT and the direct light from any ring incident on the PMT is assumed to arrive before any scattered light. To reduce computational resource usage, the multi-ring fits only consider electron-like and charged pion-like rings as the pion fit can be used as a proxy for a muon fit due to their similar mass.

1476 Multi-ring fits proceed by proposing another ring to the previous fit and then
1477 fitting the parameters in the method described above. Typically, multi-ring fits have
1478 the largest likelihood because of the additional degrees of freedom introduced. A
1479 likelihood value is calculated for the n -ring and $(n + 1)$ -ring hypotheses, where the
1480 additional ring is only included if the likelihood value is above 9.35, based on Monte
1481 Carlo studies in [184].

1482 5.2.1. Validation of Reconstruction in SK-V

1483 As an example of how the reconstruction depends on the detector conditions, the
1484 author of this thesis assessed the quality of event reconstruction for SK-V data. The
1485 detector systematics used in the T2K-only oscillation analysis are determined using
1486 data-to-Monte Carlo comparisons of the SK-IV data [185]. Due to tank-open mainte-
1487 nance occurring between SK-IV and SK-V, the dark rate of each PMT was observed to
1488 increase in SK-V due to light exposure for a significant time during the repairs. This
1489 increase can be seen in Figure 5.6. Run-10 of the T2K experiment was conducted in
1490 the SK-V period, so the consistency of SK-IV and SK-V data needs to be studied to
1491 determine whether the SK-IV-defined systematics can be applied to the run-10 data.
1492 This comparison study was performed using the stopping muon data set for both the
1493 SK-IV and SK-V periods. This data sample is used due to the high rate of interactions
1494 ($O(200)$ events per hour) as well as having similar energies to muons from CCQE
1495 ν_μ interactions from beam interactions. The rate of cosmic muons does depend on
1496 the solar activity cycle [186] but has been neglected in this comparison study. This
1497 is because the shape of the distributions is most important for the purposes of being
1498 compared to the detector systematics. The SK-IV and SK-V data samples consist of
1499 2398.42 and 626.719 hours of data which equates to 686k and 192k events respectively.

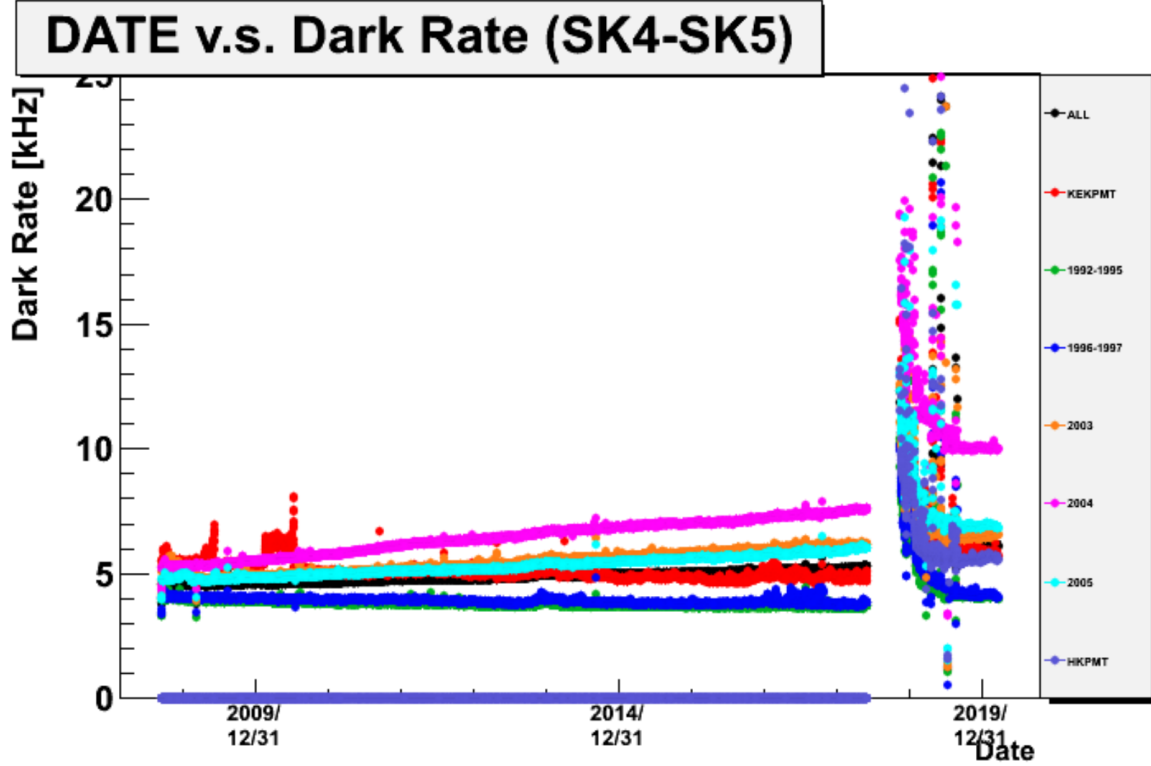


Figure 5.6.: The variation of the measured dark rate as a function of date, broken down by PMT type. The SK-IV and SK-V periods span September 2008 to May 2018 and January 2019 to July 2020, respectively. The break in measurement in 2018 corresponds to the period of tank repair and refurbishment. Figure adapted from [185].

The predicted charge calculated in the `fitQun` algorithm includes a contribution from the photoelectron emission due to dark noise. Therefore, the increase in the SK-V dark rate needs to be accounted for. In practice, the average dark rate in each SK period is calculated and used as an input in the reconstruction. This is calculated by averaging the dark rate per run for each period separately, using the calibration measurements detailed in subsection 3.1.2. The average dark rate from SK-IV and SK-V were found to be 4.57kHz and 6.30kHz, respectively. The charges associated with the muon and decay electron subevents are illustrated in Figure 5.7. The photoelectron emission from dark noise is more significant for events that have lower energy. This is because this contribution becomes more comparable to the number of photoelectrons emitted from incident photons in lower-energy events. This behaviour is observed

in the data, where the charge deposited by the muon subevent is mostly unaffected by the increase in dark rate, whilst the charge associated with the decay-electron is clearly affected.

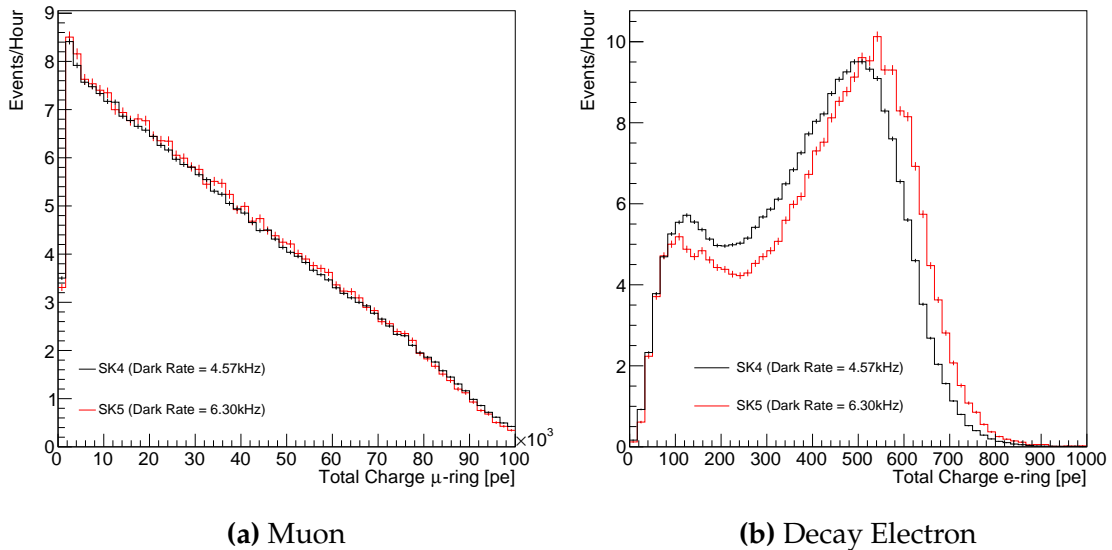


Figure 5.7.: Comparison of the measured raw charge deposited per event from the stopping muon data samples between SK-IV (Blue) and SK-V (Red), split by the primary muon subevent and the associated decay electron subevent.

The energy scale systematic is estimated from data-to-Monte Carlo differences in the stopping muon sample in [187] and found to be 2.1%. To determine the consistency of SK-IV and SK-V with respect to the energy scale systematic, the muon momentum distribution is compared between the two SK periods. As the total number of Cherenkov photons is integrated across the track length, the reconstructed momentum divided by track length (or range) is compared between SK-IV and SK-V as illustrated in Figure 5.8.

The consistency between these distributions has been computed in two ways. Firstly, a Gaussian is fit to the peak of each distribution separately, whose mean is found to be $(2.272 \pm 0.003)\text{MeV/cm}$ and $(2.267 \pm 0.006)\text{MeV/cm}$ for SK-IV and SK-V respectively. The ratio of these is equal to 1.002 ± 0.003 . The means of the

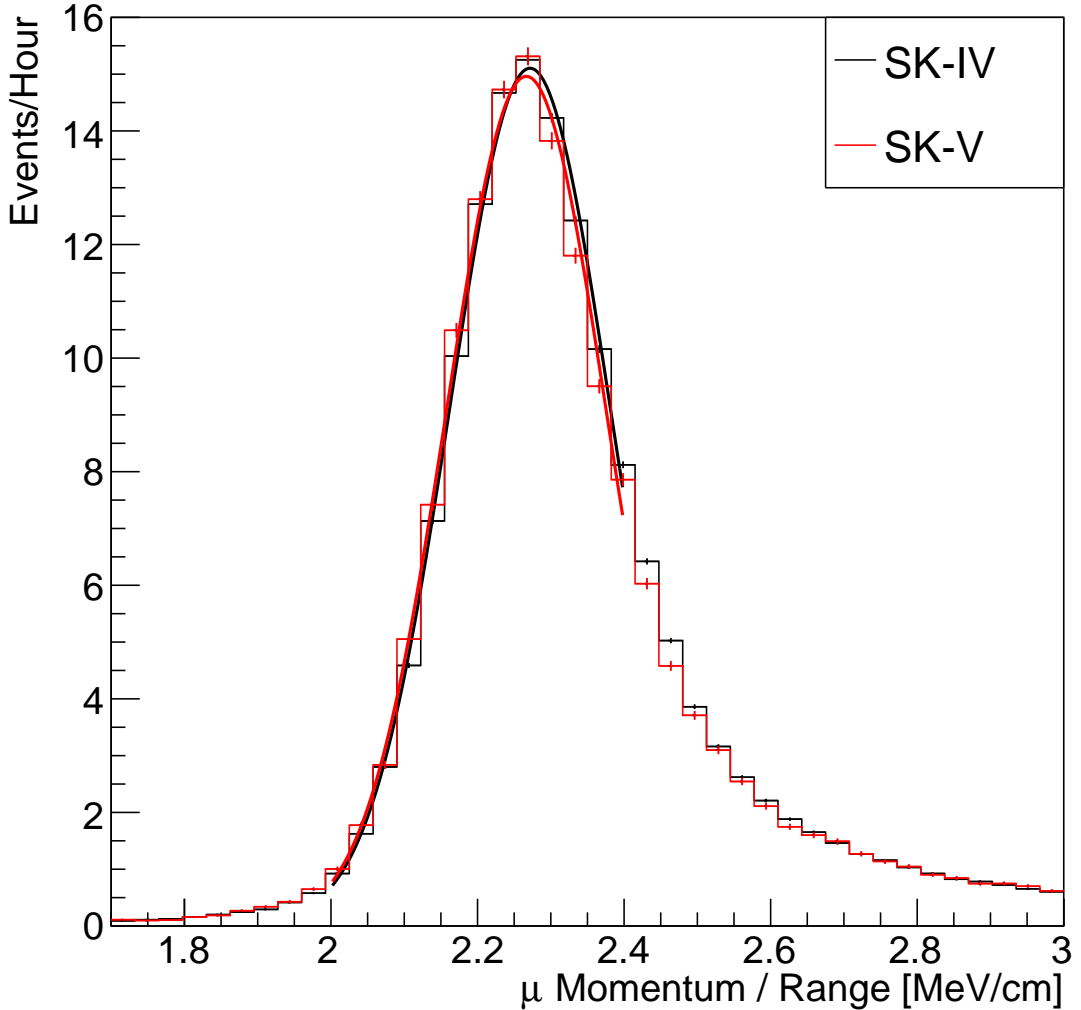


Figure 5.8.: The distribution of the reconstructed momentum from the muon ring divided by the distance between the reconstructed muon and decay electron vertices as found in the stopping muon data sets of SK-IV (Black) and SK-IV (Red). Only events with one tagged decay electron are considered. A Gaussian fit is considered in the range [2.0, 2.4] MeV/cm and illustrated as the solid curve.

1525 Gaussian fits are consistent with the expected stopping power of a minimum ionising
 1526 muon for a target material (water) with $Z/A \sim 0.5$ [188]. The second consistency
 1527 check is performed by introducing a nuisance parameter, α , which modifies the SK-
 1528 V distribution. The value of α which minimises the χ^2 value between the SK-IV
 1529 and SK-V is determined by scanning across a range of values. This is repeated by
 1530 applying the nuisance parameter as both a multiplicative factor and an additive

1531 shift. The χ^2 distributions for different values of α is illustrated in Figure 5.9. The
1532 values which minimise the χ^2 are found to be 0.0052 and 1.0024 for the additive and
1533 multiplicative implementations, respectively. No evidence of shifts larger than the
1534 2.1% uncertainty on the energy scale systematic has been found in the reconstructed
1535 momentum distribution of SK-IV and SK-V.

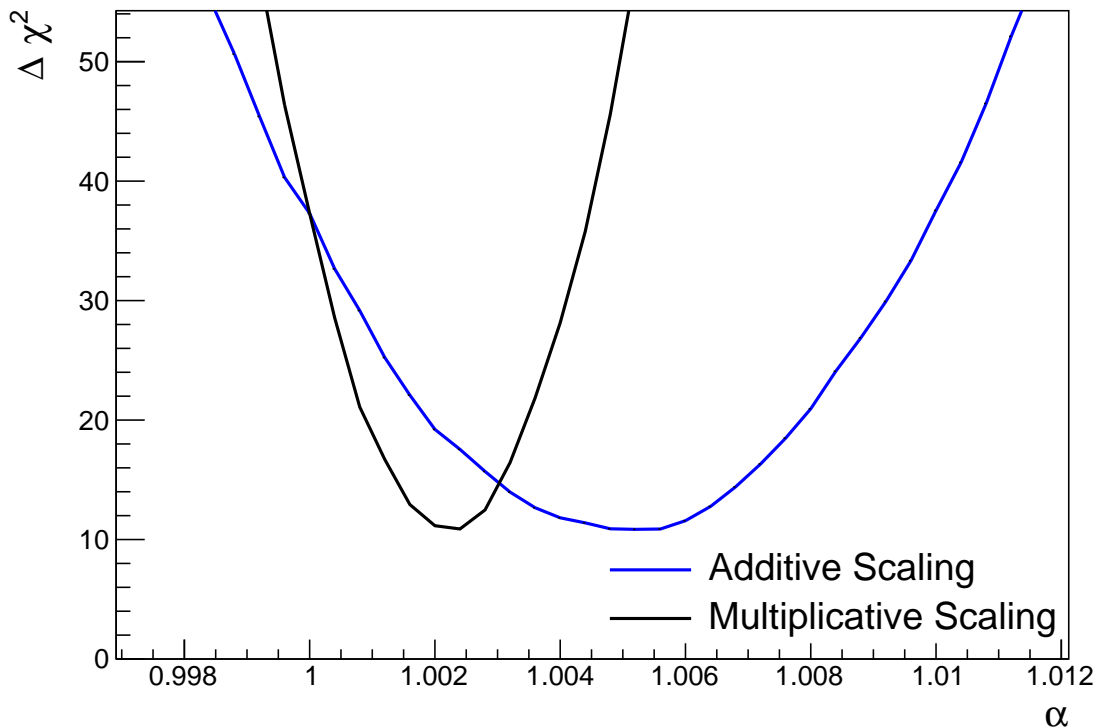


Figure 5.9.: The χ^2 difference between the SK-IV and SK-V reconstructed muon momentum divided by range when the SK-V is modified by the scaling parameter α . Both additive (Blue) and multiplicative (Black) scaling factors have been considered. In practice, the additive scaling factor actually uses the value of $(\alpha - 1.0)$ but is illustrated like this so the results can be shown on the same axis range.

1536 5.3. Event Reduction at SK

1537 Atmospheric neutrino events observed in the SK detector are categorised into three
1538 different types of samples: fully contained (FC), partially contained (PC) and up-going

1539 muon (Up- μ), using PMT hit signatures in the inner and outer detector (ID and OD,
 1540 respectively). To identify FC neutrino events, it is required that the neutrino interacts
 1541 inside the fiducial volume of the ID and that no significant OD activity is observed. For
 1542 this analysis, an event is defined to be in the fiducial volume provided the event vertex
 1543 is at least 0.5m away from the ID walls. PC events have the same ID requirements but
 1544 can have a larger signal present inside the OD. Typically, only high energy muons from
 1545 ν_μ interactions can penetrate the ID wall. The Up- μ sample contains events where muons
 1546 are created from neutrino interactions in the OD water or rock below the tank. They
 1547 then propagate upwards through the detector. Downward-going muons generated
 1548 from neutrino interactions above the tank are neglected because of the difficulty in
 1549 separating their signature from the cosmic muon shower background. The sample
 1550 categories are visually depicted in Figure 5.10.

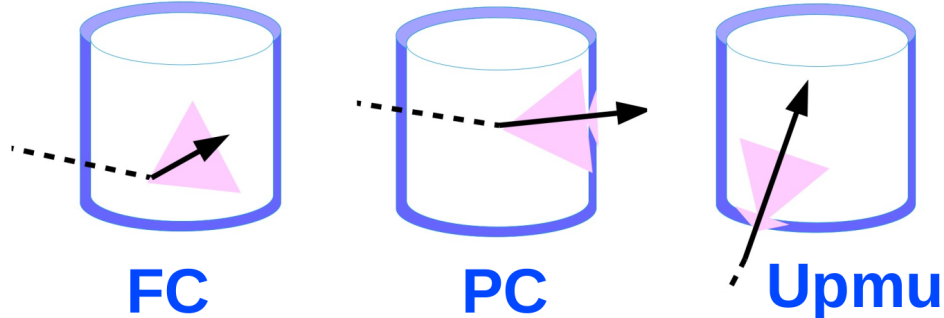


Figure 5.10.: A depiction of the topology patterns for fully-contained (FC), partially-contained (PC) and up-going muon (Up- μ) samples included in this analysis.

1551 Based on the event characteristics, as defined by the `fitQun` event reconstruction
 1552 software, the FC events are categorised by

- 1553 • **Visible Energy:** equal to the sum of the reconstructed kinetic energy of particles
 1554 above the Cerenkov threshold for all rings present in the event. The purpose is to
 1555 separate events into sub-GeV and multi-GeV categories.
- 1556 • **Number of observed Cerenkov rings.** The purpose is to separate single-ring and
 1557 multi-ring events, where single-ring events predominantly consist of quasi-elastic

1558 interactions and multi-ring events are typically resonant pion production or deep
1559 inelastic scattering events.

- 1560 • **Particle identification parameter of the most energetic ring:** A value deter-
1561 mined from the maximum likelihood value based on `fitQun`'s electron, muon, or
1562 pion hypothesis. The purpose is to separate electron-like and muon-like events.
1563 • **Number of decay electrons:** The purpose is to separate quasi-elastic events
1564 (which have one decay electron emitted from the muon decay) and resonant pion
1565 production events (which have two decay electrons emitted from the muon and
1566 pion).

1567 The PC and Up- μ categories are broken down into “through-going” and “stopping”

1568 samples depending on whether the muon leaves the detector. This is because the PC
1569 stopping events deposit the entire energy of the interaction into the detector, resulting
1570 in better reconstruction. The energy of events that exit the detector has to be estimated,
1571 with typically worse resolution, which introduces much larger systematic uncertainties.

1572 Through-going Up- μ samples are further broken down by whether any hadronic
1573 showering was observed in the event which typically indicates DIS interactions. The
1574 expected neutrino energy for the different categories is given in Figure 5.11. FC sub-
1575 GeV and multi-GeV events peak around 0.7GeV and 3GeV respectively, with slightly
1576 different peak energies for ν_e and $n\nu_\mu$ oscillation channels. PC and Up- μ are almost
1577 entirely comprised of ν_μ events and peak around 7GeV and 100GeV, respectively.

1578 In normal data-taking operations, the SK detector observes many background
1579 events alongside the beam and atmospheric neutrino signal events of physics interest
1580 for this thesis. Cosmic ray muons and flasher events, which are the spontaneous
1581 discharge of a given PMT, contribute the largest amount of background events in the
1582 energy range relevant to this thesis. Lower energy analyses like DSNB searches are
1583 also subject to radioactive backgrounds [189]. Therefore the data recorded is reduced

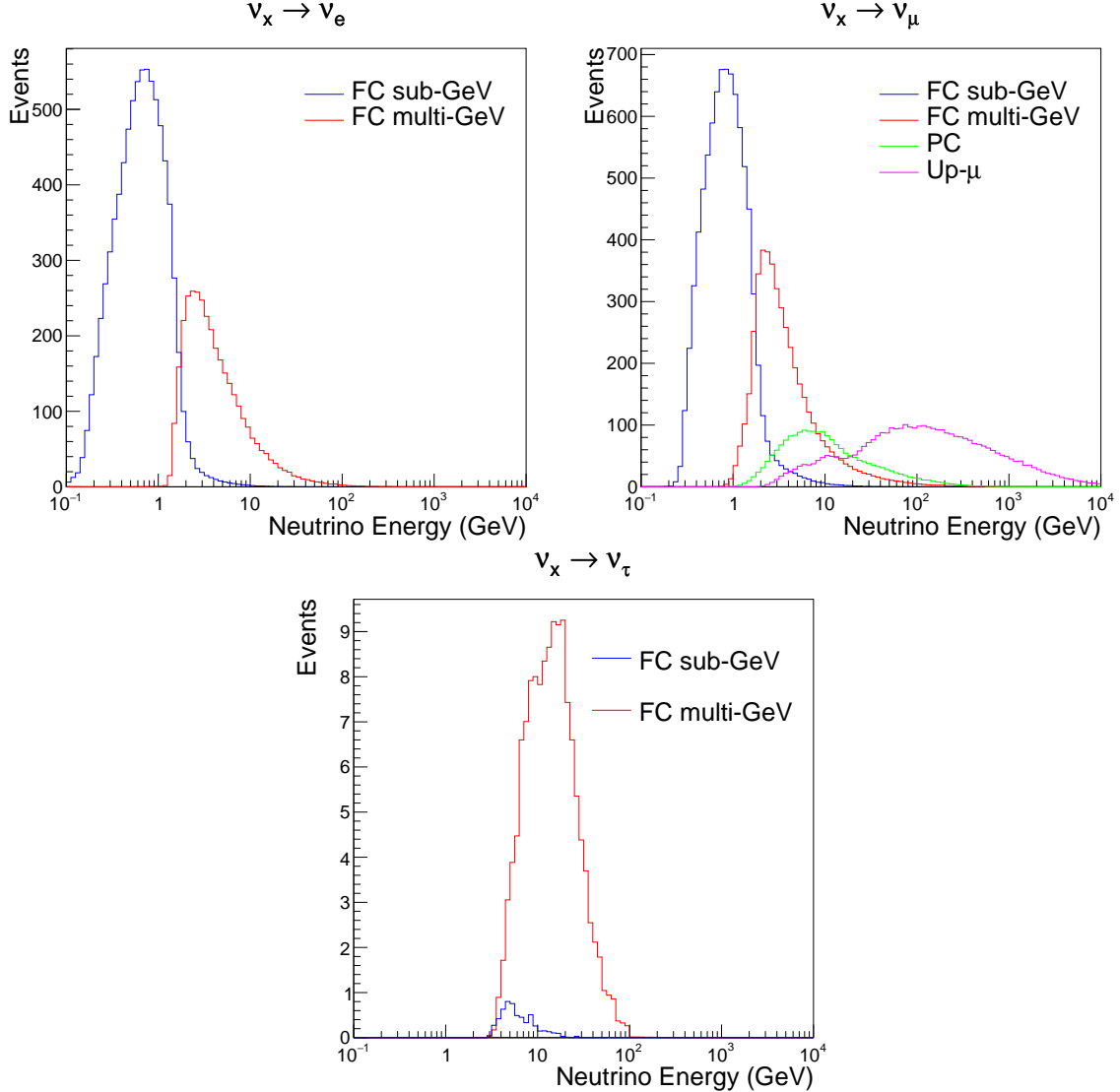


Figure 5.11.: The predicted neutrino flux of the fully contained (FC) sub-GeV and multi-GeV, partially contained (PC), and upward-going muon (Up- μ) events. The prediction is broken down by the $\nu_x \rightarrow \nu_e$ prediction (top left), $\nu_x \rightarrow \nu_\mu$ prediction (top right) and $\nu_x \rightarrow \nu_\tau$ prediction (bottom). Asimov A oscillation parameters are assumed (given in Table 2.2).

1584 with the aim of removing these background events. The reduction process is detailed
 1585 in [47, 89] and briefly summarised below.

1586 The first two steps in the FC reconstruction remove the majority of cosmic ray
 1587 muons by requiring a significant amount of ID activity compared to that measured in
 1588 the OD. Events that pass this cut are typically very high momentum muons or events
 1589 that leave very little activity in the OD. Consequently, a third reduction step is then

1590 applied to select cosmic-ray muons that pass the initial reduction step. A purpose-built
1591 cosmic muon fitter is used to determine the entrance (or exit) position of the muon and
1592 a cut is applied to OD activity contained within 8m of this position. Flasher events are
1593 removed in the fourth reduction step which is based on the close proximity of PMT
1594 hits surrounding the PMT producing the flash. Events that pass all these reduction
1595 steps are reconstructed with the APFit algorithm. The fifth step of the reduction uses
1596 information from the more precise fitter to repeat the previous two steps with tighter
1597 cuts. Muons below the Cherenkov threshold can not generate optical photons in the
1598 ID but the associated decay electron can due to its lower mass. These are the types of
1599 events targeted in the fifth reduction step. The final cuts require the event vertex to be
1600 within the fiducial volume (0.5m from the wall although the nominal distance is 2.0m),
1601 visible energy $E_{vis} > 30\text{MeV}$ and fewer than 16 hits within the higher energy OD
1602 cluster. The culmination of the fully contained reduction results in 8.09 events/day in
1603 the nominal fiducial volume [190]. The uncertainty in the reconstruction is calculated
1604 by comparing Monte Carlo prediction to data. The largest discrepancy is found to be
1605 1.3% in the fourth reduction step.

1606 The PC and Up- μ events are processed through their own reduction processes
1607 detailed in [47]. Both of these samples are reconstructed with the APFit algorithm
1608 rather than fitQun. This is because the efficiency of reconstructing events that leave
1609 the detector has not been sufficiently studied for reliable systematic uncertainties wth
1610 fitQun. The PC and Up- μ samples acquire events at approximately 0.66 and 1.44
1611 events/day.

1612 Events due to beam neutrinos undergo the same reduction steps as FC events and
1613 are then subject to further cuts [191]. The GPS system which links the timing between
1614 the beam facility and SK needs to be operating correctly and there should be no activity

₁₆₁₅ within the detector in the previous $100\mu\text{s}$ before the trigger. The events then need to
₁₆₁₆ triggered between $-2\mu\text{s}$ and $10\mu\text{s}$ of the expected spill timing.

₁₆₁₇ The beam neutrino samples are not split by visible energy since their energy range
₁₆₁₈ is smaller than the atmospheric neutrino events. Following the T2K analysis in [80],
₁₆₁₉ only single-ring beam neutrino events are considered. Similar to atmospheric event
₁₆₂₀ selection, the number of decay electrons is used as a proxy for distinguishing CCQE
₁₆₂₁ and CCRES events. The expected neutrino energy, broken down by number of decay
₁₆₂₂ electrons, is given in Figure 5.12.

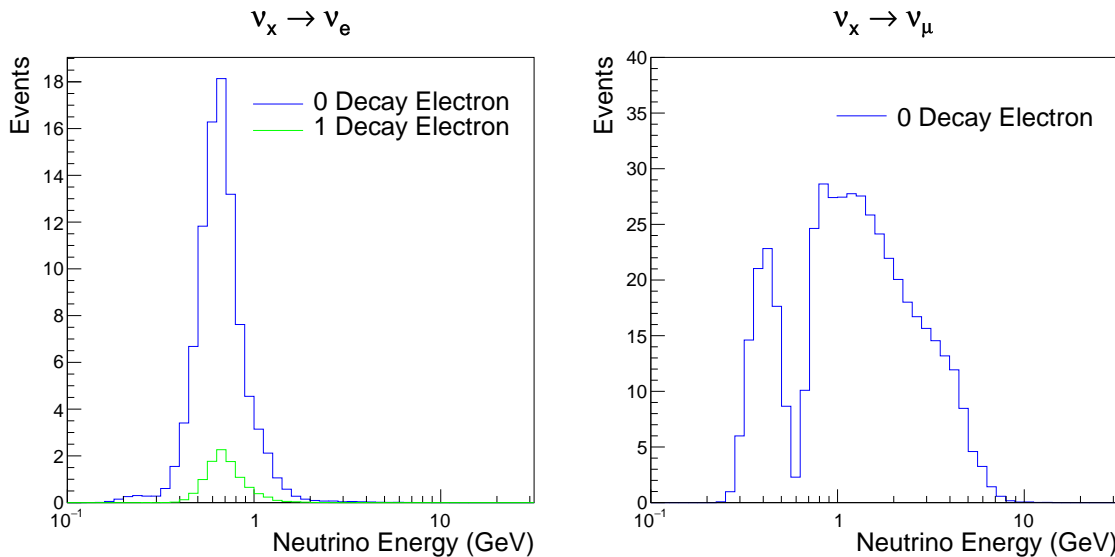


Figure 5.12.: The predicted flux of beam neutrinos, as a function of neutrino energy. The predictions are broken down by the number of decay electrons associated with the particular events. Asimov A oscillation parameters are assumed (given in Table 2.2).

₁₆₂₃ **Chapter 6**

₁₆₂₄ **Sample Selections and Systematics**

₁₆₂₅ The oscillation analysis presented within this thesis is built upon a simultaneous
₁₆₂₆ fit to atmospheric data at SK, neutrino beam data in the near detector, and beam
₁₆₂₇ data measured at SK. The definitions of these samples are documented in section 6.1,
₁₆₂₈ section 6.2, and section 6.3, respectively. The data collected and used within this
₁₆₂₉ analysis is detailed in Table 6.1. The near and far detector data corresponds to T2K
₁₆₃₀ runs 2-9 and runs 1-10, respectively. The accumulated POT and beam power for runs
₁₆₃₁ 1 – 10 are illustrated in Figure 6.1.

Data Type	Total
Near Detector FHC	1.15×10^{21} POT
Near Detector RHC	8.34×10^{20} POT
Far Detector FHC	1.97×10^{21} POT
Far Detector RHC	1.63×10^{21} POT
Atmospheric SK-IV	3244.4 days

Table 6.1.: The amount of data collected in each detector used within this analysis. The data collected at the near and far detector, for both neutrino beam (FHC) and antineutrino beam (RHC), is measured as the number of protons on target (POT).

₁₆₃₂ The difference in POT recorded at the near and far detector is due to the difference
₁₆₃₃ in downtime of the respective detector. The SK detector is very stable with almost 100%
₁₆₃₄ of data recorded during beam operation. Due to various technical and operational
₁₆₃₅ issues, the downtime of the near detector is significantly higher due to its more
₁₆₃₆ complex design and operating requirements.

1637 The systematic parameters invoked within the flux, detector, and interaction models
 1638 used within this analysis are documented in section 6.4. The standard configuration of
 1639 the joint beam and atmospheric data fit utilises far detector systematics provided in
 1640 the official inputs from the two experiments. Additionally, a correlated detector model
 1641 which fits the parameters used in sample selections to data has been developed and
 1642 documented in subsection 6.4.5.

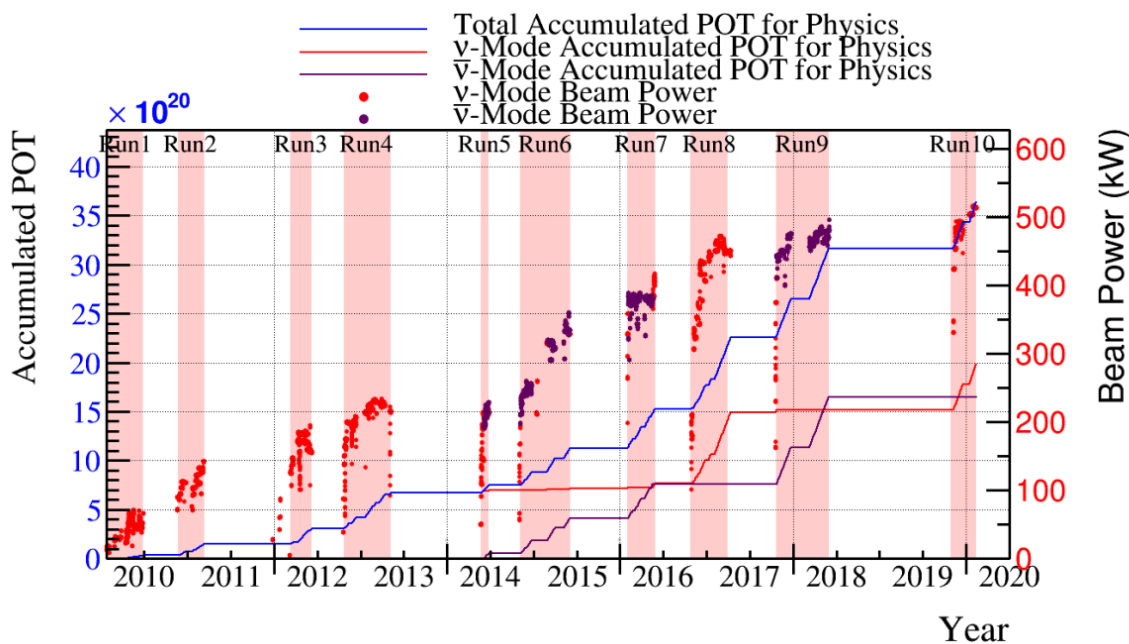


Figure 6.1.: The accumulated beam data, measured as the number of protons on target (POT). The total data (blue) is given which comprises of the neutrino beam (red) and antineutrino (purple) components. The beam power for neutrino and antineutrino beams is given as the markers using the same colour scheme. The timescale runs from Run 1 which started in January 2010 until Run 10 which ended in February 2020. The ratio of accumulated data in neutrino and antineutrino beam is 54.7% : 45.3%.

¹⁶⁴³ 6.1. Atmospheric Samples

¹⁶⁴⁴ The atmospheric event selection follows the official SK-IV analysis presented in [89]
¹⁶⁴⁵ and is documented below. The Monte Carlo prediction used within this analysis
¹⁶⁴⁶ corresponds to 500 years worth of neutrino events, which is scaled down to match the
¹⁶⁴⁷ SK-IV livetime of 3244.4 days.

¹⁶⁴⁸ The fully contained (FC), partially contained (PC), and upward going muon events
¹⁶⁴⁹ ($\text{up-}\mu$) which pass the reduction cuts discussed in section 5.3 are further broken down
¹⁶⁵⁰ into different samples based on reconstruction information. This section details the
¹⁶⁵¹ samples used within this oscillation analysis, alongside the chosen binning, used
¹⁶⁵² within the fit.

¹⁶⁵³ FC events are first separated by the visible energy deposited within the detector.
¹⁶⁵⁴ This is calculated as the sum of the reconstructed kinetic energy above the Cherenkov
¹⁶⁵⁵ threshold for all rings present in the event. Events are separated by whether they were
¹⁶⁵⁶ above or below $E_{\text{vis}} = 1.33\text{GeV}$. This separates “subGeV” and “multiGeV” events.
¹⁶⁵⁷ Typically, lower energy events consist of charge current quasi-elastic (CCQE) inter-
¹⁶⁵⁸ actions which are better understood and simpler to reconstruct resulting in smaller
¹⁶⁵⁹ systematic uncertainties. Events are further separated by the number of rings as-
¹⁶⁶⁰ sociated with the event due to similar reasoning. As the oscillation probability is
¹⁶⁶¹ dependent upon the flavour of neutrino, electron and muon events are separated
¹⁶⁶² using a similar likelihood method to that discussed in section 5.2. To reduce computa-
¹⁶⁶³ tional resources required for the reconstruction, only electron and pion hypotheses are
¹⁶⁶⁴ considered so this separation cut depends on the ratio of the electron to pion likeli-
¹⁶⁶⁵ hoods, $\log(L_e/L_\pi)$. Finally, the number of decay electrons is used to classify events.
¹⁶⁶⁶ Charged current resonant pion production (CCRES) interactions generate a final-state
¹⁶⁶⁷ pion. This can decay, mostly likely through a muon, into a decay electron. Therefore

₁₆₆₈ any electron-like event with one decay electron or muon-like event with two decay
₁₆₆₉ electrons was most likely produced by a CCRES interaction. Consequently, the number
₁₆₇₀ of decay electrons can be used to distinguish CCQE and CCRES interaction modes.
₁₆₇₁ Ultimately, FC subGeV events are separated into the samples listed in Table 6.2.

Sample Name	Description
SubGeV-e-like-0dcy	Single ring e -like events with zero decay electrons
SubGeV-e-like-1dcy	Single ring e -like events with one or more decay electrons
SubGeV-mulike-0dcy	Single ring μ -like events with zero decay electrons
SubGeV-mulike-1dcy	Single ring μ -like events with one decay electrons
SubGeV-mulike-2dcy	Single ring μ -like events with two or more decay electrons
SubGeV-pi0like	Two e -like ring events with zero decay electrons and reconstructed π^0 mass $85 \leq m_{\pi^0} < 215$ MeV

Table 6.2.: The fully contained subGeV samples, defined as events with visible energy $E_{vis} < 1.33$ GeV, used within this oscillation analysis.

₁₆₇₂ In addition to the cuts discussed above, multiGeV samples also have additional cuts
₁₆₇₃ to separate samples which target neutrino and antineutrino separation. As discussed
₁₆₇₄ in section 7.1, the matter resonance only occurs for neutrinos in normal hierarchy
₁₆₇₅ and antineutrinos in an inverted mass hierarchy. Therefore, having flavour-enriched
₁₆₇₆ samples aids in the determination of the mass hierarchy. For a CCRES interaction,

$$\begin{aligned}
 \bar{\nu}_e + N &\rightarrow e^+ + N' + \pi^-, \\
 \nu_e + N &\rightarrow e^- + N' + \pi^+ \\
 &\quad \downarrow \mu^+ + \nu_\mu \\
 &\quad \downarrow e^+ + \nu_e + \bar{\nu}_\mu.
 \end{aligned} \tag{6.1}$$

₁₆₇₇ The π^- emitted from a $\bar{\nu}_e$ interaction is more likely to be absorbed within the
₁₆₇₈ oxygen nucleus compared to the π^+ from ν_e interactions [192]. These pions then

1679 decay, mostly through muons, to electrons. Therefore the number of tagged decay
1680 electrons associated with an event gives an indication of whether the interaction
1681 was due to a neutrino or antineutrino: zero for $\bar{\nu}_e$ events, and one for ν_e events.
1682 The ability to separate neutrino from antineutrino events is illustrated in Table 6.4,
1683 where the MultiGeV-*e*like-nue has 78% purity of neutrino interactions with only 7%
1684 antineutrino background in that sample and the rest of the sample comprising of
1685 neutral current backgrounds.

1686 This relatively simple discriminator works reasonably well for single-ring events.
1687 However, this is not the case for multi-ring events. A multiGeV multiring separation
1688 (MME) likelihood cut which specifically targets multiGeV multiRing electron-like
1689 events was introduced in [193, 194]. This is a two-stage likelihood selection cut. Four
1690 observables are used within the first likelihood cut to distinguish CC ν_e and CC $\bar{\nu}_e$
1691 events from background:

- 1692 • The number of decay electrons
- 1693 • The maximum distance between the vertex of the neutrino and the decay electrons
- 1694 • The energy deposited by the leading energy ring
- 1695 • The reconstructed particle identification of that highest energy ring

1696 Background events consist of CC ν_μ and NC interactions. Typically these produce
1697 events where the majority of the energy is carried by the hadronic system. Additionally,
1698 muons tend to travel further than the pions from CC ν_e before decaying. Consequently,
1699 the parameters used within the likelihood cut target the typical background interaction
1700 kinematics.

1701 Neutrino and antineutrino events are then separated by a second likelihood method
1702 ($\nu/\bar{\nu}$ separation) detailed in [52]. This uses the number of decay electrons, the number
1703 of reconstructed rings, and the event's transverse momentum. The last two parameters

Sample Name	Description
MultiGeV- <i>e</i> -like-nue	Single ring <i>e</i> -like events with zero decay electrons
MultiGeV- <i>e</i> -like-nuebar	Single ring <i>e</i> -like events with one or more decay electrons
MultiGeV- <i>μ</i> -like	Single ring <i>μ</i> -like events
MultiRing- <i>e</i> -like-nue	Two or more ring events with leading energy <i>e</i> -like ring and passed both MME and $\nu/\bar{\nu}$ separation cuts
MultiRing- <i>e</i> -like-nuebar	Two or more ring events with leading energy <i>e</i> -like ring and passed MME and failed $\nu/\bar{\nu}$ separation cuts
MultiRing- <i>μ</i> -like	Two or more ring events with leading energy <i>μ</i> -like ring and only requires $E_{vis} > 0.6\text{GeV}$ DB: Why is this not }1.33\text{GeV? N
MultiRing-Other1	Two or more ring events with leading energy <i>e</i> -like ring and failed the MME likelihood cut

Table 6.3.: The fully contained multiGeV samples used within this oscillation analysis. Both the sample name and description are given.

1704 are used because higher-energy samples tend to have more pions produced above
 1705 the Cherenkov threshold which results in more rings compared to an antineutrino
 1706 interaction. Furthermore, the angular distribution also tends to be more forward
 1707 peaked in antineutrino interactions as compared to neutrino interactions [89]. These
 1708 FC multiGeV sample definitions are detailed in Table 6.3.

1709 The PC and up- μ events are split by the amount of energy deposited within the
 1710 outer detector, into “stopping” and “through-going” samples. This is because the
 1711 momentum of events leaving the detector has to be approximated, which increases the
 1712 systematic uncertainty. This estimate is particularly poor for very high-energy events.
 1713 This is why up- μ through-going events are not binned in reconstructed momentum.
 1714 If an event leaves the detector, the energy it takes with it has to be estimated which
 1715 increases the systematic uncertainty compared to events entirely contained within the
 1716 inner detector. The through-going up- μ are further separated by the presence of any
 1717 electromagnetic showering in the event, as the assumption of non-showering muon

¹⁷¹⁸ does not give reliable reconstruction for these types of events [47]. In total, 13 FC, 2
¹⁷¹⁹ PC, and 3 up- μ atmospheric samples are included within this analysis.

Sample	CC ν_e	CC $\bar{\nu}_e$	CC($\nu_\mu + \bar{\nu}_\mu$)	CC($\nu_\tau + \bar{\nu}_\tau$)	NC
SubGeV- e -like-0dcy	72.17	23.3	0.724	0.033	3.77
SubGeV- e -like-1dcy	86.81	1.773	7.002	0.062	4.351
SubGeV- μ -like-0dcy	1.003	0.380	90.07	0.036	8.511
SubGeV- μ -like-1dcy	0.023	0.	98.46	0.029	1.484
SubGeV- μ -like-2dcy	0.012	0.	99.25	0.030	0.711
SubGeV- π 0-like	6.923	2.368	0.928	0.011	89.77
MultiGeV- e -like-nue	78.18	7.041	3.439	1.886	9.451
MultiGeV- e -like-nuebar	56.68	37.81	0.174	0.614	4.718
MultiGeV- μ -like	0.024	0.005	99.67	0.245	0.058
MultiRing- e -like-nue	59.32	12.39	4.906	3.385	20
MultiRing- e -like-nuebar	52.39	31.03	1.854	1.585	13.14
MultiRing- μ -like	0.673	0.080	97.33	0.342	1.578
MultiRingOther-1	27.98	2.366	34.93	4.946	29.78
PCStop	8.216	3.118	84.45	0.	4.214
PCThrus	0.564	0.207	98.65	0.	0.576
UpStop- μ	0.829	0.370	98.51	0.	0.289
UpThruNonShower- μ	0.206	0.073	99.62	0.	0.103
UpThruShower- μ	0.128	0.054	99.69	0.	0.132

Table 6.4: The purity of each atmospheric sample used within this analysis, broken down by charged current (CC) and neutral current (NC) interactions and which neutrino flavour interacted within the detector. Asimov A oscillation parameter sets are assumed (given in Table 2.2). Electron neutrino and antineutrino events are separated to illustrate the ability of the separation likelihood cuts used within the multiGeV and multiring sample selections.

¹⁷²⁰ The atmospheric samples are binned in direct observables: reconstructed lepton
¹⁷²¹ momentum and direction, as given by Table A.1. The distribution of the reconstructed
¹⁷²² lepton momentum (for samples that only have one bin reconstructed zenith angle)
¹⁷²³ and reconstructed direction for each atmospheric sample used within this analysis is
¹⁷²⁴ illustrated in Figure 6.2. The by-mode breakdown of each of the atmospheric samples
¹⁷²⁵ is given in Appendix A.

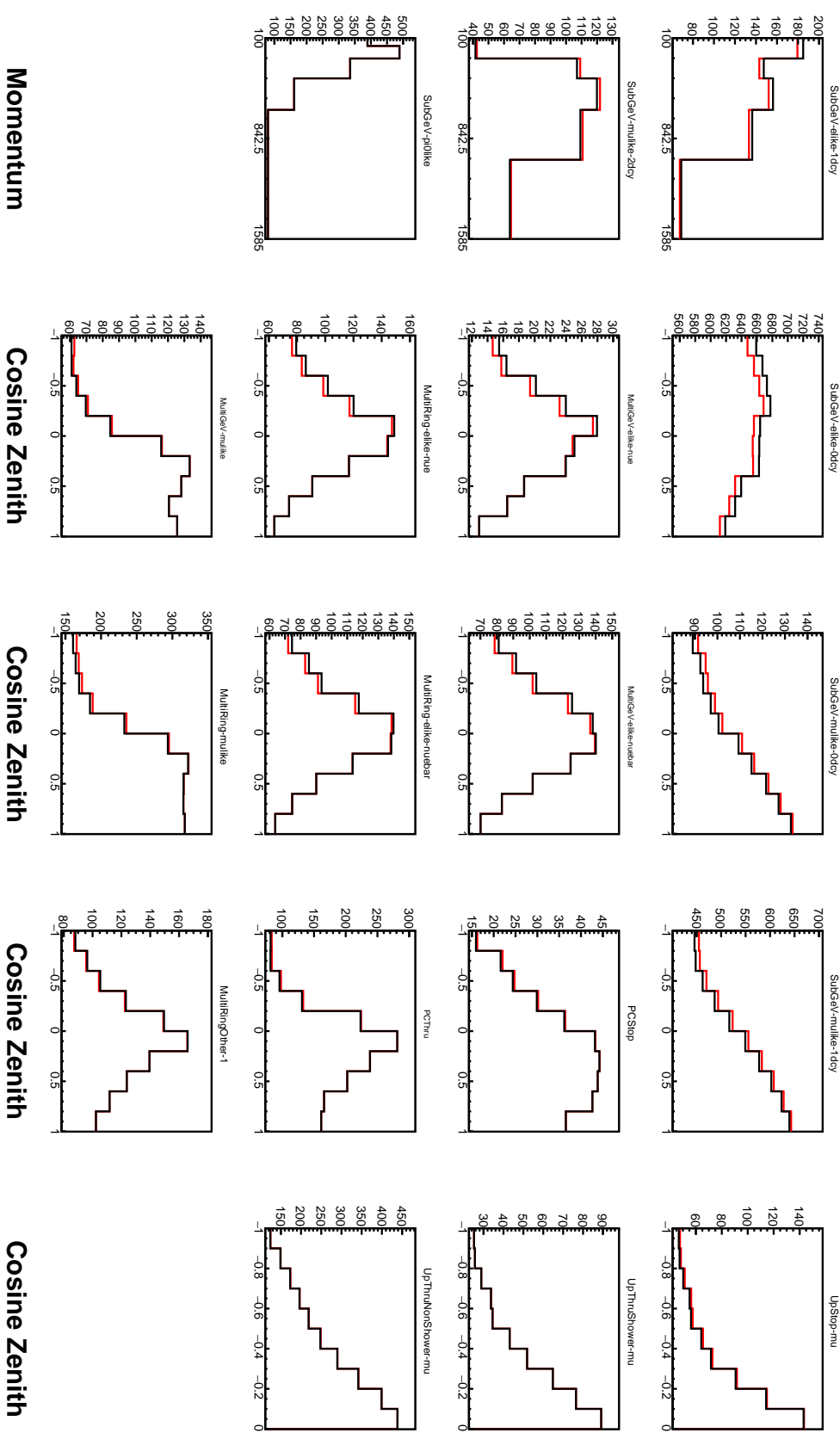


Figure 6.2: Comparison of the SK-IV atmospheric samples between predictions made with the CP-violating Asimov A (Black) and CP-conserving Asimov B (Red) oscillation parameter sets (given in Table 2.2). The subGeV samples CCRES and π^0 -like samples are given in their reconstructed lepton momentum. All other samples are presented in their reconstructed zenith angle projection.

1726 6.2. Near Detector Beam Samples

1727 The near detector sample selections are documented in detail within [195] and sum-
1728 marised below. Samples are selected based upon the which Fine Grained Detector
1729 (FGD) that the vertex is reconstructed in as well as the operating mode of the beam:
1730 FHC or RHC. For additional constraints on model parameters, wrong-sign neutrino
1731 samples are also considered when the beam is operating in RHC mode. Samples
1732 from the wrong-sign component of the FHC beam mode are not included as they are
1733 statistically insignificant compared to those samples already listed.

1734 **The below paragraph has been added** The reconstruction algorithm uses a cluster-
1735 ing algorithm to group hits within the TPC. It then adds information from the upstream
1736 FGD to form a track which passes through both sub-detectors. In FHC(RHC), the
1737 highest momentum negative(positive) curvature track is defined as the muon candi-
1738 date. Before being assigned a sample, these candidate muon events must undergo
1739 CC-inclusive cuts, as defined in [196]:

- 1740 • Event Timing: The DAQ must be operational and the event must occur within
1741 the expected beam time window consistent with the beam spill
- 1742 • TPC Requirement: The muon-candidate track path must intercept one or more
1743 TPCs
- 1744 • Fiducial volume: The event must originate from within the fiducial volume. The
1745 fiducial volumes are defined as a region within each sub-detector [197].
- 1746 • Upstream Background: Remove events that have muons tracks that originate
1747 upstream of the FGDs by requiring no high-momentum tracks within 150mm
1748 upstream of the candidate vertex. Additionally, events that occur within the
1749 downstream FGD are vetoed if a secondary track starts within the upstream FGD

- 1750 • Broken track removal: All candidates where the muon candidate is broken in two
- 1751 are removed
- 1752 • Muon PID: Measurements of dE/dx in a TPC are used to distinguish muon-like
- 1753 events using a likelihood cut

1754 In addition to these cuts, RHC neutrino events also have to undergo the following

1755 cuts to aid in the separation of neutrino and antineutrino [198]:

- 1756 • TPC Requirement: The track path must intercept TPC2
- 1757 • Positive Track: The highest momentum track must be positive
- 1758 • TPC1 Veto: Remove any events originating upstream of TPC1

1759 Once all CC-inclusive events have been determined, they are further separated into

1760 sub-samples that target the constraints on interaction modes most relevant at the far

1761 detector. They are split by pion multiplicity: CC0 π , CC1 π , and CCOther. These target

1762 specific interaction modes CCQE, CCRES, and other CC background interactions,

1763 respectively. Pions in the TPCs and FGDs are selected by requiring a second track to be

1764 observed, which is separate from the muon track and is in the same beam spill window

1765 and sub-detector. If the pion originated within a FGD, it must also pass through the

1766 sequential downstream TPC (TPC2 for FGD1, TPC3 for FGD2).

1767 CC0 π , CC1 π , and CCOther samples are defined with the following cuts:

- 1768 • ν_μ **CC0 π Selection:** No electrons in TPC and no charged pions or decay electrons
- 1769 within the TPC or FGD
- 1770 • ν_μ **CC1 π Selection:** Exactly one charged pion in either the TPC or FGD, where
- 1771 the number of charged pions in the FGD is equal to the number of decay electrons

- 1772 • ν_μ CCOther Selection: All events which are not classified into the above two
1773 selections.

1774 Counting the three selections for each FGD in FHC and RHC running, including
1775 the wrong-sign background in RHC, 18 near detector samples are used within this
1776 analysis. These samples are binned in reconstructed lepton momentum (illustrated in
1777 Figure 6.3) and direction with respect to the beam. The binning is chosen such that
1778 each event has at least 20 Monte Carlo events in each bin [197]. This is to ensure that
1779 the bins are coarse enough to ensure the reduction of statistical errors, whilst also
1780 being fine enough to sample the high-resolution peak regions. The exact binning is
1781 detailed in [197].

1782 6.3. Far Detector Beam Samples

1783 The beam neutrino events which occur at the SK detector, which pass the reduction cuts
1784 detailed in section 5.3, are separated depending on whether the beam was operating
1785 in FH or RHC mode. The events are then separated into three samples: electron-like
1786 ($1Re$), muon-like ($1R\mu$), and CC $1\pi^+$ -like ($1Re1de$) which are observed as electron-like
1787 events with an associated decay electron [185]. As discussed in section 6.1, positively
1788 charged pions emitted from neutrino interactions are more likely to produce decay
1789 electrons than negatively charged pions. Consequently, the CC $1\pi^+$ -like sample is only
1790 selected when the beam is operating in FHC mode. Therefore, five beam samples
1791 measured at SK are used in this analysis.

1792 The fiducial volume definition for beam samples is slightly different from that used
1793 within the atmospheric samples. It uses both the distance to the closest wall ($dWall$)
1794 and the distance to the wall along the trajectory of the particle ($toWall$). This allows
1795 events that originate close to the wall but are facing into the tank to be included within

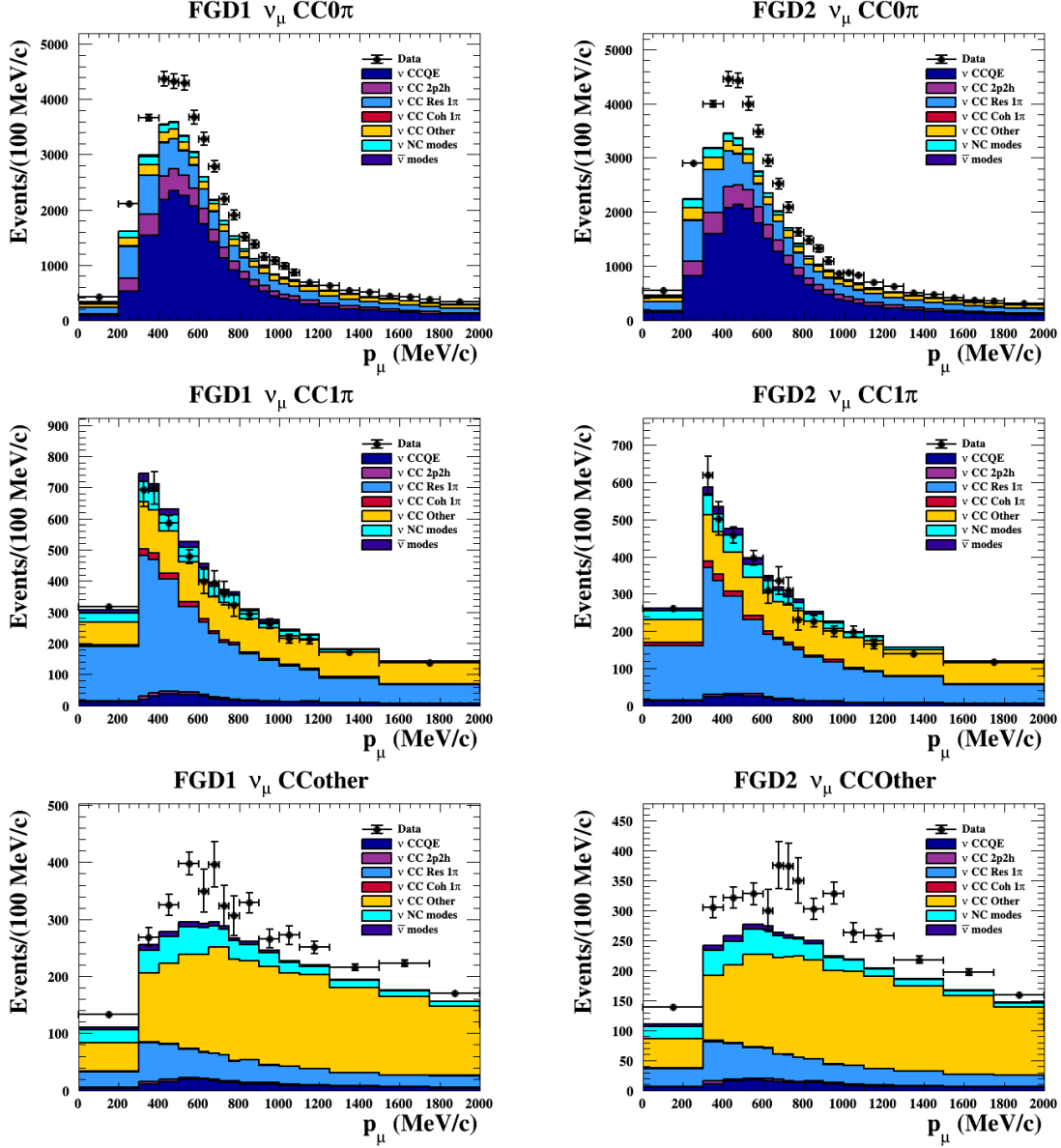


Figure 6.3.: The nominal Monte Carlo predictions for the FGD1 and FGD2 samples in neutrino beam mode, broken down into the $\text{CC}\nu_\mu 0\pi$, $\text{CC}\nu_\mu 1\pi$ and $\text{CC}\nu_\mu$ Other categories. Figures taken from [195].

the analysis, which would have otherwise been removed. These additional events are beneficial for a statistics-limited experiment. The exact cut values for both dWall and toWall are different for each of the three types of sample and are optimised based on T2K sensitivity to δ_{CP} [183, 199]. They are:

1800 1Re event selection For an event to be classified as a 1Re-like, the event must follow:

- 1801 • Fully-contained and within $d_{\text{Wall}} > 80\text{cm}$ and $t_{\text{toWall}} > 170\text{cm}$
- 1802 • Total of one ring which is reconstructed as electron-like with reconstructed momentum $P_e > 100\text{MeV}$
- 1803
- 1804 • Zero decay electrons are associated with the event
- 1805 • Passes π^0 rejection cut discussed in section 5.2
- 1806 The zero decay electron cut specifically targets CCQE interactions. Whereas, the π^0
- 1807 rejection cut is designed to remove neutral current π^0 background events which can
- 1808 be easily reconstructed as 1Re-like events.

1809 **CC1 π^+ event selection** This event selection is very similar to that of the 1Re sample.
1810 The only difference is that the d_{Wall} and t_{toWall} criteria are changed to $> 50\text{cm}$ and
1811 $> 270\text{cm}$, respectively. Furthermore, exactly one decay electron is required from the
1812 π^+ decay.

1813 **1R μ event selection** A 1R μ -like event is determined by the following cuts:

- 1814 • Fully-contained and within $d_{\text{Wall}} > 50\text{cm}$ and $t_{\text{toWall}} > 250\text{cm}$
- 1815 • Total of one ring which is reconstructed as muon-like with reconstructed momen-
- 1816 tum $P_\mu > 200\text{MeV}$
- 1817 • Fewer than two decay electrons are associated with the event
- 1818 • Passes π^+ rejection cut discussed in section 5.2

1819 As pions and muons have similar masses, the Cherenkov rings they generate have
1820 similar opening angles. To enhance the purity, the events have to pass the π^+ rejection
1821 cut which is specifically optimised to separate the two types of events.

1822 All of these samples are binned in reconstructed neutrino energy. This is possible
1823 as the direction from the source is known extremely well. This value is calculated for
1824 the 1Re-like and 1R μ -like samples assuming CCQE interactions,

$$E_\nu^{rec} = \frac{(M_N - V_{nuc})E_l - m_l^2/2 + M_N V_{nuc} - V_{nuc}^2/2 + (M_P^2 + M_N^2)/2}{M_N - V_{nuc} - E_l + P_l \cos(\theta_{beam})} \quad (6.2)$$

1825 Where M_N , M_P and m_l are the masses of the neutron, proton and outgoing lepton,
1826 respectively. $V_{nuc} = 27\text{MeV}$ is the binding energy of the oxygen nuclei [185], θ_{beam} is
1827 the angle between the beam and the direction of the outgoing lepton, and E_l and P_l
1828 are the energy and momentum of that outgoing lepton.

1829 The reconstructed neutrino energy of the CC1 π^+ -like events is modified to include
1830 the delta resonance produced within the interaction,

$$E_\nu^{rec} = \frac{2M_N E_l + M_{\Delta^{++}}^2 - M_N^2 - m_l^2}{2(M_N - E_l + P_l \cos(\theta_{beam}))} \quad (6.3)$$

1831 Where $M_{\Delta^{++}}$ is the mass of the delta baryon. Binding energy effects are not
1832 considered as a two-body process with the delta baryon is assumed. This follows
1833 the T2K oscillation analysis presented in [80], although recent developments of the
1834 interaction model in the latest T2K oscillation analysis do include effects from binding
1835 energy in this calculation [200].

1836 The reconstructed neutrino energy for the FHC samples is illustrated in Figure 6.4.
1837 As expected, the 1R μ -like and 1Re-like samples are heavily dominated by CCQE in-
1838 teractions, with smaller contributions from 2p2h meson exchange and resonant pion
1839 production interactions. The CC1 π^+ -like sample predominantly consists of charged

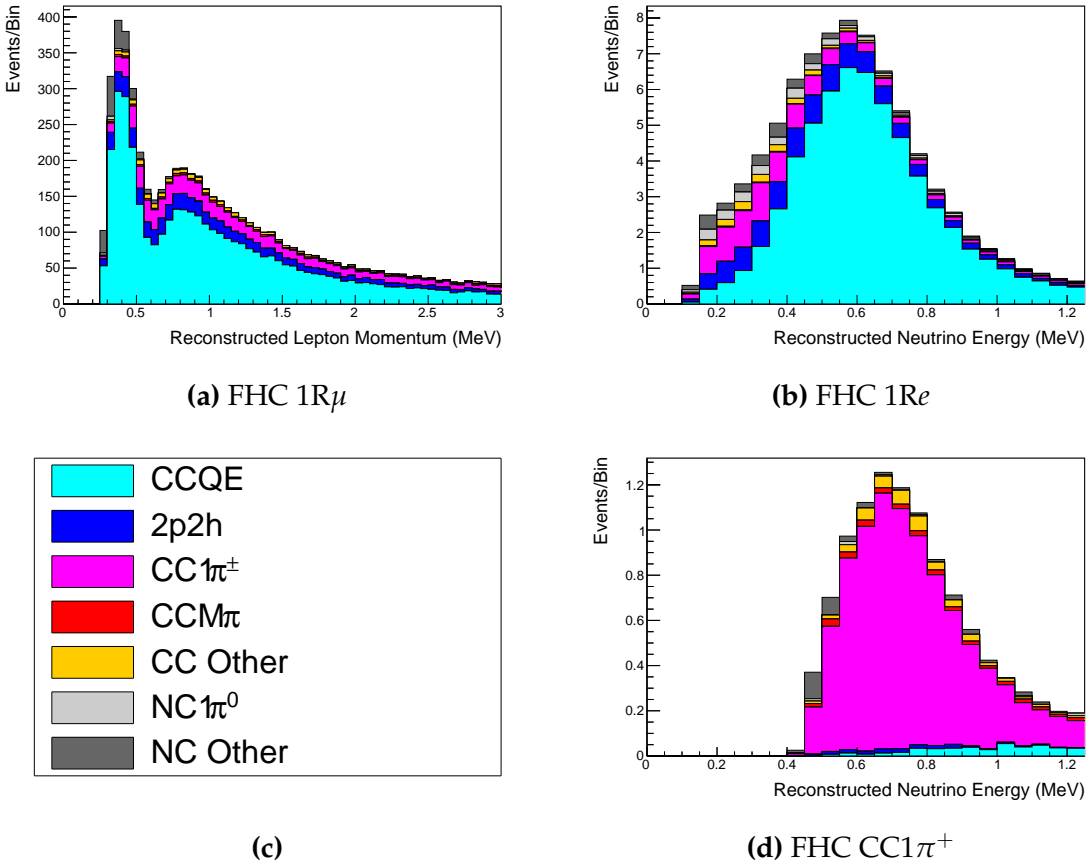


Figure 6.4.: The reconstructed neutrino energy, as defined by Equation 6.2 and Equation 6.3, for the 1R μ -like, 1Re-like and CC1 π^+ -like samples. Asimov A oscillation parameter sets are assumed (given in Table 2.2). These samples are the FHC mode samples. For ease of viewing, the 1R μ sample only shows the $0. \leq E_\nu^{rec} < 3.0\text{GeV}$ but the binning extends to 30.0GeV.

1840 current resonant pion production interactions. The 1Re-like and CC1 π^+ -like samples
 1841 are also binned by the angle between the neutrino beam and the reconstructed lepton
 1842 momentum. This is to aid in charged current and neutral current separation, as indi-
 1843 cated in Figure 6.5. This is because the neutral current backgrounds are predominantly
 1844 due to π^0 -decays, where the opening angle of the two gammas alongside the different
 1845 final state kinematics produces a slightly broader angular distribution compared to
 1846 the final state particles originating from charged current ν_e interactions.

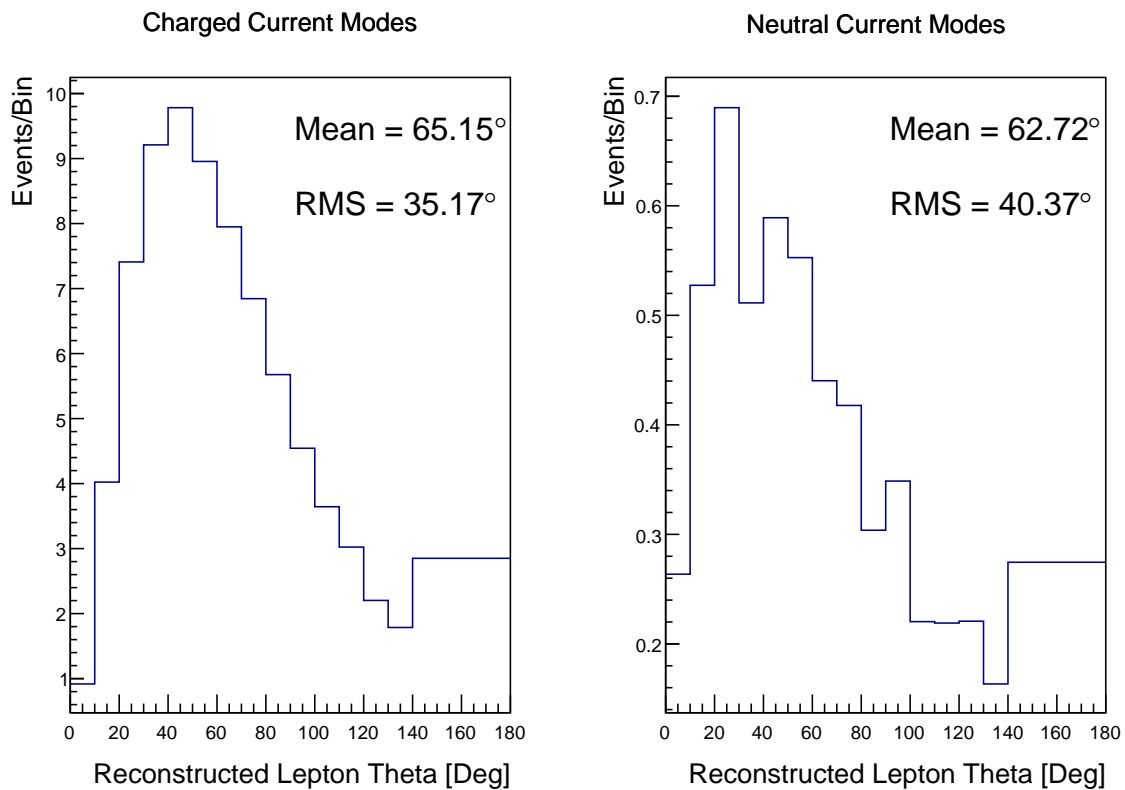


Figure 6.5.: The distribution of the angle between the neutrino beam direction and the reconstructed final state lepton, for the FHC 1Re-like sample. The distribution is broken down by neutrino interaction mode into charged current (left) and neutral current (right) components. Asimov A oscillation parameter sets are assumed (given in Table 2.2). The RMS of the charged and neutral current plots are 35.17° and 40.37° , respectively.

¹⁸⁴⁷ 6.4. Systematic Uncertainties

¹⁸⁴⁸ The systematic model parameters for this analysis are split into groups, or blocks,
¹⁸⁴⁹ depending on their purpose. They consist of flux uncertainties, neutrino-matter
¹⁸⁵⁰ interaction systematics, and detector efficiencies. There are also uncertainties on the
¹⁸⁵¹ oscillation parameters which this analysis will not be sensitive to, Δm_{12}^2 and $\sin^2(\theta_{12})$.
¹⁸⁵² These uncertainties are taken from the 2018 PDG measurements [81]. As described in
¹⁸⁵³ chapter 4, each model parameter used within this analysis requires a prior uncertainty.
¹⁸⁵⁴ This is provided via separate covariance matrices for each block. The covariance
¹⁸⁵⁵ matrices can include prior correlations between parameters within a single block, but
¹⁸⁵⁶ the separate treatment means prior uncertainties can not be included for parameters
¹⁸⁵⁷ in different groups. Some parameters in these models have no reasonably motivated
¹⁸⁵⁸ uncertainties and are assigned flat priors which do not modify the likelihood penalty.
¹⁸⁵⁹ The flux, neutrino interaction, and detector modeling simulations have already been
¹⁸⁶⁰ discussed in section 5.1 and section 5.2. The uncertainties invoked within each of these
¹⁸⁶¹ models are described below.

¹⁸⁶² 6.4.1. Beam Flux

¹⁸⁶³ The neutrino beam flux systematics is based upon the uncertainty in the modeling of
¹⁸⁶⁴ the components of the beam. This includes the hadron production model and their re-
¹⁸⁶⁵ interactions, the shape, intensity, and alignment of the beam with respect to the target,
¹⁸⁶⁶ and the uniformity of the magnetic field produced by the horn, alongside other effects.
¹⁸⁶⁷ The uncertainty, as a function of neutrino energy, is illustrated in Figure 6.6 which
¹⁸⁶⁸ includes a depiction of the total uncertainty as well as the contribution from individual
¹⁸⁶⁹ components. The uncertainty around the peak of the energy distribution ($E_\nu \sim 0.6\text{GeV}$)

¹⁸⁷⁰ is dominated by the measurements of the beam profile and alignment. Outside of this
¹⁸⁷¹ region, the uncertainties within hadron production dominate the uncertainty.

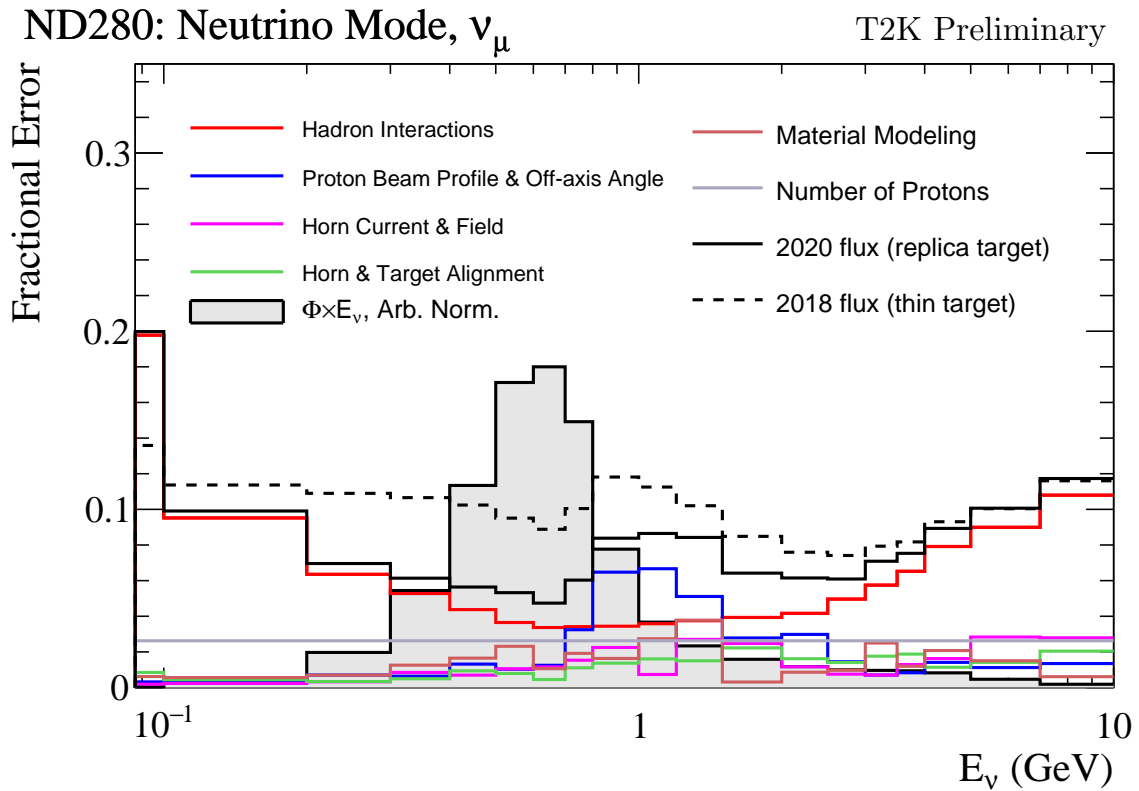


Figure 6.6.: The total uncertainty evaluated on the near detector ν_μ flux prediction constrained by the replica-target data, illustrated as a function of neutrino energy. The solid(dashed) line indicates the uncertainty used within this analysis(the T2K 2018 analysis [201]). The solid histogram indicates the neutrino flux as a function of energy. Figure taken from [202].

¹⁸⁷² The beam flux uncertainties are described by one hundred parameters. They are
¹⁸⁷³ split between the ND280 and SK detectors and binned by neutrino flavour: ν_μ , $\bar{\nu}_\mu$, ν_e
¹⁸⁷⁴ and $\bar{\nu}_e$. The response is then broken down as a function of neutrino energy. The bin
¹⁸⁷⁵ density in the neutrino energy is the same for the ν_μ in FHC and $\bar{\nu}_\mu$ in RHC beams,
¹⁸⁷⁶ and narrows for neutrino energies close to the oscillation maxima of $E_\nu = 0.6\text{GeV}$.
¹⁸⁷⁷ This binning is specified in Table 6.5. All of these systematic uncertainties are applied
¹⁸⁷⁸ as normalisation parameters with Gaussian priors centered at 1.0 and error specified
¹⁸⁷⁹ from a covariance matrix provided by the T2K beam group [202].

Neutrino Flavour	Sign	Neutrino Energy Bin Edges (GeV)
μ	Right	0., 0.4, 0.5, 0.6, 0.7, 1., 1.5, 2.5, 3.5, 5., 7., 30.
μ	Wrong	0., 0.7, 1., 1.5, 2.5, 30.
e	Right	0., 0.5, 0.7, 0.8, 1.5, 2.5, 4., 30.
e	Wrong	0., 2.5, 30.

Table 6.5.: The neutrino energy binning for the different neutrino flavours. “Right” sign indicates neutrinos in the FHC beam and antineutrinos in the RHC beam. “Wrong” sign indicates antineutrinos in the FHC beam and neutrinos in the RHC beam. The binning of the detector response is identical for the FHC and RHC modes as well as at ND280 and SK.

1880 6.4.2. Atmospheric Flux

1881 The atmospheric neutrino flux is modeled by the HKKM model [43]. 16 systematic
 1882 uncertainties are applied to control the normalisation of each neutrino flavour, energy,
 1883 and direction. All of the parameters are given Gaussian priors centered at 0 and width
 1884 equal to one. They are summarised below:

- 1885 • **Absolute Normalisation:** The overall normalisation of each neutrino flavour is
 1886 controlled by two independent systematic uncertainties, for $E_\nu < 1\text{GeV}$ and $E_\nu >$
 1887 1GeV , respectively. This is driven mostly by hadronic interaction uncertainties for
 1888 the production of pions and kaons [43]. The strength of the response is dependent
 1889 upon the neutrino energy.
- 1890 • **Relative Normalisation:** Uncertainties on the ratio of $(\nu_\mu + \bar{\nu}_\mu) / (\nu_e + \bar{\nu}_e)$ are
 1891 controlled by the difference between the HKKM model [43], FLUKA [46] and
 1892 Bartol models [42]. Three independent parameters are applied in the energy
 1893 ranges: $E_\nu < 1\text{GeV}$, $1\text{GeV} < E_\nu < 10\text{GeV}$, and $E_\nu > 10\text{GeV}$.
- 1894 • **$\nu/\bar{\nu}$ Normalisation:** The uncertainties in the π^+/π^- (and kaon equivalent) pro-
 1895 duction uncertainties in the flux of $\nu/\bar{\nu}$. The response is applied using the same
 1896 methodology as the relative normalisation parameters.

1897 • **Up/Down and Vertical/Horizontal Ratio:** Similar to the above two systematics,
1898 the difference between the HKKM, FLUKA, and Bartol model predictions, as a
1899 function of $\cos(\theta_Z)$, is used to control the normalisation of events as a function of
1900 zenith angle.

1901 • **K/π Ratio:** Higher energy neutrinos ($E_\nu > 10\text{GeV}$) become dependent upon
1902 kaon decay as the dominant source of neutrinos. Measurements of the ratio of
1903 K/π [203] are used to control the systematic uncertainty of the expected ratio of
1904 pion and kaon production.

1905 • **Solar Activity:** As the 11-year solar cycle can affect the Earth's magnetic field,
1906 the flux of primary cosmic rays varies across the same period. The uncertainty is
1907 calculated by taking a ± 1 year variation, equating to a 10% uncertainty for the
1908 SK-IV period.

1909 • **Atmospheric Density:** The height of the interaction of the primary cosmic rays is
1910 dependent upon the atmospheric density. The HKKM assumes the US standard
1911 1976 [153] profile. This systematic controls the uncertainty in that model.

1912 Updates to the HKKM and Bartol models are underway [158] to use a similar
1913 tuning technique to that used in the beam flux predictions. After those updates, it may
1914 be possible to include correlations in the hadron production uncertainty systematics
1915 for beam and atmospheric flux predictions.

1916 6.4.3. Neutrino Interaction

1917 The neutrino interactions which occur within all the detectors are modeled by NEUT.
1918 The two independent oscillation analyses, T2K-only [204] and the SK-only [52], have
1919 developed separate interaction models. To leverage the most sensitivity out of this
1920 simultaneous beam and atmospheric analysis, a correlated interaction model has been

1921 defined. Where applicable, correlations allow the systematic uncertainties applied to
1922 the atmospheric samples to be constrained by measurements of the near detector in
1923 the beam experiment. This can lead to stronger sensitivity to oscillation parameters as
1924 compared to an uncorrelated model.

1925 The low energy T2K systematic model has a more sophisticated treatment of CCQE,
1926 CCMEC, and CCRES uncertainties which is due to the purpose-made cross-section
1927 measurements made by the near detector. Furthermore, extensive comparisons of this
1928 model have been performed to external data [204]. However, the model is not designed
1929 for high-energy atmospheric events, like those illustrated in Figure 5.11. Therefore
1930 the high energy systematic model from the SK-only analysis is implemented for the
1931 relevant multiGeV, PC, and up- μ samples. The CCQE systematic parameters invoked
1932 within the SK high energy model are actually contained within T2K's CCQE model.
1933 Consequently, the more sophisticated CCQE and CCMEC T2K model parameters
1934 have been incorporated into the high energy model but are uncorrelated from the low
1935 energy counterparts.

1936 The high energy systematic model includes parameters developed from com-
1937 parisons of Nieves and Rein-Seghal models which affect resonant pion producing
1938 interactions, comparisons of the GRV98 and CKMT models which control DIS interac-
1939 tions, and hadron multiplicity measurements which modulate the normalisation of
1940 multi-pion producing events. The uncertainty of the ν_τ cross-section is particularly
1941 large and is controlled by a 25% normalisation uncertainty. These parameters are
1942 applied via normalisation or shape parameters. The former linearly scales the weight
1943 of all affected Monte-Carlo events, whereas the latter can increase or decrease a partic-
1944 ular event's weight depending on its neutrino energy and mode of interaction. The
1945 response of the shape parameters is defined by third-order polynomial splines which
1946 return a weight for a particular neutrino energy. To reduce computational resources

for the far detector fit, the response is binned by neutrino energy and sample binning: lepton momentum and cosine zenith binning for atmospheric splined responses and reconstructed neutrino energy and direction binning for beam samples. In total, 17 normalisation and 15 shape parameters are included in the high-energy model within this analysis.

Figure 6.7 indicates the predicted neutrino energy distribution for both beam and subGeV atmospheric samples. There is clearly significant overlap in neutrino energy between the subGeV atmospheric and beam samples, allowing similar kinematics in the final state particles. Figure 6.8 illustrates the fractional contribution of the different interaction modes per sample.

Comparing beam and atmospheric samples which target CCQE interactions (S.G. e-like 0de, S.G. μ -like [0,1]de, [FHC,RHC] 1R μ -like and [FHC,RHC] 1R e-like samples), there is a very similar contribution of CCQE, CC 2p2h, and CC1 π^\pm interactions. The samples which target CC1 π^\pm interactions, (S.G. e-like 0de, S.G. μ -like 2de and FHC 1R+1d.e e-like) also consist of very similar mode interactions.

As a consequence of the similarity in energy and mode contributions, correlating the systematic model between the beam and subGeV atmospheric samples ensures that this analysis attains the largest sensitivity to oscillation parameters while still ensuring neutrino interaction systematics are correctly accounted for. Due to its more sophisticated CCQE and 2p2h model, the T2K systematic model was chosen as the basis of the correlated model.

The T2K systematic model [204] is applied in a similar methodology to the SK model parameters. It consists of 19 shape parameters and 24 normalisation parameters. Four additional parameters, which model the uncertainty in the binding energy, are applied in a way to shift the momentum of the lepton emitted from a nucleus. This controls the uncertainty specified on the 27MeV binding energy assumed within Equation 6.2.

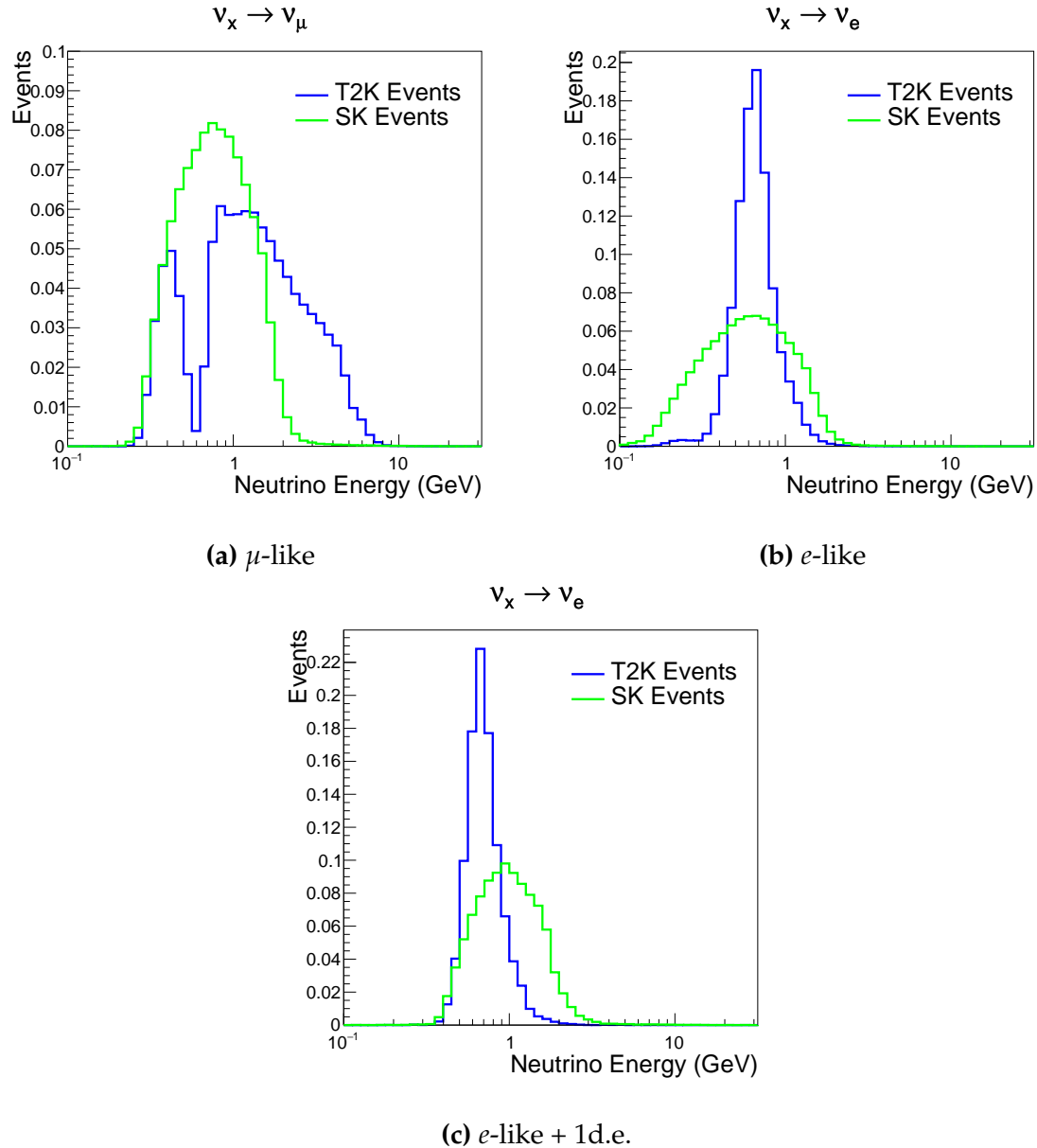


Figure 6.7.: The predicted neutrino energy distribution for subGeV atmospheric and beam samples. FHC and RHC beam samples are summed together Asimov A oscillation parameters are assumed (given in Table 2.2). Beam and atmospheric samples with similar cuts are compared against one another.

¹⁹⁷³ The majority of these parameters are assigned a Gaussian prior uncertainty. Those
¹⁹⁷⁴ that have no reasonably motivated uncertainty, or those which have not been fit to
¹⁹⁷⁵ external data, are assigned a flat prior which does not affect the penalty term.

¹⁹⁷⁶ There are three particular tunes of the T2K flux and low energy cross section model
¹⁹⁷⁷ typically considered. Firstly, the “generated” tune which is the set of dial values with

	CC QE	CC 2p2h	CC $1\pi^\pm$	CC $M\pi$	CC Other	NC π^0	NC $1\pi^\pm$	NC $M\pi$	NC Coh.	NC Other
FHC 1R+1d.e. e-like	0.04	0.02	0.83	0.03	0.04	0.01	0.01	0.01	0.00	0.01
RHC 1R e-like	0.62	0.12	0.11	0.01	0.02	0.06	0.01	0.01	0.01	0.04
FHC 1R e-like	0.68	0.12	0.10	0.00	0.02	0.04	0.01	0.00	0.00	0.02
RHC 1R μ -like	0.62	0.13	0.17	0.02	0.03	0.00	0.02	0.00	0.00	0.00
FHC 1R μ -like	0.62	0.12	0.16	0.02	0.03	0.00	0.03	0.00	0.00	0.00
S.G. π^0 -like	0.05	0.01	0.02	0.00	0.01	0.68	0.06	0.07	0.06	0.04
S.G. μ -like 2de	0.04	0.01	0.80	0.10	0.04	0.00	0.00	0.00	0.00	0.00
S.G. μ -like 1de	0.72	0.11	0.12	0.01	0.02	0.00	0.01	0.00	0.00	0.00
S.G. μ -like 0de	0.68	0.11	0.10	0.01	0.02	0.01	0.05	0.01	0.00	0.02
S.G. e-like 1de	0.05	0.01	0.75	0.10	0.05	0.00	0.01	0.02	0.00	0.01
S.G. e-like 0de	0.73	0.11	0.10	0.01	0.02	0.02	0.00	0.00	0.00	0.00

Figure 6.8.: The interaction mode contribution of each sample given as a fraction of the total event rate in that sample. Asimov A oscillation parameters are assumed (given in Table 2.2). The Charged Current (CC) modes are broken into quasi-elastic (QE), 2p2h, resonant charged pion production ($1\pi^\pm$), multi-pion production ($M\pi$), and other interaction categories. Neutral Current (NC) interaction modes are given in interaction mode categories: π^0 production, resonant charged pion production, multi-pion production, and others.

which the Monte Carlo was generated. Secondly, the set of dial values which are taken from external data measurements and used as inputs. These are the “pre-fit” dial values. The reason these two sets of dial values are different is that the external data measurements are continually updated but it is very computationally intensive to regenerate a Monte Carlo prediction after each update. The final tune is the “post-fit”, “post-ND fit” or “post-BANFF” dial values. These are the values taken from a fit to the beam near detector data. This fit is performed by two independent fitting frameworks, MaCh3 and BANFF, which ensures reliable measurements. The output of each fitter is converted into a covariance matrix to describe the error and correlations between all the flux and cross-section parameters. This is then propagated to the far-detector

1988 oscillation analysis group for use in the P-Theta fitting framework. As MaCh3 can
1989 perform a near detector fit, it is included within the simultaneous fit of the far-detector
1990 beam and atmospheric oscillation analysis. This is because this technique does not
1991 require any assumption of Gaussian posterior distributions which is required in the
1992 covariance matrix methodology.

1993 On top of the combination of the SK and T2K interaction models, several other
1994 parameters have been specifically developed for the joint oscillation analysis. The
1995 majority of the atmospheric samples' δ_{CP} sensitivity comes from the normalisation
1996 of subGeV electron-like events. These are modeled using a spectral function model
1997 to approximate the nuclear ground state. However, the near detector is not able to
1998 constrain the model. Therefore, an additional systematic is introduced which models
1999 an alternative Continous Random Phase Approximation (CRPA) nuclear ground
2000 state. The reasoning is documented in [205]. As the near detector can not sufficiently
2001 constrain the model, this dial approximates the event weights if a CRPA model had
2002 been assumed rather than a spectral function. This dial only effects ν_e and $\bar{\nu}_e$ and is
2003 applied as a shape parameter.

2004 Further additions to the model have been introduced due to the inclusion of the
2005 subGeV π^0 atmospheric sample. This particularly targets charged current and neutral
2006 current π^0 producing interactions to help constrain the systematic uncertainties. There
2007 is no analogous sample in the T2K beam-only analysis so no significant effort has
2008 been placed into building a sufficient uncertainty model. Therefore, an uncertainty
2009 that affects neutral current resonant π^0 production is incorporated into this analysis.
2010 Comparisons of NEUT's NC resonant pion production predictions have been made to
2011 MiniBooNE [206] data and a consistent 16% to 21% underprediction is observed [205].
2012 Consequently, a conservative 30% normalisation parameter is invoked.

2013 Down-going events are mostly insensitive to oscillation parameters and can act
 2014 similar to the near detector within an accelerator experiment (Details will be dis-
 2015 cussed in chapter 7). This region of phase space can act as a sideband and allows the
 2016 cross-section model and near detector constraint to be studied. The distribution of
 2017 events in this region is calculated using the technique outlined in subsection 4.3.4. For
 2018 CCQE-targeting samples, the application of the near detector constraint is well within
 2019 the statistical fluctuation of the down-going data such that no significant tension is
 2020 observed between the data and the Monte Carlo prediction after the near detector
 2021 constraint is applied. This is not the case for samples with target CCRES interac-
 2022 tions. The electron-like data is consistent with the constrained prediction at high
 2023 reconstructed momenta but diverges at lower momentum, whereas the muon-like
 2024 sample is under-predicted throughout the range of momenta. To combat this disagree-
 2025 ment, an additional cross-section systematic dial, specifically designed to inflate the
 2026 low pion momentum systematics was developed in [205]. This is a shape parameter
 2027 implemented through a splined response.

2028 6.4.4. Near Detector

2029 The systematics applied due to uncertainties arising from the response of the near
 2030 detector is documented in [133]. The response is described by 574 normalisation param-
 2031 eters binned in the selected sample as well as momentum and angle, P_μ and $\cos(\theta_\mu)$,
 2032 of the final-state muon. These are applied via a covariance matrix with each parameter
 2033 being assigned a Gaussian prior from that covariance matrix. These normalisation
 2034 parameters are built from underlying systematics, e.g. pion secondary interaction
 2035 systematics, which are randomly thrown and the variation in each $P_\mu \times \cos(\theta_\mu)$ bin is
 2036 determined. Two thousand throws are evaluated and a covariance matrix response is
 2037 created. This allows significant correlations between FGD1 and FGD2 samples, as well

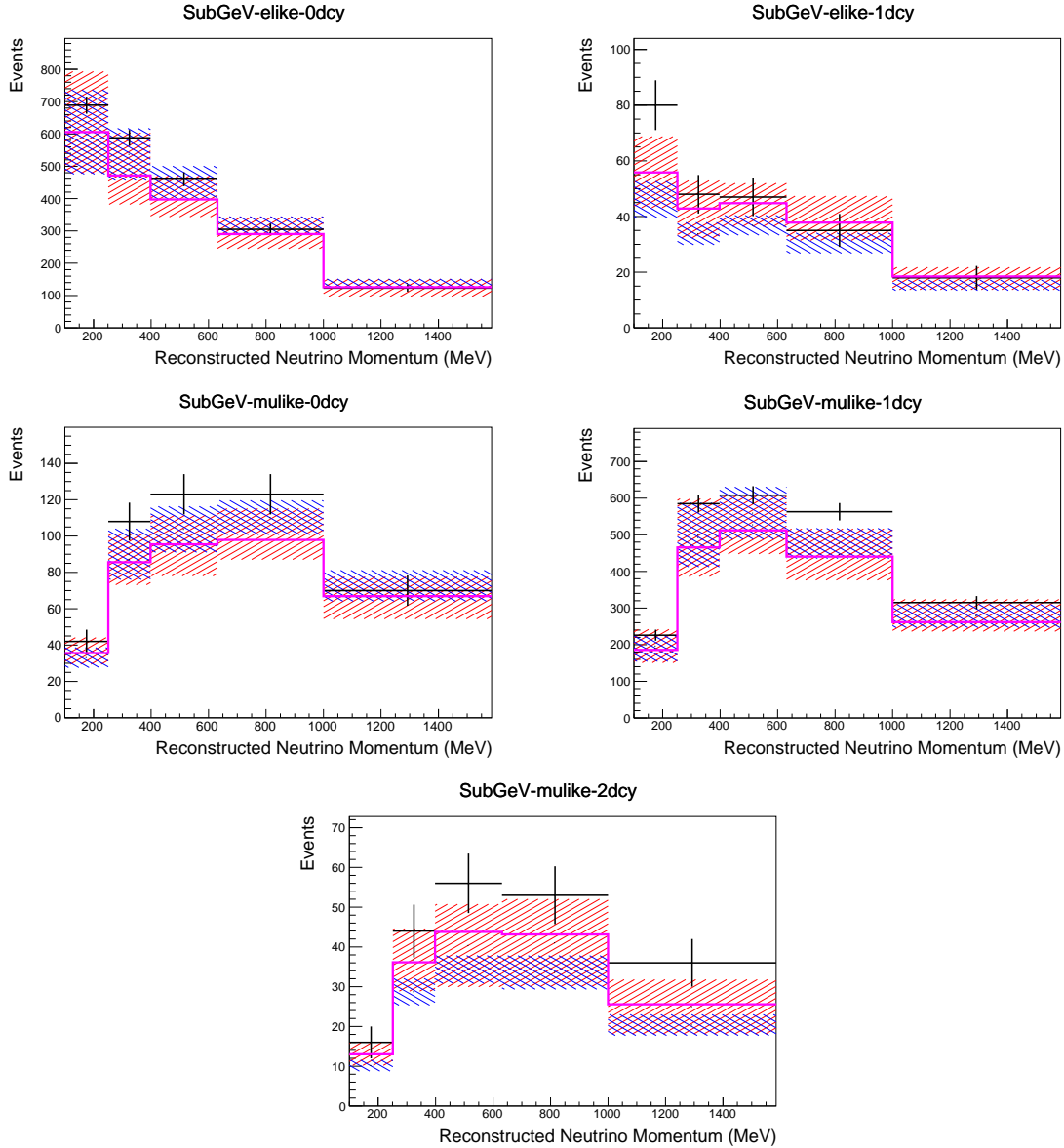


Figure 6.9.: Down-going atmospheric subGeV single-ring samples comparing the mean and error of the pre-fit and post-fit Monte Carlo predictions in red and blue, respectively. The magenta histogram illustrates the Monte Carlo prediction using the generated dial values. The black points illustrate the down-going data with statistical errors given. The mean and errors of the Monte Carlo predictions are calculated by the techniques documented in subsection 4.3.4. The pre-fit spectrum is calculated by throwing the cross-section and atmospheric flux dial values from the pre-fit covariance matrix. The post-fit spectrum is calculated by sampling the cross-section dial values from an ND fit MCMC chain, whilst still throwing the atmospheric flux dials from the pre-fit covariance.

²⁰³⁸ as adjacent $P_\mu \times \cos(\theta_\mu)$ bins. Statistical uncertainties are accounted for by including
²⁰³⁹ fluctuations of each event's weight from a Poisson distribution.

2040 Similar to the cross-section systematics, MaCh3 and BANFF are used to constrain
2041 the uncertainty of these systematics through independent validations. Each fitter
2042 generates a post-fit covariance matrix which is compared and passed to the far-detector
2043 oscillation analysis working group. As the analysis presented within this thesis uses
2044 the MaCh3 framework, a joint oscillation analysis fit of all three sets of samples and
2045 their respective systematics is performed.

2046 **6.4.5. Far Detector**

2047 Two configurations of the far detector systematic model implementation have been
2048 considered. Firstly, the far detector systematic uncertainties for beam and atmospheric
2049 samples are taken from their respective analysis inputs, denoted “official inputs” anal-
2050 ysis. Consequently, no correlations are assumed between the beam and atmospheric
2051 samples. The generation of the beam- and atmospheric-specific inputs are documented
2052 in subsubsection 6.4.5.1 and subsubsection 6.4.5.2. Secondly, a correlated detector
2053 model has been developed. Here, the distribution of parameters used for applying
2054 event cuts (e.g. electron-muon PID separation) is modified within the fit. It follows
2055 a similar methodology to the beam far detector systematics implementation but per-
2056 forms a joint fit of the beam and atmospheric data. This alternative implementation is
2057 detailed in subsubsection 6.4.5.3.

2058 **6.4.5.1. Beam Samples**

2059 There are 45 systematics which describe the response of the far detector to beam
2060 events [185], split into 44 normalisation parameters and one energy scale systematic.
2061 The energy scale systematic is applied as a multiplicative scaling of the reconstructed
2062 neutrino energy. It is described by a Gaussian, centered at one with equal to the

2063 difference in Monte Carlo to data comparisons performed in [187]. The normalisation
 2064 parameters are assigned a Gaussian error centralised at one with width taken from a
 2065 covariance matrix. A detailed breakdown of the generation of the covariance matrix
 2066 is found in [199]. To build the covariance matrix, a fit is performed on atmospheric
 2067 data which has been selected using beam sample selection cuts. These cuts use the
 2068 variables, L^i , where the index i is detailed in Table 6.6. Each L^i is a smear, α , and shift,
 2069 β parameter such that,

$$L_j^i \rightarrow \bar{L}_j^i = \alpha_j^i L + \beta_j^i \quad (6.4)$$

2070 Where L_j^i (\bar{L}_j^i) correspond to nominal(varied) PID cut parameters given in Table 6.6.
 2071 The shift and smear parameters are binned by final-state topology, j , where the binning
 2072 is given in Table 6.7. The final-state topology binning is because the detector will
 2073 respond differently to events that have one or multiple rings. For example, the detector
 2074 will be able to distinguish single-ring events better than two overlapping ring events,
 2075 resulting in smaller systematic uncertainty for one-ring events compared to two-ring
 2076 events. This approach is used to allow the cut parameter distributions to be modified
 2077 within the fit, allowing for better data to Monte Carlo agreement. Only the shape
 2078 of each of the cut variables is used within this fit, such that physics effects are not
 2079 considered.

Cut Variable	Parameter Name
0	<code>fitQun e/mu PID</code>
1	<code>fitQun e/pi0 PID</code>
2	<code>fitQun mu/pi PID</code>
3	<code>fitQun Ring-Counting Parameter</code>

Table 6.6.: List of cut variables that are included within the shift/smear fit documented in [199].

Category	Description
$1e$	Only one electron above Cherenkov threshold in the final state
1μ	Only one muon above Cherenkov threshold in the final state
$1e+other$	One electron and one or more other charged particles above Cherenkov threshold in the final state
$1\mu+other$	One muon and one or more other charged particles above Cherenkov threshold in the final state
$1\pi^0$	Only one π^0 in the final state
$1\pi^\pm$ or $1p$	Only one hadron (typically charged pion or proton) in the final state
Other	Any other final state

Table 6.7.: Reconstructed event topology categories on which the SK detector systematics [199] are based.

2080 Beyond the uncertainty on the PID cut criteria, the mis-modeling of π^0 events
 2081 is also considered. If one of the two rings from a π^0 event is missed, this will be
 2082 reconstructed as a $CC\nu_e$ -like event. This is one of the largest systematics hindering the
 2083 electron neutrino appearance analyses. Consequently, additional systematics has been
 2084 introduced to constrain the mis-modeling of π^0 events in SK, binned by reconstructed
 2085 neutrino energy. To evaluate this systematic uncertainty, a set of “hybrid- π^0 ” samples
 2086 is constructed. These events are built by overlaying one electron-like ring from the
 2087 SK atmospheric neutrino samples or decay electron ring from a stopping cosmic ray
 2088 muon with one simulated photon ring. Both rings are chosen so that momenta and
 2089 opening angle follow the decay kinematics of NC π^0 events from the T2K-MC. Hybrid-
 2090 π^0 Monte Carlo samples with both rings from the SK Monte Carlo are produced
 2091 to compare with the hybrid- π^0 data samples and the difference in the fraction of
 2092 events that pass the ν_e selection criteria is used to assign the systematic errors. In
 2093 order to investigate any data to Monte Carlo differences that may originate from
 2094 either the higher energy ring or lower energy ring, two samples are built; a sample
 2095 in which the electron constitutes the higher energy ring from the π^0 decay called the
 2096 primary sample and another one in which it constitutes the lower energy ring called

2097 the secondary sample. The standard T2K ν_e fiTQun event selection criteria are used to
2098 select events.

2099 Final contributions to the covariance matrix are determined by supplementary
2100 uncertainties attained by comparing stopping muon data to Monte Carlo prediction,
2101 as first introduced in section 5.2. The efficiency of tagging decay electrons is estimated
2102 by the stopping muon data to Monte Carlo differences by comparing the number
2103 of one decay electron events to the number of events with one or fewer decay elec-
2104 trons. Similarly, the rate at which fake decay electrons are reconstructed by fiTQun
2105 is estimated by comparing the number of two decay electron events to the number
2106 of events with one or two reconstructed decay electrons. The two sources of sys-
2107 tematics are added in quadrature weighted by the number of events with one true
2108 decay electron yielding a 0.2% systematic uncertainty. A fiducial volume systematic of
2109 $\pm 2.5\text{cm}$ which corresponds to a 0.5% shift in the normalisation of events. Additional
2110 normalisation uncertainties based on neutrino flavour and interaction mode are also
2111 defined in [185, 207, 208].

2112 Two additional sources of uncertainty are included: secondary and photo-nuclear
2113 interactions. These are estimated by varying the underlying parameters are building a
2114 distribution of sample event rates. These contributions are then added in quadrature
2115 to the above covariance matrix.

2116 6.4.5.2. Atmospheric Samples

2117 The systematic parameters which control the detector systematics for atmospheric
2118 samples, documented in [89], are split into two sub-groups. Those which are related
2119 to particle identification and ring counting systematics and those which are related to
2120 calibration, separation, and reduction uncertainties.

2121 The particle identification systematics consist of five parameters. The ring separation systematic enforces an anti-correlated response between the single-ring and
 2122 multi-ring samples. This is implemented as a fractional increase/decrease in the
 2123 overall normalisation of each sample, depending on the distance to the nearest wall
 2124 from an event's vertex. The coefficients of the normalisation are estimated prior to the
 2125 fit and depend on the particular atmospheric sample. The single-ring and multi-ring
 2126 PID systematics encode the detector's ability to separate electron-like and muon-like
 2127 events and are implemented in a similar way to the ring separation systematic.
 2128

2129 The multi-ring electron-like separation likelihood, discussed in section 6.1, encodes
 2130 the ability of the detector to separate neutrino from anti-neutrino events. As an impor-
 2131 tant systematic in the mass hierarchy determination, systematic uncertainties control
 2132 the relative normalisations of the ν_e and $\bar{\nu}_e$ enriched samples. Two normalisation
 2133 parameters are implemented which vary the event rate of each multi-ring sample,
 2134 whilst ensuring the total event rate is conserved.

2135 There are 22 systematics related to calibration measurements, including effects
 2136 from backgrounds, reduction, and showering effects. They are documented in [89] and
 2137 briefly summarised in Table 6.8. They are applied via normalisation parameters, with
 2138 the separation systematics requiring the conservation of event rate across all samples.

2139 **6.4.5.3. Correlated Detector Model**

2140 A complete uncertainty model of the SK detector would be able to determine the
 2141 systematic shift on the sample spectra for a variation of the underlying parameters,
 2142 e.g. PMT angular acceptance. However, this is computationally intensive, requiring
 2143 Monte Carlo predictions to be made for each plausible variation. Consequently, an
 2144 effective parameter model has been utilised for a correlated detector model following
 2145 from the T2K-only model implementation documented in subsubsection 6.4.5.1. The

Table 6.8.: Sources of systematic errors specified within the grouped into the “calibration” systematics model.

Index	Description
0	Partially contained reduction
1	Fully contained reduction
2	Separation of fully contained and partially contained events
3	Separation of stopping and through-going partially contained events in top of detector
4	Separation of stopping and through-going partially contained events in barrel of detector
5	Separation of stopping and through-going partially contained events in bottom of detector
6	Background due to cosmic rays
7	Background due to flasher events
8	Vertex systematic moving events into and out of fiducial volume
9	Upward going muon event reduction
10	Separation of stopping and through-going in upward going muon events
11	Energy systematic in upward going muon events
12	Reconstruction of the path length of upward going muon events
13	Separation of showering and non-showering upward going muon events
14	Background of stopping upward going muon events
15	Background of non-showering through-going upward going muon events
16	Background of showering through-going upward going muon events
17	Efficiency of tagging two rings from π^0 decay
18	Efficiency of decay electron tagging
19	Background from downgoing cosmic muons
20	Asymmetry of energy deposition in tank
21	Energy scale deposition

²¹⁴⁶ implementation performs a simultaneous fit of detector and oscillation parameters,
²¹⁴⁷ for the detector parameters given in Table 6.6.

²¹⁴⁸ The correlated detector model utilises the same smear and shift parameters docu-
²¹⁴⁹ mented in subsubsection 6.4.5.1, split by final state topology. Beyond this, the shift
²¹⁵⁰ and smear parameters are split by visible energy deposited within the detector, with

binning specified in Table 6.9. This is because atmospheric events are categorised by subGeV and multiGeV events based on visible energy, so this splitting is required when correlating the systematic model for beam and atmospheric events. Alongside the technical requirement, higher energy events will be better reconstructed due to fractionally less noise within the detector. This implementation correlates the detector systematics between the far-detector beam and subGeV atmospheric samples due to their similar energies and interaction types. As a result of the inclusion of visible energy binning, Equation 6.4 becomes

$$L_{jk}^i \rightarrow \bar{L}_{jk}^i = \alpha_{jk}^i L + \beta_{jk}^i, \quad (6.5)$$

where k is the visible energy bin. As there are no equivalent beam samples, the multiGeV, multiring, PC, and Up- μ samples will be subject to the ATMPD particle identification systematics implementation as described in subsubsection 6.4.5.2 rather than using this correlated detector model. The calibration systematics also described in the aforementioned chapter still apply to all atmospheric samples.

Index	Range (MeV)
0	$30 \geq x > 300$
1	$300 \geq x > 700$
2	$700 \geq x > 1330$
3	$1330 \geq x$

Table 6.9.: Visible energy binning for which the correlated SK detector systematics are based

The implementation of this systematic model takes the events reconstructed values of the cut parameters, modifies them by the particular shift and smear parameter for that event, and then re-applies event selection. This invokes event migration, which is

2167 a new feature incorporated into the MaCh3 framework which is only achievable due
2168 to the event-by-event reweighting scheme.

2169 Particular care has to be taken when varying the ring counting parameter. This
2170 is because the number of rings is a finite value (one-ring, two-rings, etc.) which can
2171 not be continuously varied through this shift and smear technique. Consequently a
2172 ring counting parameter, RC_i , is calculated for the i^{th} event, following the definition
2173 in [184]. The likelihood from all considered one-ring (L_{1R}) and two-ring (L_{2R}) fits
2174 are compared to determine the preferred hypothesis. The difference is computed as
2175 $\Delta_{LLH} = \log(L_{1R}) - \log(L_{2R})$. The ring counting parameter is then defined as,

$$RC_i = \text{sgn}(\Delta_{LLH}) \times \sqrt{|\Delta_{LLH}|}, \quad (6.6)$$

2176 where $\text{sgn}(x) = x/|x|$. This ring counting parameter corresponds to an intermedi-
2177 ate likelihood value used within the `fitQun` algorithm to decide the number of rings
2178 associated with a particular event. However, fake-ring merging algorithms are applied
2179 after this likelihood value is used. Consequently, this ring counting parameter does
2180 not always exactly correspond to the number of reconstructed rings. This can be seen
2181 in Figure 6.10.

2182 As the `fitQun` algorithm does not provide a likelihood value after the fake-ring
2183 algorithms have been applied, the ring counting parameter distribution is correlated to
2184 the final number of reconstructed rings through “maps”. These are two-dimensional
2185 distributions of the ring counting parameter and the final number of reconstructed
2186 rings. An example is illustrated in Figure 6.11. In principle, the `fitQun` reconstruction
2187 algorithm should be re-run after the variation in the ring counting parameter. However,

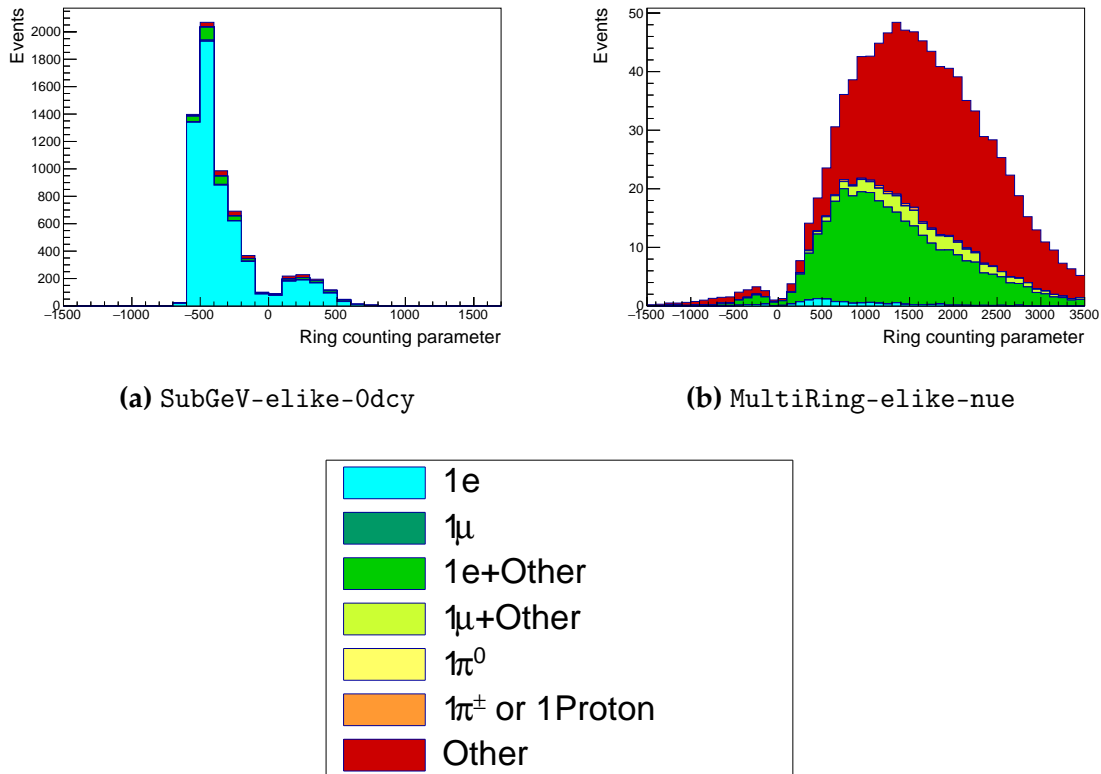


Figure 6.10.: The ring counting parameter as defined in Equation 6.6 for the SubGeV-*elike*-0dcy and MultiRing-*elike*-*nue* samples.

²¹⁸⁸ this is not computationally viable. Therefore the “maps” are used as a reweighting
²¹⁸⁹ template.

The maps are split by final state topology and true neutrino flavour and all fitQun
 -reconstructed Monte Carlo events are used to fill them. The maps are row-normalised
 to represent the probability of X number of rings for a given RC_i value. Prior to the
 fit, an event's nominal weight is calculated as $W^i(N_{Rings}^i, L_{jk}^i)$, where N_{Rings}^i is the
 reconstructed number of rings for the i^{th} event and $W^i(x, y)$ is the bin content in map
 associated with the i^{th} event, where x number of rings and y is ring counting parameter.
 Then during the fit, the value of $R = W^i(N_{Rings}^i, \bar{L}_{jk}^i) / W^i(N_{Rings}^i, L_{jk}^i)$ is calculated as
 the event weight for the i^{th} event. This is the only cut variable that uses a reweighting
 scheme rather than event migration.

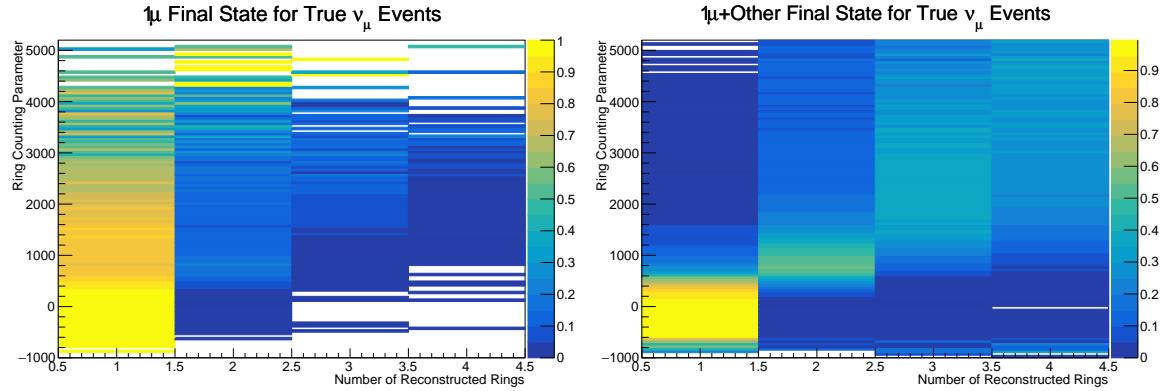


Figure 6.11.: The ring counting parameter, defined in Equation 6.6, as a function of the number of reconstructed rings as found by the `fitQun` reconstruction algorithm. Left: true ν_μ events with only one muon above the Cherenkov threshold in the final state. Right: true ν_μ events with one muon and at least one other charged particle above the Cherenkov threshold in the final state.

2199 The π^0 systematics introduced in subsection 6.4.4 are applied via a covariance
 2200 matrix. This is not possible in the alternative model as no covariance matrix is used.
 2201 Thus, the implementation of the π^0 systematics has been modified. The inputs from
 2202 the hybrid π^0 sample is included via the use of “ χ^2 maps”, which are two-dimensional
 2203 histograms in α_{jk}^i and β_{jk}^i parameters over some range. Illustrative examples of the χ^2
 2204 maps are given in Figure 6.12. Due to their nature, the shift and smear parameters are
 2205 typically very correlated. A map is produced for each cut parameter given in Table 6.6
 2206 and for each visible energy bin given in Table 6.9.

2207 The maps are filled through the χ^2 comparison of the hybrid π^0 Monte Carlo and
 2208 data in the particle identification parameters documented in Table 6.6. The Monte
 2209 Carlo distribution is modified by the α_{jk}^i and β_{jk}^i scaling, whilst cross-section and flux
 2210 nuisance parameters are thrown from their prior uncertainties. The χ^2 between the
 2211 scaled Monte Carlo and data is calculated and the relevant point in the χ^2 map is filled.

2212 The implementation within this alternative detector model is to add the bin contents
 2213 of the maps, for the relevant values of the α_{jk}^i and β_{jk}^i parameters, to the likelihood
 2214 penalty. Only $1\pi^0$ final state topology shift and smear parameters use this prior
 2215 uncertainty.

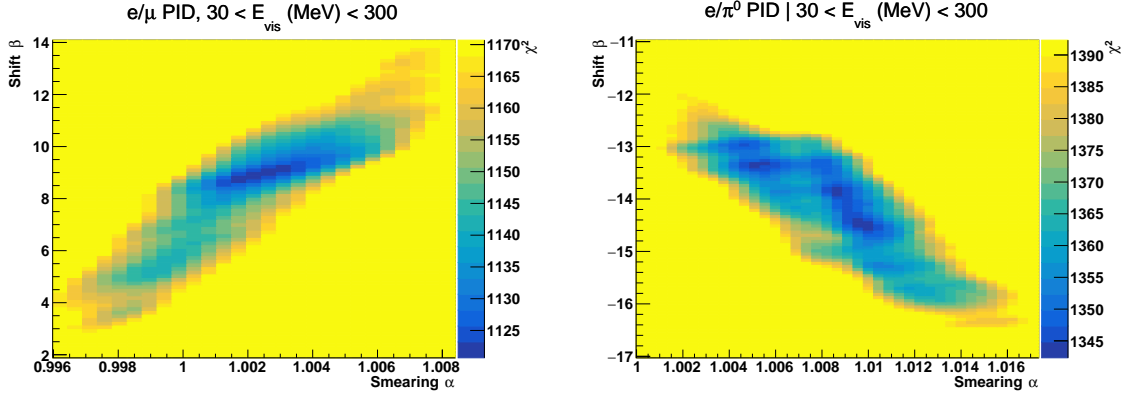


Figure 6.12.: The χ^2 between the hybrid- π^0 Monte Carlo and data samples, as a function of smear (α) and shift (β) parameters, for events which have $1\pi^0$ final state topology. Left: Electron-muon separation PID parameter for events with $30 \geq E_{vis}(\text{MeV}) < 300$. Right: Electron- π^0 separation PID parameter for events with $30 \geq E_{vis}(\text{MeV}) < 300$.

Similarly, the implementation of the supplementary systematics documented in subsubsection 6.4.5.1 needs to be modified. A new framework [209] was built in tandem with the T2K-SK working group [185] so the additional parameters can be incorporated into the MaCh3 framework. These are applied as normalisation parameters, depending on the particular interaction mode, number of tagged decay electrons, and whether the primary particle generated Cherenkov light. They are assigned Gaussian uncertainties with widths described by a covariance matrix. Furthermore, the secondary interaction and photo-nuclear effects need to be accounted for in this detector model using a different implementation than that in subsubsection 6.4.5.1. This was done by including a shape parameter for each of the secondary interactions and the photo-nuclear systematic parameters.

There are a total of 224 α_{jk}^i and β_{jk}^i parameters, of which 32 have prior constraints from the hybrid π^0 samples.

One final complexity of this correlated detector model is that the two sets of samples, beam and subGeV atmospheric, use slightly different parameters to distinguish electron and muon-like events. The T2K samples use the value of $\log(L_e/L_\mu)$ whereas the atmospheric samples use the value of $\log(L_e/L_\pi)$, where L_X is the likelihood for

2233 hypothesis X. This is because the T2K fits use single-ring `fitQun` fitting techniques,
 2234 whereas multi-ring fits are applied to the atmospheric samples where only the electron
 2235 and pion hypothesis are considered. The correlation between the two likelihood ratios
 2236 is illustrated in Figure 6.13. As discussed in section 5.2, the pion hypothesis is a very
 2237 good approximation of the muon hypothesis due to their similar mass. Consequently,
 2238 using the same shift and smear parameters correlated between the beam and subGeV
 2239 atmospheric samples is deemed a good approximation.

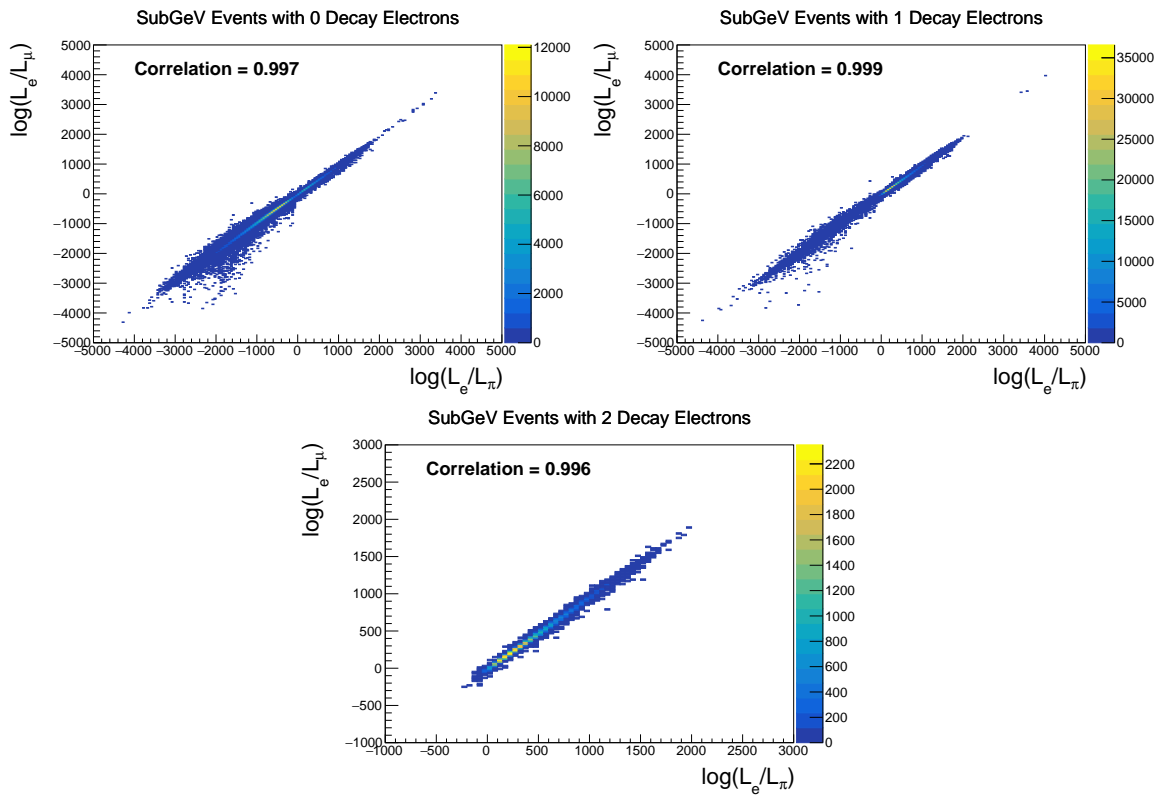


Figure 6.13.: The distribution of $\log(L_e/L_\mu)$ compared to $\log(L_e/L_\pi)$ for subGeV events with zero (top left), one (top right) or two (bottom) decay electrons. The correlation in the distribution is calculated as 0.997, 0.999 and 0.996, respectively.

2240

Chapter 7

2241

Oscillation Probability Calculation

2242 It is important to understand how and where the sensitivity to the oscillation pa-
2243 rameters comes from for both atmospheric and beam samples. An overview of how
2244 these samples observe changes in δ_{CP} , Δm_{23}^2 , and $\sin^2(\theta_{23})$ is given in section 7.1. It
2245 also explains the additional complexities involved when performing an atmospheric
2246 neutrino analysis as compared to a beam-only analysis.

2247 Without additional techniques, atmospheric sub-GeV upward-going neutrinos
2248 ($E_\nu < 1.33\text{GeV}, \cos(\theta_Z) < 0.$) can artificially inflate the sensitivity to δ_{CP} due to the
2249 quickly varying oscillation probability in this region. Therefore, a “sub-sampling”
2250 approach has been developed to reduce these biases ensuring accurate and reliable
2251 sensitivity measurements. This technique ensures that small-scale unresolvable fea-
2252 tures of the oscillation probability have been averaged over whilst the large-scale
2253 features in the oscillation probability are unaffected. The documentation and valida-
2254 tion of this technique are found in section 7.2. The oscillation probability calculation is
2255 computationally intensive due to the large number of matrix multiplications needed.
2256 Consequently, the CUDAProb3 implementation choice made within the fitting frame-
2257 work, as detailed in section 7.3, ensures that the analysis can be done in a timely
2258 manner.

2259 Whilst the beam neutrinos are assumed to propagate through a constant density
2260 slab of material, the density variations through the Earth result in more complex
2261 oscillation patterns. Furthermore, the uncertainty in the electron density can modify
2262 the oscillation probability for the denser core layers of the Earth. The model of the

2263 Earth used within this analysis is detailed in section 7.4. This includes information
2264 about the official SK-only methodology as well as improvements that can be made
2265 to remove some of the approximations made in that analysis. Another complexity of
2266 atmospheric neutrinos oscillation studies is that the height of production in the atmo-
2267 sphere is not known on an event-by-event basis. An analytical averaging technique
2268 that approximates the uncertainty of the oscillation probability has been followed,
2269 with the author of this thesis being responsible for the implementation and validation.
2270 This implementation of an external technique is illustrated in section 7.5.

2271 7.1. Overview

2272 DB: Should this be moved into an earlier chapter? The selections chapter references
2273 the matter resonance which has not yet been explained at that point

2274 The analysis presented within this thesis focuses on the determination of oscillation
2275 parameters from atmospheric and beam neutrinos. Whilst subject to the same oscil-
2276 lation formalism, the way in which the two samples have sensitivity to the different
2277 oscillation parameters differs quite significantly.

2278 Atmospheric neutrinos have a varying baseline, or “path length”, L , such that
2279 the distance each neutrino travels before interacting is dependent upon the zenith
2280 angle, θ_Z . As primary cosmic rays can interact anywhere between the Earth’s surface
2281 and $\sim 50\text{km}$ above that, the height, h , in the atmosphere at which the neutrino was
2282 generated also affects the path length,

$$L = \sqrt{(R_E + h)^2 - R_E^2 (1 - \cos^2(\theta_Z))} - R_E \cos(\theta_Z). \quad (7.1)$$

2283 Where $R_E = 6,371\text{km}$ is the Earth's radius. Consequently, the oscillation probability
2284 is dependent upon two parameters, $\cos(\theta_Z)$ and E_ν .

2285 The oscillation probability used within this analysis is based on [21]. The neutrino
2286 wavefunction in the vacuum Hamiltonian evolves in each layer of constant matter
2287 density via

$$i \frac{d\psi_j(t)}{dt} = \frac{m_j^2}{2E_\nu} \psi_j(t) - \sum_k \sqrt{2} G_F N_e U_{ej} U_{ke}^\dagger \psi_k(t), \quad (7.2)$$

2288 where m_j^2 is the square of the j^{th} vacuum eigenstate mass, E_ν is the neutrino
2289 energy, G_F is Fermi's constant, N_e is the electron number density and U is the PMNS
2290 matrix. The transformation $N_e \rightarrow -N_e$ and $\delta_{CP} \rightarrow -\delta_{CP}$ is applied for antineutrino
2291 propagation. Thus, a model of the Earth's density is required for atmospheric neutrino
2292 propagation. Following the official SK-only methodology [210], this analysis uses the
2293 Preliminary Reference Earth Model (PREM) [211]. This model provides piecewise cubic
2294 polynomials as a function of the Earth's radius which results in the density profile
2295 illustrated in Figure 7.1. As discussed, the propagator requires layers of constant
2296 density. The SK methodology approximates the PREM model by using four layers of
2297 constant density [210]. The details of these layers are detailed in Table 7.1.

Layer	Outer Radius [km]	Density [g/cm^3]	Chemical composition (Z/A)
Inner Core	1220	13	0.468 ± 0.029
Outer Core	3480	11.3	0.468 ± 0.029
Lower Mantle	5701	5.0	0.496
Transition Zone	6371	3.3	0.496

Table 7.1.: Description of the four layers of the Earth invoked within the constant density approximation of the PREM model [211].

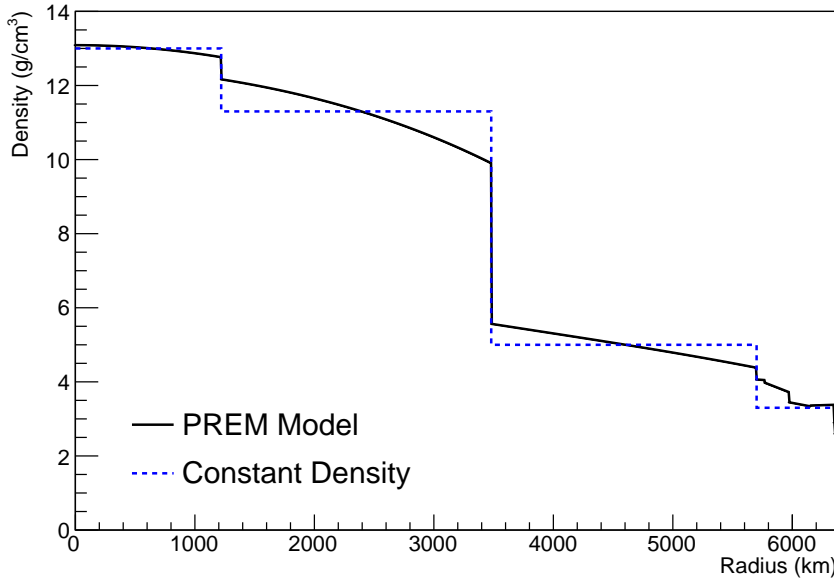


Figure 7.1.: The density of the Earth given as a function of the radius, as given by the PREM model (Black), and the constant density four-layer approximation (Blue), as used in the official SK-only analysis.

2298 The atmospheric neutrino oscillation probabilities can be presented as two dimen-
 2299 sional “oscillograms” as illustrated in Figure 7.2. The distinct discontinuities, as a
 2300 function of $\cos(\theta_Z)$, are due to the discrete change in density invoked within the PREM
 2301 model.

2302 Atmospheric neutrinos do have sensitivity to δ_{CP} through a normalisation term.
 2303 Figure 7.3 illustrates the difference in oscillation probability between CP-conserving
 2304 ($\delta_{CP} = 0$) and a CP-violating ($\delta_{CP} = -1.601$) value taken from Asimov A oscillation
 2305 parameter set (Table 2.2). The result is a complicated oscillation pattern in the appear-
 2306 ance probability for sub-GeV upgoing neutrinos. The detector does not have sufficient
 2307 resolution to resolve these individual patterns so the sensitivity to δ_{CP} for atmospheric
 2308 neutrinos comes via the overall normalisation of these events.

2309 The presence of matter means that the effect δ_{CP} has on the oscillation probability
 2310 is not equal between neutrinos and antineutrinos, which would be expected when
 2311 propagating through a vacuum. This is further extenuated by the fact that SK can

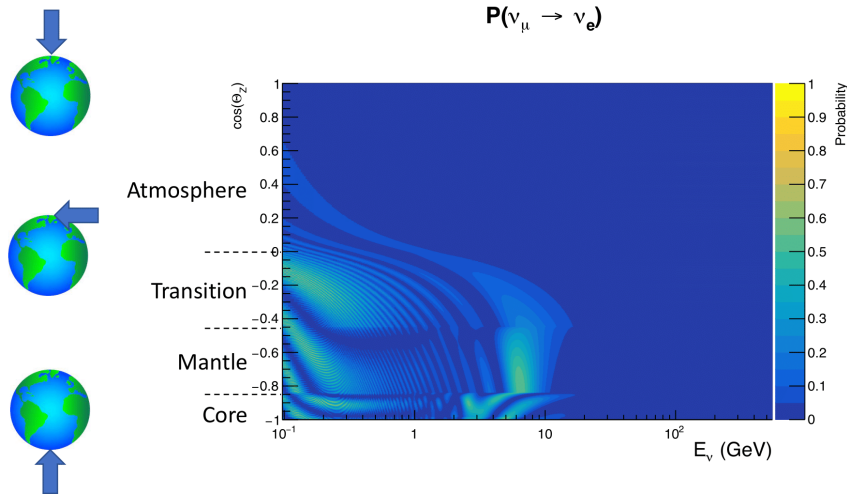


Figure 7.2.: An “oscillogram” that depicts the $P(\nu_\mu \rightarrow \nu_e)$ oscillation probability as a function of neutrino energy and cosine of the zenith angle. The zenith angle is defined such that $\cos(\theta_Z) = 1.0$ represents neutrinos that travel from directly above the detector. The four-layer constant density PREM model approximation is used and Asimov A oscillation parameters are assumed (Table 2.2).

not distinguish neutrinos and antineutrinos well and that the cross-section neutrino interaction is larger than that for antineutrinos. Finally, sample selections (discussed in section 6.1) targeting different neutrino interaction modes result in an imbalance in the percentage of neutrinos to anti-neutrinos. This is because negatively charged pions from antineutrino interactions are more likely to be captured by a nucleus compared to a positively charged pion. All of these effects lead to a difference in the number of neutrinos detected compared to antineutrinos. This changes how the δ_{CP} normalisation term is observed, resulting in a very complex sensitivity to δ_{CP} .

Atmospheric neutrinos are subject to matter effects as they travel through the dense matter in the Earth. The vacuum and matter oscillation probabilities for $P(\nu_e \rightarrow \nu_e)$ and $P(\bar{\nu}_e \rightarrow \bar{\nu}_e)$ are presented in Figure 7.4, where the PREM model has been assumed. The oscillation probability for both neutrinos and antineutrinos is affected in the presence of matter. However, the resonance effects around $O(5)$ GeV only occur for neutrinos in normal mass hierarchy and antineutrinos in inverse mass hierarchy. The

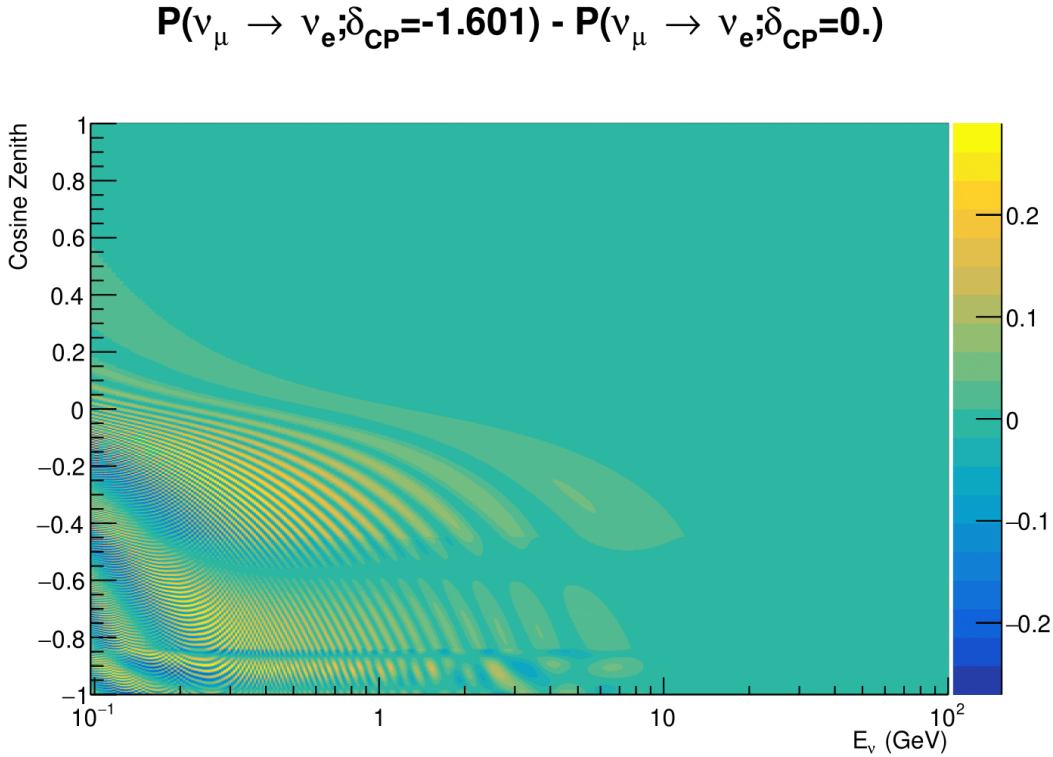


Figure 7.3.: The effect of δ_{CP} for atmospheric neutrinos given in terms of the neutrino energy and zenith angle. This oscillogram compares the $P(\nu_\mu \rightarrow \nu_e)$ oscillation probability for a CP conserving ($\delta_{CP} = 0.0$) and a CP violating ($\delta_{CP} = -1.601$) value taken from the Asimov A parameter set. The other oscillation parameters assume the Asimov A oscillation parameter set given in Table 2.2.

exact position and amplitude of the resonance depend on $\sin^2(\theta_{23})$ meaning that the atmospheric neutrinos have sensitivity to $\sin^2(\theta_{23})$.

As the T2K beam flux is centered at the first oscillation maximum ($E_\nu = 0.6\text{GeV}$), the sensitivity to δ_{CP} is predominantly observed as a change in the event-rate of e-like samples in $\nu/\bar{\nu}$ modes. Figure 7.5 illustrates the $P(\nu_\mu \rightarrow \nu_e)$ oscillation probability for a range of δ_{CP} values. A circular modulation of the first oscillation peak (in both magnitude and position) is observed when varying throughout the allowable values of δ_{CP} . The CP-conserving values of $\delta_{CP} = 0, \pi$ have a lower(higher) oscillation maximum than the CP-violating values of $\delta_{CP} = -\pi/2(\delta_{CP} = \pi/2)$. A sub-dominant

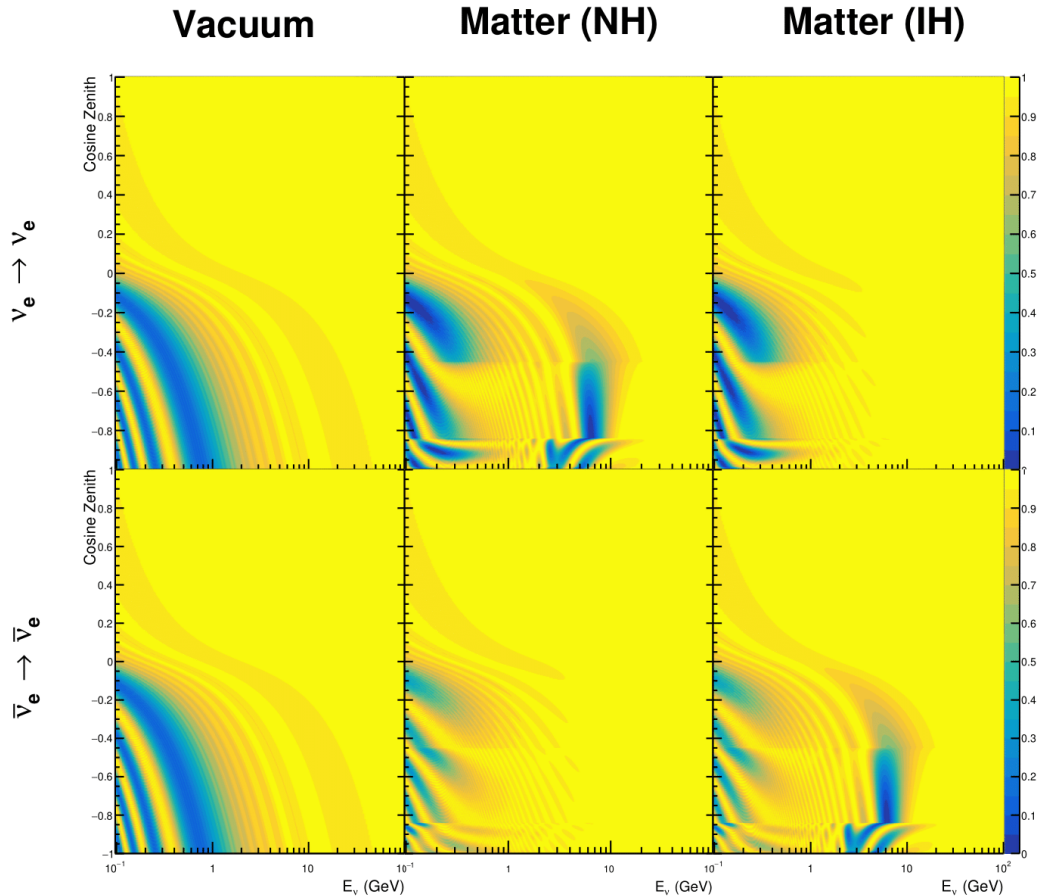


Figure 7.4.: An illustration of the matter-induced effects on the oscillation probability, given as a function of neutrino energy and zenith angle. The top row of panels gives the $P(\nu_e \rightarrow \nu_e)$ oscillation probability and the bottom row illustrates the $P(\bar{\nu}_e \rightarrow \bar{\nu}_e)$ oscillation probability. The left column highlights the oscillation probability in a vacuum, whereas the middle and right column represents the oscillation probabilities when the four-layer fixed density PREM model is assumed. All oscillation probabilities assume the “Asimov A” set given in Table 2.2, but importantly, the right column sets an inverted mass hierarchy. The “matter resonance” effects at $E_\nu \sim 5\text{GeV}$ can be seen in the $P(\nu_e \rightarrow \nu_e)$ for normal mass hierarchy and $P(\bar{\nu}_e \rightarrow \bar{\nu}_e)$ for inverted hierarchy.

shift in the energy of the oscillation peak is also present to aid in separating the two
₂₃₃₅ CP-conserving values of δ_{CP} .

T2K’s sensitivity to the $\sin^2(\theta_{23})$ and Δm_{23}^2 is observed as a shape-based variation
₂₃₃₇ of the muon-like samples, as illustrated in Figure 7.5. The value of Δm_{32}^2 laterally shifts
₂₃₃₈ the position of the oscillation dip (around $E_\nu \sim 0.6\text{GeV}$) in the $P(\nu_\mu \rightarrow \nu_\mu)$ oscillation
₂₃₃₉

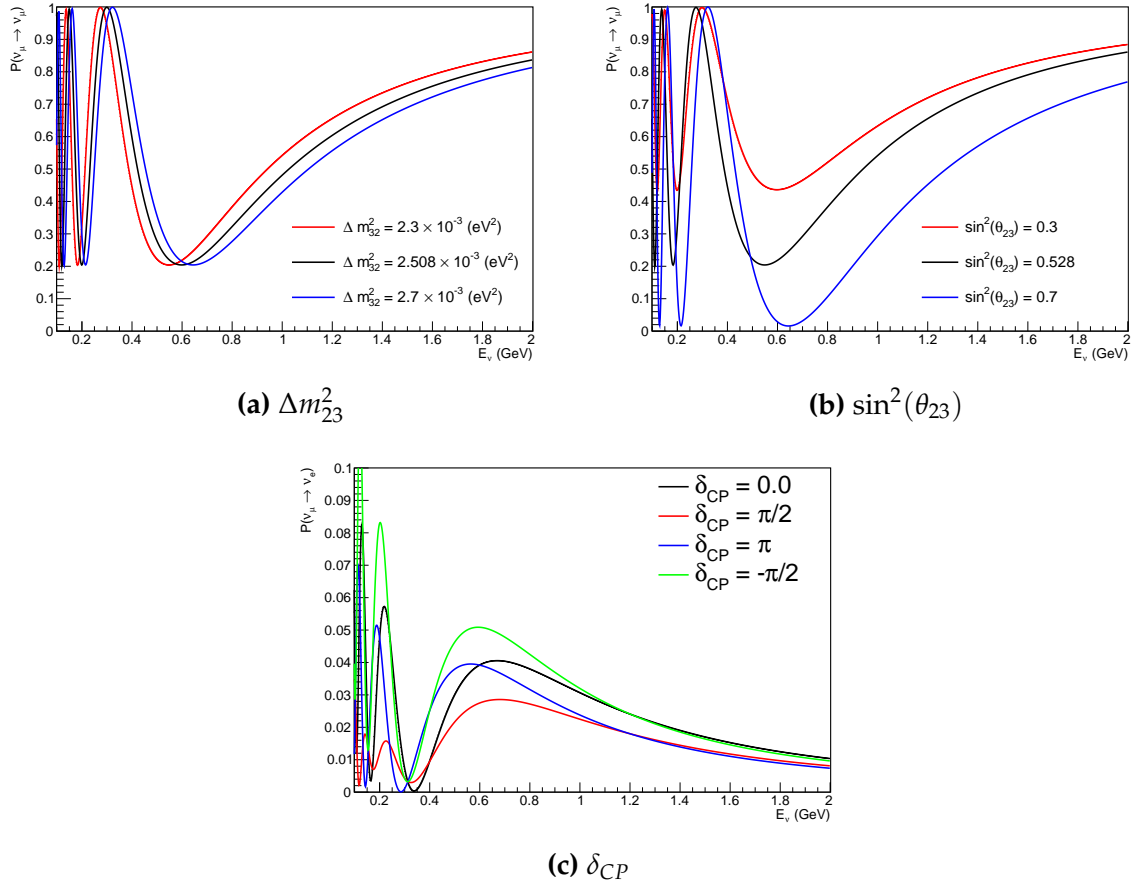


Figure 7.5.: The oscillation probability for beam neutrino events given as a function of neutrino energy. All oscillation parameters assume the “Asimov A” set given in Table 2.2 unless otherwise stated. Each panel represents a change in one of the oscillation parameters whilst keeping the remaining parameters fixed.

probability. A variation of $\sin^2(\theta_{23})$ is predominantly observed as a vertical shift of the oscillation dip with second-order horizontal shifts being due to matter effects. The beam neutrinos have limited sensitivity to matter effects due to the relatively shorter baseline as well as the Earth’s mantle being a relatively low-density material (as compared to the Earth’s core). For some values of δ_{CP} , the degeneracy in the number of e-like events allows the mass hierarchy to be resolved. This leads to a δ_{CP} -dependent mass hierarchy sensitivity which can be seen in Figure 7.6.

Whilst all oscillation channels should be included for completeness, the computational resources required to run a fit are limited and any reasonable approximations

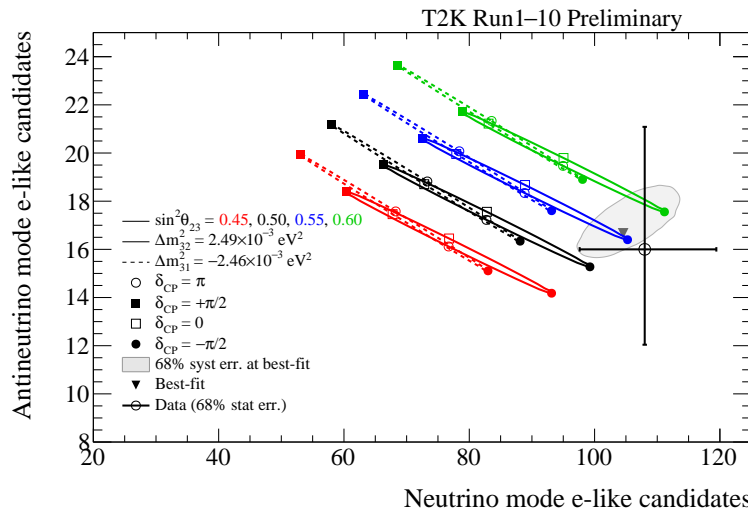


Figure 7.6.: The number of electron-like events in the FHC and RHC operating mode of the beam, as a function of the oscillation probabilities. Both normal hierarchy (Solid) and inverse hierarchy (Dashed) values of Δm_{23}^2 are given.

which reduce the number of oscillation probability calculations that need to be made should be applied. The $\nu_e \rightarrow \nu_{e,\mu,\tau}$ (and antineutrino equivalent) oscillations can be ignored for beam neutrinos as the $\nu_e/\bar{\nu}_e$ fluxes are approximately two orders of magnitude smaller than the corresponding $\nu_\mu/\bar{\nu}_\mu$ flux. Furthermore, as the peak neutrino energy of the beam is well below the threshold for charged current tau production ($E_\nu = 3.5\text{GeV}$ [51], only a small proportion of the neutrinos produced in the beam have the required energy. For the few neutrinos that have sufficient energy, the oscillation probability is very small due to the short baseline. Whilst these approximations can be made for the beam neutrinos, the atmospheric flux of ν_e is of the same order of magnitude as the ν_μ flux and the energy distribution of atmospheric neutrinos extends well above the tau production threshold.

2360 7.2. Treatment of Fast Oscillations

2361 As shown in Figure 7.7, atmospheric neutrino oscillations have a significantly more
2362 complex structure for upgoing neutrinos with energy below 1GeV. This is because the
2363 L/E dependence of the oscillation probability in this region induces rapid variations
2364 for small changes in L or E . As discussed in section 7.1, this is also the region in which
2365 atmospheric neutrinos have sensitivity to δ_{CP} . In practice, the direction of the neutrino
2366 is inferred from the direction of the final state particles traveling in the detector, which
2367 can be poor for low-energy neutrino interactions. This creates a distinct difference
2368 from the beam neutrinos where the position of the source is very precisely known.

2369 As a consequence of the unresolvable structure, an average oscillation probability
2370 is observed in the subGeV upgoing region. This creates a computational problem; A
2371 significantly large amount of Monte Carlo statistics would be required to accurately
2372 predict the number of events if Monte Carlo averaging was the only technique used.
2373 This section describes the ‘sub-sampling’ approach developed for this analysis and
2374 compares it to the methodology used within the SK-only analysis.

2375 The official SK-only analysis uses the osc3++ oscillation parameter fitter [210].
2376 To perform the fast oscillation averaging, it uses a ‘nearest-neighbour’ technique.
2377 For a given neutrino event, the nearest twenty neighbours in reconstructed lepton
2378 momentum and zenith angle are found and a distribution of their neutrino energies is
2379 built. The RMS, σ , of this distribution is then used to compute an average oscillation
2380 probability for the given neutrino Monte Carlo event.

2381 For the i^{th} event, the oscillation weight is calculated as

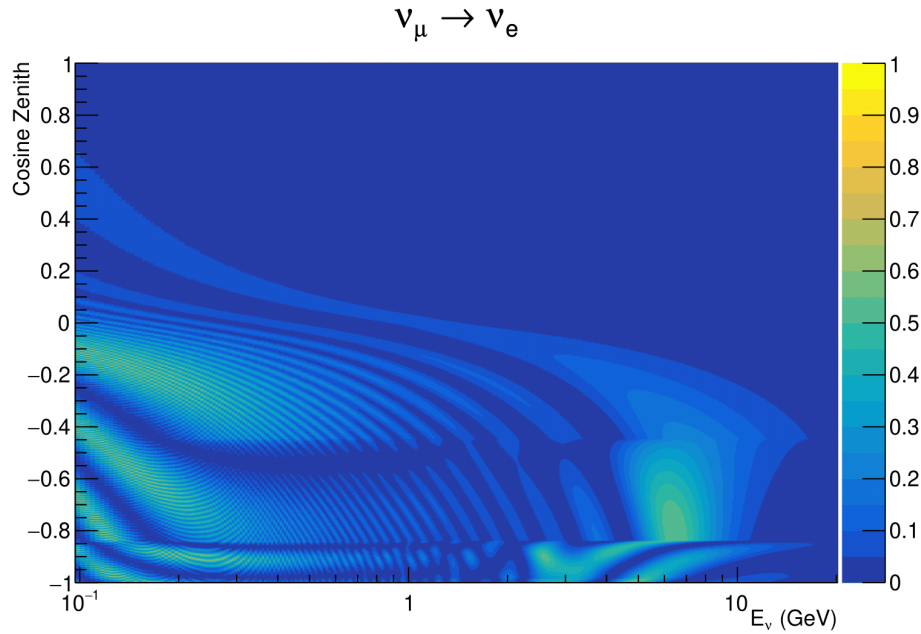


Figure 7.7.: The oscillation probability $P(\nu_\mu \rightarrow \nu_e)$, given as a function of neutrino energy and zenith angle, which highlights an example of the “fast” oscillations in the sub-GeV upgoing region.

$$W_i = \frac{1}{5}P(E_i, \bar{L}_i) + \frac{1}{5} \sum_{\beta=-1,-0.5,0.5,1} P(E_i + \beta\sigma_i, L_\beta), \quad (7.3)$$

where $P(E, L)$ is the oscillation probability calculation for neutrino energy E and path length L and the two path lengths, \bar{L}_i and L_β are discussed below. All of the oscillation probability calculations are performed with a fixed zenith angle such that the same density profile is used.

The uncertainty in the production height is controlled by using an “average” production height, \bar{L}_i , which represents the average path length computed using twenty production heights taken from the Honda flux model’s prediction [45]. For a given event, the production heights are sampled in steps of 5% of their cumulative distribution function. L_β values are similarly calculated but instead use different combinations of four production heights,

$$\begin{aligned}
 L_{-1.0} &= \frac{1}{4}L(45, 50, 55, 60), \\
 L_{-0.5} &= \frac{1}{4}L(35, 40, 65, 70), \\
 L_{+0.5} &= \frac{1}{4}L(25, 30, 75, 68), \\
 L_{+1.0} &= \frac{1}{4}L(15, 20, 85, 89).
 \end{aligned} \tag{7.4}$$

2392 This averaging technique works because of the inference between the zenith angle
 2393 and the reconstructed direction of final state particles in the detector. For low-energy
 2394 neutrinos, where the resolution of the true neutrino direction is poor, σ_i will be large,
 2395 resulting in significant averaging effects. Contrary to this, the inferred direction of
 2396 high-energy neutrinos will be much closer to the true value, meaning that σ_i will be
 2397 smaller, culminating in small averaging effects.

2398 In practice, this technique is performed before the fit in order to deal with the
 2399 computational cost. This is possible as the Osc3++ framework uses binned oscillation
 2400 parameters rather than continuous so the oscillation parameters used in the fit are
 2401 known prior to run-time. The framework used in this analysis uses continuous
 2402 oscillation parameters, and due to the MCMC fitting technique, there is no way to
 2403 know which oscillation parameter values will be selected *a priori*. Therefore, the
 2404 oscillation parameter calculation has to be performed at run-time. Computing five
 2405 oscillation probabilities per event would require far too many computational resources
 2406 to be viable. Therefore SK technique can not be used within this analysis. However,
 2407 the concept of the averaging technique can be taken from it.

2408 To perform a similar averaging as the SK analysis, a sub-sampling approach using
 2409 binned oscillograms has been devised. The technique can be explained by considering
 2410 a “fine” and “coarse” oscillogram. The fine oscillograms are used to define the array of

²⁴¹¹ $\cos(\theta_Z)$ and E_ν used in the oscillation engine. The coarse oscillograms cover the same
²⁴¹² phase-space but have fewer bins, where the value of a particular coarse bin is taken
²⁴¹³ as the linear average (flat prior in E_ν and $\cos(\theta_Z)$) of all fine bins which falls into it.
²⁴¹⁴ The coarse oscillogram is then used for determining the oscillation weight for a given
²⁴¹⁵ event. The binning which is used to calculate the oscillation probabilities, known as
²⁴¹⁶ the ‘fine’ binning, has $N \times N$ subdivisions per coarse bin. Figure 7.8 illustrates the
²⁴¹⁷ $N = 2$ example where the assigned value to a coarse bin is the average of the four fine
²⁴¹⁸ bins which fall in that coarse bin. Whilst the coarse bin edges do not have to be linear
²⁴¹⁹ on either axis, the sub-division of the fine bins is linear over the range of a coarse bin.

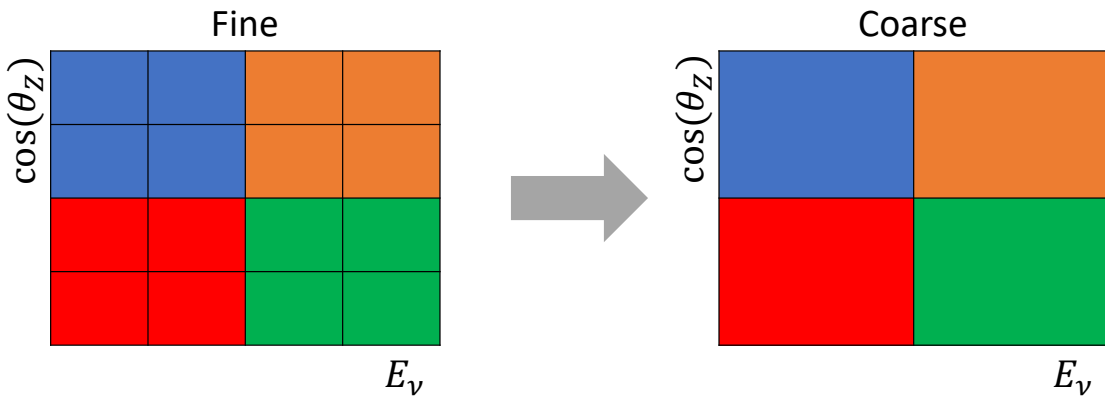


Figure 7.8.: Illustration of the averaging procedure for $N = 2$. The oscillation probabilities calculated on the finer left binning are averaged to obtain the oscillation probabilities in the coarser right binning. These averaged oscillation probabilities with the coarser binning are then applied to each event during the fit.

²⁴²⁰ The coarse binning is defined with 67×52 bins in true neutrino energy \times cosine
²⁴²¹ zenith. It is picked to be identical to that provided in [212]. In general, the binning is
²⁴²² logarithmically spaced in neutrino energy but has some hand-picked bin edges. Firstly,
²⁴²³ the bin density around the matter resonance is smoothly increased around the matter
²⁴²⁴ resonance region. This is to avoid smearing this region which can be well sampled by
²⁴²⁵ the Monte Carlo. Secondly, bin edges are selected to hit $0.4, 0.6, 1, 10, 30, 50, 100\text{GeV}$.
²⁴²⁶ This is to ensure that the Coulomb correction systematic and the atmospheric flux
²⁴²⁷ systematics definitions in neutrino energy can be hit. The cosine zenith binning is

2428 approximately linearly spaced across the allowable range but the values of layer
2429 transitions are hit precisely: -0.8376 (core-mantle) and -0.4464 (mantle/transition
2430 zone). Bins are spread further apart for downgoing events as this is a region unaffected
2431 by the fast oscillation wavelengths and reduces the total number of calculations
2432 required to perform the calculation.

2433 The choice of N is justified based on two studies. Firstly, the variation of event rates
2434 of each sample is studied as a function of N . For a given set of oscillation parameters
2435 thrown from the PDG prior constraints (detailed in Table 2.1), the oscillation probabili-
2436 ties are calculated using a given value of N . Each sample is re-weighted and the event
2437 rate is stored. The value of N is scanned from 1, which corresponds to no averaging, to
2438 19, which corresponds to the largest computationally viable subdivision binning. The
2439 event rate of each sample at large N is expected to converge to a stationary value due
2440 to the fine binning fully sampling the small-scale structure. Figure 7.9 illustrates this
2441 behaviour for the SubGeV_elike_0dcy sample for 9 different throws of the oscillation
2442 parameters.

2443 Denoting the event rate for one sample for a given throw t at each N by λ_t^N , the
2444 average over all considered N values ($\bar{\lambda}_t = \frac{1}{24} \sum_{N=1}^{24} \lambda_t^N$) is computed. The variance in
2445 the event rate at each N is then calculated as

$$\text{Var}[\lambda^N] = \frac{1}{N_{\text{throws}}} \sum_{t=1}^{N_{\text{throws}}} \left(\lambda_t^N - \bar{\lambda}_t \right)^2 - \left[\frac{1}{N_{\text{throws}}} \sum_{t=1}^{N_{\text{throws}}} \left(\lambda_t^N - \bar{\lambda}_t \right) \right]^2. \quad (7.5)$$

2446 **The Below (and associated figures) has been added** In practice the following
2447 procedure is undertaken. For a particular throw, the difference between the event
2448 rate at a particular choice of N and the mean of the distribution is calculated. This
2449 is illustrated in Figure 7.10. This value is then calculated for all the 2000 throws,

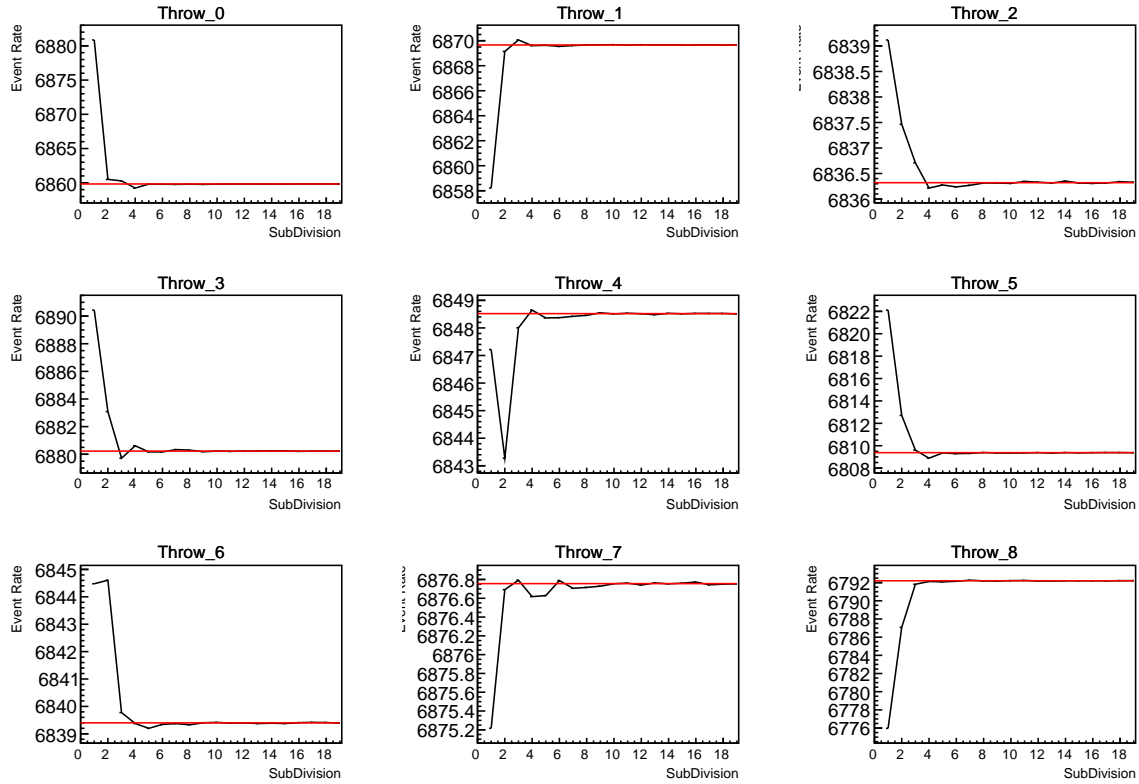


Figure 7.9.: Event rate of the SubGeV_elike_0dcy sample as a function of the number of subdivisions per coarse bin. Each subplot represents the event rate of the sample at a different oscillation parameter set thrown from the PDG priors detailed in Table 2.1. The red line in each subplot represents the mean of the event rate over the different values of sub-divisions for that particular oscillation parameter throw.

generating a distribution of $\lambda_t^N - \bar{\lambda}_t$. This is repeated for each of the values of N considered within this study. The distributions of this value, for $N = \{1, 5\}$, are given in Figure 7.11. As expected, the distribution gets narrower and tends towards zero for the higher values of N .

2454 End Review

The aim of the study is to find the lowest value of N such that this variance is below 0.001. This utilises the width of the distributions given in Figure 7.11. This is the typical threshold used by T2K fitters to validate systematic implementation so has been set as the same criteria. The results of this study for each atmospheric sample used within this thesis are illustrated in Figure 7.12 for 2000 throws of the oscillation

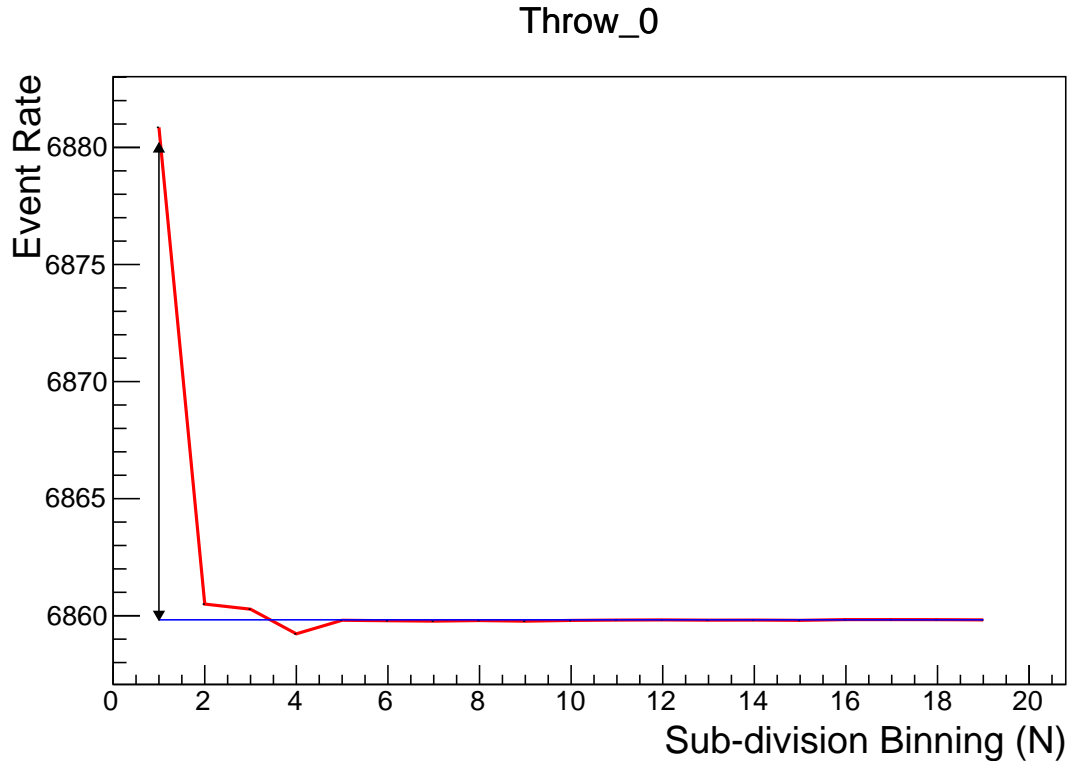


Figure 7.10.

parameters. As can be seen, the variance is below the threshold at $N = 10$, and is driven primarily by the SubGeV_mulike_1dcy and SubGeV_elike_0dcy samples.

The second study to determine the value of N is as follows. The likelihood for each sample is computed against an Asimov data set created with Asimov A oscillation parameters (Table 2.2). Following Equation 7.5, the variance of the log-likelihood over all considered N is computed. The results are shown in Figure 7.13.

A choice of $N = 10$ sub-divisions per coarse bin has a variance in both event rate and log-likelihood residuals less than the required threshold of 0.001. The largest value of the likelihood variance is of order 10^{-7} , corresponding to an error on the log-likelihood of about 3×10^{-4} which is small enough to be negligible for the oscillation analysis.

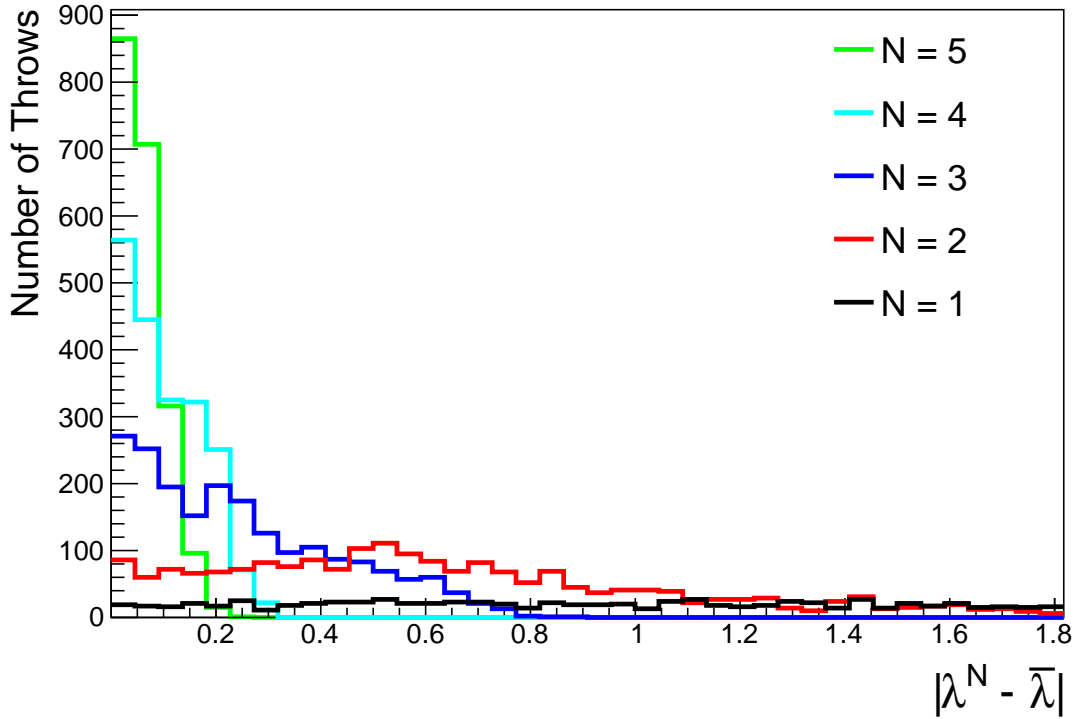


Figure 7.11.

2471 Figure 7.14 illustrates the effect of the smearing using $N = 10$. The fast oscillations
 2472 in the sub-GeV upgoing region have been replaced with a normalisation effect whilst
 2473 the large matter resonance structure remains.

2474 **7.3. Calculation Engine**

2475 As previously discussed in section 7.2, the calculation of oscillation probabilities is per-
 2476 formed at run-time due to utilising continuous oscillation parameters. Consequently,
 2477 the time per calculation is crucial for fit performance. The initial fitting framework
 2478 used for this analysis was developed with ProbGPU [213]. This is a GPU-only implemen-
 2479 tation of the prob3 engine [214]. It is primarily designed for neutrino propagation in a
 2480 beam experiment (single layer of constant density) with the atmospheric propagation
 2481 code not being used prior to the analysis in this thesis.

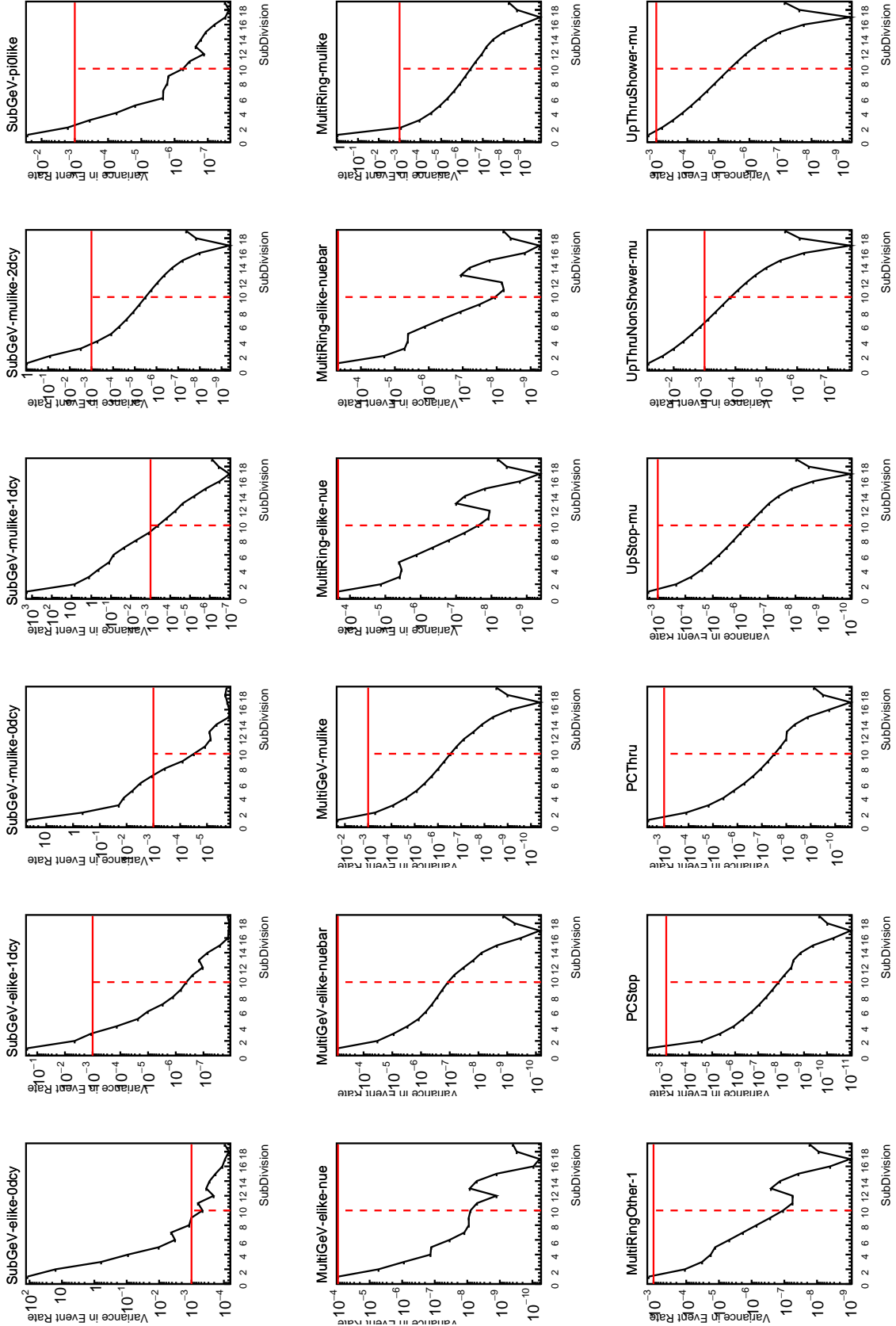


Figure 7.12.: Variance of event rate for each atmospheric sample as a function of the number of sub-divisions per coarse bin. The solid red line indicates the 0.1% threshold and the dashed red line indicates the variance at a sub-division $N = 10$.

Oscillation Probability Calculation

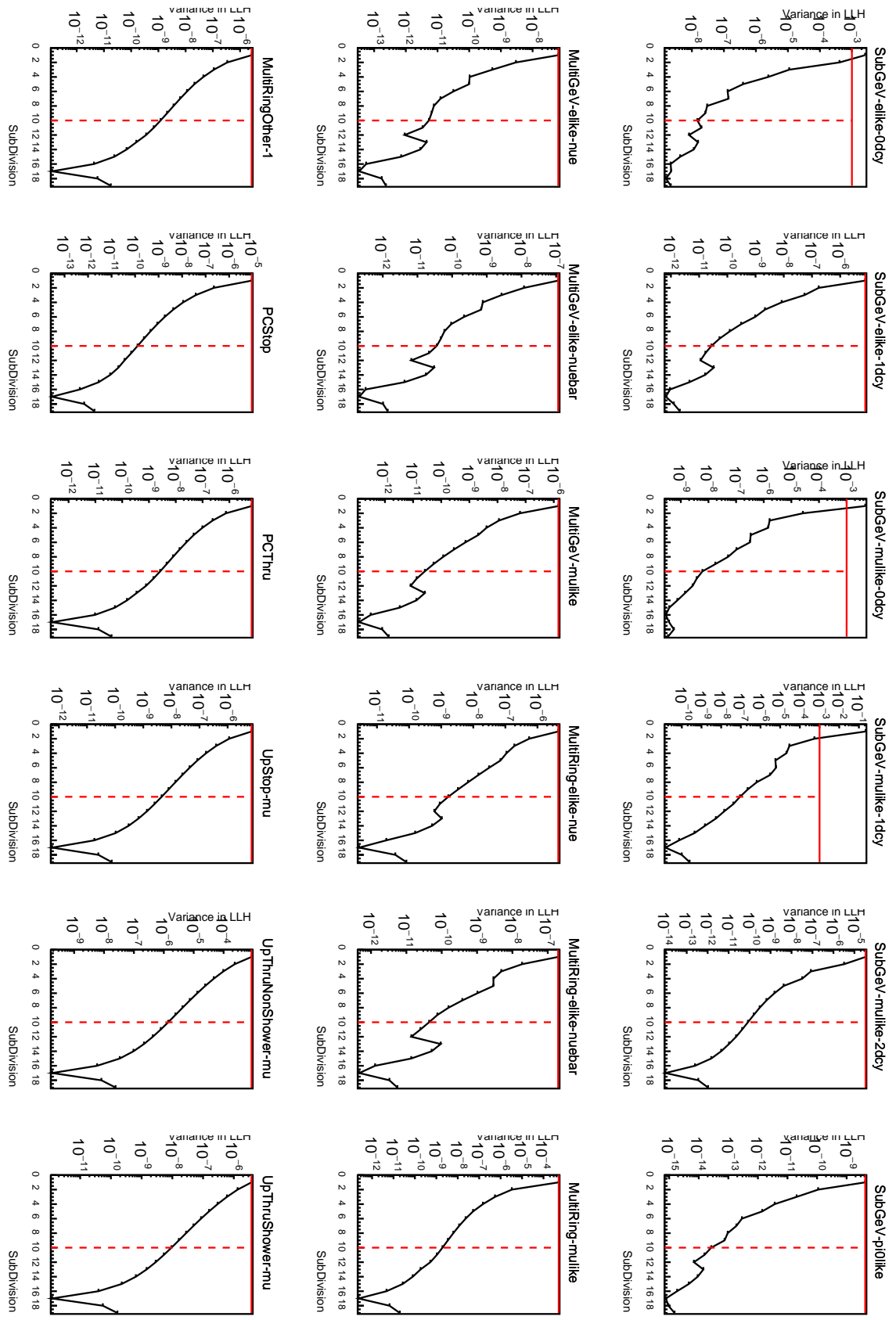


Figure 7.13: Variance of sample likelihood, when compared to 'Asimov data' set at Asimov A, for each atmospheric sample as a function of the number of sub-divisions per coarse bin. The solid red line indicates the 0.1% threshold and the dashed red line is a graphical indication of the variance at a sub-division $N = 10$.

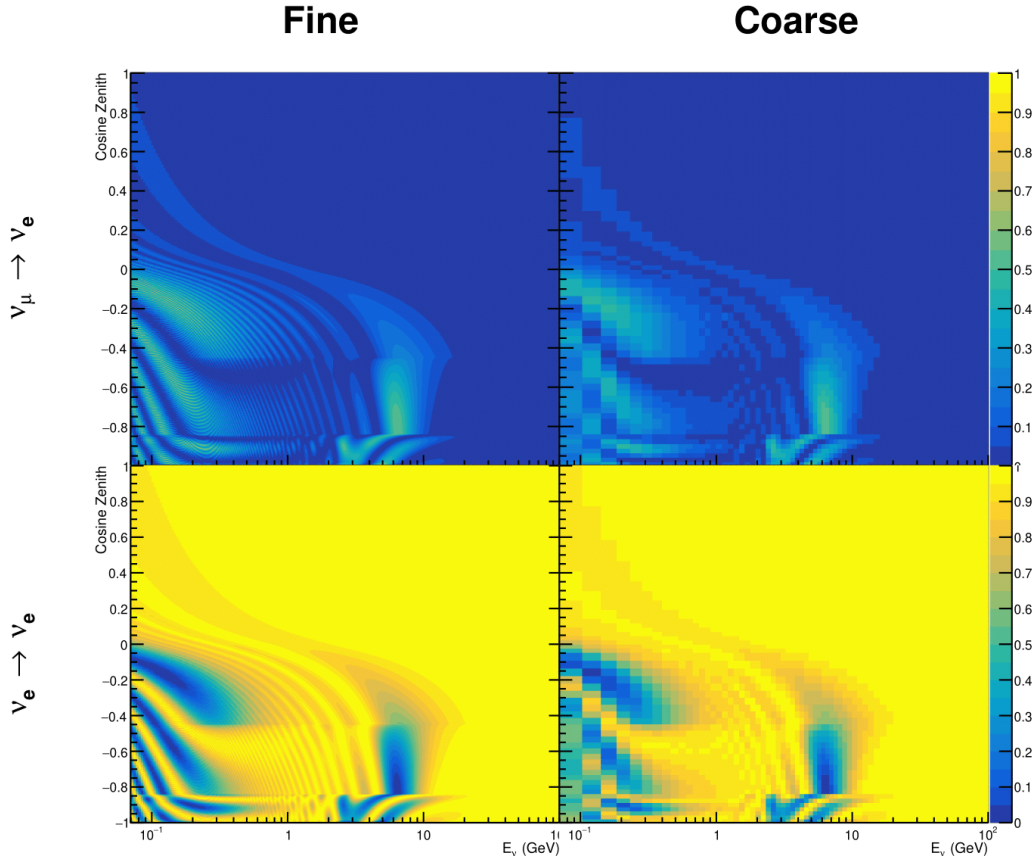


Figure 7.14.: The oscillation probability, $P(\nu_\mu \rightarrow \nu_e)$ (top row) and $P(\nu_e \rightarrow \nu_e)$ (bottom row), given as a function of neutrino energy and zenith angle. The left column gives the “fine” binning used to calculate the oscillation probabilities and the right column illustrates the “coarse” binning used to reweight the Monte Carlo events. The fine binning choice is given with $N = 10$, which was determined to be below the threshold from Figure 7.12 and Figure 7.13.

Another engine, CUDAProb3 [215], has been implemented within the fitting frame-work used in this analysis. It has been specifically optimised for atmospheric neutrino oscillation calculation so does not contain the code to replace the beam oscillation calculation. The engine utilises object-orientated techniques as compared to the functional implementation of ProbGPU. This allows the energy and cosine zenith arrays to be kept on GPU memory, rather than having to load these arrays onto GPU memory for each calculation. General memory interfacing is one of the slowest tasks which

2489 GPUs can do, so being able to eliminate this significantly reduces the time required
2490 for calculation. This can be seen in Figure 7.15, where the GPU implementation of
2491 CUDAProb3 is approximately three times faster than the ProbGPU engine.

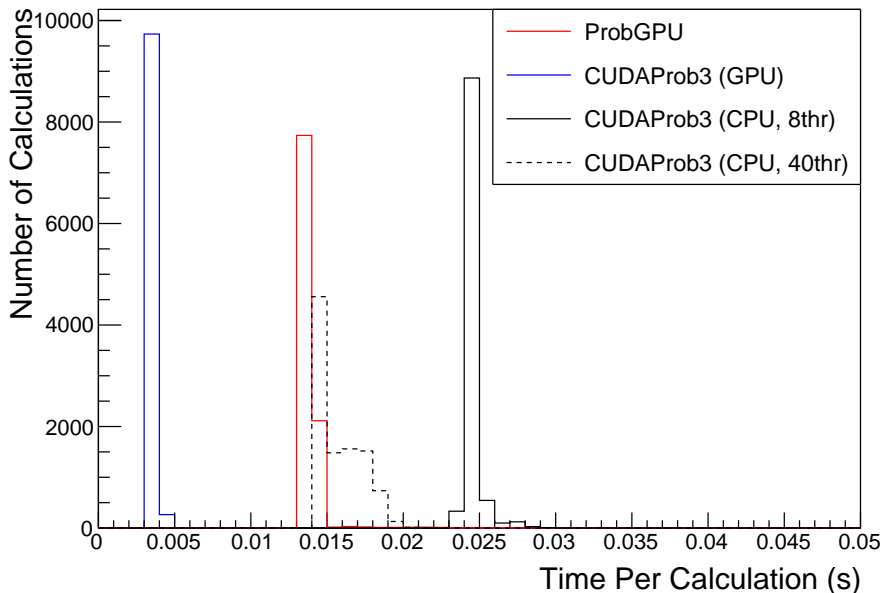


Figure 7.15.: The calculation time taken to both calculate the oscillation probabilities and fill the “coarse” oscilloscopes, following the technique given in section 7.2, for the CUDAProb3 and ProbGPU (Red) calculation engines. CUDAProb3 has both a GPU (Blue) and CPU (Black) implementation, where the CPU implementation is multithreaded. Therefore, 8-threads (solid) and 40-threads (dashed) configurations have been tested. Prob3, which is a CPU single-thread implementation has a mean step time of 1.142s.

2492 Another significant advantage of CUDAProb3 is that it contains a CPU multithreaded
2493 implementation which is not possible with the ProbGPU or prob3 engines. This elimi-
2494 nates the requirement for GPU resources when submitting jobs to batch systems. As
2495 illustrated in Figure 7.15, the calculation speed depends on the number of available
2496 threads. Using 8 threads (which is typical of the batch systems being used) is ap-
2497 proximately twice as slow as the ProbGPU engine implementation, but would allow
2498 the fitting framework to be run on many more resources. This fact is utilised for any
2499 SK-only fits but GPU resources are required for any fits which include beam samples
2500 due to the ProbGPU requirement. Based on the benefits shown by the implementation

2501 in this section, efforts are being placed into including linear propagation for beam
2502 neutrino propagation into the engine [216].

2503 **7.4. Matter Density Profile**

2504 For an experiment observing atmospheric neutrinos propagating through the Earth, a
2505 model of the Earth's density profile is required. The model used within this analysis is
2506 the Preliminary Reference Earth Model (PREM) [211], as illustrated in Figure 7.1. As
2507 discussed in section 7.1, the propagator used within the calculation engine requires
2508 constant density layers. To follow the official SK-only analysis [210], the average
2509 density of each layer has been taken from the PREM model. Table 7.1 documents
2510 the density and radii of the layers used within this approximation. The density
2511 measurements provided in the PREM model are provided in terms of mass density,
2512 whereas neutrino oscillations are sensitive to the electron number density. This value
2513 can be computed as the product of the chemical composition, or the Z/A value, and
2514 the mass density of each layer. Currently, the only way to calculate the chemical
2515 composition value for layers close to the Earth's core is through neutrino oscillations.
2516 The chemical composition of the upper layers of the Earth's Mantle and the Transition
2517 zone is well known due to it being predominantly pyrolite which has a chemical
2518 composition value of 0.496 [217]. The components of the Earth's core region are less
2519 well known. Consequently, the chemical composition dial for the core layers is set to a
2520 value of 0.468, as calculated in [218]. This value is assigned a Gaussian error with a
2521 standard deviation equivalent to the difference in chemical composition in core and
2522 mantle layers. Figure 7.16 illustrates the effect of moving from the $Z/A = 0.5$ method
2523 which is used in the official SK-only analysis [210] to these more precise values.

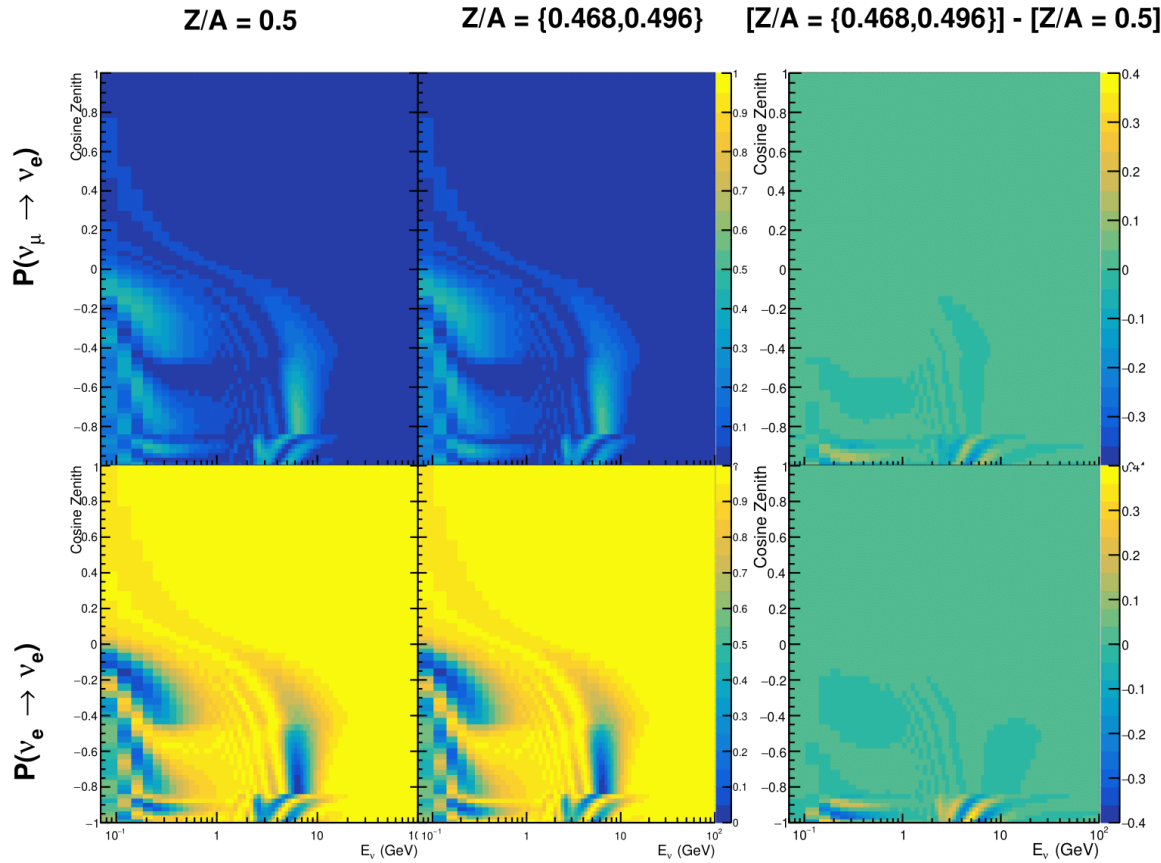


Figure 7.16.: The oscillation probability, $P(\nu_\mu \rightarrow \nu_e)$ (top row) and $P(\nu_e \rightarrow \nu_e)$ (bottom row), given as a function of neutrino energy and zenith angle. The left column gives probabilities where the constant $Z/A = 0.5$ approximation which is used in the official SK-only analysis. The middle column gives the probabilities where $Z/A = [0.468, 0.498]$ values are used, as given in Table 7.1. The right column illustrates the difference in oscillation probability between the two different techniques.

2524 The beam oscillation probability in this thesis uses a baseline of 295km, density
 2525 2.6g/cm^3 , and chemical composition 0.5 as is done by the official T2K-only analysis
 2526 [219].

2527 Whilst the propagator requires a fixed density layer model of the Earth, the density
 2528 only has to be fixed for a specific $E_\nu \times \cos(\theta_Z)$ bin in a given layer. As the density is a
 2529 function of radius, which is a function of the direction in which a neutrino propagates,

2530 a better approximation of the PREM model can be made if a $\cos(\theta_Z)$ -specific density is
2531 calculated.

2532 To achieve this, the average density, $\langle \rho \rangle_i$, in the i^{th} layer, is calculated as the density,
2533 $\rho(t)$, integrated over the track a given $\cos(\theta_Z)$,

$$\langle \rho \rangle_i = \frac{1}{t_{i+1} - t_i} \int_{t_i}^{t_{i+1}} \rho(t) dt \quad (7.6)$$

2534 where t_i are the intersection points between each layer and t is the path length of
2535 the trajectory across the layer.

2536 The oscillation probability calculation speed is approximately linear in the number
2537 of layers invoked within the Earth model. Therefore a four-layer model is still utilized
2538 with the only difference to the official SK-only analysis being that the four-layer model
2539 used for each value of $\cos(\theta_Z)$ is different. Following the method outlined in [220],
2540 a four-layer piecewise quadratic polynomial is fit to the PREM model for the four
2541 layers defined in Table 7.1. This fit was not performed by the author of the thesis
2542 and is documented in [212]. The coefficients of the quadratic fit to each layer are
2543 given in Table 7.2 with the final distribution illustrated in Figure 7.17. The quadratic
2544 approximation is clearly much closer to the PREM model as compared to the constant
2545 density approximation.

2546 The effect of using the quadratic density per $\cos(\theta_Z)$ model is highlighted in
2547 Figure 7.18. The slight discontinuity in the oscillation probability around $\cos(\theta_Z) \sim -$
2548 0.45 in the fixed density model, which is due to the transition to mantle layer boundary,
2549 has been reduced. This is expected as the difference in the density across this boundary
2550 is significantly smaller in the quadratic density model as compared to the constant
2551 density model. Whilst the difference in density across the other layer transitions

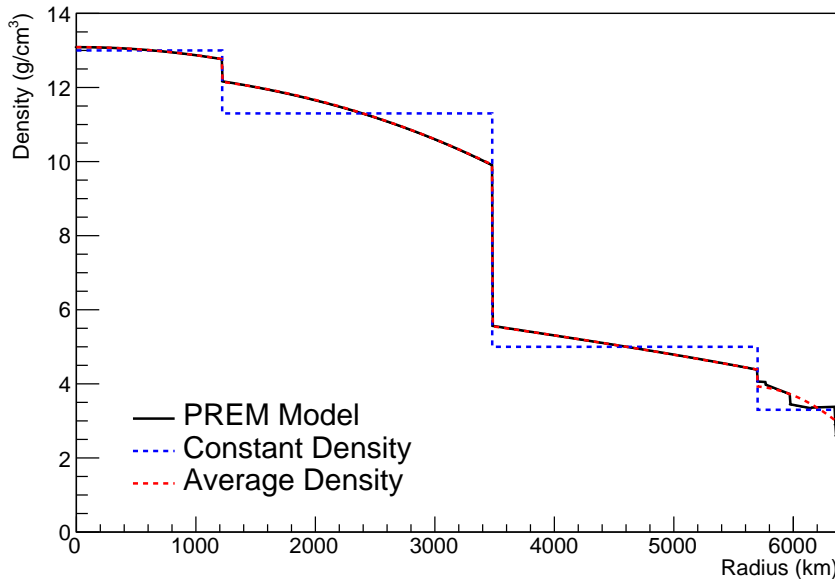


Figure 7.17.: The density of the Earth given as a function of the radius, as given by the PREM model (Black), the constant density four-layer approximation (Blue), as used in the official SK-only analysis, and the quadratic approximation of the PREM model (Red).

Layer	Outer Radius [km]	Density [g/cm ³]
Inner Core	1220	$13.09 - 8.84x^2$
Outer Core	3480	$12.31 + 1.09x - 10.02x^2$
Lower Mantle	5701	$6.78 - 1.56x - 1.25x^2$
Transition Zone	6371	$-50.42 + 123.33x - 69.95x^2$

Table 7.2.: The quadratic polynomial fits to the PREM model for four assumed layers of the PREM model. The fit to calculate the coefficients is given in [212], where $x = R/R_{Earth}$.

is reduced, there is still a significant difference. This means the discontinuities in the oscillation probabilities remain but are significantly reduced. However, as the quadratic density approximation matches the PREM model well in this region, these discontinuities are due to the Earth model rather than an artifact of the oscillation calculation.

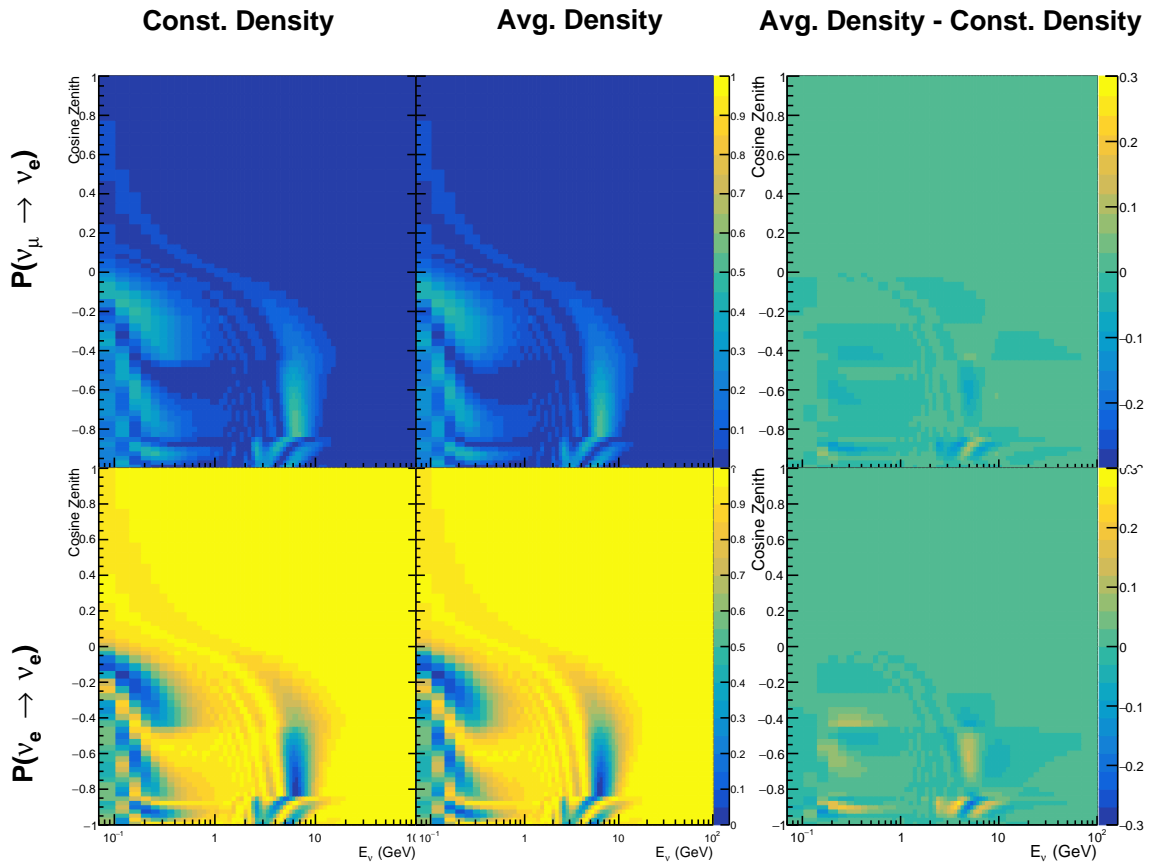


Figure 7.18.: The oscillation probability, $P(\nu_\mu \rightarrow \nu_e)$ (top row) and $P(\nu_e \rightarrow \nu_\mu)$ (bottom row), given as a function of neutrino energy and zenith angle. The left column gives probabilities where the four-layer constant density approximation is used. The middle column gives the probabilities where the density is integrated over the trajectory, using the quadratic PREM approximation, for each $\cos(\theta_Z)$ is used. The right column illustrates the difference in oscillation probability between the two different techniques.

2557 7.5. Production Height Averaging

2558 As discussed in section 7.1, the height at which the cosmic ray flux interacts in the
2559 atmosphere is not known on an event-by-event basis. The production height can vary
2560 from the Earth’s surface to $\sim 50\text{km}$ above that. The SK-only analysis methodology
2561 (described in section 7.2) for including the uncertainty on the production height is
2562 to include variations from the Honda model when pre-calculating the oscillation
2563 probabilities prior to the fit. This technique is not possible for this analysis which
2564 uses continuous oscillation parameters that can not be known prior to the fit. Conse-
2565 quently, an analytical averaging technique was developed in [212]. The author of this
2566 thesis was not responsible for the derivation of the technique but has performed the
2567 implementation and validation of the technique for this analysis alone.

2568 Using the 20 production heights per Monte Carlo neutrino event, provided as 5%
2569 percentiles from the Honda flux model, a production height distribution $p_j(h|E_\nu, \cos\theta_Z)$
2570 is built for each neutrino flavour $j = \nu_e, \bar{\nu}_e, \nu_\mu, \bar{\nu}_\mu$. In practice, a histogram is filled with
2571 20 evenly spaced bins in production height h between 0 and 50km. The neutrino energy
2572 and cosine zenith binning of the histogram is the same as that provided in section 7.2.
2573 The average production height, $\bar{h} = \int dh \frac{1}{4} \sum_j p_j(h|E_\nu, \cos(\theta_Z))$, is calculated. The
2574 production height binning of this histogram is then translated into $\delta t(h) = t(\bar{h}) - t(h)$,
2575 where $t(h)$ is the distance travelled along the trajectory.

2576 For the i^{th} traversed layer, the transition amplitude, $D_i(t_{i+1}, t_i)$, is computed. The
2577 time-ordered product of these is then used as the overall transition amplitude via

$$A(t_{n+1}, t_0) = D_n(t_{n+1}, t_n) \dots D_1(t_2, t_1) D_0(t_1, t_0), \quad (7.7)$$

2578

where,

$$\begin{aligned} D_n(t_{n+1}, t_n) &= \exp[-iH_n(t_{n+1} - t_n)] \\ &= \sum_{k=1}^3 C_k \exp[ia_k(t_{n+1} - t_n)] \end{aligned} \quad (7.8)$$

2579

is expressed as a diagonalised time-dependent solution to the Schrodinger equation.

2580 The 0^{th} layer is the propagation through the atmosphere and is the only term that
 2581 depends on the production height. Using the substitution $t_0 = t(\bar{h}) - \delta t(h)$, it can be
 2582 shown that

$$D_0(t_1, t_0) = D_0(t_1, \bar{h})D_0(\delta t). \quad (7.9)$$

2583

Thus Equation 7.7 becomes

$$\begin{aligned} A(t_{n+1}, t_0) &= D_n(t_{n+1}, t_n) \dots D_1(t_2, t_1) D_0(t_1, \bar{h}) D(\delta t) \\ &= A(t_{n+1}, \bar{h}) \sum_{k=1}^3 C_k \exp[ia_k \delta t], \\ &= \sum_{k=1}^3 B_k \exp[ia_k \delta t]. \end{aligned} \quad (7.10)$$

2584

The oscillation probability averaged over production height is then calculated as

$$\begin{aligned}
 \bar{P}(\nu_j \rightarrow \nu_i) &= \int d(\delta t) p_j(\delta t | E_\nu, \cos \theta_Z) P(\nu_j \rightarrow \nu_i) \\
 &= \int d(\delta t) p_j(\delta t | E_\nu, \cos \theta_Z) A(t_{n+1}, t_0) A^*(t_{n+1}, t_0) \\
 &= \sum_{km} (B_k)_{ij} (B_m)_{ij}^* \int d(\delta t) p_j(\delta t | E_\nu, \cos \theta_Z) \exp[i(a_k - a_m)\delta t]
 \end{aligned} \tag{7.11}$$

2585 In practice, implementation in CUDAProb3 [215] is relatively straightforward as
 2586 the majority of these terms are already calculated in the standard oscillation calculation.
 2587 Figure 7.19 illustrates the results of the production height averaging. As expected,
 2588 the main effect is observed in the low-energy downward-going and horizontal-going
 2589 events. Upward-going events have to travel the radius of the Earth, $R_E = 6371\text{km}$,
 2590 where the production height uncertainty is a small fraction of the total path length.

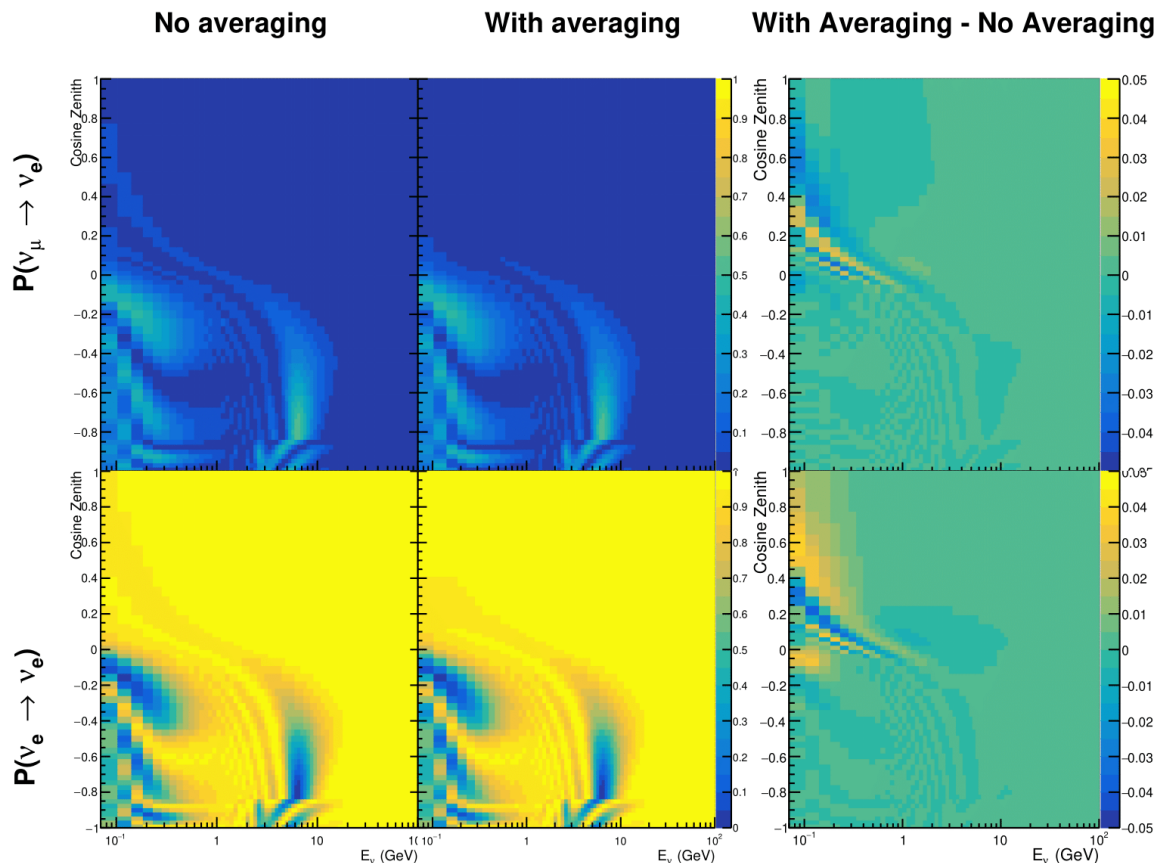


Figure 7.19.: The oscillation probability, $P(\nu_\mu \rightarrow \nu_e)$ (top row) and $P(\nu_e \rightarrow \nu_\mu)$ (bottom row), given as a function of neutrino energy and zenith angle. The left column gives probabilities where a fixed production height of 25km is used. The middle column gives the probabilities where the production height is analytically averaged. The right column illustrates the difference in oscillation probability between the two different techniques.

2591 **Chapter 8**

2592 **Oscillation Analysis**

2593 **8.1. Likelihood Calculation**

2594 This analysis performs a joint oscillation parameter fit of the ND280, and the SK
2595 atmospheric samples.

2596 Once the Monte Carlo predictions of each beam and atmospheric sample has been
2597 built, following from chapter 6, a likelihood needs to be constructed. This is done
2598 by comparing the Monte Carlo prediction to “data”. The data can consist of either
2599 an Asmiov Monte Carlo prediction, which is typically used for sensitivity studies,
2600 or real data. The Monte Carlo prediction is calculated at a particular point, $\vec{\theta}$, in the
2601 model parameter space, $N_i^{MC} = N_i^{MC}(\vec{\theta})$. Both the data and Monte Carlo spectra are
2602 binned, where the i^{th} bin content is represented by N_i^D and N_i^{MC} , respectively. The bin
2603 contents for the beam near detector, beam far detector and atmospheric samples are
2604 denoted with ND , FD and Atm , respectively. The binning index, i , runs over all the
2605 bins within the sample and all samples with that set. Taking the beam far detector
2606 samples as example, it would run over all the reconstructed neutrino energy bins in all
2607 samples (FHC1R μ , RHC1R μ , etc.). The likelihood calculation between data and Monte
2608 Carlo for a particular bin follows a Poisson distribution, where the data is treated as a
2609 fluctuation of the simulation.

2610 Following the T2K analysis presented in [80], the likelihood contribution from the
2611 near detector also includes a Monte Carlo statistical uncertainty term, derived from

2612 the Barlow and Beeston statistical treatment [221, 222]. In addition to treating the data
 2613 as a fluctuation of the Monte Carlo prediction, it includes a contribution from the
 2614 likelihood that the generated simulation is a statistical fluctuation of the actual true
 2615 simulation assuming infinite statistics. The technical implementation of this additional
 2616 likelihood term is documented in [195]. The term is defined as,

$$\frac{(\beta_i - 1)^2}{2\sigma_{\beta_i}^2}, \quad (8.1)$$

2617 where β_i represents a scaling parameter for each bin i , which is a value based on
 2618 the amount of Monte Carlo statistics in a bin [195]. $\sigma_{\beta_i} = \sqrt{\sum_i w_i^2 / N_i^{MC}}$, and $\sqrt{\sum_i w_i^2}$
 2619 represents the sum of the square of the weights of the Monte Carlo events which fall
 2620 into bin i .

2621 Additional contributions to the likelihood come from the variation of the systematic
 2622 model parameters. For those parameters with well-motivated uncertainty estimates,
 2623 a covariance matrix, V describes the prior knowledge of each parameter as well as
 2624 any correlations between the parameters. Due to the technical implementation, a
 2625 single covariance matrix describes each “block” of model parameters, e.g. beam flux
 2626 systematics. For simplicity, the covariance matrix associated with the k^{th} block is
 2627 denoted V^k . This substitution results in $\vec{\theta} = \sum_k^{N_b} \vec{\theta}^k$ and $V = \sum_k^{N_b} V^k$, for N_b number
 2628 of blocks describing: oscillation parameters, beam flux, atmospheric flux, neutrino
 2629 interaction, near detector, beam far detector and atmospheric far detector systematics
 2630 detailed in section 6.4. The number of parameters in the k^{th} block is defined as $n(k)$.

2631 The final likelihood term is defined as,

$$\begin{aligned}
& -\ln(\mathcal{L}) = \tag{8.2} \\
& \sum_i^{\text{NDbins}} N_i^{\text{ND},MC}(\vec{\theta}) - N_i^{\text{ND},D} + N_i^{\text{ND},D} \times \ln \left[N_i^{\text{ND},D} / N_i^{\text{ND},MC}(\vec{\theta}) \right] + \frac{(\beta_i - 1)^2}{2\sigma_{\beta_i}^2} \\
& + \sum_i^{\text{FDbins}} N_i^{\text{FD},MC}(\vec{\theta}) - N_i^{\text{FD},D} + N_i^{\text{FD},D} \times \ln \left[N_i^{\text{FD},D} / N_i^{\text{FD},MC}(\vec{\theta}) \right] \\
& + \sum_i^{\text{Atmbins}} N_i^{\text{Atm},MC}(\vec{\theta}) - N_i^{\text{Atm},D} + N_i^{\text{Atm},D} \times \ln \left[N_i^{\text{Atm},D} / N_i^{\text{Atm},MC}(\vec{\theta}) \right] \\
& + \frac{1}{2} \sum_k^{N_b} \sum_i^{n(k)} \sum_j^{n(k)} (\vec{\theta}^k)_i (V^k)_{ij}^{-1} (\vec{\theta}^k)_j.
\end{aligned}$$

2632 This is the value determined at each step of the MCMC to build the posterior
2633 distribution, as discussed in chapter 4.

2634 8.1.1. Likelihood Scans

2635 Using the defintion of the likelihood presented in section 8.1, the response of each
2636 sample to a variation particular parameter can be studied. Figure 8.1 presents the
2637 variation of all the samples (beam and atmospheric) at SK. Each plot represents a
2638 “scan”, where a particular parameter is scanned in some range. The “data” being
2639 used within the definition of the likelihood equation is built using the Asimov A
2640 oscillation parameter values defined in Table 2.2 alongside the pre-fit dial values as
2641 discussed in subsection 6.4.3. Due to the correlations between oscillation parameters,
2642 the value of $\chi^2 \sim 1$ does not equate to the typical 1σ sensitivity. However, it does give
2643 an indication of which samples response the strongest to a variation in the oscillation
2644 parameters. The point at which the likelihood tends to zero illustrates the value of the
2645 parameter used to build the Asimov data prediction. The likelihood scans only include
2646 the sample response and ignore the penalty contribution term from the variation of
2647 the parameter.

2648 The response to Δm_{23}^2 is much larger in beam samples, specifically μ -like samples,
2649 compared to atmospheric samples. This is to be expected as the beam neutrino
2650 energy can be specifically tuned to match the maximal disappearance probability.
2651 As discussed in section 7.1, the determination of the mass hierarchy is significantly
2652 enhanced when using the atmospheric samples due to them transitioning through the
2653 Earth’s core. So whilst the atmospheric samples do not add much information to the
2654 constraint of $|\Delta m_{32}^2|$ beyond that of the beam analysis, they do enhance the ability to
2655 determine the sign of the parameter.

2656 The sensitivity to $\sin^2(\theta_{23})$ is again dominated by the T2K experiment. However,
2657 the difference in the response for atmospheric and beam samples is much smaller. Con-
2658 sequently, one would expect that the joint fit would become more sensivity to $\sin^2(\theta_{23})$

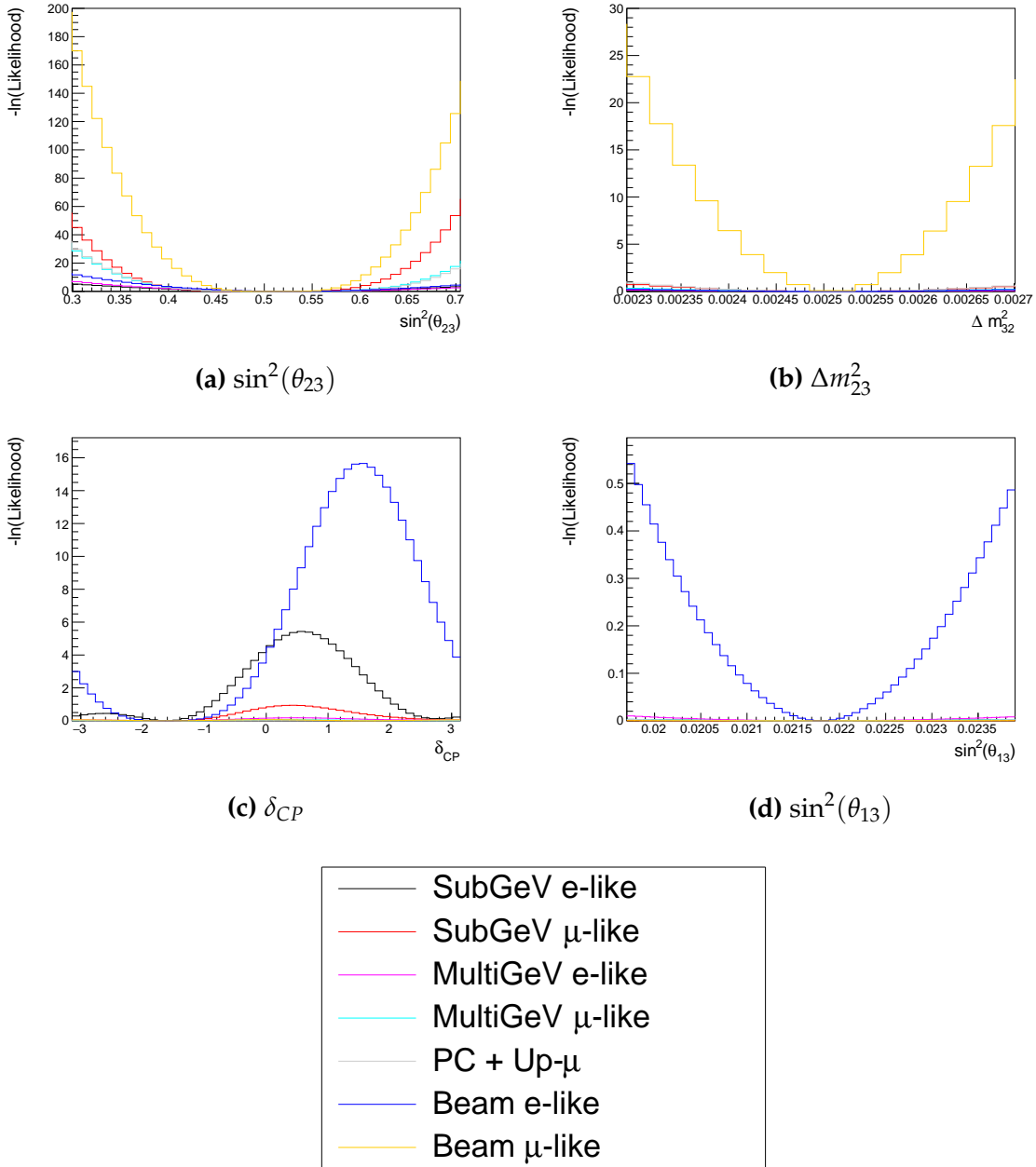


Figure 8.1.: The response of the likelihood, as defined in section 8.1, illustrating the response of the samples to the oscillation parameters. Δm_{12}^2 and $\sin^2(\theta_{12})$ are negated because these samples have no sensitivity to those parameters. The Asimov data set is built using the pre-fit dial values assuming Asimov A oscillation parameters defined in Table 2.2. DB: Need finer binning on delmsq23

than just T2K experiment alone. The summed response over all atmospheric samples becomes comparable to that of the muon-like beam samples. For this particular choice of Asimov point, the only samples which respond to the $\sin^2(\theta_{13})$ parameter are the

2662 electron-like beam samples. Consequently, no increase in sensitivity beyond that of
2663 the T2K-only analysis is expected at that Asimov point. The Δm_{12}^2 and $\sin^2(\theta_{12})$ are
2664 not considered as there is simply no sensitivity in any sample considered within this
2665 analysis.

2666 As discussed, the correlations between oscillation parameters induce marginali-
2667 sation effects within the response of the likelihood. That is to say, the response to
2668 δ_{CP} is affected by the choice of $\sin^2(\theta_{13})$ or $\sin^2(\theta_{23})$. The two-dimensional scans of
2669 the appearance ($\sin^2(\theta_{13}) - \delta_{CP}$) and disappearance ($\sin^2(\theta_{23}) - \Delta m_{23}^2$) parameters are
2670 illustrated in Figure 8.2 and Figure 8.3, respectively.

2671 The appearance log-likelihood scans show the distinct difference in how the beam
2672 and atmospheric samples respond. The beam samples have an approximately constant
2673 width of the 2σ and 3σ contours, throughout all ranges of δ_{CP} . The atmospheric
2674 samples response to δ_{CP} is very strongly correlated to the choice of $\sin^2(\theta_{13})$, with
2675 the strongest constraints around $\delta_{CP} \sim 1$. Consequently, this difference allows some
2676 of the degeneracy in a beam-only fit to be broken. Comparing the beam and joint
2677 fit log-likelihood scans, the 2σ continuous contour in δ_{CP} for beam samples is broken
2678 when the atmospheric samples are added. Furthermore, the width of the 3σ contours
2679 also becomes dependent upon the value of δ_{CP} . Whilst these are encouraging results
2680 for the joint fit, these are not sensitivity measurements as the nuisance parameters are
2681 fixed.

2682 The disappearance log-likelihood scans in $\sin^2(\theta_{23}) - \Delta m_{23}^2$ space show the expected
2683 result when considering the one-dimensional scans already discussed. The uncertainty
2684 on the width of $|\Delta m_{32}^2|$ is mostly driven by the beam-only sensitivities. However, the
2685 width of this contour in the inverted mass region ($\Delta m_{32}^2 < 0$) is significantly reduced
2686 due to the ability of the atmospheric samples to select the correct mass hierarchy (these
2687 log-likelihood scans use the Asimov A oscillation probabilities which assumes true

2688 normal hierarchy). The width of the uncertainty in $\sin^2(\theta_{23})$ is also reduce compared
 2689 to a beam-only analysis, with a further decrease in the inverted hierarchy region due
 2690 to mass hierarchy determination.

2691 In addition to the oscillation parameters, the response to the systematic model
 2692 parameters can also be considered. Due to the correlated cross section model, the most
 2693 informative DB: Finish this

2694 8.2. Monte Carlo Prediction

2695 Using the three sets of dial values defined in subsection 6.4.3, the predicted event rates
 2696 for each sample are defined in Table 8.1. Both the oscillated event rates assuming
 2697 Asimov A oscillation parameters (defined in Table 2.2) and the un-oscillated event
 2698 rates are given.

2699 Generally, samples which target CCQE interaction modes observe a decrease in
 2700 prediction when using the pre-fit dial values. This is in accordance with the Monte
 2701 Carlo being produced assumed $M_A^{QE} = 1.21\text{GeV}$ whilst the pre-fit dial value should
 2702 be $M_A^{QE} = 1.03\text{GeV}$, as suggested by [204]. Furthermore, the predicted event rates
 2703 of samples which target CCRES interaction modes is significantly reduced when
 2704 considering the post-ND fit. This follows the observations in subsection 6.4.3. The
 2705 strength of the accelerator neutrino experiment can also be seen in the remarkable
 2706 difference between the oscillated and unoscillated predictions in the FHC1Rmu and
 2707 RHC1Rmu samples. There is a very obvious decrease in the expected event rate between
 2708 the two predictions which is not as clearly observed in the atmospheric samples.
 2709 This is due to the fact that the beam energy is tuned to the maximum disappearance
 2710 probability, which is not the case for the naturally generated atmospheric neutrinos.

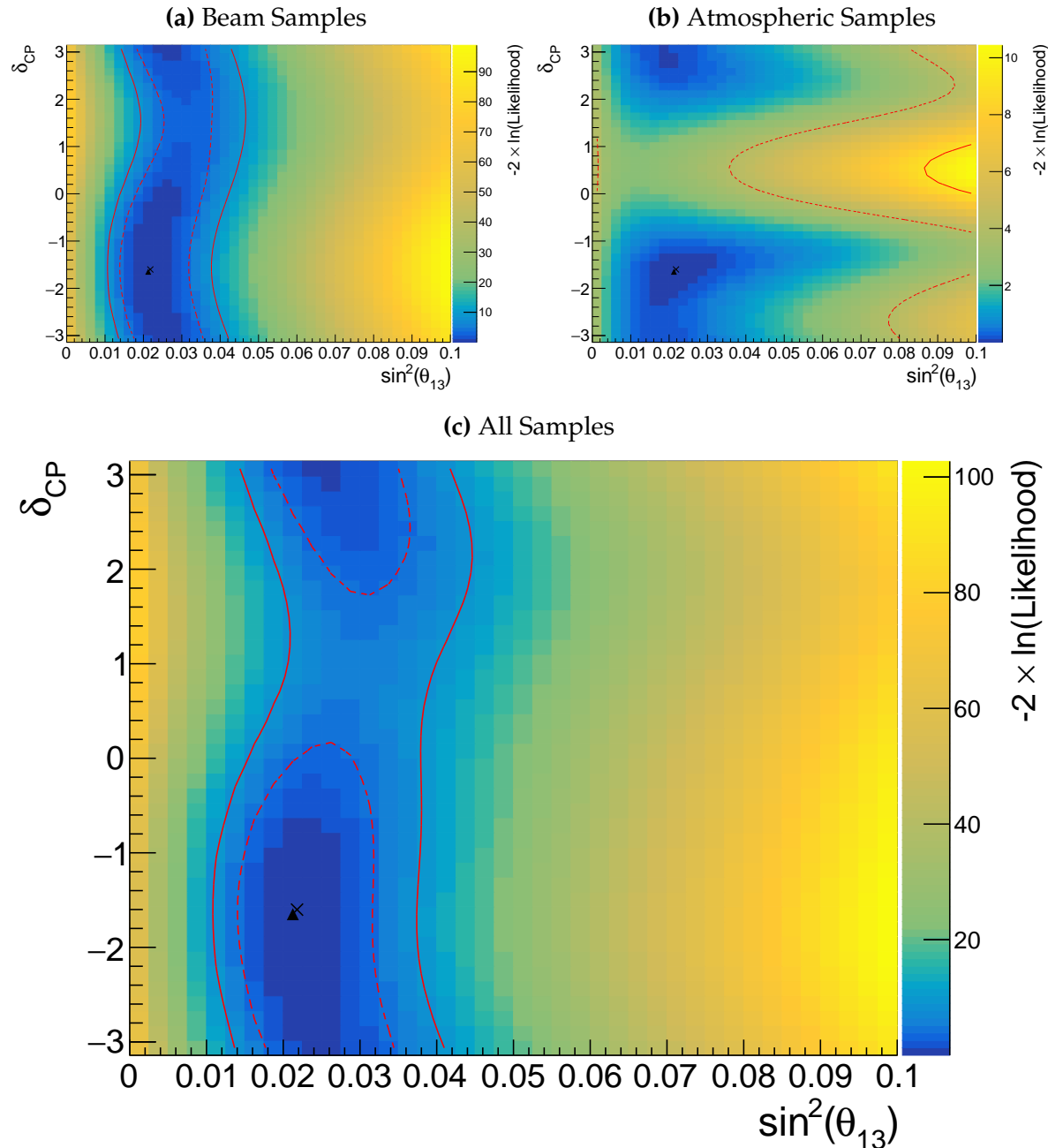


Figure 8.2.: Two-dimensional log-likelihood scan of the appearance ($\sin^2(\theta_{13})$ - δ_{CP}) parameters showing the response of the beam samples (top), atmospheric samples (middle) and the summed response (bottom). The Asimov A oscillation parameters, defined in Table 2.2, are assumed to be the true point (Black Cross). The position of the smallest log-likelihood is highlighted with the triangle. Prior uncertainty terms of the oscillation parameters are neglected. The two(three) sigma contour levels are illustrated with the dashed(solid) red line.

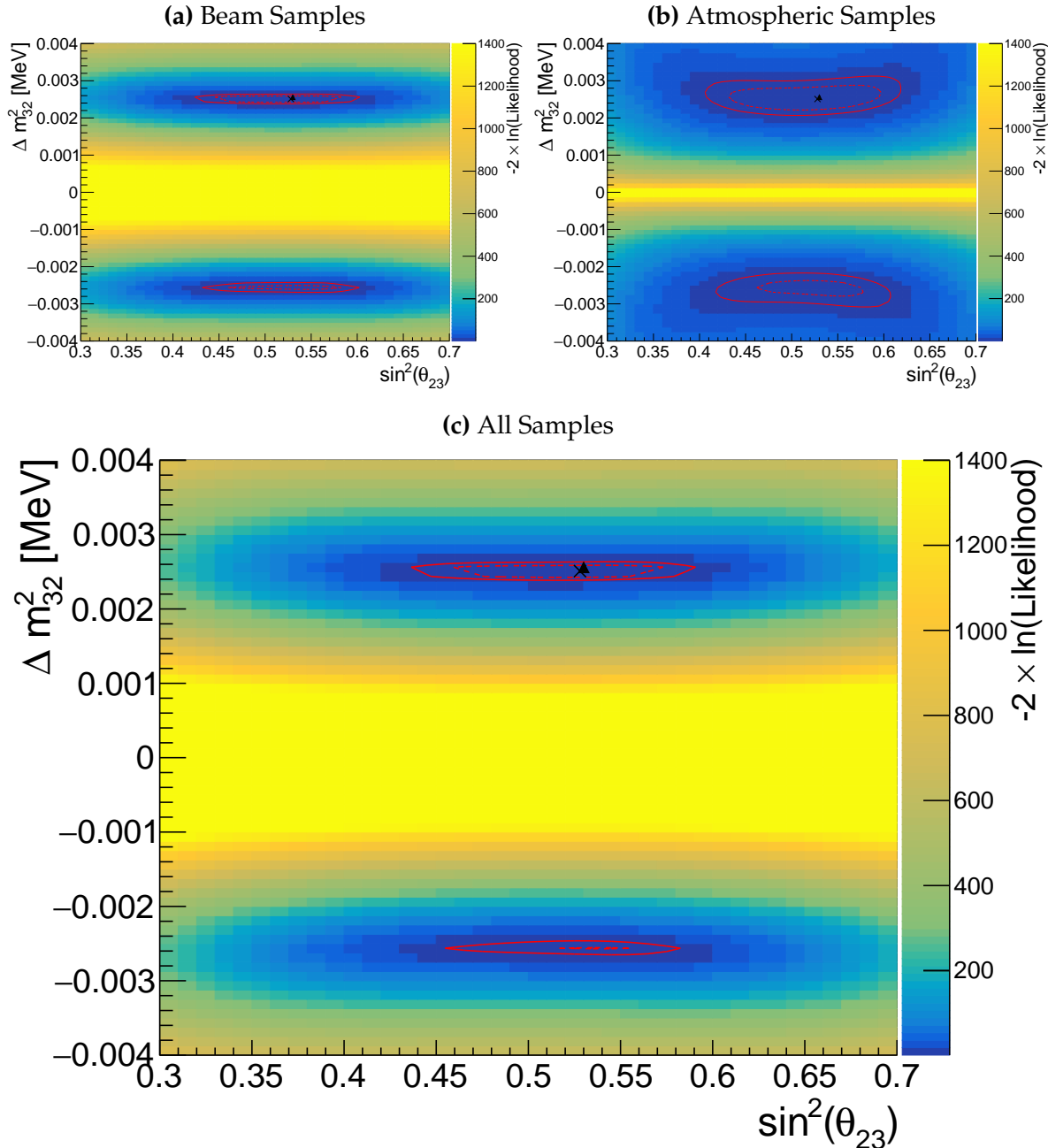


Figure 8.3.: Two-dimensional log-likelihood scan of the disappearance ($\sin^2(\theta_{23})$ - Δm_{23}^2) parameters showing the response of the beam samples (top), atmospheric samples (middle) and the summed response (bottom). The Asimov A oscillation parameters, defined in Table 2.2, are assumed to be the true point (Black Cross). The position of the smallest log-likelihood is highlighted with the triangle. Prior uncertainty terms of the oscillation parameters are neglected. The two(three) sigma contour levels are illustrated with the dashed(solid) red line.

Sample	Total Predicted Events					
	Generated		Pre-fit		Post-fit	
	Osc	UnOsc	Osc	UnOsc	Osc	UnOsc
SubGeV- <i>elike</i> -0d _c y	7121.0	7102.6	6556.8	6540.0	7035.2	7015.7
SubGeV- <i>elike</i> -1d _c y	704.8	725.5	693.8	712.8	565.7	586.0
SubGeV- <i>mulike</i> -0d _c y	1176.5	1737.2	1078.6	1588.1	1182.7	1757.1
SubGeV- <i>mulike</i> -1d _c y	5850.7	8978.1	5351.7	8205.1	5867.0	9009.9
SubGeV- <i>mulike</i> -2d _c y	446.9	655.2	441.6	647.7	345.9	505.6
SubGeV- <i>pi0like</i>	1438.8	1445.4	1454.9	1461.1	1131.1	1136.2
MultiGeV- <i>elike</i> - <i>nue</i>	201.4	195.6	201.1	195.3	202.6	196.7
MultiGeV- <i>elike</i> - <i>nuebar</i>	1141.5	1118.3	1060.7	1039.5	1118.5	1095.7
MultiGeV- <i>mulike</i>	1036.7	1435.8	963.1	1334.1	1015.2	1405.9
MultiRing- <i>elike</i> - <i>nue</i>	1025.1	982.2	1026.8	984.3	1029.8	986.4
MultiRing- <i>elike</i> - <i>nuebar</i>	1014.8	984.5	991.0	962.0	1008.9	978.5
MultiRing- <i>mulike</i>	2510.0	3474.4	2475.6	3425.8	2514.6	3480.4
MultiRingOther-1	1204.5	1279.1	1205.8	1280.3	1207.4	1281.0
PCStop	349.2	459.2	338.4	444.7	346.8	456.1
PCThr	1692.8	2192.5	1661.5	2149.8	1689.2	2187.8
UpStop- <i>mu</i>	751.2	1295.0	739.7	1271.6	750.4	1293.0
UpThruNonShower- <i>mu</i>	2584.4	3031.6	2577.9	3019.4	2586.8	3034.0
UpThruShower- <i>mu</i>	473.0	488.6	473.2	488.7	473.8	489.4
FHC1R <i>mu</i>	328.0	1409.2	301.1	1274.7	345.1	1568.0
RHC1R <i>mu</i>	133.0	432.3	122.7	396.2	135.0	443.9
FHC1Re	84.6	19.2	77.4	18.2	93.7	19.7
RHC1Re	15.7	6.4	14.6	6.1	15.9	6.3
FHC1Re1de	10.5	3.2	10.3	3.1	8.8	2.9

Table 8.1.: The Monte Carlo prediction of each sample observed at SK used within this analysis. Three model parameter tunes are considered, as defined in subsection 6.4.3. The oscillated predictions assumed Asimov A oscillation parameters provided in Table 2.2.

2712 **Appendix A**

2713 **Atmospheric Sample Spectra**

2714 This appendix documents the interaction mode breakdown of all the atmospheric
2715 samples used within the analysis. The generated tune of the model parameters and the
2716 Asimov A oscillation parameter set (defined in Table 2.2) are assumed. The livetime of
2717 SK-IV is taken to be 3244.4 days.

2718 **A.1. Binning**

2719 The lepton momentum and cosine zenith binning edges for the atmospheric samples
2720 used within this analysis are defined in Table A.1.

2721 **A.2. Fully Contained Sub-GeV Samples**

2722 The interaction mode breakdown of the fully contained Sub-GeV samples are shown
2723 in Figure A.1 and Figure A.2, for the samples with enriched CC0 π and CC1 π^\pm
2724 respectively.

2725 The CC0 π sample are dominated by CCQE events ($\sim 70\%$) with smaller contributions
2726 of 2p2h ($\sim 12\%$) and CC1 π ($\sim 10\%$) components. The energy peaks around
2727 300 MeV, which is slightly below that of the T2K samples but still has significant
2728 contribution upto 1 GeV which overlaps the T2K sample energy range.

2729 The one-ring CC1 π samples, where the pion is tagged via its decay electron, are
2730 dominated by CC1 π events ($\sim 75\%$) with a small contribution of CCM π ($\sim 10\%$).
2731 The two-ring pion sample is mostly dominated by the NC1 π^0 via resonances, and
2732 has several equally-sized contributions from CCQE, NC1 π^\pm via resonances, and NC
2733 coherent pion production, where the π^0 likely comes from nucleon and π^\pm final state
2734 interactions in the nucleus.

Sample	$\cos(\theta_Z)$ Bins	Momentum Bin Edges ($\log_{10}(P)$ MeV)
SubGeV- <i>elike</i> -0dcy	10	2.0, 2.4, 2.6, 2.8, 3.0, 3.2
SubGeV- <i>elike</i> -1dcy	1	2.0, 2.4, 2.6, 2.8, 3.0, 3.2
SubGeV- <i>mulike</i> -0dcy	10	2.0, 2.4, 2.6, 2.8, 3.0, 3.2
SubGeV- <i>mulike</i> -1dcy	10	2.0, 2.4, 2.6, 2.8, 3.0, 3.2
SubGeV- <i>mulike</i> -2dcy	1	2.0, 2.4, 2.6, 2.8, 3.0, 3.2
SubGeV- <i>pi0like</i>	1	2.0, 2.2, 2.4, 2.6, 2.8, 3.2
MultiGeV- <i>elike</i> -nue	10	3.0, 3.4, 3.7, 4.0, 5.0
MultiGeV- <i>elike</i> -nuebar	10	3.0, 3.4, 3.7, 4.0, 5.0
MultiGeV- <i>mulike</i>	10	3.0, 3.4, 5.0
MultiRing- <i>elike</i> -nue	10	3.0, 3.4, 3.7, 5.0
MultiRing- <i>elike</i> -nuebar	10	3.0, 3.4, 3.7, 5.0
MultiRing- <i>mulike</i>	10	2.0, 3.124, 3.4, 3.7, 5.0
MultiRing- <i>Other1</i>	10	3.0, 3.4, 3.7, 4.0, 5.0
PC-Stop	10	2.0, 3.4, 5.0
PC-Through	10	2.0, 3.124, 3.4, 3.7, 5.0
Upmu-Stop	10	3.2, 3.4, 3.7, 8.0
Upmu-Through-Showering	10	2.0, 8.0
Upmu-Through-NonShowering	10	2.0, 8.0

Table A.1.: The reconstructed cosine zenith and lepton momentum binning assigned to the atmospheric samples. The “ $\cos(\theta_Z)$ Bins” column illustrates the number of bins uniformly distributed over the $-1.0 \leq \cos(\theta_Z) \leq 1.0$ region for fully and partially contained samples and $-1.0 \leq \cos(\theta_Z) \leq 0.0$ region for up- μ samples.

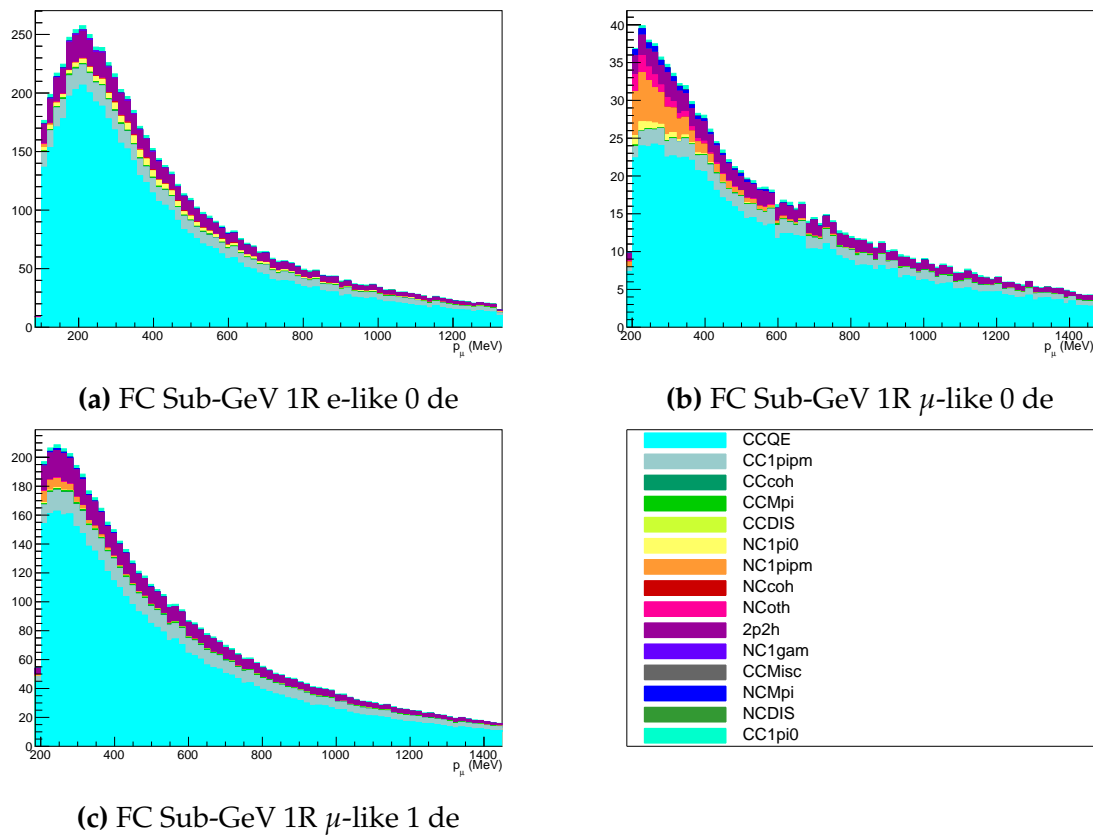


Figure A.1.: Breakdown by interaction mode of the FC Sub-GeV atmospheric samples targeting CC 0π events.

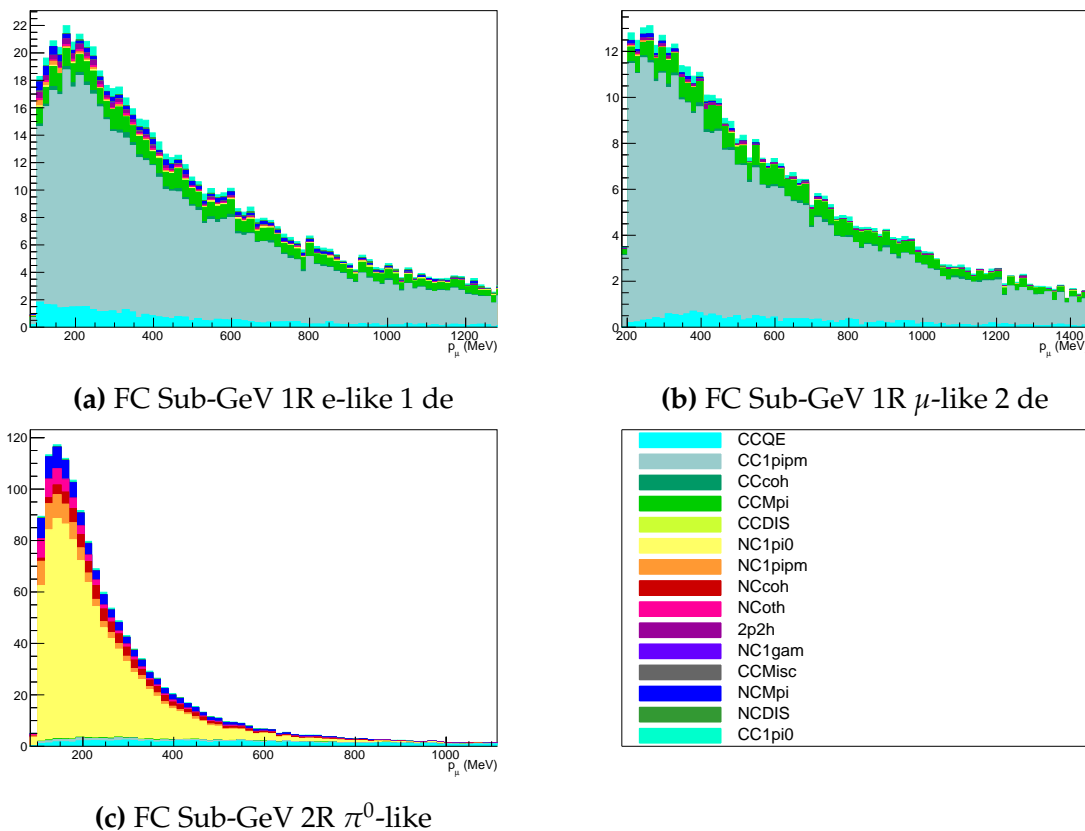
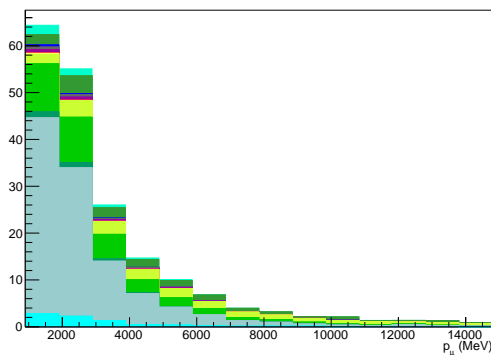


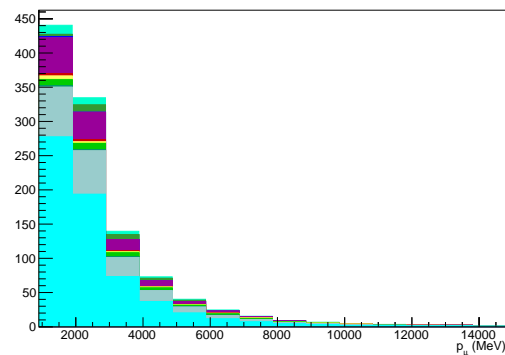
Figure A.2: Breakdown by interaction mode of the FC Sub-GeV atmospheric samples targeting single pion events.

A.3. Fully Contained Multi-GeV Samples

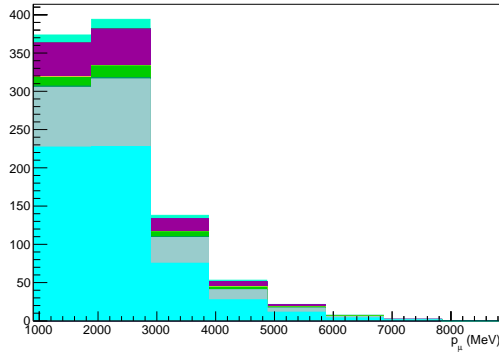
The interaction mode breakdown of fully contained multi-GeV samples is highlighted in Figure A.3. Due to the event selection applied in SK which targets π^+ and π^- separation, the ν_e sample mainly consists of events with pions (single pion production or multi-pion/DIS interactions). The pion separation is explained in Section section 6.1. This reasoning also explains the significant CCQE contribution of the $\bar{\nu}_e$ sample. The muon-like sample is dominated by CCQE interactions with $\sim 10 - 15\%$ 2p2h and CC1 π contribution of events.



(a) FC Multi-GeV single ring ν_e -like



(b) FC Multi-GeV single ring $\bar{\nu}_e$ -like



(c) FC Multi-GeV single ring μ -like

Figure A.3: Breakdown by interaction mode of the FC Multi-GeV single ring atmospheric samples.

²⁷⁴³ A.4. Fully Contained Multi-Ring Samples

²⁷⁴⁴ The interaction mode breakdown of fully contained multi-ring events is shown in Figure A.4. These samples see more interaction modes contributing in general, and there
²⁷⁴⁵ is a much larger contribution from multi-pion and DIS interaction modes, compared
²⁷⁴⁶ to the other samples.

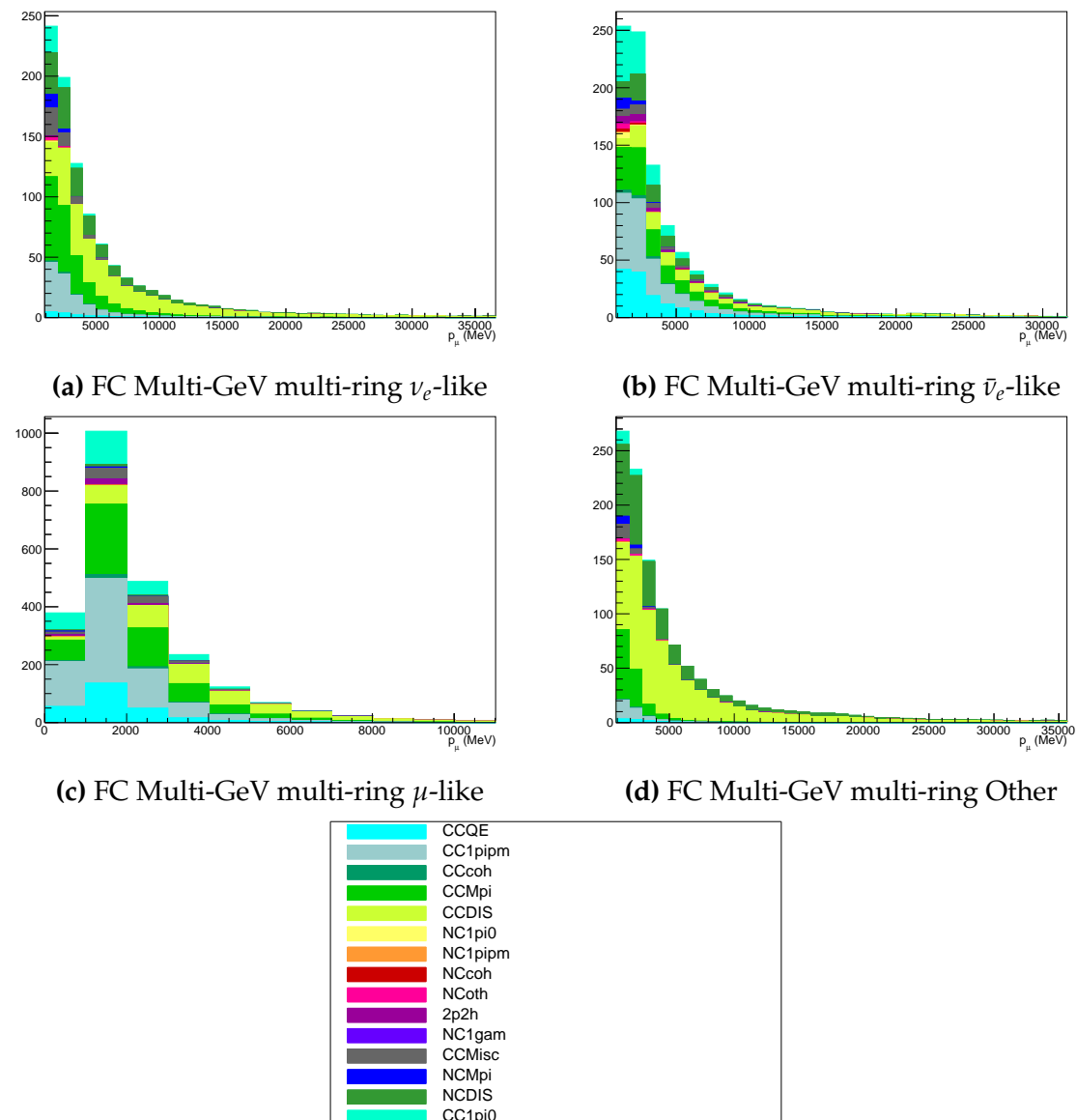


Figure A.4: Breakdown by interaction mode of the FC Multi-GeV multi-ring atmospheric samples.

²⁷⁴⁸ A.5. Partially Contained Samples

²⁷⁴⁹ The breakdown for partially contained samples is highlighted in Figure A.5. As with
²⁷⁵⁰ the multi-ring samples, there is no dominating interaction mode. The neutrino energies
²⁷⁵¹ of events in this sample extend into the tens of GeV and become dominated by DIS
²⁷⁵² interaction modes in the high energy limit.

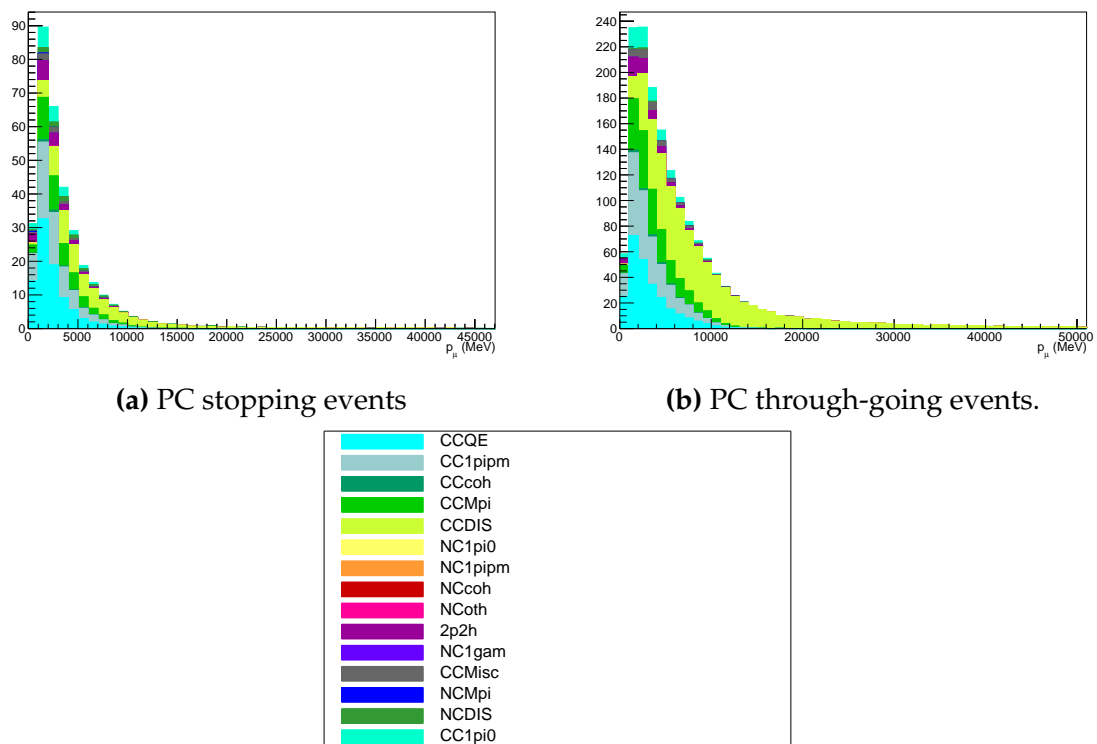
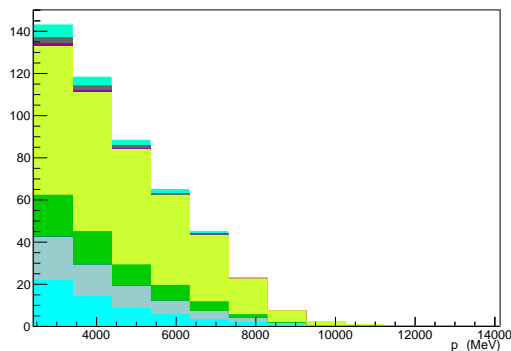
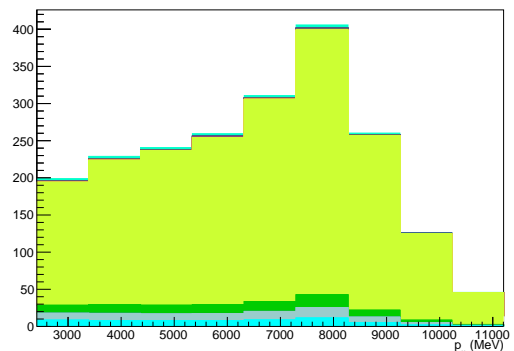
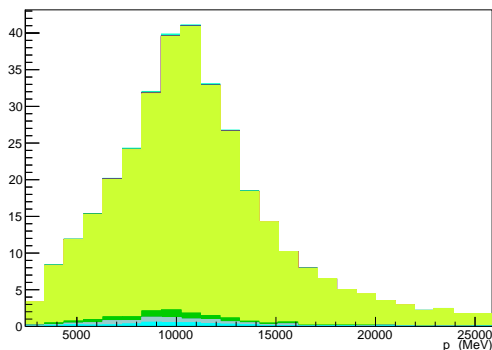
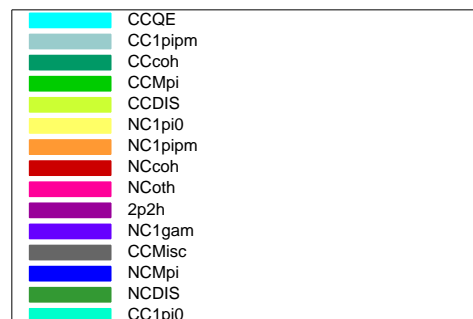


Figure A.5.: Breakdown by interaction mode of the PC atmospheric samples.

²⁷⁵³ A.6. Upward-Going Muon Samples

²⁷⁵⁴ The breakdown for upward-going muons is illustrated in Figure A.6. These samples
²⁷⁵⁵ are significantly dominated by DIS interactions with energies extending up into the
²⁷⁵⁶ hundreds of GeV.

(a) Up- μ stopping events(b) Up- μ through going non showering events(c) Up- μ through going showering events**Figure A.6.:** Breakdown by interaction mode of the atmospheric upward going muon samples.

₂₇₅₈ **Bibliography**

- ₂₇₅₉ [1] J. Chadwick, Verhandl. Dtsc. Phys. Ges. **16**, 383 (1914).
- ₂₇₆₀ [2] C. D. Ellis and W. A. Wooster, Proc. R. Soc. Lond. A Math. Phys. Sci. **117**, 109
₂₇₆₁ (1927).
- ₂₇₆₂ [3] W. Pauli, Phys. Today **31N9**, 27 (1978).
- ₂₇₆₃ [4] E. Fermi, Z. Phys. **88**, 161 (1934).
- ₂₇₆₄ [5] F. Reines and C. L. Cowan, Phys. Rev. **92**, 830 (1953).
- ₂₇₆₅ [6] C. L. Cowan, F. Reines, F. B. Harrison, H. W. Kruse, and A. D. McGuire, Science
₂₇₆₆ **124**, 103 (1956), <http://science.sciencemag.org/content/124/3212/103.full.pdf>.
- ₂₇₆₇ [7] G. Danby *et al.*, Phys. Rev. Lett. **9**, 36 (1962).
- ₂₇₆₈ [8] K. Kodama *et al.*, Physics Letters B **504**, 218 (2001).
- ₂₇₆₉ [9] LSND, A. Aguilar-Arevalo *et al.*, Phys. Rev. **D64**, 112007 (2001), hep-ex/0104049.
- ₂₇₇₀ [10] MiniBooNE Collaboration, A. A. Aguilar-Arevalo *et al.*, Phys. Rev. Lett. **110**,
₂₇₇₁ 161801 (2013).
- ₂₇₇₂ [11] Planck Collaboration *et al.*, aap **641** (2020).
- ₂₇₇₃ [12] The ALEPH Collaboration, The Delphi Collaboration, The L3 Collaboration, The
₂₇₇₄ SLD Collaboration, The LEP Electroweak Working Group, The SLD Electroweak
₂₇₇₅ and Heavy Flavour Groups, J. A. Bagger *et al.*, Physics Reports **427**, 257 (2006).
- ₂₇₇₆ [13] B. Pontecorvo, Sov. Phys. JETP **26**, 984 (1968), [Zh. Eksp. Teor. Fiz. 53, 1717 (1967)].
- ₂₇₇₇ [14] B. Pontecorvo, Sov. Phys. JETP **7**, 172 (1958), [Zh. Eksp. Teor. Fiz. 34, 247 (1957)].
- ₂₇₇₈ [15] M. Kobayashi and T. Maskawa, Progress of Theoretical Physics **49**, 652 (1973).
- ₂₇₇₉ [16] N. Cabibbo, Phys. Rev. Lett. **10**, 531 (1963).
- ₂₇₈₀ [17] A. M. and, Journal of Physics: Conference Series **587**, 012030 (2015).
- ₂₇₈₁ [18] A. Y. Smirnov, (2003).
- ₂₇₈₂ [19] S. Mikheyev and A. Smirnov, Soviet Journal of Nuclear Physics **42**, 913 (1985).

- 2783 [20] L. Wolfenstein, Phys. Rev. D **17**, 2369 (1978).
- 2784 [21] V. D. Barger, K. Whisnant, S. Pakvasa, and R. J. N. Phillips, Phys. Rev. D **22**, 2718
2785 (1980).
- 2786 [22] The Super-Kamiokande Collaboration, Y. Ashie *et al.*, Phys. Rev. Lett. **93**, 101801
2787 (2004).
- 2788 [23] SNO Collaboration, Q. R. Ahmad *et al.*, Phys. Rev. Lett. **89**, 011301 (2002).
- 2789 [24] 2015 Nobel prize in Physics as listed by Nobelprize.org, [https://www.](https://www.nobelprize.org/nobel_prizes/physics/laureates/2015/)
2790 [nobelprize.org/nobel_prizes/physics/laureates/2015/](https://www.nobelprize.org/nobel_prizes/physics/laureates/2015/), Accessed: 22-06-
2791 2022.
- 2792 [25] J. A. Formaggio and G. P. Zeller, Rev. Mod. Phys. **84**, 1307 (2012), 1305.7513.
- 2793 [26] A. Bellerive, Int. J. Mod. Phys. A **19**, 1167 (2004).
- 2794 [27] R. Davis, D. S. Harmer, and K. C. Hoffman, Phys. Rev. Lett. **20**, 1205 (1968).
- 2795 [28] N. Vinyoles *et al.*, Astrophys. J. **835**, 202 (2017).
- 2796 [29] V. Gribov and B. Pontecorvo, Phys. Lett. B **28**, 493 (1969).
- 2797 [30] K. S. Hirata *et al.*, Phys. Rev. Lett. **63**, 16 (1989).
- 2798 [31] W. Hampel *et al.*, Phys. Lett. B **447**, 127 (1999).
- 2799 [32] SAGE Collaboration, J. N. Abdurashitov *et al.*, Phys. Rev. C **60**, 055801 (1999).
- 2800 [33] Q. R. Ahmad *et al.*, Phys. Rev. Lett. **89** (2002).
- 2801 [34] Borexino Collaboration, Nature **562**, 505 (2018).
- 2802 [35] B. Aharmim *et al.*, Astrophys. J. **653**, 1545 (2006).
- 2803 [36] M. Agostini *et al.*, (2020).
- 2804 [37] S. Andringa *et al.*, Adv. High Energy Phys. **2016**, 1 (2016).
- 2805 [38] J. F. Beacom *et al.*, Chin. phys. C **41**, 023002 (2017).
- 2806 [39] F. An *et al.*, J. Phys. G Nucl. Part. Phys. **43**, 030401 (2016).
- 2807 [40] J. Aalbers *et al.*, (2020), 2006.03114.
- 2808 [41] T. K. Gaisser and M. Honda, (2002).

- 2809 [42] G. D. Barr, T. K. Gaisser, P. Lipari, S. Robbins, and T. Stanev, Physical Review D
2810 **70** (2004).
- 2811 [43] M. Honda, T. Kajita, K. Kasahara, S. Midorikawa, and T. Sanuki, Physical Review
2812 D **75** (2007).
- 2813 [44] M. Honda, T. Kajita, K. Kasahara, and S. Midorikawa, Phys. Rev. D **70**, 043008
2814 (2004).
- 2815 [45] M. Honda, T. Kajita, K. Kasahara, and S. Midorikawa, Phys. Rev. D **83**, 123001
2816 (2011).
- 2817 [46] A. Fasso, A. Ferrari, P. R. Sala, and J. Ranft, (2001).
- 2818 [47] Y. Ashie *et al.*, Physical Review D **71** (2005).
- 2819 [48] F. Reines *et al.*, Phys. Rev. Lett. **15**, 429 (1965).
- 2820 [49] D. Casper *et al.*, Phys. Rev. Lett. **66**, 2561 (1991).
- 2821 [50] K. S. Hirata *et al.*, Phys. Lett. B **280**, 146 (1992).
- 2822 [51] Z. Li *et al.*, Physical Review D **98** (2018).
- 2823 [52] Kamiokande Collaboration *et al.*, (2017).
- 2824 [53] T2K Collaboration, Nature **580**, 339 (2020).
- 2825 [54] M. A. Acero *et al.*, Phys. Rev. Lett. **123**, 151803 (2019).
- 2826 [55] M. G. Aartsen *et al.*, Phys. Rev. Lett. **120** (2018).
- 2827 [56] P. Adamson *et al.*, Phys. Rev. Lett. **112** (2014).
- 2828 [57] M. S. Athar *et al.*, Progress in Particle and Nuclear Physics **124**, 103947 (2022).
- 2829 [58] G. Danby *et al.*, Phys. Rev. Lett. **9**, 36 (1962).
- 2830 [59] K. Abe *et al.*, Physical Review D **87** (2013).
- 2831 [60] MINOS Collaboration, D. G. Michael *et al.*, Phys. Rev. Lett. **97**, 191801 (2006).
- 2832 [61] G. Danby *et al.*, Phys. Rev. Lett. **9**, 36 (1962).
- 2833 [62] NOvA Collaboration, M. A. Acero *et al.*, Phys. Rev. Lett. **123**, 151803 (2019).
- 2834 [63] B. Abi, R. Acciarri, M. A. Acero, and G. e. a. Adamov, Eur. Phys. J. C Part. Fields

- 2835 **80** (2020).
- 2836 [64] Hyper-Kamiokande Proto-Collaboration *et al.*, Prog. Theor. Exp. Phys. **2015**,
2837 53C02 (2015).
- 2838 [65] C. Blanco, D. Hooper, and P. Machado, Physical Review D **101** (2020).
- 2839 [66] MicroBooNE Collaboration *et al.*, Search for an Excess of Electron Neutrino
2840 Interactions in MicroBooNE Using Multiple Final State Topologies, 2021.
- 2841 [67] KARMEN Collaboration, B. Armbruster *et al.*, Phys. Rev. D **65**, 112001 (2002).
- 2842 [68] S.-B. Kim, T. Lasserre, and Y. Wang, Adv. High Energy Phys. **2013**, 1 (2013).
- 2843 [69] M. Sajjad Athar *et al.*, Prog. Part. Nucl. Phys. **124**, 103947 (2022), 2111.07586.
- 2844 [70] K. Abe *et al.*, Nucl. Instrum. Methods Phys. Res. A **1027**, 166248 (2022).
- 2845 [71] F. P. An *et al.*, Phys. Rev. Lett. **108**, 171803 (2012).
- 2846 [72] RENO Collaboration, J. K. Ahn *et al.*, Phys. Rev. Lett. **108**, 191802 (2012).
- 2847 [73] Double Chooz Collaboration, Y. Abe *et al.*, Phys. Rev. Lett. **108**, 131801 (2012).
- 2848 [74] J. Collaboration *et al.*, TAO Conceptual Design Report: A Precision Measurement
2849 of the Reactor Antineutrino Spectrum with Sub-percent Energy Resolution, 2020,
2850 2005.08745.
- 2851 [75] for the RENO Collaboration, New results from RENO and the 5 MeV excess,
2852 AIP Publishing LLC, 2015.
- 2853 [76] Y. Abe *et al.*, Journal of High Energy Physics **2014** (2014).
- 2854 [77] Daya Bay Collaboration, D. Adey *et al.*, Phys. Rev. Lett. **123**, 111801 (2019).
- 2855 [78] M. P. Decowski, Nucl. Phys. B. **908**, 52 (2016).
- 2856 [79] The KamLAND Collaboration, A. Gando *et al.*, Phys. Rev. D **83**, 052002 (2011).
- 2857 [80] P. Dunne, Latest Neutrino oscillation results from T2K, 2020.
- 2858 [81] M. Tanabashi *et al.*, Phys. Rev. D. **98** (2018).
- 2859 [82] Particle Data Group, R. L. Workman and Others, PTEP **2022**, 083C01 (2022).
- 2860 [83] T2K Collaboration, K. Abe *et al.*, Phys. Rev. Lett. **112**, 181801 (2014).

- [84] Y. Fukuda *et al.*, Phys. Rev. Lett. **81**, 1562 (1998).
- [85] Linyan Wan, (2022).
- [86] K. Abe *et al.*, Nuclear Instruments and Methods in Physics Research Section A: Accelerators, Spectrometers, Detectors and Associated Equipment **737**, 253 (2014).
- [87] S. Fukuda *et al.*, Nucl. Instrum. Methods Phys. Res. A **501**, 418 (2003).
- [88] Y. Itow *et al.*, (2001).
- [89] M. Jiang *et al.*, Prog. Theor. Exp. Phys. **2019** (2019).
- [90] S. Fukuda *et al.*, Nuclear Instruments and Methods in Physics Research Section A: Accelerators, Spectrometers, Detectors and Associated Equipment **501**, 418 (2003), <http://www.sciencedirect.com/science/article/pii/S016890020300425X>.
- [91] Y. Nakano *et al.*, Nucl. Instrum. Methods Phys. Res. A **977**, 164297 (2020).
- [92] Hamamatsu, Hamamatsu Photonics Photomultiplier Tubes Handbook.
- [93] K. Abe *et al.*, Nucl. Instrum. Methods Phys. Res. A **1027**, 166248 (2022).
- [94] J. F. Beacom and M. R. Vagins, Phys. Rev. Lett. **93**, 171101 (2004).
- [95] L. Marti *et al.*, Nucl. Instrum. Methods Phys. Res. A **959**, 163549 (2020).
- [96] L. Marti *et al.*, (2019).
- [97] M. Vagins, Solar/DSNB Neutrino_SK-Gd, 2022.
- [98] J. Focht, PhD thesis, Massachusetts Institute of Technology, 2004.
- [99] T. Tanimori *et al.*, IEEE Transactions on Nuclear Science **36**, 497 (1989).
- [100] Super-Kamiokande Collaboration, J. Hosaka *et al.*, Phys. Rev. D **73**, 112001 (2006).
- [101] H. Nishino *et al.*, Nucl. Instrum. Methods Phys. Res. A **610**, 710 (2009).
- [102] S. Yamada *et al.*, IEEE Transactions on Nuclear Science **57**, 428 (2010).
- [103] S. Yamada, Y. Hayato, Y. Obayashi, and M. Shiozawa, New online system without hardware trigger for the Super-Kamiokande experiment, in *2007 IEEE Nuclear Science Symposium Conference Record*, IEEE, 2007.

- 2888 [104] G. Carminati, Phys. Procedia **61**, 666 (2015).
- 2889 [105] P. A. Čerenkov, Phys. Rev. **52**, 378 (1937).
- 2890 [106] I. Frank and I. Tamm, Coherent visible radiation of fast electrons passing
2891 through matter, in *Selected Papers*, pp. 29–35, Springer Berlin Heidelberg, Berlin,
2892 Heidelberg, 1991.
- 2893 [107] The T2K Collaboration, KEK Proposal (2001),
2894 <http://neutrino.kek.jp/jhfnu/loi/loi.v2.030528.pdf>.
- 2895 [108] Y. Itow *et al.*, (2001), hep-ex/0106019.
- 2896 [109] The K2K Collaboration and S. H. Ahn, (2001), hep-ex/0103001.
- 2897 [110] The T2K Collaboration, KEK Proposal (2006), http://j-parc.jp/researcher/Hadron/en/pac_0606/pdf/p11-Nishikawa.pdf.
- 2899 [111] C. Bronner, Accelerator Neutrino I_Recent results from T2K, 2022.
- 2900 [112] T2K Collaboration, K. Abe *et al.*, Phys. Rev. Lett. **112**, 061802 (2014),
2901 <https://link.aps.org/doi/10.1103/PhysRevLett.112.061802>.
- 2902 [113] NINJA Collaboration, T. Fukuda *et al.*, Proposal for precise measurement of
2903 neutrino-water cross-section in NINJA physics run, Proposal for J-PARC and
2904 KEK, 2017.
- 2905 [114] T. Ovsiannikova *et al.*, Physics of Particles and Nuclei **48**, 1014 (2017),
2906 <https://doi.org/10.1134/S1063779617060478>.
- 2907 [115] M. Antonova *et al.*, Journal of Instrumentation **12**, C07028 (2017),
2908 <http://stacks.iop.org/1748-0221/12/i=07/a=C07028>.
- 2909 [116] The T2K Collaboration, K. Abe *et al.*, Phys. Rev. D **102**, 012007 (2020).
- 2910 [117] K. Abe *et al.*, Progress of Theoretical and Experimental Physics **2021** (2021).
- 2911 [118] The T2K Collaboration, K. Abe *et al.*, Nuclear Instruments
2912 and Methods in Physics Research Section A: Accelerators, Spectrometers,
2913 Detectors and Associated Equipment **659**, 106 (2011),
2914 <http://www.sciencedirect.com/science/article/pii/S0168900211011910>.
- 2915 [119] K. Matsuoka *et al.*, Nuclear Instruments and Methods in Physics Research Section
2916 A: Accelerators, Spectrometers, Detectors and Associated Equipment **624**, 591

- 2917 (2010), <http://www.sciencedirect.com/science/article/pii/S016890021002098X>.
- 2918 [120] K. Abe *et al.*, Phys. Rev. D. **103** (2021).
- 2919 [121] T. Vladisavljevic, *Predicting the T2K neutrino flux and measuring oscillation parameters* Springer theses, 1 ed. (Springer Nature, Cham, Switzerland, 2020).
- 2920
- 2921 [122] D. Beavis, A. Carroll, and I. Chiang, (1995).
- 2922 [123] P.-A. Amaudruz *et al.*, Nuclear Instruments and Methods in Physics Research
2923 Section A: Accelerators, Spectrometers, Detectors and Associated Equipment
2924 **696**, 1 (2012).
- 2925 [124] N. Abgrall *et al.*, Nuclear Instruments and Methods in Physics Research Section
2926 A: Accelerators, Spectrometers, Detectors and Associated Equipment **637**, 25
2927 (2011).
- 2928 [125] S. Assylbekov *et al.*, Nuclear Instruments and Methods in Physics Research
2929 Section A: Accelerators, Spectrometers, Detectors and Associated Equipment
2930 **686**, 48 (2012).
- 2931 [126] D. Allan *et al.*, Journal of Instrumentation **8**, P10019 (2013).
- 2932 [127] F. Vannucci, Advances in High Energy Physics **2014**, 1 (2014).
- 2933 [128] UA1 magnet sets off for a second new life, 2022.
- 2934 [129] S. Aoki *et al.*, Nuclear Instruments and Methods in Physics Research Section
2935 A: Accelerators, Spectrometers, Detectors and Associated Equipment **698**, 135
2936 (2013).
- 2937 [130] K. Suzuki *et al.*, Progress of Theoretical and Experimental Physics **2015**, 53C01
2938 (2015).
- 2939 [131] S. Brooks, A. Gelman, G. L. Jones, and X.-L. Meng, *Handbook of Markov Chain
2940 Monte Carlo* (CRC Press, 2011).
- 2941 [132] W. R. Gilks, S. Richardson, and D. J. Spiegelhalter, *Markov Chain Monte Carlo in
2942 Practice* (Chapman & Hall/CRC Interdisciplinary Statistics, 1995).
- 2943 [133] C. Wret, *Minimising systematic uncertainties in the T2K experiment using near-
2944 detector and external data*, PhD thesis, Imperial College London, 2018.
- 2945 [134] K. E. Duffy, *Measurement of the Neutrino Oscillation Parameters $\sin^2 \theta_{23}$, Δm_{32}^2 ,*

- 2946 $\sin^2 \theta_{13}$, and δ_{CP} in Neutrino and Antineutrino Oscillation at T2K, PhD thesis, Oriel
2947 College, University of Oxford, 2016.
- 2948 [135] T. Bayes, Rev. Phil. Trans. Roy. Soc. Lond. **53**, 370 (1764).
- 2949 [136] N. Metropolis, A. W. Rosenbluth, M. N. Rosenbluth, A. H. Teller, and E. Teller,
2950 Journal of Chemical Physics **21** (1970).
- 2951 [137] W. K. Hastings, Biometrika **57** (1970).
- 2952 [138] J. Dunkley, M. Bucher, P. G. Ferreira, K. Moodley, and C. Skordis, Mon. Not. R.
2953 Astron. Soc. **356**, 925 (2005).
- 2954 [139] Particle Data Group *et al.*, Prog. Theor. Exp. Phys. **2020** (2020).
- 2955 [140] H. Jeffreys, *The Theory of Probability* Oxford Classic Texts in the Physical Sciences
2956 (, 1939).
- 2957 [141] R. E. Kass and A. E. Raftery, J. Am. Stat. Assoc. **90**, 773 (1995).
- 2958 [142] T. Böhlen *et al.*, Nuclear Data Sheets **120**, 211 (2014),
2959 <http://www.sciencedirect.com/science/article/pii/S0090375214005018>.
- 2960 [143] R. Brun *et al.*, GEANT: Detector Description and Simulation Tool; Oct 1994 CERN
2961 Program Library (CERN, Geneva, 1993), <http://cds.cern.ch/record/1082634>,
2962 Long Writeup W5013.
- 2963 [144] T2K Collaboration, K. Abe *et al.*, Phys. Rev. D **87**, 012001 (2013).
- 2964 [145] C. Zeitnitz and T. Gabriel, Nuclear Instruments and Methods in Physics Research Section A: Accelerators, Spectrometers, Detectors and Associated Equipment **349**, 106 (1994),
2965 <http://www.sciencedirect.com/science/article/pii/0168900294906130>.
- 2966 [146] A. Fiorentini *et al.*, T2K Technical Note **217** (2017).
- 2967 [147] N. Abgrall *et al.*, Physical Review C **84** (2011).
- 2968 [148] N. Abgrall *et al.*, Physical Review C **85** (2012).
- 2969 [149] N. Abgrall *et al.*, Nuclear Instruments and Methods in Physics Research Section
2970 A: Accelerators, Spectrometers, Detectors and Associated Equipment **701**, 99
2971 (2013), <http://www.sciencedirect.com/science/article/pii/S016890021201234X>.

- 2974 [150] HARP Collaboration, M. Apollonio *et al.*, Phys. Rev. C **80**, 035208 (2009),
2975 <https://link.aps.org/doi/10.1103/PhysRevC.80.035208>.
- 2976 [151] B. Blau *et al.*, Nuclear Physics B - Proceedings Supplements **113**, 125 (2002).
- 2977 [152] S. Haino *et al.*, Physics Letters B **594**, 35 (2004).
- 2978 [153] NASA, U.S. Standard Atmosphere, 1976, 1976.
- 2979 [154] S. Roesler, R. Engel, and J. Ranft, The Monte Carlo Event Generator DPMJET-III,
2980 in *Advanced Monte Carlo for Radiation Physics, Particle Transport Simulation and*
2981 *Applications*, pp. 1033–1038, Springer Berlin Heidelberg, 2001.
- 2982 [155] K. Niita *et al.*, Radiation Measurements **41**, 1080 (2006).
- 2983 [156] T. Sanuki *et al.*, Physics Letters B **541**, 234 (2002).
- 2984 [157] P. Achard *et al.*, Physics Letters B **598**, 15 (2004).
- 2985 [158] K. Sato, Atmospheric Neutrino_Reviews on neutrino fluxes (low E atm nu),
2986 2022.
- 2987 [159] Y. Hayato and L. Pickering, The European Physical Journal Special Topics **230**,
2988 4469 (2021).
- 2989 [160] Y. Hayato, Acta Physica Polonica B **40** (2009).
- 2990 [161] C. L. Smith, Physics Reports **3**, 261 (1972),
2991 <http://www.sciencedirect.com/science/article/pii/0370157372900105>.
- 2992 [162] O. Benhar, A. Fabrocini, and S. Fantoni, Nuclear Physics A **497**, 423 (1989).
- 2993 [163] R. Bradford, A. Bodek, H. Budd, and J. Arrington, Nuclear
2994 Physics B - Proceedings Supplements **159**, 127 (2006),
2995 <http://www.sciencedirect.com/science/article/pii/S0920563206005184>,
2996 Proceedings of the 4th International Workshop on Neutrino-Nucleus Interac-
2997 tions in the Few-GeV Region.
- 2998 [164] A. A. Aguilar-Arevalo *et al.*, Physical Review D **81** (2010).
- 2999 [165] R. Gran, J. Nieves, F. Sanchez, and M. J. V. Vacas, Phys. Rev. D **88**, 113007 (2013),
3000 <https://link.aps.org/doi/10.1103/PhysRevD.88.113007>.
- 3001 [166] C. Berger and L. M. Sehgal, Phys. Rev. D **76**, 113004 (2007).

- 3002 [167] C. Berger and L. M. Sehgal, Phys. Rev. D **79**, 053003 (2009),
3003 <https://link.aps.org/doi/10.1103/PhysRevD.79.053003>.
- 3004 [168] T. Sjöstrand, Computer Physics Communications **82**, 74 (1994).
- 3005 [169] C. Bronner and M. Hartz, Tuning of the Charged Hadrons Multiplicities for Deep
3006 Inelastic Interactions in NEUT, in *Proceedings of the 10th International Workshop on*
3007 *Neutrino-Nucleus Interactions in Few-GeV Region (NuInt15)*, Journal of the Physical
3008 Society of Japan, 2016.
- 3009 [170] M. Glück, E. Reya, and A. Vogt, The European Physical Journal C **5**, 461 (1998).
- 3010 [171] A. Bodek and U.-k. Yang, Axial and Vector Structure Functions for Electron- and
3011 Neutrino- Nucleon Scattering Cross Sections at all Q^2 using Effective Leading
3012 order Parton Distribution Functions, 2010.
- 3013 [172] A. Bodek and U.-K. Yang, (2010).
- 3014 [173] S. Gollapinni, (2016).
- 3015 [174] E. S. P. Guerra *et al.*, Phys. Rev. D **99**, 052007 (2019).
- 3016 [175] GEANT4, S. Agostinelli *et al.*, Nucl. Instrum. Meth. **A506**, 250 (2003).
- 3017 [176] R. Brun, F. Bruyant, M. Maire, A. C. McPherson, and P. Zanarini, (1987).
- 3018 [177] K. Abe *et al.*, Physical Review Letters **121** (2018).
- 3019 [178] K. Abe *et al.*, Physical Review D **91** (2015).
- 3020 [179] R. Patterson *et al.*, Nuclear Instruments and Methods in Physics Research Section
3021 A: Accelerators, Spectrometers, Detectors and Associated Equipment **608**, 206
3022 (2009).
- 3023 [180] e. a. S. Berkman, T2K Technical Note **146** (2013).
- 3024 [181] e. a. A. Himmel, T2K Technical Note **219** (2015).
- 3025 [182] F. a. James, (1998), CERN Program Library Long Writeups.
- 3026 [183] X. Li and M. Wilking, T2K Technical Note **319** (2017).
- 3027 [184] S. Tobayama, *An Analysis of the Oscillation of Atmospheric Neutrinos*, PhD thesis,
3028 British Columbia U., 2016.

- 3029 [185] e. a. D. Barrow, T2K Technical Note **399** (2020).
- 3030 [186] A. Maghrabi, A. Aldosari, and M. Almutairi, Advances in Space Research **68**,
3031 2941 (2021).
- 3032 [187] Super-Kamiokande Collaboration, K. Abe *et al.*, Phys. Rev. D **97**, 072001 (2018),
3033 <https://link.aps.org/doi/10.1103/PhysRevD.97.072001>.
- 3034 [188] Particle Data Group, J. Beringer *et al.*, Phys. Rev. D **86**, 010001 (2012).
- 3035 [189] Y. N. and, Journal of Physics: Conference Series **888**, 012191 (2017).
- 3036 [190] M. Jiang, *Study of the neutrino mass hierarchy with the atmospheric neutrino data*
3037 *collected in Super-Kamiokande IV*, PhD thesis, Kyoto University, 2019.
- 3038 [191] S. N. K. Iyogi and Y. Obayashi., T2K Technical Note **027** (2011).
- 3039 [192] LeeKaPik, *Study of the neutrino mass hierarchy with the atmospheric neutrino data*
3040 *observed in Super-Kamiokande*, PhD thesis, Tokyo University, 2012.
- 3041 [193] The Super-Kamiokande Collaboration, R. Wendell *et al.*, Phys. Rev. D **81**, 092004
3042 (2010).
- 3043 [194] Super-Kamiokande Collaboration, J. Hosaka *et al.*, Phys. Rev. D **74**, 032002
3044 (2006).
- 3045 [195] L. M. et al, T2K Technical Note **395** (2020).
- 3046 [196] P. B. et al., T2K Technical Note **212** (2015).
- 3047 [197] W. Parker, *Constraining Systematic Uncertainties at T2K using Near Detector Data*,
3048 PhD thesis, Royal Holloway University of London, 2020.
- 3049 [198] V. B. et al., T2K Technical Note **246** (2015).
- 3050 [199] J. Missert, T2K Technical Note **318** (2017).
- 3051 [200] e. a. J. Chakrani, T2K Technical Note **414** (2022).
- 3052 [201] T2K Collaboration, M. Wascko, T2K Status, Results, and Plans, Neutrino 2018,
3053 2018.
- 3054 [202] e. a. Tomislav Vladisavljevic, T2K Technical Note **354** (2020).
- 3055 [203] G. Ambrosini *et al.*, Phys. Lett. B **420**, 225 (1998).

- 3056 [204] e. a. Edward Atkin, T2K Technical Note **344** (2019).
- 3057 [205] e. a. D. Barrow, T2K Technical Note **422** (2022).
- 3058 [206] The MiniBooNE Collaboration, A. A. Aguilar-Arevalo *et al.*, Phys. Rev. D **81**,
3059 013005 (2010), <https://link.aps.org/doi/10.1103/PhysRevD.81.013005>.
- 3060 [207] P. de Perio and J. Imber, T2K Technical Note **186** (2014).
- 3061 [208] P. de Perio and J. Imber, T2K Technical Note **107** (2012).
- 3062 [209] C. V. Daniel Barrow, T2K-SK Detector Matrix Uncertainties - MaCh3 In-
3063 tegration, <https://git.t2k.org/t2k-sk/t2ksk-detcovmat/-/tree/feature/MaCh3Integration>, Accessed: 22-06-2022.
- 3064
- 3065 [210] R. Wendell, *Three Flavor Oscillation Analysis of Atmospheric Neutrinos in Super-*
3066 *Kamiokande*, PhD thesis, University of North Carolina, 2008.
- 3067 [211] A. M. Dziewonski and D. L. Anderson, Phys. Earth Planet. Inter. **25**, 297 (1981).
- 3068 [212] e. a. D. Barrow, T2K Technical Note **425** (2022).
- 3069 [213] R. G. Calland, A. C. Kaboro, and D. Payne, **9**, P04016 (2014).
- 3070 [214] R. Wendell, <http://www.phy.duke.edu/raw22/public/Prob3++/>.
- 3071 [215] F. Kallenborn, C. Hundt, S. Böser, and B. Schmidt, Computer Physics Communi-
3072 cations **234**, 235 (2019).
- 3073 [216] L. Warsame, MaCh3 Analysis Progress.
- 3074 [217] S. Bourret, J. A. B. Coelho, and V. V. E. and, Journal of Physics: Conference Series
3075 **888**, 012114 (2017).
- 3076 [218] C. Rott, A. Taketa, and D. Bose, Scientific Reports **5** (2015).
- 3077 [219] K. Hagiwara, N. Okamura, and K. ichi Senda, Journal of High Energy Physics
3078 **2011** (2011).
- 3079 [220] D. Typinski, Earth Gravity, <http://www.typnet.net/Essays/EarthGravGraphics/EarthGrav.pdf>, Accessed: 24-06-2022.
- 3080
- 3081 [221] R. Barlow and C. Beeston, Comput. Phys. Commun. **77**, 219 (1993).
- 3082 [222] J. S. Conway, Incorporating nuisance parameters in likelihoods for multisource

3083

spectra, 2011.

3084 List of Figures

<small>3085</small>	2.1. The cross-section of neutrinos from various natural and man-made sources as a function of neutrino energy. Taken from [25]	10
<small>3086</small>		
<small>3087</small>	2.2. The solar neutrino flux as a function of neutrino energy for various fusion reactions and decay chains as predicted by the Standard Solar Model. Taken from [26].	11
<small>3088</small>		
<small>3089</small>		
<small>3090</small>	2.3. Left panel: The atmospheric neutrino flux for different neutrino flavours as a function of neutrino energy as predicted by the 2007 Honda model (“This work”) [43], the 2004 Honda model (“HKKM04”) [44], the Bartol model [42] and the FLUKA model [46]. Right panel: The ratio of the muon to electron neutrino flux as predicted by all the quoted models. Both figures taken from [43].	14
<small>3091</small>		
<small>3092</small>		
<small>3093</small>		
<small>3094</small>		
<small>3095</small>		
<small>3096</small>	2.4. A diagram illustrating the definition of zenith angle as used in the Super Kamiokande experiment [47].	14
<small>3097</small>		
<small>3098</small>	2.5. Prediction of $\nu_e, \bar{\nu}_e, \nu_\mu, \bar{\nu}_\mu$ fluxes as a function of zenith angle as calculated by the HKKM model [45]. The left, middle and right panels represent three values of neutrino energy, 0.32GeV, 1.0GeV and 3.2GeV respectively. Predictions for other models including Bartol [42], Honda [43] and FLUKA [46] are given in [47].	15
<small>3099</small>		
<small>3100</small>		
<small>3101</small>		
<small>3102</small>		
<small>3103</small>	2.6. Constraints on the atmospheric oscillation parameters, $\sin^2(\theta_{23})$ and Δm_{23}^2 , from atmospheric and long baseline experiments: SK [52], T2K [53], NO ν A [54], IceCube [55] and MINOS [56]. Figure taken from [57].	16
<small>3104</small>		
<small>3105</small>		
<small>3106</small>	2.7. Reactor electron antineutrino fluxes for ^{235}U (Black), ^{238}U (Green), ^{239}Pu (Purple), and ^{241}Pu (Orange) isotopes. The inverse β -decay cross-section (Blue) and corresponding measurable neutrino spectrum (Red) are also given. Top panel: Schematic of Inverse β -decay interaction including the eventual capture of the emitted neutron. This capture emits a γ -ray which provides a second signal of the event. Taken from [69].	19
<small>3107</small>		
<small>3108</small>		
<small>3109</small>		
<small>3110</small>		
<small>3111</small>		
<small>3112</small>	3.1. A schematic diagram of the Super-Kamiokande Detector. Taken from [88].	25

3113	3.2. The location of “standard PMTs” (red) inside the SK detector. Taken from [86].	29
3114		
3115	3.3. Schematic view of the data flow through the data acquisition and online system. Taken from [102].	32
3116		
3117	3.4. The cross-section view of the Tokai to Kamioka experiment illustrating the beam generation facility at J-PARC, the near detector situated at a baseline of 280m and the Super Kamiokande far detector situated 295km from the beam target.	35
3118		
3119		
3120		
3121	3.5. The near detector suite for the T2K experiment showing the ND280 and INGRID detectors. The distance between the detectors and the beam target is 280m.	36
3122		
3123		
3124	3.6. Top panel: Bird’s eye view of the most relevant part of primary and sec- ondary beamline used within the T2K experiment. The primary beam- line is the main-ring proton synchrotron, kicker magnet, and graphite target. The secondary beamline consists of the three focusing horns, decay volume, and beam dump. Figure taken from [118]. Bottom panel: The side-view of the secondary beamline including the focusing horns, beam dump and neutrino detectors. Figure taken from [119].	38
3125		
3126		
3127		
3128		
3129		
3130		
3131	3.7. The Monte Carlo prediction of the energy spectrum for each flavour of neutrino (ν_e , $\bar{\nu}_e$, ν_μ and $\bar{\nu}_\mu$) in the neutrino dominated beam FHC mode (Left) and antineutrino dominated beam RHC mode (Right) expected at SK. Taken from [120].	39
3132		
3133		
3134		
3135	3.8. Top panel: T2K muon neutrino disappearance probability as a function of neutrino energy. Middle panel: T2K electron neutrino appearance probability as a function of neutrino energy. Bottom panel: The neutrino flux distribution for three different off-axis angles (Arbitrary units) as a function of neutrino energy.	41
3136		
3137		
3138		
3139		
3140	3.9. The components of the ND280 detector. The neutrino beam travels from left to right. Taken from [118].	42
3141		
3142	3.10. Comparison of data to Monte Carlo prediction of integrated deposited energy as a function of track length for particles that stopped in FGD1. Taken from [123].	44
3143		
3144		

3145	3.11. Schematic design of a Time Projection Chamber detector. Taken from [124].	45
3146	3.12. The distribution of energy loss as a function of reconstructed momentum for charged particles passing through the TPC, comparing data to Monte Carlo prediction. Taken from [124].	45
3147		
3148		
3149	3.13. A schematic of the P0D side-view. Taken from [125].	47
3150	3.14. Left panel: The Interactive Neutrino GRID on-axis Detector. 14 modules are arranged in a cross-shape configuration, with the center modules being directly aligned with the on-axis beam. Right panel: The layout of a single module of the INGRID detector. Both figures are recreated from [118].	49
3151		
3152		
3153		
3154		
3155	4.1. Example of using Monte Carlo techniques to find the area under the blue line. The gradient and intercept of the line are 0.4 and 1.0 respectively. The area found to be under the curve using one thousand samples is 29.9 units.	54
3156		
3157		
3158		
3159	4.2. The area under a line of gradient 0.4 and intercept 1.0 for the range $0 \leq x \leq 10$ as calculated using Monte Carlo techniques as a function of the number of samples used in each repetition. The analytical solution to the area is 30 units as given by the red line.	54
3160		
3161		
3162		
3163	4.3. Three MCMC chains, each with a stationary distribution equal to a Gaussian centered at 0 and width 1 (As indicated by the black dotted lines). All of the chains use a Gaussian proposal function but have different widths (or 'step size σ '). The top panel has $\sigma = 0.1$, middle panel has $\sigma = 0.5$ and the bottom panel has $\sigma = 5.0$.	60
3164		
3165		
3166		
3167		
3168	4.4. The log-likelihood from the fit detailed in DB: Link to AsimovA Sensitivity Section as a function of the number of steps accumulated in each fit. Many independent MCMC chains were run in parallel and overlaid on this plot. The red line indicates the 1×10^5 step burn-in period after which the log-likelihood becomes stable.	61
3169		
3170		
3171		
3172		

3173	4.5. Left: The two dimensional probability distribution for two correlated parameters x and y . The red distribution shows the two dimensional probability distribution when $0 \leq x \leq 5$. Right: The marginalised probability distribution for the y parameter found when requiring the x to be bound between $-5 \leq x \leq 5$ and $0 \leq x \leq 5$ for the black and red distribution, respectively.	63
3179	5.1. The NEUT prediction of the ν_μ -H ₂ O cross-section overlaid on the T2K ν_μ flux. The charged current (black, solid) and neutral current (black, dashed) inclusive, charged current quasi-elastic (blue, solid), charged current 2p2h (blue, dashed), charged current single pion production (pink), and charged current multi- π and DIS (Purple) cross-sections are illustrated. Figure taken from [159].	71
3185	5.2. Illustration of the various processes which a pion can undergo before exiting the nucleus. Taken from [173].	72
3187	5.3. Event displays from Super Kamiokande illustrating the “crisp” ring from a muon and the typically “fuzzier” electron ring. Each pixel represents a PMT and the color scheme denotes the accumulated charge deposited on that PMT. Figures taken from [181].	75
3191	5.4. The difference of the electron-like and muon-like log-likelihood compared to the reconstructed single-ring fit momentum for atmospheric ν_e (left) and ν_μ (right) samples. The black line represents the cut used to discriminate electron-like and muon-like events, which coefficients obtained from Monte Carlo studies. Figures taken from [180].	79
3196	5.5. The electron/muon PID separation parameter for all sub-GeV single-ring events in SK-IV. The charged current (CC) component is broken down in four flavours of neutrino (ν_μ , $\bar{\nu}_\mu$, ν_e and $\bar{\nu}_e$). Events with positive values of the parameter are determined to be electron-like.	80
3200	5.6. The variation of the measured dark rate as a function of date, broken down by PMT type. The SK-IV and SK-V periods span September 2008 to May 2018 and January 2019 to July 2020, respectively. The break in measurement in 2018 corresponds to the period of tank repair and refurbishment. Figure adapted from [185].	82

3205	5.7. Comparison of the measured raw charge deposited per event from the 3206 stopping muon data samples between SK-IV (Blue) and SK-V (Red), 3207 split by the primary muon subevent and the associated decay electron 3208 subevent.	83
3209	5.8. The distribution of the reconstructed momentum from the muon ring 3210 divided by the distance between the reconstructed muon and decay 3211 electron vertices as found in the stopping muon data sets of SK-IV 3212 (Black) and SK-IV (Red). Only events with one tagged decay electron are 3213 considered. A Gaussian fit is considered in the range [2.0, 2.4] MeV/cm 3214 and illustrated as the solid curve.	84
3215	5.9. The χ^2 difference between the SK-IV and SK-V reconstructed muon 3216 momentum divided by range when the SK-V is modified by the scaling 3217 parameter α . Both additive (Blue) and multiplicative (Black) scaling 3218 factors have been considered. In practice, the additive scaling factor 3219 actually uses the value of $(\alpha - 1.0)$ but is illustrated like this so the 3220 results can be shown on the same axis range.	85
3221	5.10. A depiction of the topology patterns for fully-contained (FC), partially- 3222 contained (PC) and up-going muon (Up- μ) samples included in this 3223 analysis.	86
3224	5.11. The predicted neutrino flux of the fully contained (FC) sub-GeV and 3225 multi-GeV, partially contained (PC), and upward-going muon (Up- μ) 3226 events. The prediction is broken down by the $\nu_x \rightarrow \nu_e$ prediction (top 3227 left), $\nu_x \rightarrow \nu_\mu$ prediction (top right) and $\nu_x \rightarrow \nu_\tau$ prediction (bottom). 3228 Asimov A oscillation parameters are assumed (given in Table 2.2). . . .	88
3229	5.12. The predicted flux of beam neutrinos, as a function of neutrino energy. 3230 The predictions are broken down by the number of decay electrons 3231 associated with the particular events. Asimov A oscillation parameters 3232 are assumed (given in Table 2.2).	90

3266	6.7. The predicted neutrino energy distribution for subGeV atmospheric 3267 and beam samples. FHC and RHC beam samples are summed together 3268 Asimov A oscillation parameters are assumed (given in Table 2.2). Beam 3269 and atmospheric samples with similar cuts are compared against one 3270 another.	113
3271	6.8. The interaction mode contribution of each sample given as a fraction 3272 of the total event rate in that sample. Asimov A oscillation parameters 3273 are assumed (given in Table 2.2). The Charged Current (CC) modes are 3274 broken into quasi-elastic (QE), 2p2h, resonant charged pion production 3275 ($1\pi^\pm$), multi-pion production ($M\pi$), and other interaction categories. 3276 Neutral Current (NC) interaction modes are given in interaction mode 3277 categories: π^0 production, resonant charged pion production, multi- 3278 pion production, and others.	114
3279	6.9. Down-going atmospheric subGeV single-ring samples comparing the 3280 mean and error of the pre-fit and post-fit Monte Carlo predictions 3281 in red and blue, respectively. The magenta histogram illustrates the 3282 Monte Carlo prediction using the generated dial values. The black 3283 points illustrate the down-going data with statistical errors given. The 3284 mean and errors of the Monte Carlo predictions are calculated by the 3285 techniques documented in subsection 4.3.4. The pre-fit spectrum is 3286 calculated by throwing the cross-section and atmospheric flux dial 3287 values from the pre-fit covariance matrix. The post-fit spectrum is 3288 calculated by sampling the cross-section dial values from an ND fit 3289 MCMC chain, whilst still throwing the atmospheric flux dials from the 3290 pre-fit covariance.	117
3291	6.10. The ring counting parameter as defined in Equation 6.6 for the SubGeV-elike-0dcy 3292 and MultiRing-elike-nue samples.	126
3293	6.11. The ring counting parameter, defined in Equation 6.6, as a function 3294 of the number of reconstructed rings as found by the <code>fitQun</code> recon- 3295 struction algorithm. Left: true ν_μ events with only one muon above 3296 the Cherenkov threshold in the final state. Right: true ν_μ events with 3297 one muon and at least one other charged particle above the Cherenkov 3298 threshold in the final state.	127

3299	6.12. The χ^2 between the hybrid- π^0 Monte Carlo and data samples, as a function of smear (α) and shift (β) parameters, for events which have $1\pi^0$ final state topology. Left: Electron-muon separation PID parameter for events with $30 \geq E_{vis}(MeV) < 300$. Right: Electron- π^0 separation PID parameter for events with $30 \geq E_{vis}(MeV) < 300$	128
3300		
3301		
3302		
3303		
3304	6.13. The distribution of $\log(L_e/L_\mu)$ compared to $\log(L_e/L_\pi)$ for subGeV events with zero (top left), one (top right) or two (bottom) decay electrons. The correlation in the distribution is calculated as 0.997, 0.999 and 0.996, respectively.	129
3305		
3306		
3307		
3308	7.1. The density of the Earth given as a function of the radius, as given by the PREM model (Black), and the constant density four-layer approximation (Blue), as used in the official SK-only analysis.	133
3309		
3310		
3311	7.2. An “oscillogram” that depicts the $P(\nu_\mu \rightarrow \nu_e)$ oscillation probability as a function of neutrino energy and cosine of the zenith angle. The zenith angle is defined such that $\cos(\theta_Z) = 1.0$ represents neutrinos that travel from directly above the detector. The four-layer constant density PREM model approximation is used and Asimov A oscillation parameters are assumed (Table 2.2).	134
3312		
3313		
3314		
3315		
3316		
3317	7.3. The effect of δ_{CP} for atmospheric neutrinos given in terms of the neutrino energy and zenith angle. This oscillogram compares the $P(\nu_\mu \rightarrow \nu_e)$ oscillation probability for a CP conserving ($\delta_{CP} = 0.0$) and a CP violating ($\delta_{CP} = -1.601$) value taken from the Asimov A parameter set. The other oscillation parameters assume the Asimov A oscillation parameter set given in Table 2.2.	135
3318		
3319		
3320		
3321		
3322		

3323 7.4. An illustration of the matter-induced effects on the oscillation probability, given as a function of neutrino energy and zenith angle. The top row 3324 of panels gives the $P(\nu_e \rightarrow \nu_e)$ oscillation probability and the bottom 3325 row illustrates the $P(\bar{\nu}_e \rightarrow \bar{\nu}_e)$ oscillation probability. The left column 3326 highlights the oscillation probability in a vacuum, whereas the middle 3327 and right column represents the oscillation probabilities when the four- 3328 layer fixed density PREM model is assumed. All oscillation probabilities 3329 assume the “Asimov A” set given in Table 2.2, but importantly, the right 3330 column sets an inverted mass hierarchy. The “matter resonance” effects 3331 at $E_\nu \sim 5\text{GeV}$ can be seen in the $P(\nu_e \rightarrow \nu_e)$ for normal mass hierarchy 3332 and $P(\bar{\nu}_e \rightarrow \bar{\nu}_e)$ for inverted hierarchy.	136
3334 7.5. The oscillation probability for beam neutrino events given as a function 3335 of neutrino energy. All oscillation parameters assume the “Asimov A” 3336 set given in Table 2.2 unless otherwise stated. Each panel represents a 3337 change in one of the oscillation parameters whilst keeping the remaining 3338 parameters fixed.	137
3339 7.6. The number of electron-like events in the FHC and RHC operating 3340 mode of the beam, as a function of the oscillation probabilities. Both 3341 normal hierarchy (Solid) and inverse hierarchy (Dashed) values of 3342 Δm_{23}^2 are given.	138
3343 7.7. The oscillation probability $P(\nu_\mu \rightarrow \nu_e)$, given as a function of neutrino 3344 energy and zenith angle, which highlights an example of the “fast” 3345 oscillations in the sub-GeV upgoing region.	140
3346 7.8. Illustration of the averaging procedure for $N = 2$. The oscillation 3347 probabilities calculated on the finer left binning are averaged to obtain 3348 the oscillation probabilities in the coarser right binning. These averaged 3349 oscillation probabilities with the coarser binning are then applied to 3350 each event during the fit.	142
3351 7.9. Event rate of the SubGeV_elike_0dcy sample as a function of the num- 3352 ber of sub-divisions per coarse bin. Each subplot represents the event 3353 rate of the sample at a different oscillation parameter set thrown from 3354 the PDG priors detailed in Table 2.1. The red line in each subplot 3355 represents the mean of the event rate over the different values of sub- 3356 divisions for that particular oscillation parameter throw.	144

3357	7.10.	145
3358	7.11.	146
3359	7.12. Variance of event rate for each atmospheric sample as a function of the number of sub-divisions per coarse bin. The solid red line indicates the 0.1% threshold and the dashed red line indicates the variance at a sub-division $N = 10$.	147
3363	7.13. Variance of sample likelihood, when compared to ‘Asimov data’ set at Asimov A, for each atmospheric sample as a function of the number of sub-divisions per coarse bin. The solid red line indicates the 0.1% threshold and the dashed red line is a graphical indication of the variance at a sub-division $N = 10$.	148
3368	7.14. The oscillation probability, $P(\nu_\mu \rightarrow \nu_e)$ (top row) and $P(\nu_e \rightarrow \nu_e)$ (bottom row), given as a function of neutrino energy and zenith angle. The left column gives the “fine” binning used to calculate the oscillation probabilities and the right column illustrates the “coarse” binning used to reweight the Monte Carlo events. The fine binning choice is given with $N = 10$, which was determined to be below the threshold from Figure 7.12 and Figure 7.13.	149
3375	7.15. The calculation time taken to both calculate the oscillation probabilities and fill the “coarse” oscillograms, following the technique given in section 7.2, for the CUDAProb3 and ProbGPU (Red) calculation engines. CUDAProb3 has both a GPU (Blue) and CPU (Black) implementation, where the CPU implementation is multithreaded. Therefore, 8-threads (solid) and 40-threads (dashed) configurations have been tested. Prob3, which is a CPU single-thread implementation has a mean step time of 1.142s.	150
3383	7.16. The oscillation probability, $P(\nu_\mu \rightarrow \nu_e)$ (top row) and $P(\nu_e \rightarrow \nu_e)$ (bottom row), given as a function of neutrino energy and zenith angle. The left column gives probabilities where the constant $Z/A = 0.5$ approximation which is used in the official SK-only analysis. The middle column gives the probabilities where $Z/A = [0.468, 0.498]$ values are used, as given in Table 7.1. The right column illustrates the difference in oscillation probability between the two different techniques.	152

3390	7.17. The density of the Earth given as a function of the radius, as given by the PREM model (Black), the constant density four-layer approxima- tion (Blue), as used in the official SK-only analysis, and the quadratic approximation of the PREM model (Red).	154
3394	7.18. The oscillation probability, $P(\nu_\mu \rightarrow \nu_e)$ (top row) and $P(\nu_e \rightarrow \nu_e)$ (bot- tom row), given as a function of neutrino energy and zenith angle. The left column gives probabilities where the four-layer constant density ap- proximation is used. The middle column gives the probabilities where the density is integrated over the trajectory, using the quadratic PREM approximation, for each $\cos(\theta_Z)$ is used. The right column illustrates the difference in oscillation probability between the two different techniques.	155
3401	7.19. The oscillation probability, $P(\nu_\mu \rightarrow \nu_e)$ (top row) and $P(\nu_e \rightarrow \nu_e)$ (bot- tom row), given as a function of neutrino energy and zenith angle. The left column gives probabilities where a fixed production height of 25km is used. The middle column gives the probabilities where the produc- tion height is analytically averaged. The right column illustrates the difference in oscillation probability between the two different techniques.	159
3407	8.1. The response of the likelihood, as defined in section 8.1, illustrating the response of the samples to the oscillation parameters. Δm_{12}^2 and $\sin^2(\theta_{12})$ are negated because these samples have no sensitivity to those parameters. The Asimov data set is built using the pre-fit dial values assuming Asimov A oscillation parameters defined in Table 2.2. DB: Need finer binning on delmsq23	164
3413	8.2. Two-dimensional log-likelihood scan of the appearance ($\sin^2(\theta_{13})$ - δ_{CP}) parameters showing the response of the beam samples (top), atmo- spheric samples (middle) and the summed response (bottom). The Asimov A oscillation parameters, defined in Table 2.2, are assumed to be the true point (Black Cross). The position of the smallest log- likelihood is highlighted with the triangle. Prior uncertainty terms of the oscillation parameters are neglected. The two(three) sigma contour levels are illustrated with the dashed(solid) red line.	167

3421	8.3. Two-dimensional log-likelihood scan of the disappearance ($\sin^2(\theta_{23})$	
3422	- Δm_{23}^2) parameters showing the response of the beam samples (top),	
3423	atmospheric samples (middle) and the summed response (bottom). The	
3424	Asimov A oscillation parameters, defined in Table 2.2, are assumed	
3425	to be the true point (Black Cross). The position of the smallest log-	
3426	likelihood is highlighted with the triangle. Prior uncertainty terms of	
3427	the oscillation parameters are neglected. The two(three) sigma contour	
3428	levels are illlustrated with the dashed(solid) red line.	168
3429	A.1. Breakdown by interaction mode of the FC Sub-GeV atmospheric sam-	
3430	ples targeting CC0 π events.	172
3431	A.2. Breakdown by interaction mode of the FC Sub-GeV atmospheric sam-	
3432	ples targeting single pion events.	173
3433	A.3. Breakdown by interaction mode of the FC Multi-GeV single ring atmo-	
3434	spheric samples.	174
3435	A.4. Breakdown by interaction mode of the FC Multi-GeV multi-ring atmo-	
3436	spheric samples.	175
3437	A.5. Breakdown by interaction mode of the PC atmospheric samples.	176
3438	A.6. Breakdown by interaction mode of the atmospheric upward going	
3439	muon samples.	177

3440 List of Tables

3441	2.1. The 2018 Particle Data Group constraints of the oscillation parameters 3442 taken from [81]. The value of Δm_{23}^2 is given for both normal hierarchy 3443 (N.H.) and inverted hierarchy (I.H.) and $\sin^2(\theta_{23})$ is broken down by 3444 whether its value is below (Q1) or above (Q2) 0.5.	21
3445	2.2. Reference values of the neutrino oscillation parameters for two different 3446 oscillation parameter sets.	22
3447	3.1. The various SK periods and respective live-time. The SK-VI live-time is 3448 calculated until 1 st April 2022. SK-VII started during the writing of this 3449 thesis.	24
3450	3.2. The trigger thresholds and extended time windows saved around an 3451 event which were utilised throughout the SK-IV period. The exact 3452 thresholds can change and the values listed here represent the thresh- 3453 olds at the start and end of the SK-IV period.	33
3454	3.3. The threshold momentum and energy for a particle to generate Cherenkov 3455 light in ultrapure water, as calculated in Equation 3.2 in ultrapure water 3456 which has refractive index $n = 1.33$	34
3457	4.1. Jeffreys scale for strength of preference for two models A and B as a 3458 function of the calculated Bayes factor ($B_{AB} = B(A/B)$) between the 3459 two models [140]. The original scale is given in terms of $\log_{10}(B(A/B))$ 3460 but converted to linear scale for easy comparison throughout this thesis.	66
3461	6.1. The amount of data collected in each detector used within this analysis. 3462 The data collected at the near and far detector, for both neutrino beam 3463 (FHC) and antineutrino beam (RHC), is measured as the number of 3464 protons on target (POT).	91
3465	6.2. The fully contained subGeV samples, defined as events with visible 3466 energy $E_{vis} < 1.33\text{GeV}$, used within this oscillation analysis.	94

3467 6.3. The fully contained multiGeV samples used within this oscillation analysis. Both the sample name and description are given.	96
3468	
3469 6.4. The purity of each atmospheric sample used within this analysis, broken down by charged current (CC) and neutral current (NC) interactions and which neutrino flavour interacted within the detector. Asimov A oscillation parameter sets are assumed (given in Table 2.2). Electron neutrino and antineutrino events are separated to illustrate the ability of the separation likelihood cuts used within the multiGeV and multiring sample selections.	97
3470	
3471	
3472	
3473	
3474	
3475	
3476 6.5. The neutrino energy binning for the different neutrino flavours. “Right” sign indicates neutrinos in the FHC beam and antineutrinos in the RHC beam. “Wrong” sign indicates antineutrinos in the FHC beam and neutrinos in the RHC beam. The binning of the detector response is identical for the FHC and RHC modes as well as at ND280 and SK. . .	109
3477	
3478	
3479	
3480	
3481 6.6. List of cut variables that are included within the shift/smear fit documented in [199].	119
3482	
3483 6.7. Reconstructed event topology categories on which the SK detector systematics [199] are based.	120
3484	
3485 6.8. Sources of systematic errors specified within the grouped into the “calibration” systematics model.	123
3486	
3487 6.9. Visible energy binning for which the correlated SK detector systematics are based	124
3488	
3489 7.1. Description of the four layers of the Earth invoked within the constant density approximation of the PREM model [211].	132
3490	
3491 7.2. The quadratic polynomial fits to the PREM model for four assumed layers of the PREM model. The fit to calculate the coefficients is given in [212], where $x = R/R_{Earth}$	154
3492	
3493	
3494 8.1. The Monte Carlo prediction of each sample observed at SK used within this analysis. Three model parameter tunes are considered, as defined in subsection 6.4.3. The oscillated predictions assumed Asimov A oscillation parameters provided in Table 2.2.	169
3495	
3496	
3497	

